

A model-aware inexact Newton scheme for electrical impedance tomography

Zur Erlangung des akademischen Grades eines
Doktors der Naturwissenschaften (Dr. rer. nat.)

von der Fakultät für Mathematik
des Karlsruher Instituts für Technologie (KIT)
genehmigte

DISSERTATION

von

Dipl.-Math. techn. Robert Winkler

Datum der mündlichen Prüfung:	20. April 2016
Referent:	Professor Dr. Andreas Rieder
Korreferent:	Professor Dr. Christian Wieners

Abstract

Electrical impedance tomography (EIT) is a non-invasive method for imaging the electrical conductivity of an object from electrode measurements on its surface. Possible applications and the diagnostic value of EIT depend on the quality of the EIT images, that is, on their resolution and their reliability. Moreover, computational efficiency and ease of use are desired for clinical routine. To obtain a conductivity image from the measurements, a mathematical inverse conductivity problem (ICP) needs to be solved which suffers in several respects: It is highly nonlinear, severely ill-posed, highly underdetermined, and some necessary model parameters are usually not known accurately.

This work contributes to the development of EIT in two regards: By providing new theoretical insights into the underlying mathematical model, and by optimizing and extending an efficient general purpose inversion scheme to harmonize with the ICP.

In the first part, a novel analytic relation between the underlying conductivity and the observed data is derived for non-concentric circular geometries. From that relation, quantitative insights about the instability of the ICP and the resolution of a given EIT setting are derived. Based on this data, a discretization of the conductivity space is proposed which complies with the maximal resolution of the setting. In the second part, a holistic reconstruction framework is introduced which estimates unknown model parameters prior to solving the ICP with an inexact Newton-type method. The performance and reliability of this framework is improved by eliminating sources of instabilities, by abandoning generic assumptions, and by gathering and using prior knowledge about the specific setting and model. In particular, a tailored conductivity transformation decreases the nonlinearity, while a novel weighting scheme resolves the underdetermination of a subproblem by promoting non-oscillatory conductivities. The versatility of the proposed framework allows us to incorporate additional problem-specific optimizations, three of which are showcased and evaluated in this work. All theoretical findings are complemented by extensive numerical studies that verify the efficiency and robustness of the proposed framework for a variety of experiments with simulated and measured data.

Contents

1. Introduction	1
1.1. Background	1
1.2. Scope and outline	3
2. Principles of electrical impedance tomography	6
2.1. Forward models	6
2.1.1. Maxwell’s equations for electrical conductivity	6
2.1.2. Calderón’s model	7
2.1.3. The complete electrode model	9
2.1.4. Fréchet-differentiability of the forward operators	12
2.2. Noise model	13
2.2.1. Modelling data noise	13
2.2.2. Generating noisy data	14
2.3. Model discretization	15
2.3.1. Finite element discretization for solving the forward problem	15
2.3.2. Discretization of the conductivity space	15
2.3.3. Computation of the Fréchet derivative	16
2.4. The inverse conductivity problem	17
2.4.1. Nonlinearity	18
2.4.2. Constrainedness	18
2.4.3. Uniqueness	18
2.4.4. Ill-posedness	18
2.4.5. Model uncertainties	20
2.4.6. Iterative inversion methods	21
2.4.7. Inexact Newton-type methods	22
3. Sensitivity analysis of the complete electrode model	25
3.1. Sensitivity and distinguishability	26
3.2. Analytic solutions on the disk	27
3.2.1. Solutions for concentric conductivity perturbations	28
3.2.2. A generalization using conformal maps	35

Contents

3.3.	Sensitivity distribution on the disk	41
3.4.	Comparison of Calderón’s model and the complete electrode model	45
3.4.1.	A sensitivity estimate for Calderón’s model	45
3.4.2.	Comparison with results of MacMillan et al.	47
3.5.	Sensitivity-based discretizations	48
3.5.1.	Optimal resolution meshes on the disk	49
3.5.2.	A heuristic approximation of sensitivity based discretizations	53
3.5.3.	Adaptive meshes for simply connected domains	56
3.5.4.	Adaptive triangulations	58
3.6.	Sensitivity analysis: conclusions	61
4.	Model-aware inversion	62
4.1.	Initialization	63
4.1.1.	Conductivity and contact impedance initialization	64
4.1.2.	Noise level initialization	71
4.1.3.	Measurement protocol and incomplete data	73
4.2.	Nonlinearity and constrainedness	74
4.3.	Underdetermination and prior assumptions	77
4.3.1.	A reconstruction prior for the Newton update	78
4.3.2.	Continuum interpretation of the weighted inner product	83
4.3.3.	The reconstruction prior for the transformed forward operator	84
4.4.	Inexact Newton updates and regularization parameters	85
4.4.1.	Weighted conjugate gradient iteration	86
4.4.2.	Safeguarding for the linear problem	86
4.4.3.	Safeguarding for the nonlinear problem	87
4.4.4.	Regularized weighted conjugate gradient algorithm	87
4.4.5.	Stopping rule and REGINN parameters	88
4.5.	A model-aware Newton-type inversion scheme	90
5.	Problem-specific extensions to the inversion scheme	92
5.1.	Recovering model parameters	92
5.1.1.	Fréchet derivative with respect to the electrode geometry	94
5.1.2.	Fréchet derivative with respect to the contact impedances	98
5.1.3.	Assembly of the sensitivity matrix and the weight matrix	98
5.2.	Sparsity and Banach space methods	100
5.3.	Iterated nonlinear filtering	102

Contents

6. Numerical results	104
6.1. Numerical settings	105
6.1.1. Setting A: Circular perturbation inside the unit disk	106
6.1.2. Setting B: Thorax cross-section	107
6.1.3. Setting C: Mixed backgrounds and contrasts	108
6.1.4. Setting D: Non-convex domain with a non-convex inclusion	109
6.1.5. Setting E: 3D thorax model	110
6.1.6. Setting F: Saline tank experiments, part 1	111
6.1.7. Setting G: Saline tank experiments, part 2	112
6.2. Impact of the conductivity transformation and the weights	114
6.2.1. Results for setting A	114
6.2.2. Results for setting B	119
6.2.3. Results for setting C	123
6.2.4. Results for setting D	127
6.3. 3D reconstructions	128
6.4. Reconstruction on sensitivity-based meshes	131
6.4.1. Comparison of sensitivity based and uniform discretizations	131
6.4.2. Impact of the discretization refinement	134
6.5. Model parameter reconstructions	135
6.5.1. Incorrect model: “badly attached” electrodes	135
6.5.2. Incorrect model: highly fluctuating contact impedances	136
6.5.3. Incorrect model: wrong boundary geometry	137
6.5.4. Incorrect model: wrong contact impedances and boundary geometry	137
6.6. Banach space reconstructions	138
6.7. Reconstructions using nonlinear filtering	141
6.8. Tank data reconstructions	143
6.9. Behaviour of the inexact Newton parameters during inversion	145
7. Conclusions	148
7.1. Contributions to the field of research	148
7.2. Limitations and future research	151
7.3. Final considerations	152
Appendix	154
A. A wealth of inversion approaches	155
B. Fourier coefficients of the extended complete electrode model	158

1. Introduction

1.1. Background

The question of determining the distribution of electrical conductivity inside heterogeneous objects arises in various disciplines of engineering sciences including medical imaging, geophysics, and process tomography. It first appeared in the 1930s [Sli33, Lan36] as a one-dimensional geophysical problem of identifying layers of soil of varying, material-specific electrical conductivity; that is, conductivity was considered as a parameter of depth. This was particularly useful for finding underground ores, oil, and gas deposits characterized by distinct conductivities. Electrical conductivity is the ability of a material to transport electric current, and requires charge carriers like freely moving electrons in metals, ions in liquids and plasmas, or electrons and holes in crystal lattices of semiconductors. Thus, the electrical conductivity is a material property, and knowing the conductivity values can be used to localize materials inside heterogeneous objects.

Medical interest started four decades later. Henderson and Webster presented an “impedance camera” [HW78] producing a two-dimensional projection-type image of the spatial distribution of the electrical conductivity inside the human thorax, and Barber and Brown introduced the first tomographic impedance imaging system; see [BB84]. The intracellular and extracellular areas in body tissue contain salt ions making them highly conductive, while the cell membrane is resistive, so different cellular structures lead to distinct electrical conductivities. This makes it possible to localize blood, bones, and different kinds of body tissue from conductivity data. In particular, the conductivity of healthy and cancerous cells may vary significantly [FM26, SSBS88] due to cell membrane damages and a different packing density of cancerous cells.

Recognizing the value for diagnostics and patient monitoring sparked a whole field of potential applications in non-invasive medical imaging, known as *electrical impedance tomography* (EIT). A key advantage over established imaging techniques is that the EIT measurement setup consists mainly of a current source, electrodes, a voltmeter, and multiplexers, which allows for cheap and mobile measurement devices. Potential medical applications comprise mammography, thorax-imaging, bedside lung monitoring, perfusion monitoring, and time difference (functional) EIT, for example in the human brain; see e.g. [Hol93, Fre00]. Moreover, EIT has non-medical applications in process tomography, where materials or liquids are checked for defects such as inclusions, cracks, or air bubbles, causing jumps in electrical conductivity [WB95].

1. Introduction

The mathematical foundation of EIT is Calderón’s pioneering work [Cal80], a note “*on an inverse boundary value problem*”. In general, *inverse problems* conclude on an underlying cause from given observed effects as input data. Conversely, finding an effect of a known cause is called the evaluation of the corresponding *forward operator* (*forward problem*). A forward operator in EIT assigns a current-potential behaviour on the domain boundary to each conductivity distribution in the interior. The mathematical task in EIT is the *inverse conductivity problem* (ICP), i.e. to determine the spatial conductivity distribution – or some information about it – from an observed current-potential boundary behaviour. The links between the conductivity and the current-potential behaviour are Kirchhoff’s current law and the conservation of charge, forming an elliptic *partial differential equation* (PDE) for the potential inside the domain, in which the conductivity appears as a coefficient.

The central aspects of the ICP are its *uniqueness* (“Is the conductivity fully characterized by the observed data?”), its *stability* (“Can we continuously conclude from the data on the underlying conductivity?”) and its *recoverability* (“Is there a feasible inversion algorithm to solve the ICP?”). The first two questions have been solved for Calderón’s problem, with a negative answer on the stability [Ale88] and positive answers on the uniqueness in very general settings in two and three dimensions; see [AP06, Uhl09]. Moreover, a variety of inversion schemes to solve the ICP have been proposed, with an outline of popular concepts following in the next section and in Appendix A.

Calderón’s boundary model for the ICP is fully continuous, i.e. applied currents and observed potentials are represented by Neumann and Dirichlet traces of interior potentials, respectively. This is appealing from an analytical point of view, since fundamental results from functional and complex analysis can be used to investigate the forward problem and the inverse problem. However in practice, currents and potentials can only be applied and accessed through electrodes, thus the data is inherently discrete. These electrodes introduce side-effects on the boundary behaviour. Being built from highly conductive materials, electrodes have a shunting effect on the interior potential. Moreover, electro-chemical effects at the electrode-domain interface cause a highly resistive layer at current-carrying electrodes, called the *contact impedance*. As a consequence, the boundary model was successively refined, from the simple *gap model* through a *shunt model* to the gold standard *complete electrode model* (CEM), which uses mixed (Robin-type) boundary conditions to model both the shunting effect and the contact impedances. It was verified to be both mathematically sound and physically accurate up to measurement precision [CING89, SCI92] in several tank experiments.

Unlike Calderón’s continuum boundary problem, the ICP for electrode models – i.e. the recovery of the conductivity from a *finite* set of electrode current-potential observations – is underdetermined. To assign a unique conductivity to an observed set of data, a restriction of the solution space is required. Additionally, the lack of stability, called *ill-posedness* of the ICP, is inherited from Calderón’s model. Finally, the mixed boundary conditions make it difficult to analyze the CEM, in particular to quantify the local instability of the ICP in various regions of the domain. For example, boundary data in Calderón’s model can be arbitrarily localized and the instability vanishes towards the bound-

1. Introduction

ary. This does not hold for the CEM, where the localization of currents and potentials is limited by the electrode and gap widths.

A tool to investigate the instability is the *local sensitivity*, i.e. the impact of local changes in conductivity to the observed current-potential behaviour at the electrodes. The local sensitivity has been recognized valuable and studied extensively for Calderón’s model e.g. in [SYB84, Isa86, SBB87, Dob92], and recently for the CEM, where it was used to obtain resolution guarantees [HU13] and to enhance the stability of the inversion [WR14].

As a consequence, inversion schemes profit from the exact modelling of the electrode behaviour and systematically addressing problems arising from this model. Firstly, model parameters like the domain geometry, the electrode location and the contact impedances have a huge impact on the measured data, and therefore should be known accurately, and otherwise estimated during the inversion process. Next, the restriction of the solution space should be both justified by the physical problem and suitable for obtaining uniqueness and supporting stability of the inversion process. Finally, the inversion algorithm must be computationally feasible. Moreover, it should be capable of incorporating prior assumptions on the underlying conductivity and applying regularization, based on noise and sensitivity information. For ease of use, it should be free of design parameters which require problem-specific tuning.

1.2. Scope and outline

Despite its clinical potential and an abundance of theoretical research on EIT, the severe ill-posedness of the ICP and the resulting low resolution of EIT images still greatly limit its diagnostic value. While combined imaging techniques counter some of the EIT inherent problems¹, there is still a clear demand for capable and reliable inversion schemes based purely on EIT data. Since the formulation of Calderón’s problem, a wealth of approaches to analyze and solve the ICP have been proposed, reflecting entirely different points of view of electrical engineers, physicians, and mathematicians, on the “same” medical imaging problem [BB84, KV87, YWT87, SV90, CIN⁺90, SCII91, WHWT93, DS94, RGA96, VVK⁺98, BH00, KKS00, SMI00, Bru01, PL02, Hol04, CCT05, LR06, BDGV08, LHH08, LR08, KNS08, MS12]. An outline of various popular concepts, including the preceding references, is given in Appendix A.

All concepts are based on a particular theoretical or heuristic design idea and have emerged and prevailed for very different reasons, including simplicity, ease of use, model reduction, rigorous

¹There are combined imaging methods like *magnetic resonance electrical impedance tomography* [SKW05] or *frequency-difference and ultrasound modulated electrical impedance tomography* [HLU15] which drastically improve the resolution and reduce the ill-posedness, and thus counter many of the problems arising in EIT. However, the additional machinery conflicts with the idea of a simple hardware setup, and makes it impractical for many EIT applications.

1. Introduction

mathematical uniqueness theory, or explicit design of regularization strategies in standard frameworks. Among the mathematical models, the gap between theoretical findings in Calderón’s model and the inherently finite electrode data is reflected by the conceptual discrepancy of the inversion schemes designed for these models. Moreover, the approaches usually focus on the inversion itself, and are content with the input data required by the model, rather than *extensively* gathering and incorporating prior information available for the ICP. Often, required model parameters, e.g. the contact impedances or the required regularization parameters, are fit “by hand” to obtain best results, which makes it difficult to use such an approach in an automated manner. To the knowledge of the author², the two commercial EIT systems currently available on the market (by Drägerwerk AG & Co. KGaA, Germany, and by swisstom AG, Switzerland) use a simple linearization of the ICP by default, thus falling short of their full potential for nonlinear inversion.

Yet, the best hope for obtaining useful reconstructions is to *gather all available information* about the accurate physical model, the setting, and the measured data, to *analyze and address difficulties* arising from the realistic complete electrode model, and to *incorporate this knowledge* into the inversion scheme.

Consequently, the purpose of this work is to address the ICP of the CEM in a holistic manner, to provide further research in all stages of the reconstruction procedure, and to assemble this knowledge into a model-tailored, efficient, and easy-to-use inversion scheme.

Firstly, it is essential to understand and analyze electrode models, paying special attention to the nature of the instabilities which the model introduces to the inverse problem. To that end, a sensitivity analysis of the CEM is performed in chapter 3. The main tool for this analysis is a novel analytic solution to the forward problem for the CEM in the presence of non-centered conductivity perturbations on the disk, which is presented in section 3.2 and proved in Appendix B. The sensitivity behaviour of the CEM is then investigated in section 3.3 and compared to Calderón’s model in section 3.4. In section 3.5, we show how the sensitivity information can be used to design resolution-based discretizations of the conductivity space, which prove to be superior over generic discretizations in our numerical examples. This discretization strategy for disks is extended heuristically to simply connected domains.

In chapter 4, a standard nonlinear iterative output-least-squares approach is analyzed and re-designed step by step to harmonize with the CEM. To set up the inversion scheme, a novel initialization strategy for CEM model parameters is derived in section 4.1, and a symmetry property of the model is used to estimate the data noise level and to obtain a stopping criterion for the iterative inversion. Next, we investigate the nonlinearity and constrainedness of the ICP, and transform the problem to be more suitable for unconstrained iterative linearization in section 4.2. Introducing a novel

²After personal correspondence with company representatives at the “International Conference on Biomedical Applications of Electrical Impedance Tomography” in 2014 and 2015.

1. Introduction

weighting scheme in section 4.3, two fundamental problems of the linearized problem – the underdetermination and the ill-posedness – can be addressed simultaneously. We show that this weighted solution satisfies a prior assumption on the conductivity, with the consequence that spurious oscillations are avoided when resolving the underdetermination of the linear problem. The last ingredient of the tailored inversion scheme is the regularized inexact Newton-type method REGINN, which was introduced in [Rie99] and first applied to the ICP in [LR06]. With a slight modification presented in section 4.5, it is free of design parameters. At that point, all steps can be combined to a *model-aware Newton-type inversion scheme* (MANTIS), a fast, stable, and easy to use reconstruction framework carefully designed for the CEM, without the need of hand-tuning regularization parameters or using calibration data. Note that most of the presented techniques can also be used independently to improve other, existing inversion schemes which profit from a well-founded model initialization, knowing error bounds, applying parameter transformations, or incorporating sensitivity information.

Various problem-specific extensions are showcased to emphasize the versatility of the presented MANTIS framework in chapter 5. In particular, it can be readily extended to handle geometry uncertainties with concepts from [VKV⁺02, DHH⁺12, DHSS13a] (section 5.1), to incorporate sparsity information using Banach spaces [MRLa14, MR14, Mar15] (section 5.2), and to apply heuristic concepts like iterated nonlinear filtering (section 5.3).

Finally, an extensive numerical evaluation of the presented concepts is performed in chapter 6. The individual and combined impacts of the inversion scheme modifications are studied in detail for various low and high contrast conductivities in circular and non-circular domains, for simulated and measured data, and for a varying number of electrodes, varying model parameters, and different noise levels. For the 3D reconstructions, MANTIS was incorporated into the open source MATLAB toolbox EIDORS [PL02] under GNU General Public Licence. It is available, along with a test script demonstrating how to use the MANTIS code in EIDORS, at SourceForge under <http://eidors3d.sourceforge.net> (developer version).

We start by introducing the mathematical framework in chapter 2.

2. Principles of electrical impedance tomography

In this chapter, the mathematical formulations of the forward and inverse conductivity problem in EIT are introduced. To that end, the behaviour of currents and potentials inside a conducting object is derived from Maxwell's equations, and the injection of currents and observation of boundary potentials is formulated mathematically in Calderón's continuum setting and in electrode settings in section 2.1. Next, the model is discretized in section 2.3, which is necessary for numerical treatment. This has significant effects on the behaviour of the inverse problem, which is introduced in the mathematical framework in section 2.4, and basic properties and issues are discussed.

2.1. Forward models

A forward model is a mathematical relation “in direction of causality”, that is, an effect is modelled for a given underlying cause. In EIT, the electrical conductivity of an object causes a characteristic potential inside the object and on its boundary when a current is injected. At this point, it is not intuitively clear whether the conductivity or the injected current should be considered the “cause” of the potential, as both together generate the potential. However, one is usually not content with a single current injection, but tries to consider *all possible* currents and their corresponding potentials. From this perspective, the conductivity can be considered the cause for an observed current-potential relation on the boundary. The connection between the conductivity, the currents and the potential fields can be derived from Maxwell's equations, which is outlined next.

2.1.1. Maxwell's equations for electrical conductivity

This work considers real-valued isotropic conductivities and time-static (direct current) measurements, that is, all frequency coefficients and changes in time disappear in Maxwell's equations. A more general derivation for time-harmonic fields is given e.g. in [MS12]. The relevant Maxwell's

2. Principles of electrical impedance tomography

equations in the time-static case are given as

$$\nabla \times E = 0, \quad (\text{Faraday's law}) \quad (2.1)$$

$$\nabla \times H = j, \quad (\text{Ampere's law}) \quad (2.2)$$

where E , H and j are the electric field, the magnetic strength, and the current density, respectively. Moreover, Ohm's law states that

$$j = \sigma E, \quad (2.3)$$

where σ is the electrical *conductivity*, i.e. the coefficient of interest in EIT.

On a simply connected domain, Faraday's law and the Kelvin-Stokes theorem imply that the irrotational electric field E is path independent, which in turn implies that E can be expressed as the gradient of a scalar potential u :

$$E = -\nabla u. \quad (2.4)$$

Observing that $\nabla \cdot (\nabla \times H) = 0$ and applying (2.3) and (2.4) to Ampere's law yields the *conservation of charge*

$$-\nabla \cdot (\sigma \nabla u) = 0, \quad (2.5)$$

a partial differential equation relating the conductivity σ to the interior potential u .

2.1.2. Calderón's model

Motivated by (2.5), Calderón's continuum model can now be formulated by introducing the proper function spaces. However, one has to pay attention to the spatial dimension of the problem, which is emphasized in the following

Remark 2.1 (Spatial dimension of the problem). While Maxwell's equations are given in three spatial dimensions, Calderón's classical formulation [Cal80] is given in \mathbb{R}^2 . Fortunately, both the forward and the inverse problem can be formulated independently of the spatial dimension. There are however notable technical differences in the uniqueness results of the ICP, mainly due to the rich structure of complex analysis that can be used to study the $\mathbb{R}^2 \cong \mathbb{C}$ problem, which is not available in \mathbb{R}^3 . In this work, the analysis of chapter 3 uses conformal mapping properties and is thus limited to the \mathbb{R}^2 setting, while all considerations of chapters 4 and 5, including the presented inversion scheme MANTIS, are independent of the spatial dimension. Consequently, the numerical simulations in chapter 6 are performed in two and three dimensions, except for those few relying on the discretizations derived in chapter 3. Thus, both cases are considered in the following unless explicitly stated otherwise.

2. Principles of electrical impedance tomography

Consider a compact, simply connected and piecewise smooth Lipschitz domain $\Omega \subset \mathbb{R}^n$, $n \in \{2, 3\}$, and let, for some $0 < c \ll 1$,

$$\sigma \in L_+^\infty(\Omega) = \left\{ \varphi \in L^\infty(\Omega) : c \leq \varphi \leq c^{-1} \text{ a.e.} \right\} \quad (2.6)$$

be an *isotropic conductivity coefficient* in the space of essentially bounded and positive functions on Ω . In the following, the usual notation $H^s(X) = W^{s,2}(X)$ for a Sobolev space of order $s \in \mathbb{R}$ is used. The subscript “ \diamond ” for a space H denotes vanishing mean, i.e. $H_\diamond := \{\varphi \in H : \langle \varphi, 1 \rangle_{H, H^*} = 0\}$, where H^* is the dual of H . A special case of interest in this work is $\mathbb{R}_\diamond^L = \left\{ x \in \mathbb{R}^L : \sum_{l=1}^L x_l = 0 \right\}$.

Definition 2.2 (Potentials and currents). Any function $u \in H^1(\Omega)$ satisfying (2.5) on Ω is called a *potential* for σ . Its boundary trace

$$f := u|_{\partial\Omega} \in H^{1/2}(\partial\Omega)$$

is called the according *boundary potential*, and

$$j_\nu := \nu \cdot j = \sigma \frac{\partial u}{\partial \nu} \in H^{-1/2}(\partial\Omega)$$

is called the outer normal boundary current density, or simply *boundary current*, where ν denotes the outer normal on $\partial\Omega$.

If u is such that

$$(j_\nu, f) \in H_\diamond^{-1/2}(\partial\Omega) \times H_\diamond^{1/2}(\partial\Omega),$$

then the pair (j_ν, f) is called a (continuum) *Neumann-Dirichlet (ND) datum* in this work.

A classical result for elliptic systems is that for any $j_\nu \in H_\diamond^{-1/2}(\partial\Omega)$, there exists a $u \in H^1(\Omega)$ such that (j_ν, f) is a ND datum and moreover, the maps

$$\begin{aligned} \mathcal{R}_\sigma : H_\diamond^{-1/2}(\partial\Omega) &\rightarrow H_\diamond^{1/2}(\partial\Omega), & j_\nu &\mapsto f, & (\text{continuum ND operator}) \\ \Lambda_\sigma : H_\diamond^{1/2}(\partial\Omega) &\rightarrow H_\diamond^{-1/2}(\partial\Omega), & f &\mapsto j_\nu, & (\text{continuum DN operator}) \end{aligned} \quad (2.7)$$

are bounded linear operators; see e.g. [McL00]. The condition $j_\nu \in H_\diamond^{-1/2}(\partial\Omega)$ is a *conservation of charge condition* as the normal current density over the boundary integrates to zero. It is necessary for the existence of a solution. The condition $f \in H_\diamond^{1/2}(\partial\Omega)$ is a *grounding condition* for the potential, making f and $u = f|_{\partial\Omega}$ unique among all potentials which solve the elliptic system.

We are now able to formulate the forward problem in Calderón’s model.

Definition 2.3 (Calderón’s model). The map

$$\mathcal{F}: L_+^\infty(\Omega) \rightarrow \mathcal{L}(H_\diamond^{-1/2}(\partial\Omega), H_\diamond^{1/2}(\partial\Omega)), \sigma \mapsto \mathcal{F}(\sigma) := \mathcal{R}_\sigma = (j_\nu \mapsto f)$$

is called the *forward operator of Calderón’s model* (or continuum model).

In two dimensions, \mathcal{F} is one-to-one; see [AP06]. In 3D, there are several similar results for slightly different function spaces for σ ; see [Uhl09] for an overview.

2.1.3. The complete electrode model

Calderón’s continuum model is a natural choice in the mathematical treatment of boundary value problems. However, most $H_\diamond^{-1/2}(\partial\Omega)$ currents cannot be realized in practice, and potentials cannot be measured continuously along the boundary, but only through a fixed number of electrodes. Thus, it is natural to define a set of simply connected and pairwise separated electrodes as a subset of the boundary.

Definition 2.4 (Electrodes). For $L \in \mathbb{N}_{\geq 2}$, we denote by E_1, \dots, E_L a set of simply connected and pairwise separated electrodes, which we identify (in a slight abuse of notation) with the subset on $\partial\Omega$ that they cover, that is,

$$\begin{aligned} E_1, \dots, E_L &\subset \partial\Omega \quad \text{closed and simply connected on } \partial\Omega, \\ E_l \cap E_m &= \emptyset \quad \text{for } l, m \in \{1, \dots, L\}, l \neq m. \end{aligned}$$

The easiest way to discretize Calderón’s model is to restrict boundary currents j_ν to functions which are piecewise constant on the electrodes and vanishing on the gaps (*gap model*). However, electrodes are usually built from highly conductive metal, which we consider to be a perfect conductor, hence the potential along each electrode is assumed to be constant. This *shunting effect* is incompatible with the gap model, since this would require to define both Dirichlet and Neumann values simultaneously on the same part of the boundary, which is impossible. The shunting effect is considered in the *shunt model* which defines the boundary currents implicitly.

Definition 2.5 (Shunt model). The boundary conditions

$$-\nabla \cdot (\sigma \nabla u) = 0 \quad \text{on } \Omega, \tag{2.8}$$

$$f \equiv U_l \in \mathbb{R} \quad \text{on } E_l, \quad l = 1, \dots, L, \tag{2.9}$$

$$j_\nu = 0 \quad \text{on } \partial\Omega \setminus E, \quad E := E_1 \cup \dots \cup E_L, \tag{2.10}$$

$$\int_{E_l} j_\nu \, dS = I_l, \quad l = 1, \dots, L, \tag{2.11}$$

where $f = u|_{\partial\Omega}$ and $j_\nu = \nu \cdot \sigma \nabla u$, are called the *shunt model*.

2. Principles of electrical impedance tomography

A boundary current j_ν is uniquely defined in this model for a given *net current vector* $I = (I_1, \dots, I_L)^\top \in \mathbb{R}_\diamond^L$; see [SCI92]. The corresponding potentials u and f are unique up to a constant, and the previous (arbitrary) grounding condition $f \in H_\diamond^{1/2}(\partial\Omega)$, i.e. $\int_{\partial\Omega} f \, dS = 0$, can be replaced by the more convenient condition

$$\sum_{l=1}^L |E_l|^{-1} \int_{E_l} f \, dS = \sum_{l=1}^L U_l = 0, \quad \text{that is, } U = (U_1, \dots, U_L)^\top \in \mathbb{R}_\diamond^L.$$

When assessing the shunt model in practice, the predicted behaviour of the current-potential electrode data did not match the measurements observed in tank experiments [CING89]. Rather, the measurements postulate an additional resistivity at the electrode-domain interface for currents passing in normal direction, causing a potential drop. The reason is an electrochemical effect on the surface of current-carrying electrodes, forming a highly resistive layer at its surface. This effect can be incorporated into (2.8) by introducing *contact impedances* $z_1, \dots, z_L \in \mathbb{R}_{>0}$ for each electrode. Then, the electrode behaviour is fully described by

Definition 2.6 (Complete electrode model). For electrode contact impedances $z_1, \dots, z_L \in \mathbb{R}_{>0}$ and any $\sigma \in L_+^\infty(\Omega)$, the set of equations

$$-\nabla \cdot (\sigma \nabla u) = 0 \quad \text{on } \Omega, \tag{2.12}$$

$$f + z_l j_\nu = U_l \quad \text{on } E_l, \quad l = 1, \dots, L, \tag{2.13}$$

$$\int_{E_l} j_\nu \, dS = I_l, \quad l = 1, \dots, L, \tag{2.14}$$

$$j_\nu = 0 \quad \text{on } \partial\Omega \setminus \{E_1 \cup \dots \cup E_L\}, \tag{2.15}$$

where $f = u|_{\partial\Omega}$ and $j_\nu = \nu \cdot \sigma \nabla u$, is called the *complete electrode model* (CEM).

For any *current* (vector) $I = (I_1, \dots, I_L)^\top \in \mathbb{R}_\diamond^L$, there is a unique $u \in H^1(\Omega)$ and a unique *potential* (vector) $U = (U_1, \dots, U_L)^\top \in \mathbb{R}_\diamond^L$ satisfying (2.12)–(2.15). Conversely, any potential $U \in \mathbb{R}_\diamond^L$ can be reached. The current-to-potential map,

$$R_\sigma \in \mathcal{L}(\mathbb{R}_\diamond^L), \quad I \mapsto R_\sigma I = U,$$

which is the ND operator of the CEM, is thus well-defined and one-to-one and moreover bounded, linear, and symmetric; see [SCI92]. It can therefore be represented by a symmetric matrix in $\mathbb{R}^{L \times L}$. The map

$$F: L_+^\infty(\Omega) \supset \mathcal{D}(F) \rightarrow \mathcal{L}(\mathbb{R}_\diamond^L), \quad \sigma \mapsto F(\sigma) := R_\sigma = (I \mapsto U),$$

is called the *forward operator of the CEM*. Its domain of definition $\mathcal{D}(F)$ may vary depending on the context. We will later consider piecewise constant conductivities.

This refined model reproduces the tank experiments accurately up to measurement precision [CING89], and is considered the gold standard electrode model. The symmetry and the vanishing

2. Principles of electrical impedance tomography

column sums of R_σ immediately yield the upper bound

$$\dim(\text{range}(F)) \leq \frac{L(L-1)}{2},$$

for the information about σ contained in R_σ .

To “sample” R_σ , the CEM equations (2.12)–(2.15) can be solved for multiple current vectors which leads to

Definition 2.7 (Measurement pattern, data, and operator). We call any matrix $\mathcal{I} \in \mathbb{R}^{L \times M}$ consisting of $M \in \mathbb{N}$ current vectors, that is,

$$\mathcal{I} = (I^{(1)} | \dots | I^{(M)}), \quad \text{where } I^{(m)} \in \mathbb{R}_\diamond^L \text{ for } m = 1, \dots, M,$$

a *measurement pattern*. The corresponding potential matrix

$$\mathcal{U} = (U^{(1)} | \dots | U^{(M)}) = R_\sigma \mathcal{I} \in (\mathbb{R}_\diamond^L)^M \quad (\text{or, more generally, in } \mathbb{R}^{L \times M})$$

forms the (*measurement*) *data*, and the operator

$$F_{\mathcal{I}}: L_+^\infty(\Omega) \supset \mathcal{D}(F) \rightarrow (\mathbb{R}_\diamond^L)^M, \quad \sigma \mapsto F(\sigma)\mathcal{I} = \mathcal{U},$$

is called the *measurement operator* of the CEM. If $M = 1$, i.e. $\mathcal{I} = (I)$ for a single current vector $I \in \mathbb{R}_\diamond^L$, we also write F_I instead of $F_{\mathcal{I}}$.

Note that $\text{rank}(\mathcal{I}) \leq L - 1$, and $\text{rank}(\mathcal{I}) = L - 1$ if and only if $I^{(1)}, \dots, I^{(M)}$ form a frame of \mathbb{R}_\diamond^L , in which case the operators F and $F_{\mathcal{I}}$ are equivalent since $F(\sigma) = \mathcal{I}^+ F_{\mathcal{I}}(\sigma)$, where \mathcal{I}^+ denotes the Moore-Penrose inverse of the matrix \mathcal{I} with only constant vectors in the null space. From an engineering point of view, it is easiest to build an EIT system with only one single current source, which results in only two nonzero entries in each current vector. An example is the popular *adjacent current* pattern defined as

$$(I_{\text{adj}})_l^{(m)} = \begin{cases} 1, & l = m, \\ -1, & l = (m + 1 \bmod L), \\ 0, & \text{otherwise,} \end{cases}$$

for $l = 1, \dots, L$ and $m = 1, \dots, M$. If $M = L - 1$, \mathcal{I}_{adj} contains a basis of \mathbb{R}_\diamond^L , whereas for $M = L$ we have an overdetermined frame.

A current frame of theoretical interest, called \diamond -*frame* in this work, consists of $M = L - 1$ or $M = L$ current vectors with entries

$$(I_\diamond)_l^{(m)} = \begin{cases} \frac{L-1}{L}, & m = l, \\ -\frac{1}{L}, & \text{otherwise,} \end{cases}$$

for $m, l = 1, \dots, L$, yielding $\mathcal{I}_\diamond^+ = \mathcal{I}_\diamond$ and thus $F_{\mathcal{I}_\diamond} = F$. Again for $M = L$, the frame is redundant.

2. Principles of electrical impedance tomography

Remark 2.8 (Other measurement protocols and incomplete data). In practice, sometimes not the potential vectors are acquired, but other “measurement protocols” like pairwise electrode voltage measurements are used. Moreover, measurements on current-carrying electrodes are often omitted, leading to incomplete measurement data. This case is considered in more detail in section 4.1.3.

Numerous studies have investigated the performance of different current frames regarding their optimality for various noise levels, sometimes under additional current amplitude or power restrictions, both for Calderón’s model and for electrode models; see e.g. [CI92, LKM01, DHSP05]. One can also consider partial data operators, i.e. measurement operators mapping on a subset of \mathcal{U} , which is of practical interest in measurement setups where measurements on current-carrying electrodes are avoided. This will be outlined in the numerical evaluation in chapter 6.

To study the CEM, it is useful to consider it in a weak formulation. The corresponding bilinear, continuous and elliptic operator $a: (H^1(\Omega) \times \mathbb{R}_{\diamond}^L)^2 \rightarrow \mathbb{R}$ is given as

$$a((v, V), (w, W)) = \int_{\Omega} \sigma \nabla v \cdot \nabla w \, dx + \sum_{l=1}^L \frac{1}{z_l} \int_{E_l} (v - V_l)(w - W_l) \, dS. \quad (2.16)$$

By the Lax-Milgram lemma, there exists a unique solution $(u, U) \in H^1(\Omega) \times \mathbb{R}_{\diamond}^L$ of

$$a((u, U), (w, W)) = \sum_{l=1}^L I_l W_l \quad \text{for all } (w, W) \in H^1(\Omega) \times \mathbb{R}_{\diamond}^L, \quad (2.17)$$

which was shown to agree with the solution of (2.12)–(2.15); see [SCI92, Hyv04].

2.1.4. Fréchet-differentiability of the forward operators

A fundamental property of the operators \mathcal{F} , F and $F_{\mathcal{I}}$ is their Fréchet-differentiability [KKS00, LR06]. This allows us to consider Newton-type methods for inversion. Moreover in certain cases, the nonlinearity of the CEM forward problem is limited since F and $F_{\mathcal{I}}$ satisfy a tangential cone condition [LR08, Theorems 3.4 and 4.9]. The relevant results are formulated in our notation in the following for the reader’s convenience.

Theorem 2.9 (Fréchet derivative for the CEM). *Let z_1, \dots, z_L be fixed positive contact impedances and $I \in \mathbb{R}_{\diamond}^L$ be a current vector. For $\sigma \in \text{int}(\mathcal{D}(F_I))$, the measurement operator F_I is Fréchet-differentiable at σ . If $\eta \in L^\infty(\Omega)$ such that $\sigma + \eta \in \mathcal{D}(F_I)$, then the Fréchet-derivative of F_I at σ in direction η is given as $F_{\mathcal{I}}'(\sigma)\eta := U'$, where U' is the second component of the unique solution $(u', U') \in H^1(\Omega) \times \mathbb{R}_{\diamond}^L$ to the variational problem*

$$a((u', U'), (w, W)) = - \int_{\Omega} \eta \nabla u_I \nabla w \, dx \quad \text{for all } (w, W) \in H^1(\Omega) \times \mathbb{R}_{\diamond}^L, \quad (2.18)$$

and u_I is the first component of the solution of (2.17) for a given current vector I .

2. Principles of electrical impedance tomography

Proof. See [LR06, Theorem 4.1] and [KKS00]. □

By concatenating $F'_{I(1)}, \dots, F'_{I(M)}$ for a given current frame, we obtain the Fréchet derivative of $F_{\mathcal{I}}$ (and in particular F' for $\mathcal{I} = \mathcal{I}_\diamond$). Moreover, F' is Lipschitz continuous [JM12]. In a discretized setting, the nonlinearity is also limited by a tangential cone condition; see section 2.3.

2.2. Noise model

In this section, we formulate a noise model for EIT data and explain how pseudo-random noise is generated in our numerical examples.

2.2.1. Modelling data noise

There are various sources of data errors in EIT. The most obvious source is noise in the measured data caused by imperfections of the measurement equipment: The potentials recorded by the voltmeter are correct only up to measurement precision, and other electrical components like imperfect current sources introduce additional errors. There are several ways to measure the electrode potentials, for example by recording the voltages between each electrode and a reference point in turn, or by recording pairwise voltages between the electrodes e.g. on adjacent electrodes. Thus, the measurement protocol has an impact of the amplification of noise in \mathcal{U} . Moreover, there are errors from imperfect modelling (e.g. when dealing with anisotropic materials) and from imperfect model parameters, such as geometry errors and incorrect contact impedances.

These quantities are very problem-specific and usually impossible to access or to correlate exactly. For that reason, additive Gaussian white noise is often assumed to perturb the model data [MS12].

Definition 2.10 (Noise model). In this work, we consider noisy data to be potentials perturbed entry-wise by independent and identically distributed (iid) additive Gaussian white noise of (usually unknown) variance $v > 0$, that is,

$$\mathcal{U}^v = \mathcal{U} + N^v, \quad (N^v)_{lm} \stackrel{\text{iid}}{\sim} \mathcal{N}(0, v) \text{ for } l = 1, \dots, L, m = 1, \dots, M. \quad (2.19)$$

The Frobenius norm of the noise matrix N^v , called *noise level* in this work, will be of special interest, thus we denote it by

$$\delta := \|\mathcal{U} - \mathcal{U}^v\|_{\text{Fro}} = \|N^v\|_{\text{Fro}}.$$

In chapter 4, this noise model will be used to obtain a stopping criterion for the iterative inversion algorithm.

Regarding the justification of additive noise, we give the following

2. Principles of electrical impedance tomography

Remark 2.11 (additive vs. multiplicative noise). Due to the arbitrary grounding condition of the measured potentials, a multiplicative noise model for \mathcal{U} is usually not justified since any entry could be set to zero by shifting the grounding correspondingly, resulting in zero noise in that entry. However for measurement protocols like the adjacent electrode voltages, a multiplicative/proportional error for this “potential difference” measurement might be justified, leading to a different noise model.

In our numerical implementations, the MATLAB function `randn` was used to generate pseudo-random Gaussian noise. If not stated otherwise, the default setting (Mersenne twister with seed 1) was used to initialize the pseudo-random number generator.

2.2.2. Generating noisy data

For our numerical evaluations in chapter 6, we need to simulate noisy data by adding pseudo-random noise to the simulated forward solutions. In principle, we could specify a variance $v > 0$ explicitly and generate a realization of N^v using a pseudo-random number generator, but what is a realistic value for v ? We assume a measurement equipment to have a precision which is relative to the magnitude of a single measurement vector, i.e.

$$\frac{\|(U^v)^{(m)} - U^{(m)}\|_2}{\|U^{(m)}\|_2} \approx \delta^{\text{rel}} > 0 \quad \text{for all } m = 1, \dots, M,$$

and we call δ^{rel} the *relative measurement noise*. In particular, we have for all $m = 1, \dots, M$ that

$$\delta^{\text{rel}} \approx \mathbb{E} \frac{\|(U^v)^{(m)} - U^{(m)}\|_2}{\|U^{(m)}\|_2} = \|U^{(m)}\|_2^{-1} \mathbb{E} \|(N^v)^{(m)}\|_2 = \sqrt{2v} \|U^{(m)}\|_2^{-1} \frac{\Gamma\left(\frac{L+1}{2}\right)}{\Gamma\left(\frac{L}{2}\right)},$$

with Euler’s gamma function Γ . The last equality is due to the Chi distribution of $\|(N^v)^{(m)}\|_2$ for $N_l^{(m)} \stackrel{\text{iid}}{\sim} \mathcal{N}(0, v)$; see standard literature [FEHP11]. Solving for v yields

$$v \approx \frac{1}{2} (\delta^{\text{rel}})^2 \|U^{(m)}\|_2^2 \left(\frac{\Gamma\left(\frac{L}{2}\right)}{\Gamma\left(\frac{L+1}{2}\right)} \right)^2, \quad m = 1, \dots, M.$$

By a least-squares fit for v over all measurements, we get the minimizer

$$\hat{v} = \hat{v}(\delta^{\text{rel}}) := \frac{(\delta^{\text{rel}})^2}{2M} \left(\frac{\Gamma\left(\frac{L}{2}\right)}{\Gamma\left(\frac{L+1}{2}\right)} \right)^2 \sum_{m=1}^M \|U^{(m)}\|_2^2.$$

Thus, for a given set of simulated potential data \mathcal{U} and a given relative measurement noise $\delta^{\text{rel}} > 0$, we simulate noisy data by

$$\mathcal{U}^{\hat{v}} = \mathcal{U} + N^{\hat{v}(\delta^{\text{rel}})}, \quad (2.20)$$

2. Principles of electrical impedance tomography

where $N^{\widehat{v}(\delta^{\text{rel}})}$ is a realization of a pseudo-random noise matrix as in (2.19).

2.3. Model discretization

So far, very general EIT settings were considered regarding the choice of the domain geometry and the space of admissible conductivities. These spaces are suitable for a theoretical analysis of the problem, but analytic solutions of the forward problem are known only for a tiny set of particular domain geometries and conductivity distributions, namely concentric conductivities on a disk and some conformally equivalent settings.

Solving any more general forward problem requires the use of numerical methods, which in turn require a discretization of the setting. This means that both the domain geometry and the conductivity space need to be discretized.

2.3.1. Finite element discretization for solving the forward problem

In our numerical experiments, we use the finite element method (FEM) to approximate forward solutions of the CEM. Thus, we assume Ω to be (or to be approximated by) an n -dimensional polytope, where each electrode surface is a set of facets connected by ridges. A decomposition of Ω into $Q \in \mathbb{N}$ tetrahedral cells $\Delta_1, \dots, \Delta_Q$ is called a *finite element mesh* (or *FEM discretization*, *FEM triangulation*) and is denoted by $\Delta = \{\Delta_1, \dots, \Delta_Q\}$. In the remainder of this work, we consider piecewise linear basis functions for the potential.

2.3.2. Discretization of the conductivity space

For numerical inversion, conductivities should be represented in a finite dimensional basis, thus it is necessary to reduce the set of admissible conductivities to a finite dimensional subset of $L_+^\infty(\Omega)$. As the electrical conductivity is a material property, σ is assumed to be constant throughout each object inside the domain. Thus, it is reasonable to restrict σ to piecewise constant functions on a partition $\mathcal{P} = \{\Omega_1, \dots, \Omega_P\}$, $P \in \mathbb{N}$, of Ω :

$$\sigma \in \mathcal{D}_{\mathcal{P}} = \left\{ \sigma_1 \chi_{\Omega_1} + \dots + \sigma_P \chi_{\Omega_P} \mid c \leq \sigma_1, \dots, \sigma_P \leq c^{-1} \right\} \subset L_+^\infty(\Omega).$$

Here, the cells $\{\Omega_1, \dots, \Omega_P\}$ can be any partition of Ω into simply connected – not necessarily tetrahedral – subdomains. For example, we will design sensitivity based domain discretizations \mathcal{P} in chapter 3 which are Voronoi tessellations on Ω .

2. Principles of electrical impedance tomography

In particular, \mathcal{P} and Δ do not need to coincide. However if Δ is not a refinement of \mathcal{P} , nontrivial projection operators are required to solve the forward problem for $\sigma \in \mathcal{D}_{\mathcal{P}}$ numerically on Δ , possibly introducing additional errors to the forward solution. In the remainder of this work, boldface symbols denote the coefficient vectors corresponding to conductivities and conductivity updates, e.g. $\boldsymbol{\sigma} \in \mathbb{R}_+^P$ and $\boldsymbol{\eta} \in \mathbb{R}^P$ such that

$$\boldsymbol{\sigma} \hat{=} \sigma = \boldsymbol{\sigma}_1 \chi_{\Omega_1} + \dots + \boldsymbol{\sigma}_P \chi_{\Omega_P} \in \mathcal{D}_{\mathcal{P}} \subset L_+^\infty(\Omega)$$

and

$$\boldsymbol{\eta} \hat{=} \eta = \boldsymbol{\eta}_1 \chi_{\Omega_1} + \dots + \boldsymbol{\eta}_P \chi_{\Omega_P} \in L^\infty(\Omega),$$

respectively.

In this discretized setting, the nonlinearity of the forward map is limited locally in the following sense:

Theorem 2.12 (Tangential cone condition). *Let \mathcal{P} be a fixed triangulation of Ω . For any $\sigma \in \text{int}(\mathcal{D}_{\mathcal{P}})$, there is an $l \in \mathbb{N}$ such that for $L \geq l$ and $\tilde{\sigma} \in \mathcal{D}_{\mathcal{P}}$ sufficiently close to σ , the **tangential cone condition***

$$\|F(\tilde{\sigma}) - F(\sigma) - F'(\sigma)(\tilde{\sigma} - \sigma)\|_{\mathcal{L}(\mathbb{R}^L)} \lesssim \|\tilde{\sigma} - \sigma\|_\infty \|F(\tilde{\sigma}) - F(\sigma)\|_{\mathcal{L}(\mathbb{R}^L)} \quad (2.21)$$

holds uniformly in L .

Proof. See¹ [LR08, Theorem 4.5]. □

Note that $\|\cdot\|_{\mathcal{L}(\mathbb{R}^L)} = \|\cdot\|_{\text{Fro}}$ is the Frobenius norm when we identify the linear maps with their coefficient matrices if \mathbb{R}^L is equipped with the Euclidean norm. The tangential cone condition also holds for the FEM approximations uniformly in Δ provided the FEM triangulation is sufficiently fine [LR08, Theorem 4.9].

2.3.3. Computation of the Fréchet derivative

Generally, the Fréchet derivative of the forward operator $F_{\mathcal{I}}$ can be evaluated by solving the system weak formulation (2.18) given in Theorem 2.9. In our numerical evaluations, we compute it by sampling its entries for the \diamond -frame and $M = L$ by

$$(F'_{\mathcal{I}\diamond}(\sigma)[\boldsymbol{\eta}])_{l,m} = - \int_{\Omega} \eta \nabla u^{(l)} \nabla u^{(m)} \, dx, \quad l, m = 1, \dots, L, \quad (2.22)$$

where $u^{(m)}$ is the second component of the solution of (2.17) for current $I_\diamond^{(m)}$; see [PL02, Hol04] for details. Note that in these references, non-normalized unit currents with entries $I_l^{(m)} = \delta_{ml}$ are

¹The cited work considers the more general case of piecewise polynomial conductivities and non-polyhedral domains.

2. Principles of electrical impedance tomography

considered, which are not in \mathbb{R}_\diamond^L . However, the variational problem (2.17) has a solution also in this more general setting, and the gradient of the second component agrees with $\nabla u^{(m)}$ for the m -th vector of the \diamond -frame. By linearity, the Fréchet derivative for an arbitrary current vector I is then given by

$$F'_I(\sigma)[\eta] = F'_{\mathcal{I}_\diamond}(\sigma)[\eta]I \in \mathbb{R}_\diamond^L.$$

After solving the forward problem (2.17) numerically using finite elements with linear ansatz functions on a triangulation Δ , the gradients on each cell can be approximated by the corresponding constants $\{\nabla u_1^{(m)}, \dots, \nabla u_Q^{(m)}\}$ obtained from the FEM forward solution, that is, $\nabla u^{(m)}(x)|_{\Delta_q} \approx \nabla u_q^{(m)}$ and

$$\int_{\Delta_q} \nabla u^{(l)}(x) \nabla u^{(m)}(x) dx \approx |\Delta_q| \nabla u_q^{(l)} \cdot \nabla u_q^{(m)}.$$

This yields

$$\int_{\Omega_p} \nabla u^{(l)}(x) \nabla u^{(m)}(x) dx \approx \sum_{\{q: \Delta_q \cap \Omega_p \neq \emptyset\}} |\Delta_q \cap \Omega_p| \nabla u_q^{(l)} \cdot \nabla u_q^{(m)}. \quad (2.23)$$

In MATLAB, the FEM gradient approximations $\nabla u_q^{(m)}$ can be obtained from the FEM solution using the PDE toolbox function `pdetrg`.

Remark 2.13. For computing the forward solution using the FEM, the conductivity must be projected from \mathcal{D}_P onto Δ . If Δ is not a refinement of \mathcal{D}_P , this can again be achieved by the projection

$$\sigma|_{\Delta_q} \approx \frac{1}{|\Delta_q|} \sum_{\{p: \Omega_p \cap \Delta_q \neq \emptyset\}} |\Delta_q \cap \Omega_p| \sigma_p.$$

2.4. The inverse conductivity problem

The inverse conductivity problem (ICP) is the mathematical task of concluding on the underlying conductivity of a setting from the observed boundary data. In Calderón's model, this means to evaluate the inverse \mathcal{F}^{-1} of the forward operator. However for measured data and electrode models, instability and non-uniqueness need to be considered carefully. Given noisy potentials \mathcal{U}^v as in (2.19), a very general formulation of the problem of interest is

$$\text{“Given } \mathcal{U}^v, \text{ find a conductivity } \hat{\sigma} \in \mathcal{D}_P \text{ satisfying } F_{\mathcal{I}}(\hat{\sigma}) \approx \mathcal{U}^v.” \quad (2.24)$$

In this section, the main issues of the ICP for the CEM with noisy measured data are described. They arise from the nonlinearity (section 2.4.1), the constrainedness (sec. 2.4.2), the non-uniqueness (sec. 2.4.3) and the ill-posedness (sec. 2.4.4) inherent to the model, and from geometry and parameter uncertainties of the setting (sec. 2.4.5). After remarking on iterative inversion in general (sec. 2.4.6),

the inexact Newton-type algorithm REGINN [Rie99] is presented in section 2.4.7 as a basis for designing a model-aware inversion scheme for the CEM in chapter 4.

2.4.1. Nonlinearity

The measurement operator $F_{\mathcal{I}}$ is highly nonlinear. The nonlinearity of the ICP entails the typical issues of nonlinear inverse problems, in particular the existence of local minima of the function $\sigma \mapsto \|F(\sigma) - \mathcal{U}^v\|$ and possible convergence issues of iterative solvers.

2.4.2. Constrainedness

On top of being nonlinear, the measurement operator is also constrained by the positivity of the conductivity $\sigma \in L_{+}^{\infty}(\Omega)$. This must be accounted for when applying iterative inversion to ensure that the sequence of conductivities generated during the iteration satisfies this constraint. A common method is to apply a transformation $t: L_{+}^{\infty}(\Omega) \rightarrow L^{\infty}(\Omega)$ acting “pointwise” on the conductivity values, and to apply the iterative inversion to the transformed, unconstrained quantity. A popular transformation is the log-conductivity $t(\sigma) = \log(\sigma)$, but many other choices are possible. In chapter 4, the σ - ρ -transform is introduced and studied, complemented by numerical examples in 6.

2.4.3. Uniqueness

In Calderón’s model, uniqueness was shown for all spatial dimensions $n \geq 2$ for very general conductivity spaces; see [AP06] for the most general result in 2D and [Uhl09] for an overview of various uniqueness results in slightly different functions spaces for $n \geq 3$. All uniqueness results only hold for isotropic conductivities, as diffeomorphisms can be used to transform the setting into a new setting with a different, anisotropic conductivity having the same ND map [Syl90].

In contrast, the ICP for the CEM is highly underdetermined: Since $F_{\mathcal{I}}$ has finite-dimensional range and $\mathcal{D}(F_{\mathcal{I}})$ is infinite dimensional in the general setting, there are different conductivities resulting in the same measurement operator.

2.4.4. Ill-posedness

An inverse problem is *well-posed* in the sense of Hadamard if it is uniquely solvable and the solution depends continuously on the data. Otherwise, it is *ill-posed*.

In that sense, the ICP is ill-posed both for Calderón’s model and for the CEM. The former is shown by a classical example due to Alessandrini [Ale88]. Since Alessandrini considers the map $\sigma \rightarrow \Lambda_{\sigma}$ (cf. (2.7)) in slightly different function spaces, we restate a variant of this example from [Bru99,

2. Principles of electrical impedance tomography

section 3.2], considering the ND map \mathcal{R}_σ as a linear bounded operator on $L^2(\partial\Omega)$. Let $\Omega = B_1(0)$, $\sigma_1(x) \equiv 1$ and

$$\sigma_k(x) = \begin{cases} 1, & k^{-1} < |x| \leq 1, \\ 1 + k\pi^{-\frac{1}{2}}, & 0 \leq |x| \leq k^{-1}, \end{cases} \quad \text{for } k \in \mathbb{N}_{\geq 2}. \quad (2.25)$$

Then we have

$$\|\sigma_k - \sigma_1\|_{L^2(\Omega)} = 1 \text{ for all } k \geq 2, \quad \text{but} \quad \|\mathcal{R}_{\sigma_k} - \mathcal{R}_{\sigma_1}\|_{\mathcal{L}(L^2(\partial\Omega))} \rightarrow 0 \text{ as } k \rightarrow \infty, \quad (2.26)$$

which shows that \mathcal{F}^{-1} is discontinuous. This example uses an explicit singular value decomposition of \mathcal{R}_σ for conductivities with concentric jump-discontinuities on a disk, which will also be an ingredient for the sensitivity analysis presented in chapter 3.

Alessandrini also presents two stability estimates for spatial dimensions $n \geq 3$. The *global estimate* [Ale88, Theorem 1]

$$\|\sigma - \tilde{\sigma}\|_{L^\infty(\Omega)} \lesssim \log \left(\|\Lambda_\sigma - \Lambda_{\tilde{\sigma}}\|_{\mathcal{L}(H^{1/2}(\Omega), H^{-1/2}(\Omega))}^{-\delta} \right) \quad (2.27)$$

for smooth conductivities $0 < c \leq \sigma, \tilde{\sigma} \in H^\alpha(\Omega)$, $\alpha > 2 + \frac{n}{2}$, $\delta \in (0, 1)$, is a very “weak” stability estimate of logarithmic type, and thus the ICP is usually said to be exponentially unstable. However, the local (boundary) estimate [Ale90, Theorem 1.2]

$$\|\sigma - \tilde{\sigma}\|_{L^\infty(\partial\Omega)} \lesssim \|\Lambda_\sigma - \Lambda_{\tilde{\sigma}}\|_{\mathcal{L}(H^{1/2}(\Omega), H^{-1/2}(\Omega))} \quad (2.28)$$

for $\sigma, \tilde{\sigma} \in H^{1,p}(\Omega)$, $p > n$, $c \leq \sigma, \tilde{\sigma} \leq c^{-1}$ for some $c > 0$, shows that a sufficiently smooth conductivity can be obtained stably *at the boundary* from DN data.

These two results characterize the main issue of the ICP: The information about the conductivity contained in the boundary data decays rapidly away from the boundary in typical norms. This has been further investigated e.g. in [Dob92, Pal02, MMM04].

Next, we conclude from these continuum model results on the instability of the ICP for the CEM. To that end, an interesting observation is that the measurement operator $F_{\mathcal{I}}$ is “contained” in Λ_σ . Let $u^{(1)}, \dots, u^{(M)}$ be the first components of the solutions to (2.17) for some conductivity σ and current vectors $I^{(1)}, \dots, I^{(M)}$. For $f^{(m)} := u^{(m)}|_{\partial\Omega}$, $m = 1, \dots, M$, we find from (2.13) that $U_l^{(m)} = |E_l|^{-1} \int_{E_l} f^{(m)}(x) + z_l \Lambda_\sigma f^{(m)}(x) dS$. Thus, the entries of $F_{\mathcal{I}}(\sigma)$ are basically projections of $(\text{Id} + z_l \Lambda_\sigma)|_{\text{span}\{j_\nu^{(1)}, \dots, j_\nu^{(M)}\}}$, and we cannot expect a better stability for the CEM than for the continuum model. Even worse, we cannot expect results of the type (2.27), (2.28) for two reasons: Obviously, underdetermination for the CEM is in contrast to both estimates. Moreover, Calderón’s model and the CEM are fundamentally different since potentials or normal currents can be arbitrarily localized in the continuum model, which is prohibited in the CEM by the electrode and gap sizes. This makes it impossible to formulate results like [Ale90, Lemma 3.1] for the CEM, which

2. Principles of electrical impedance tomography

guarantees the existence of potentials satisfying (2.5) and having “nice” properties at arbitrarily chosen locations inside Ω .

As a consequence, the non-uniqueness and instability must be accounted for to obtain a unique and stable solution for (2.24), which is complicated by the severe nonlinearity of the problem. This requires regularization methods for nonlinear ill-posed problems. These issues are being investigated and model-tailored solutions are proposed in sections 4.2–4.4

2.4.5. Model uncertainties

The terms “model uncertainties” and “model errors” are used ambiguously in the literature, and all aspects should be considered for solving the ICP.

Firstly, they may refer to a mismatch between the physical properties of a phenomenon and its mathematical description, like the propagation of electrical currents inside a conducting medium or the behaviour at electrodes. Here, the CEM was evaluated to reproduce physical measurements up to measurement precision, at least for a set of saline tank experiments [CING89, SCI92].

Secondly, these terms may refer to an inexact reproduction of the setting under investigation within a model. This could be geometry errors for the underlying domain, wrong sizes and locations for the electrodes, or wrong contact impedances for the CEM. The impact of such a mis-modelling on the ICP can be rather severe; see e.g. [DHSS13a]. This means that all measures should be taken to obtain this information from the outside, i.e. by other imaging or measurement modalities, before solving the ICP. For example, a wearable electrode belt was demonstrated recently that uses sensors to detect the shape of the chest cross-section in real-time [NKI⁺15]. The contact impedances are usually impossible to obtain from the outside, which means they need to be estimated by hand or from the data. In section 4.1.1, a direct (non-iterative) estimator for the contact impedances will be presented, along with an estimate for the background conductivity of a setting. In chapter 5, we will outline how these initial estimates, as well as the electrode positions and sizes, can be updated simultaneously while solving the ICP, incorporating ideas of [VKV⁺02] and [DHSS13a] in the model-aware inversion scheme presented in this work.

Thirdly, “model uncertainties” may refer to the choice of design parameters, sometimes called hyperparameters, steering the amount of regularization to stabilize the inversion scheme. Classical examples are Tikhonov-type regularization methods with a regularization parameter in front of the penalty/smoothing term of the Tikhonov functional. A “good” choice is usually highly problem specific and may vary over many orders of magnitude depending on the setting, the data noise, the problem discretization, etc. The inversion scheme presented in this work does not rely on abstract design parameters. Instead, it relies on the knowledge of the noise level δ for applying regularization. For that reason, a method to estimate δ for a given set of measurement data will be presented in section 4.1.2.

2.4.6. Iterative inversion methods

It is outlined briefly in the introduction and (in more detail) in Appendix A that there are many approaches for solving the ICP numerically. Yet, only few methods are capable of modelling the electrode behaviour of the CEM, and among those, iterative methods are the only² methods for solving the ICP in the sense of (2.24).

Iterative inversion schemes generate a sequence of conductivities $\{\sigma^{(1)}, \sigma^{(2)}, \dots\} \subset \mathcal{D}(F_{\mathcal{I}})$ such that $F_{\mathcal{I}}(\sigma^{(k)})$ approximates the noisy data \mathcal{U}^v as k increases. Note however that we can't expect convergence to \mathcal{U}^v since it is usually not in the range of the measurement operator $F_{\mathcal{I}}$, thus we need to abandon the idea of *solving* the equation $F_{\mathcal{I}}(\sigma) = \mathcal{U}^v$. Moreover due to the underdetermination and instability of the problem, one should take care generate a “nice” sequence $\{\sigma^{(k)}\}_k$ that avoids noise amplification. This can be done by using a regularization strategy.

Two methods are commonly used to resolve these issues. The first one is to alter the nonlinear operator to obtain a stable and (uniquely) solvable problem. Arguably the most popular method is the *nonlinear Tikhonov regularization*:

$$\text{Find } \hat{\sigma}_\alpha = \arg \min_{\sigma \in \mathcal{D}(F_{\mathcal{I}})} J_\alpha(\sigma), \quad \text{where } J_\alpha(\sigma) = \|F_{\mathcal{I}}(\sigma) - \mathcal{U}^v\|_Y^2 + \alpha \|\sigma\|_X^2, \quad (2.29)$$

$\|\cdot\|_X$ and $\|\cdot\|_Y$ are norms in $\mathcal{D}(F_{\mathcal{I}})$ and $\mathbb{R}^{L \times M}$, respectively, and α is a design parameter. A (local) minimum can then be approached using an iterative method to minimize $J_\alpha(\sigma)$, which is a locally well-posed problem. The local minimizer is usually obtained by a Newton iteration; see e.g. [VVK⁺98]. On the existence and uniqueness of such a minimizer, as well as a parameter strategy $\alpha = \alpha(\delta)$ for a known noise level $\delta = \|\mathcal{U} - \mathcal{U}^v\|$, see e.g. [JM12]. The nonlinear Tikhonov-Phillips regularization is sometimes used as a performance benchmark for other methods, but parameter strategies for α like the discrepancy principle, L-curve methods [Han92] or generalized cross-validation [Wah77] often require to solve (2.29) for many parameters α , each by an iterative method, which is a great computational effort.

The second popular class of methods for iteratively solving the ICP are Gauß-Newton methods. Instead of modifying the nonlinear problem by applying regularization, Newton's method is applied to (2.24) directly, but the *linearized problem is regularized* in each Newton step. This has the advantage that the wealth of theory for linear ill-posed problems can be used to stabilize the linearized problem, e.g. by applying a Landweber iteration, ν -methods, the conjugate gradient method, or linear Tikhonov-Phillips regularization [Rie99]; the latter yields the popular Levenberg-Marquardt method. Combining regularized linearization with a suitable stopping criterion for New-

²There are only two other methods considering the CEM known to the author that do not use a Newton-type iteration in one way or another: The localized potentials method reconstructs the support of inclusions, rather than a full EIT image, and artificial neural network approaches are blind to the model (non-phenomenological) and rely purely on the provided training data.

ton's method, a regularization strategy for the nonlinear problem can be obtained. A variant of this approach, the class of *inexact Newton-type methods*, is introduced in the following section.

2.4.7. Inexact Newton-type methods

Inexact Newton-type methods for nonlinear ill-posed problems in the sense of Hadamard were introduced in [Han97], and further convergence theory was established in [Rie99, Rie05, LR10] in a general scope and in [LR06, LR08] for EIT. The basic concept will be introduced in the following.

Let $\mathcal{D}(F_{\mathcal{I}}) = \mathcal{D}_{\mathcal{P}}$ and let $F_{\mathcal{I}}(\sigma^+) = \mathcal{U}$ for some $\sigma^+ \in \text{int}(\mathcal{D}_{\mathcal{P}})$. Moreover, let $\|\mathcal{U}^v - \mathcal{U}\|_{\text{Fro}} = \delta$ and let $\sigma^{(0)} \in \mathcal{D}_{\mathcal{P}}$ be an initial guess. We want to generate a sequence $\{\sigma^{(k)}\}_k \subset \mathcal{D}_{\mathcal{P}}$ approaching σ^+ by

$$\sigma^{(k+1)} = \sigma^{(k)} + \eta^{(k)}, \quad k \in \mathbb{N}_0.$$

The idea of Newton-type methods is to approximate the inaccessible *exact* update $\eta_e^{(k)} := \sigma^+ - \sigma^{(k)}$ by a linearization of the operator $F_{\mathcal{I}}$. For $\mathcal{U}^{(k)} := F_{\mathcal{I}}(\sigma^{(k)})$, the exact update satisfies

$$F'_{\mathcal{I}}(\sigma^{(k)})\eta_e^{(k)} = \mathcal{U} - \mathcal{U}^{(k)} - E(\sigma^+, \sigma^{(k)}),$$

where $E(\sigma, \tilde{\sigma}) := F_{\mathcal{I}}(\sigma) - F_{\mathcal{I}}(\tilde{\sigma}) - F'_{\mathcal{I}}(\tilde{\sigma})(\sigma - \tilde{\sigma})$ is the linearization error. Since this error and the exact data \mathcal{U} are unknown, Newton-type methods consider the linearized system

$$F'_{\mathcal{I}}(\sigma^{(k)})\eta^{(k)} = d^{(k)}, \quad (2.30)$$

where $d^{(k)} := \mathcal{U}^v - \mathcal{U}^{(k)}$.

The ill-posedness of the ICP is inherited by this linearization, thus a regularization strategy is required to solve (2.30) in each Newton step.

The idea of *inexact Newton-type methods* is to solve the system (2.30) only to a certain relative precision $\theta_k \in (0, 1]$ in each iteration. To that end, an *inner sequence*

$$\eta^{(k,l)}, \quad l = 0, 1, \dots \quad (2.31)$$

is generated. The sequence is stopped at the unique index L_k where the relative residual criterion

$$\left\| F'_{\mathcal{I}}(\sigma^{(k)})\eta^{(k,L_k)} - d^{(k)} \right\|_{\text{Fro}} \leq \theta_k \left\| d^{(k)} \right\|_{\text{Fro}} < \left\| F'_{\mathcal{I}}(\sigma^{(k)})\eta^{(k,l)} - d^{(k)} \right\|_{\text{Fro}} \quad (2.32)$$

for all $l = 1, \dots, L_k - 1$ is reached, and the Newton update is set to $\eta^{(k)} = \eta^{(k,L_k)}$.

This scheme is called REGINN (REGularized INexact Newton method) [Rie99]. It is essential to choose the parameters θ_k large enough to obtain a *stable* approximation to the linearized problem, but small enough to obtain *convergence* of the Newton iteration. An a-posteriori parameter strategy for choosing θ_k , $k = 0, 1, 2, \dots$, is given in [Rie99, eq. (6.1) and (6.2)], and a slightly modified version of this strategy will be used later in this work.

2. Principles of electrical impedance tomography

Since \mathcal{U}^v is usually not in the range of $F_{\mathcal{I}}$, we cannot hope to obtain convergence of the type $\sigma^{(k)} \rightarrow \sigma^+$ ($k \rightarrow \infty$) for some $\sigma^+ \in \mathcal{D}_{\mathcal{P}}$ satisfying $F_{\mathcal{I}}(\sigma^+) = \mathcal{U}^v$. Instead, we are content with a conductivity giving a nonlinear residual reasonably close to the data error. This is called *Morozov's discrepancy principle*, and the Newton iteration is stopped at the index $K \in \mathbb{N}$ satisfying

$$K = K(\delta, \mathcal{U}^v) = \min \left\{ k \in \mathbb{N} : \left\| F_{\mathcal{I}}(\sigma^{(k)}) - \mathcal{U}^v \right\|_{\text{Fro}} \leq \tau \delta \right\}, \quad (2.33)$$

for some constant $\tau > 1$.

REGINN for the ICP of the CEM is summarized in Algorithm 1. It will serve as a ‘‘prototype’’ for our model-tailored inversion in chapter 4.

Algorithm 1: REGINN for the CEM

input : Measurement pattern \mathcal{I} , noisy data \mathcal{U}^v , initialization $\sigma^{(0)} \in \mathcal{D}_{\mathcal{P}}$, noise level δ , tolerance $\tau > 1$.

output: Conductivity estimate σ .

- 1 Set $k = 0$, $d^{(0)} = \mathcal{U}^v - F_{\mathcal{I}}(\sigma^{(0)})$;
 - 2 **while** $\left\| d^{(k)} \right\|_{\text{Fro}} > \tau \delta$ **do**
 - 3 Find $\eta^{(k)}$ satisfying $\left\| F'_{\mathcal{I}}(\sigma^{(k)})\eta^{(k)} - d^{(k)} \right\|_{\text{Fro}} \leq \theta_k \left\| d^{(k)} \right\|_{\text{Fro}}$;
 - 4 Set $\sigma^{(k+1)} = \sigma^{(k)} + \eta^{(k)}$;
 - 5 Set $d^{(k+1)} = \mathcal{U} - F_{\mathcal{I}}(\sigma^{(k+1)})$;
 - 6 Set $k = k + 1$;
 - 7 **end**
 - 8 Set $\sigma = \sigma^{(k)}$;
-

To be computationally efficient, it is desirable to reach (2.32) with few inner iterations, i.e. for L_k small for each $k = 0, \dots, K$. Since the stopping criterion is a relative decrease of the linear residual, a natural choice is the *conjugate gradient* (cg) method, which decreases the linear residual faster than any other Krylov subspace method:

$$\eta_{\text{cg}}^{(l,k)} = \arg \min \left\{ \left\| F'(\sigma^{(k)})\eta - d^{(k)} \right\|_{\text{Fro}} : \eta \in \mathcal{K}_l \left(F'_{\mathcal{I}}(\sigma^{(k)})^* F'_{\mathcal{I}}(\sigma^{(k)}), F'_{\mathcal{I}}(\sigma^{(k)})^* r^{(k)} \right) \right\}, \quad (2.34)$$

where

$$\mathcal{K}_l(A, x) := \text{span} \left\{ x, Ax, \dots, A^{l-1}x \right\} \quad (2.35)$$

is the l -th Krylov subspace for A and x , and $r^{(k)} = d^{(k)}$ usually. REGINN with a conjugate gradient inner iteration is called CG-REGINN.

Lechleiter and Rieder showed in [LR08, Remark after Theorem 4.9] that when τ large enough and the tangential cone condition holds (in particular, sufficiently many electrodes and $\sigma^{(0)}$ sufficiently close to σ^+), one gets

$$\left\| \mathcal{U}^v - F_{\mathcal{I}}(\sigma^{(k+1)}) \right\|_{\text{Fro}} \leq C \left\| \mathcal{U}^v - F_{\mathcal{I}}(\sigma^{(k)}) \right\|_{\text{Fro}} \quad \text{for } k = 0, 1, \dots, K-1 \text{ and some } C < 1.$$

2. Principles of electrical impedance tomography

This means that CG-REGINN is well-defined locally, in particular $K < \infty$, and the nonlinear residual decreases monotonically. Moreover, $\lim_{\delta \rightarrow 0} \sigma_{K(\delta, \mathcal{U}^v)} \rightarrow \sigma^+$. Thus, CG-REGINN with the discrepancy principle yields stable convergence locally under these assumptions. Our numerical examples will show that a modification of CG-REGINN is a competitive solver even when the assumptions for the tangential cone condition are not satisfied, in particular when F' is not injective. The key ingredient will be the treatment of the underdetermination of the linearized problem by introducing a weighted minimum norm solution in section 4.4.

Remark 2.14 (Evaluation of the Fréchet derivative for CG-REGINN). When using the cg method³ to solve the linear system (2.30), it is, in principle, *not* necessary to compute the Fréchet derivative $F'_{\mathcal{I}}$ explicitly. Instead, we only need to evaluate it and its adjoint in *one direction in each cg iteration*. This means that instead of assembling $F'_{\mathcal{I}}$, we can successively solve the system given in Theorem (2.9) and its adjoint problem in each cg iteration.

However, sampling the entries of $F'_{\mathcal{I}}$ by (2.22) is fast, especially when using linear ansatz functions for the forward problem, as the gradients appearing in (2.22) are constants in that case. Thus from our experience made in the numerical examples, it is only recommended to iteratively solve (2.30) if an explicit initialization of $F'_{\mathcal{I}}$ leads to memory problems.

³Or other Krylov space methods.

3. Sensitivity analysis of the complete electrode model

The conductivities defined in (2.25) have inhomogeneities which are successively localized about the origin, but with increasing contrast. The instability result (2.26) suggests that the *support size* of a conductivity perturbation has a higher impact on the boundary behaviour than the contrast, at least locally. However for a fixed discretization, that is, with a lower bound for the support size of conductivity changes, we have (under additional assumptions) the tangential cone condition (2.21), which is a local stability property. This means that setting a certain minimum discretization size of the conductivity space has a stabilizing effect on the ICP.

The purpose of this chapter is to investigate the sensitivity of the boundary data to changes in conductivity, depending on the size and location of the change. To that end, definitions of sensitivity and distinguishability of conductivities are introduced in section 3.1. For calculating sensitivities, it is necessary to evaluate the measurement operator. To do so, a novel analytic solution to compute R_σ for circular, non-centric geometries is derived in section 3.2. This solution relies on the properties of conformal maps. Thus, the results of this chapter are restricted to the 2D case.

The conformal mapping solution is used to evaluate sensitivities at arbitrary locations inside a disk in section 3.3, which can be used to generate a “sensitivity map” of the domain. The sensitivity behaviour of Calderón’s model and the CEM are compared in section 3.4. Based on these findings, a discretization of the conductivity space \mathcal{D}_P using a Voronoi tessellation is proposed in section 3.5. The key idea of this discretization is that changes in each conductivity coefficient have a roughly homogeneous sensitivity, i.e. they change the boundary data by the same amount. This realizes a trade-off for numerical inversion: We can greatly reduce the number of degrees of freedom in regions of low resolution and recover finer details in regions of high resolution by adaptive discretization sizes.

Finally, an approximation scheme is introduced which heuristically extends this concept to non-circular domains and speeds up the discretization.

Part of the work presented in this chapter was previously published – with slight modifications – in the *SIAM Journal of Imaging Sciences* [WR14].

3.1. Sensitivity and distinguishability

The *sensitivity* for distinguishing a conductivity $\sigma \in L_+^\infty(\Omega)$ from a reference conductivity $\tilde{\sigma} \in L_+^\infty(\Omega)$ is a measure of the difference of their corresponding boundary data. The exact definition may vary depending on which boundary model and measurement model is considered.

For Calderón's model, it is common to consider the difference of the ND maps (as operators on $L^2(\partial\Omega)$) in the induced operator norm, that is,

$$\lambda_{\sigma, \tilde{\sigma}}^* := \|\mathcal{R}_\sigma - \mathcal{R}_{\tilde{\sigma}}\|_{L^2(\partial\Omega)}, \quad (3.1)$$

see e.g. [Isa86, section III]. The corresponding equivalent for the CEM is the spectral norm $\|R_\sigma - R_{\tilde{\sigma}}\|_2$ of the CEM current-to-voltage map, which is considered e.g. in [HU13].

However for solving the ICP, it is natural to consider the information contained in the *measured* data rather than considering the full current-to-voltage map which might be unavailable. Moreover, the spectral norm of a matrix is its maximum singular value and thus, the spectral norm neglects a large amount of information in the difference of the operators.

Thus to distinguish conductivities by their boundary behaviour, it is arguably more adequate to consider the measurement operators in a Frobenius-type norm instead of the current-to-voltage map with the spectral norm. In this work, we consider the following two definitions of sensitivity:

Definition 3.1 (Absolute and relative measurement sensitivity). For a current frame \mathcal{I} and $\sigma, \tilde{\sigma} \in L_+^\infty(\Omega)$, we call

$$|\lambda|_{\sigma, \tilde{\sigma}} := \|F_{\mathcal{I}}(\sigma) - F_{\mathcal{I}}(\tilde{\sigma})\|_{\text{Fro}} = \left(\sum_{m=1}^M \|F_{I^{(m)}}(\sigma) - F_{I^{(m)}}(\tilde{\sigma})\|_2^2 \right)^{1/2} \quad \text{and} \quad (3.2)$$

$$\lambda_{\sigma, \tilde{\sigma}} := \left(\sum_{m=1}^M \frac{\|F_{I^{(m)}}(\sigma) - F_{I^{(m)}}(\tilde{\sigma})\|_2^2}{\|F_{I^{(m)}}(\tilde{\sigma})\|_2^2} \right)^{1/2} \quad (3.3)$$

the *absolute* and *relative (measurement) sensitivity* for distinguishing σ from the reference conductivity $\tilde{\sigma}$, respectively.

Both absolute and relative sensitivity have their purpose for investigating the ICP. In the presence of measurement noise, two conductivities can be distinguished if their absolute sensitivity exceeds the data noise level.

Definition 3.2 (Distinguishability). Two conductivities $\sigma, \tilde{\sigma} \in L_+^\infty(\Omega)$ are called *distinguishable* under a given noise level δ if

$$|\lambda|_{\sigma, \tilde{\sigma}} > \delta.$$

However, the norms of $F_{\mathcal{I}}(\sigma)$ and $F_{\mathcal{I}}(\tilde{\sigma})$ are very sensitive to the absolute values of the conductivi-

3. Sensitivity analysis of the complete electrode model

ties σ and $\tilde{\sigma}$ and the current amplitudes $\|I^{(m)}\|_2$, $m = 1, \dots, M$. When normalizing by the reference measurements in (3.3), these effects are reduced greatly. Figure 3.1 shows absolute and relative measurement sensitivities for a circular setting with 8 electrodes and varying σ and $\tilde{\sigma}$. For designing a sensitivity-based conductivity discretization $\mathcal{D}_{\mathcal{P}}$ (section 3.5) prior to solving the ICP, we consider it more appropriate to use $\lambda_{\sigma, \tilde{\sigma}}$, which is less sensitive to the a-priori unknown quantities. From an engineering point of view, the relative sensitivity corresponds to a measurement precision relative to the voltage amplitudes.

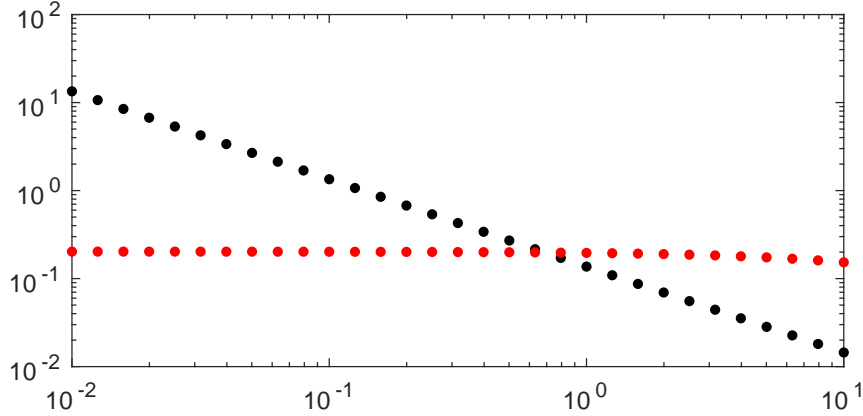


Figure 3.1.: For conductivities $\tilde{\sigma} = s\chi_{B_1(0)}$ and $\sigma = s(\chi_{B_1(0)} + \chi_{B_{0.5}(0)})$, the figure shows $s \mapsto |\lambda|_{\sigma, \tilde{\sigma}}$ (black) and $s \mapsto \lambda_{\sigma, \tilde{\sigma}}$ (red) plots for $s \in [10^{-2}, 10^1]$. The absolute measurement sensitivity is highly sensitive to the absolute conductivity values. Setting: Unit disk with 8 equi-spaced electrodes covering 50% of the boundary, contact impedances $z_1, \dots, z_L = 0.01$, adjacent current frame. To evaluate $|\lambda|_{\sigma, \tilde{\sigma}}$ and $\lambda_{\sigma, \tilde{\sigma}}$, the current-to-voltage maps $F_{\mathcal{I}}(\sigma)$ and $F_{\mathcal{I}}(\tilde{\sigma})$ were computed by the analytic solution presented in the next section (equation (3.14)).

3.2. Analytic solutions on the disk

Boundary value problems for PDEs, like the forward problem in EIT, are usually solved with numerical methods like the FEM. However for some basic geometries, nontrivial solutions to (2.5) are known and analytic properties of the DN and ND operators can be obtained. This was used already in the first work on this topic by Calderón [Cal80] for the continuum model to obtain injectivity of \mathcal{F}' on a disk at a homogeneous conductivity.

Two beautiful properties of Calderón's model on the disk will be the ingredients of this section:

1. For concentric conductivities, the trigonometric functions are eigenfunctions of the ND operator \mathcal{R}_σ . Thus, if the corresponding eigenvalues can be determined, the forward problem can be solved analytically by expanding a normal current $j_\nu \in L^2(\partial\Omega)$ in the trigonometric basis.

3. Sensitivity analysis of the complete electrode model

2. Equation (2.5) remains valid under conformal mapping; cf. standard literature [Neh52, SL91]. This allows us to conclude from a concentric setting to the ND map of a conformal image; see section 3.2.2.

Computing analytic forward solutions for the CEM is less obvious due to the indirect nature of the boundary conditions (2.13) and (2.14). A solution for the concentric “N-ring case”, i.e. for a finite number of concentric rings in the disk, each having a constant conductivity, is given in [SCI92]. A simpler approach for homogeneous conductivities on the disk is given by Demidenko in [Dem11].

In section 3.2.1, Demidenko’s approach is applied to a conductivity with a single centered perturbation, using the representation of [SCI92, Appendix 3]. Then, conformal maps are applied to non-centered conductivities, resulting in a “generalized” CEM with non-constant contact impedances along each electrode, in section 3.2.2. By extending the solution of section 3.2.1 to this generalized setting, a novel analytic forward solution for the CEM in a non-concentric setting is obtained.

3.2.1. Solutions for concentric conductivity perturbations

Throughout this chapter, we assume that $\Omega = B_1(\mathcal{O})$ is the unit disk¹ in \mathbb{R}^2 . For $\sigma_0, \sigma_1 > 0$ and $r_0 \in (0, 1)$, we consider the conductivity

$$\sigma(r, \theta) = \begin{cases} \sigma_0, & 0 \leq r \leq r_0, \\ \sigma_1, & r_0 < r \leq 1, \end{cases} \quad (3.4)$$

in a polar coordinate system $(r, \theta) \in [0, 1] \times [0, 2\pi)$. For Neumann data $j_\nu \in L^2_\diamond(\partial\Omega)$ in Calderón’s model, let $u = u(r, \theta)$ be a corresponding interior potential and $f = u|_{\partial\Omega} \in L^2(\partial\Omega)$ its Dirichlet data. We will express u as a Fourier series in polar coordinates. To that end, u can be split into even and odd parts in θ , and each part can be treated separately. Thus, assume first that u is even in θ . By [SCI92, eqn. (A3.4)], u is of the form

$$u(r, \theta) = u_0 + \begin{cases} \sum_{k=1}^{\infty} \left(\frac{r}{r_0}\right)^k a_k^{(1)} \cos(k\theta), & 0 \leq r \leq r_0, \\ \sum_{k=1}^{\infty} \left(r^{-k} a_k^{(2)} + r^k a_k^{(3)}\right) \cos(k\theta), & r_0 \leq r \leq 1, \end{cases}$$

for some coefficients u_0 and $a_k^{(1,2,3)} \in \mathbb{R}$. For $r > 0$, the current field in radial direction is

$$\sigma \frac{\partial u}{\partial r}(r, \theta) = \sigma \begin{cases} \sum_{k=1}^{\infty} k \left(\frac{r}{r_0}\right)^{k-1} a_k^{(1)} \cos(k\theta), & 0 < r \leq r_0, \\ \sum_{k=1}^{\infty} \left(kr^{k-1} a_k^{(3)} - kr^{-k-1} a_k^{(2)}\right) \cos(k\theta), & r_0 \leq r \leq 1. \end{cases}$$

¹All calculations can easily be extended to disks of arbitrary radius; see Remark 3.11.

3. Sensitivity analysis of the complete electrode model

By matching the continuous functions u and $\sigma \partial u / \partial r$ at $r = r_0$ for $r \rightarrow r_0^-$ and $r \rightarrow r_0^+$, we find from the orthogonality of the Fourier basis that

$$a_k^{(1)} = a_k^{(3)} r_0^k + a_k^{(2)} r_0^{-k} \quad \text{and} \quad \sigma_0 a_k^{(1)} = \sigma_1 \left(a_k^{(3)} r_0^k - a_k^{(2)} r_0^{-k} \right).$$

Substituting the first into the second equation, we get

$$a_k^{(2)} = c_k a_k^{(3)} \quad \text{with} \quad c_k := \frac{\sigma_1 / \sigma_0 - 1}{\sigma_1 / \sigma_0 + 1} r_0^{2k},$$

thus outside the perturbation, u has the representation

$$\begin{aligned} u(r, \theta) &= u_0 + \sum_{k=1}^{\infty} \left(r^k + r^{-k} c_k \right) a_k^{(3)} \cos(k\theta), \\ \frac{\partial u}{\partial r}(r, \theta) &= \sum_{k=1}^{\infty} k \left(r^{k-1} - r^{-k-1} c_k \right) a_k^{(3)} \cos(k\theta). \end{aligned}$$

By evaluating u at $r = 1$ and defining $a_k := (1 + c_k) a_k^{(3)}$, we can express the potential and normal current at the boundary as

$$\begin{aligned} u(1, \theta) &= u_0 + \sum_{k=1}^{\infty} a_k \cos(k\theta), \\ \sigma_1 \frac{\partial u}{\partial r}(1, \theta) &= \sigma_1 \sum_{k=1}^{\infty} d_k a_k \cos(k\theta), \quad \text{where} \quad d_k := k \frac{1 - c_k}{1 + c_k}. \end{aligned} \quad (3.5)$$

For the odd part of u in θ we can do the same calculations, replacing the cosine terms by sine terms and introducing coefficients b_k . Combining both, we get the representations

$$f(\theta) = u(1, \theta) = u_0 + \sum_{k=1}^{\infty} a_k \cos(k\theta) + b_k \sin(k\theta), \quad (3.6)$$

$$j_\nu(\theta) = \sigma_1 \frac{\partial u}{\partial r}(1, \theta) = \sigma_1 \sum_{k=1}^{\infty} d_k (a_k \cos(k\theta) + b_k \sin(k\theta)), \quad (3.7)$$

for some Fourier coefficients $u_0, a_k, b_k \in \mathbb{R}$ ($u_0 = 0$ if $f \in L_\diamond^2(\partial\Omega)$) and d_k as above, $k \in \mathbb{N}$. This means that for centered perturbations, the trigonometric functions are eigenfunctions of \mathcal{R}_σ with eigenvalues $\tau_{\sigma,k} = (\sigma_1 d_k)^{-1}$.

To obtain analytic forward solutions for the CEM from the continuum representations (3.6)–(3.7), we can interpret the interior potential u as the first component of the solution (u, U) to the variational approach (2.17) for some current vector $I \in \mathbb{R}_\diamond^L$. For the CEM and σ smooth near $\partial\Omega$, we have that $u|_{\partial\Omega} \in H^{3/2-\alpha}(\partial\Omega)$ and $j_\nu \in H^{1/2-\alpha}(\partial\Omega)$ for all $\alpha > 0$; see [DHH⁺12, Remark 1] and the references therein. This guarantees a sufficiently fast decay of the coefficients for the convergence of (3.6) and (3.7) in the classical sense.

3. Sensitivity analysis of the complete electrode model

Then, the current vector I can be expressed by substituting equation (3.7) into (2.14), which gives

$$I_l = \int_{E_l} j_\nu \, dS = \sigma_1 \sum_{k=1}^{\infty} d_k (a_k s_l(k) - b_k c_l(k)) \quad (3.8)$$

with definite integrals

$$s_l(k) = \frac{\sin(k(\theta_l + \omega_l)) - \sin(k(\theta_l - \omega_l))}{k}, \quad c_l(k) = \frac{\cos(k(\theta_l + \omega_l)) - \cos(k(\theta_l - \omega_l))}{k}, \quad (3.9)$$

where $\theta_l \in [0, 2\pi)$ is the angular coordinate of the l th electrode center and $\omega_l > 0$ is its angular half-width. However, it is advisable to exploit relation (2.13) by rewriting the normal current as

$$j_\nu = z_l^{-1}(U_l - u) \quad \text{on } E_l, \quad l = 1, \dots, L. \quad (3.10)$$

Then, the electrode currents can be expressed by the faster converging Fourier series (3.6) as

$$I_l = \frac{1}{z_l} \left(|E_l| (U_l - u_0) - \sum_{k=1}^{\infty} a_k s_l(k) - b_k c_l(k) \right). \quad (3.11)$$

This expression is free of the $\mathcal{O}(k)$ coefficients d_k .

By extending the result of Demidenko [Dem11, Appendix] to non-homogeneous conductivities, the unknown Fourier coefficients can be obtained. To that end, the approach of [Dem11, Appendix] can be applied to (3.6) and (3.7) for obtaining the Fourier coefficients u_0 and a_k, b_k , $k \in \mathbb{N}$ corresponding to a given voltage pattern $U = (U_1, \dots, U_L)^\top$ in the CEM. To achieve this, we substitute these representations of $u(1, \theta)$ and $j_\nu(\theta)$ into (3.10) which yields

$$\begin{aligned} & \sigma_1 \sum_{k=1}^{\infty} d_k (a_k \cos(k\theta) + b_k \sin(k\theta)) \\ &= \begin{cases} \frac{1}{z_l} \left(U_l - u_0 - \sum_{k=1}^{\infty} a_k \cos(k\theta) + b_k \sin(k\theta) \right) & \text{on } E_l, \quad l = 1, \dots, L, \\ 0, & \text{otherwise.} \end{cases} \end{aligned} \quad (3.12)$$

Then, we multiply (3.12) with $\cos(n\theta)$, $n \in \mathbb{N}_0$, and $\sin(n\theta)$, $n \in \mathbb{N}$, respectively and integrate in θ

3. Sensitivity analysis of the complete electrode model

over $[0, 2\pi)$ which leads to the set of equations

$$\begin{aligned}
0 &= \sum_{l=1}^L \frac{U_l - u_0}{z_l} 2\omega_l \\
&\quad - \sum_{k=1}^{\infty} \frac{a_k}{z_l} \int_{\theta_l - \omega_l}^{\theta_l + \omega_l} \cos(k\theta) \, d\theta + \frac{b_k}{z_l} \int_{\theta_l - \omega_l}^{\theta_l + \omega_l} \sin(k\theta) \, d\theta \quad \text{for } n = 0, \\
\sigma_1 \pi d_n a_n &= \sum_{l=1}^L \frac{U_l - u_0}{z_l} \int_{\theta_l - \omega_l}^{\theta_l + \omega_l} \cos(n\theta) \, d\theta \\
&\quad - \sum_{k=1}^{\infty} \frac{a_k}{z_l} \int_{\theta_l - \omega_l}^{\theta_l + \omega_l} \cos(n\theta) \cos(k\theta) \, d\theta + \frac{b_k}{z_l} \int_{\theta_l - \omega_l}^{\theta_l + \omega_l} \cos(n\theta) \sin(k\theta) \, d\theta, \quad n \in \mathbb{N}, \\
\sigma_1 \pi d_n b_n &= \sum_{l=1}^L \frac{U_l - u_0}{z_l} \int_{\theta_l - \omega_l}^{\theta_l + \omega_l} \sin(n\theta) \, d\theta \\
&\quad - \sum_{k=1}^{\infty} \frac{a_k}{z_l} \int_{\theta_l - \omega_l}^{\theta_l + \omega_l} \sin(n\theta) \cos(k\theta) \, d\theta + \frac{b_k}{z_l} \int_{\theta_l - \omega_l}^{\theta_l + \omega_l} \sin(n\theta) \sin(k\theta) \, d\theta, \quad n \in \mathbb{N}, \quad (3.13)
\end{aligned}$$

where $\theta_l \in [0, 2\pi)$ is the angular coordinate of the l th electrode center and $\omega_l > 0$ is its angular half-width. These equations can be rewritten as an infinite system of linear equations² for u_0, a_k, b_k as

$$\begin{pmatrix} A & B \\ B^\top & C \end{pmatrix} (u_0, a_1, a_2, \dots, b_1, b_2, \dots)^\top = \begin{pmatrix} r^U \\ s^U \end{pmatrix} \quad (3.14)$$

with the sequences

$$r^U = (r_0^U, r_1^U, \dots)^\top, \quad s^U = (s_1^U, s_2^U, \dots)^\top,$$

and matrices

$$A = \begin{pmatrix} A_{00} & A_{01} & \dots \\ A_{10} & A_{11} & \dots \\ \vdots & \vdots & \ddots \end{pmatrix}, \quad B = \begin{pmatrix} B_{01} & B_{02} & \dots \\ B_{11} & B_{12} & \dots \\ \vdots & \vdots & \ddots \end{pmatrix}, \quad C = \begin{pmatrix} C_{11} & C_{12} & \dots \\ C_{21} & C_{22} & \dots \\ \vdots & \vdots & \ddots \end{pmatrix},$$

²In an abusive order of the coefficients (since A is infinite dimensional). However, this notation will be convenient when considering truncated versions of the system.

3. Sensitivity analysis of the complete electrode model

with entries

$$\begin{aligned}
A_{nk} &= \sum_{l=1}^L \frac{1}{z_l} \underbrace{\int_{\theta_l - \omega_l}^{\theta_l + \omega_l} \cos(n\theta) \cos(k\theta) d\theta}_{=\frac{1}{2}[s_l(k-n) + s_l(k+n)]} + \delta_{nk} \sigma_1 \pi d_k, & n \in \mathbb{N}_0, k \in \mathbb{N}_0, \\
B_{nk} &= \sum_{l=1}^L \frac{1}{z_l} \underbrace{\int_{\theta_l - \omega_l}^{\theta_l + \omega_l} \cos(n\theta) \sin(k\theta) d\theta}_{=-\frac{1}{2}[c_l(k-n) + c_l(k+n)]}, & n \in \mathbb{N}_0, k \in \mathbb{N}, \\
C_{nk} &= \sum_{l=1}^L \frac{1}{z_l} \underbrace{\int_{\theta_l - \omega_l}^{\theta_l + \omega_l} \sin(n\theta) \sin(k\theta) d\theta}_{=\frac{1}{2}[s_l(k-n) - s_l(k+n)]} + \delta_{nk} \sigma_1 \pi d_k, & n \in \mathbb{N}, k \in \mathbb{N}, \\
r_n^U &= \sum_{l=1}^L \frac{U_l}{z_l} \underbrace{\int_{\theta_l - \omega_l}^{\theta_l + \omega_l} \cos(n\theta) d\theta}_{=s_l(n)}, & n \in \mathbb{N}_0, \\
s_n^U &= \sum_{l=1}^L \frac{U_l}{z_l} \underbrace{\int_{\theta_l - \omega_l}^{\theta_l + \omega_l} \sin(n\theta) d\theta}_{=-c_l(n)}, & n \in \mathbb{N},
\end{aligned} \tag{3.15}$$

where δ_{nk} is the Kronecker delta. The above integrals have analytic solutions with $s_l(k)$ and $c_l(k)$ given by (3.9) for $k \neq 0$ and $s_l(0) := 2\omega_l$, $c_l(0) := 0$. By solving (a truncated version of) equation (3.14), the Fourier coefficients of the potential f and current j_ν can be obtained from the electrode potentials U_1, \dots, U_L . In summary, we have proved the following theorem:

Theorem 3.3 (Fourier coefficients for the CEM). *The coefficients u_0 and $a_k, b_k, k \in \mathbb{N}$, of (3.6) and (3.7) satisfy the linear system of equations (3.14).*

In practice, the Fourier series must be truncated to get a finite system of linear equations.

Remark 3.4 (Truncation index of the Fourier series). The truncation index N should be chosen with respect to the electrode widths such that the potentials and normal currents along all electrodes are approximated well by the truncated Fourier series. In particular, if $|E|_{\min}$ is the smallest electrode angular width, the truncation index should be chosen well above the ‘‘critical’’ index $N_{\min} := \lceil 2\pi/|E|_{\min} \rceil$ of a Fourier sum that can resolve details of size $|E|_{\min}$. In our implementations, we found $N = 1000 + 32N_{\min}$ to give results of very high accuracy. In [Dem11], $N = 500$ is used for settings with 4 and 16 electrodes.

For σ as in (3.4), we can now compute the current-to-voltage map R_σ as follows:

1. Choose a basis $\mathcal{U} = (U^{(1)} | \dots | U^{(L-1)})$ of \mathbb{R}_\diamond^L .
2. Define a truncation index N .

3. Sensitivity analysis of the complete electrode model

3. For each $U^{(m)}$, $m = 1, \dots, L-1$, compute the Fourier coefficients $u_0^{(m)}, a_k^{(m)}, b_k^{(m)}$, $k = 1, \dots, N$, by solving the truncated linear system (3.14).
4. Compute the corresponding electrode currents $I_l^{(m)}$, $m = 1, \dots, L-1$, $l = 1, \dots, L$, by equation (3.11).
5. Compute the current-to-voltage map as $R_\sigma = \mathcal{U}\mathcal{I}^+$.

By evaluating $R_{\sigma_1 \chi_\Omega}$ (i.e. for constant conductivity) and R_σ for σ as in (3.4), we can compute the sensitivities $|\lambda|_{\sigma, \sigma_1}$ and $\lambda_{\sigma, \sigma_1}$ for distinguishing a conductivity with centered circular perturbation from the homogeneous background. Clearly, $|\lambda|_{\sigma, \sigma_1}$ and $\lambda_{\sigma, \sigma_1}$ depend (nonlinearly) on the values σ_0 and σ_1 and the radius r_0 of the perturbation.

From this sensitivity information, we get a stability argument by the following monotonicity property:

Theorem 3.5 (Monotonicity property of the sensitivity). *Let $\sigma_1, \eta > 0$ and let*

$$\sigma_B = \sigma_1 + \eta \chi_B, \quad \sigma_D = \sigma_1 + \eta \chi_D \quad \text{on } \Omega \quad \text{for some subsets } B \subset D \subset \Omega.$$

Then, $|\lambda|_{\sigma_D, \sigma_1} \geq |\lambda|_{\sigma_B, \sigma_1}$ and $\lambda_{\sigma_D, \sigma_1} \geq \lambda_{\sigma_B, \sigma_1}$.

Proof. This is a CEM version of [GIN90, Appendix I]. The energy functional

$$J(w, W) = \frac{1}{2} a((w, W), (w, W)) - \sum_{l=1}^L I_l W_l$$

of the bilinear elliptic operator a from (2.16) has the minimizing property

$$J(u, U) = \min_{(w, W) \in H^1(\Omega) \times \mathbb{R}^L} J(w, W),$$

where (u, U) is the solution of the variational CEM problem (2.17) for current vector I . For the conductivities σ_B and σ_D , denote by a_B and a_D their corresponding bilinear operators, by J_B and J_D their energy functionals, and by (u_B, U_B) and (u_D, U_D) their CEM solutions for I , respectively. Comparing the definitions of J_B and J_D with (2.17), we immediately get

$$J_B(u_B, U_B) = -\frac{1}{2} \langle I, U_B \rangle \quad \text{and} \quad J_D(u_D, U_D) = -\frac{1}{2} \langle I, U_D \rangle.$$

From $\sigma_D \geq \sigma_B$ on Ω , it follows that

$$J_D(u_D, U_D) - J_B(u_D, U_D) = \frac{1}{2} \int_{\Omega} (\sigma_D - \sigma_B) |\nabla u_D|^2 \, dx \geq 0.$$

By the minimizing property for J_B , we get

$$-\langle I, U_D \rangle = 2J_D(u_D, U_D) \geq 2J_B(u_D, U_D) \geq 2J_B(u_B, U_B) = -\langle I, U_B \rangle.$$

3. Sensitivity analysis of the complete electrode model

In terms of ND maps, we have that $U_B = R_{\sigma_B} I$ and $U_D = R_{\sigma_D} I$, thus

$$\langle I, (R_{\sigma_D} - R_{\sigma_B}) I \rangle \leq 0 \quad (3.16)$$

for all $I \in \mathbb{R}^L$. Similarly, we get $\langle I, (R_{\sigma_D} - R_{\sigma_1}) I \rangle \leq 0$ and $\langle I, (R_{\sigma_B} - R_{\sigma_1}) I \rangle \leq 0$, which means that both operator differences are negative semi-definite on \mathbb{R}^L (the eigenvalue for constant vectors is 0). Combined with (3.16), we have

$$\langle I, (R_{\sigma_D} - R_{\sigma_1}) I \rangle \leq \langle I, (R_{\sigma_B} - R_{\sigma_1}) I \rangle \leq 0 \quad \forall I \in \mathbb{R}^L. \quad (3.17)$$

The first consequence of (3.17) is that the sensitivity is monotonous in the spectral norm:

$$\|R_{\sigma_D} - R_{\sigma_1}\|_2 \geq \|R_{\sigma_B} - R_{\sigma_1}\|_2,$$

which was presented in [WR14, Appendix C]. Moreover as (3.17) holds on any subspace of \mathbb{R}^L , the Courant-Fischer min-max theorem yields

$$\kappa_l^D \leq \kappa_l^B \leq 0, \quad l = 1, \dots, L,$$

where $\kappa_1^D \leq \kappa_2^D \leq \dots \leq \kappa_L^D = 0$ and $\kappa_1^B \leq \kappa_2^B \leq \dots \leq \kappa_L^B = 0$ are the eigenvalues of $R_{\sigma_D} - R_{\sigma_1}$ and $R_{\sigma_B} - R_{\sigma_1}$, respectively. From this we get the monotonicity in the Frobenius norm

$$\begin{aligned} |\lambda|_{\sigma_D, \sigma_1}^2 &= \|R_{\sigma_D} - R_{\sigma_1}\|_{\text{Fro}}^2 = \text{tr} \left((R_{\sigma_D} - R_{\sigma_1})^2 \right) = (\kappa_1^D)^2 + \dots + (\kappa_L^D)^2 \\ &\geq (\kappa_1^B)^2 + \dots + (\kappa_L^B)^2 = \text{tr} \left((R_{\sigma_B} - R_{\sigma_1})^2 \right) = \|R_{\sigma_B} - R_{\sigma_1}\|_{\text{Fro}}^2 = |\lambda|_{\sigma_B, \sigma_1}^2. \end{aligned}$$

Moreover, by considering each measurement individually, we have for $m = 1, \dots, M$ that

$$\begin{aligned} \|F_{I^{(m)}}(\sigma_D) - F_{I^{(m)}}(\sigma_1)\|_2^2 &= \|F_{I^{(m)}}(\sigma_D) - F_{I^{(m)}}(\sigma_1)\|_{\text{Fro}}^2 \\ &\leq \|F_{I^{(m)}}(\sigma_B) - F_{I^{(m)}}(\sigma_1)\|_{\text{Fro}}^2 = \|F_{I^{(m)}}(\sigma_B) - F_{I^{(m)}}(\sigma_1)\|_2^2. \end{aligned}$$

Dividing by $\|F_{I^{(m)}}(\sigma_1)\|_2^2$ and summing over m yields the monotonicity of the relative sensitivity $\lambda_{\sigma_D, \sigma_1}^2 \geq \lambda_{\sigma_B, \sigma_1}^2$, which completes the proof. \square

A similar monotonicity holds for increasing contrast:

Theorem 3.6 (Monotonicity property continued). *Let $\sigma_1, \eta, \tilde{\eta} > 0$, $\tilde{\eta} > \eta$. Then for*

$$\sigma = \sigma_1 + \eta \chi_B, \quad \tilde{\sigma} = \sigma_1 + \tilde{\eta} \chi_B \quad \text{on } \Omega \quad \text{for some } B \subset \Omega,$$

we have $|\lambda|_{\tilde{\sigma}, \sigma_1} \geq |\lambda|_{\sigma, \sigma_1}$ and $\lambda_{\tilde{\sigma}, \sigma_1} \geq \lambda_{\sigma, \sigma_1}$.

The proof is analogous to the previous one. From theorems 3.5 and 3.6, we obtain the following corollary, which is helpful for designing sensitivity-based discretizations:

Corollary 3.7. *If for $\sigma_1, \eta > 0$, $B \subset \Omega$, a perturbed conductivity $\sigma_1 + \eta \chi_B$ is distinguishable from a homogeneous background σ_1 , then any conductivity $\sigma_1 + \tilde{\eta} \chi_D$ with $\tilde{\eta} \geq \eta$, $D \supset B$, is also distinguishable from σ_1 .*

3.2.2. A generalization using conformal maps

Conformal maps have been used for analyzing Calderón's model on the unit disk [SYB84] and for investigating its resolution [SBB87]. Moreover, quasi-conformal maps have been used for reconstructing quasi-conformal (anisotropic) images of realistic boundary shape settings for Calderón's model and electrode models [KLO05].

Using conformal diffeomorphisms on the unit disk, we will compute R_σ analytically for conductivities with circular perturbations at arbitrary locations inside the unit disk by reducing the non-centered situation to the centered case of the previous section. This will be done by mapping the disk conformally onto itself such that the non-centered perturbation is centered about the origin (Lemma 3.8), then transforming the CEM boundary description accordingly (Theorem 3.9) and solving the forward problem in this transformed setting (Theorem 3.10).

Due to the nature of conformal maps, the current-to-voltage map of the conformally mapped setting agrees with the one of the initial geometry when the boundary parameters are modified accordingly. With this technique, we can determine sensitivities of all circular conductivity perturbations inside a disk.

Let $w: B_1(\mathcal{O}) \rightarrow B_1(\mathcal{O})$ be a conformal diffeomorphism on the unit disk that maps a point $\mathcal{T} = (T, \varphi) \in [0, 1] \times [0, 2\pi)$ to the origin \mathcal{O} . Then for³ $\mathbb{C} \sim \mathbb{R}^2$, w and its inverse are given (up to rotation) by⁴

$$z \mapsto w(z) = \frac{e^{-i\varphi}z - T}{1 - Te^{-i\varphi}z} \quad \text{and} \quad y \mapsto w^{-1}(y) = e^{i\varphi} \frac{y + T}{1 + Ty}. \quad (3.18)$$

In particular, a point on the boundary is again mapped to the boundary since

$$\left| w(e^{i\theta}) \right| = \left| w^{-1}(e^{i\theta}) \right| = 1, \quad \theta \in [0, 2\pi). \quad (3.19)$$

Our aim is to transform an EIT setting conformally such that a disk

$$B_{r_{\mathcal{Q}}}(\mathcal{Q}), \quad \mathcal{Q} = (Q, \varphi) \in [0, 1] \times [0, 2\pi) \quad \text{and} \quad 0 < r_{\mathcal{Q}} < 1 - Q,$$

is mapped by w to a disk $B_{r_0}(\mathcal{O})$ centered about the origin for some $0 < r_0 < 1$. This is depicted in Figure 3.2.

³We identify \mathbb{R}^2 in polar coordinates with the complex plane, using whatever notation is more convenient.

⁴The arguments (T, φ) are omitted. They denote the geometric parameters of w and w^{-1} throughout this work.

3. Sensitivity analysis of the complete electrode model

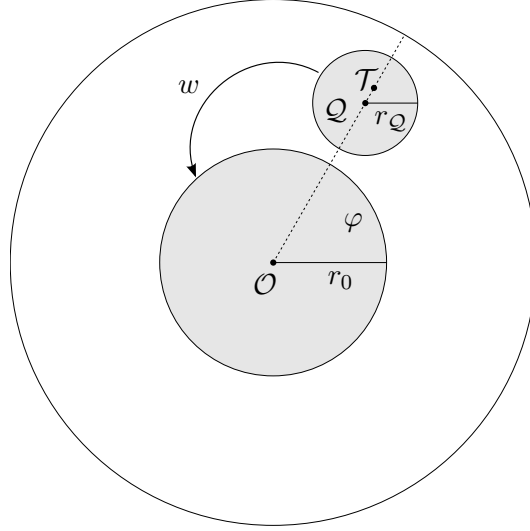


Figure 3.2.: The conformal map w maps $B_1(\mathcal{O})$ onto itself, \mathcal{T} to \mathcal{O} and $B_{r_Q}(\mathcal{Q})$ onto $B_{r_0}(\mathcal{O})$.

The relations between the perturbation parameters Q and r_Q , the parameters T and φ of the according conformal map w and the resulting radius r_0 are summarized in the following Lemma.

Lemma 3.8. *Let $\mathcal{Q} = (Q, \varphi) \in [0, 1) \times [0, 2\pi)$ and $0 < r_Q < 1 - Q$. If w is such that*

$$w(B_{r_Q}(\mathcal{Q})) = B_{r_0}(\mathcal{O}) \quad \text{for some } 0 < r_0 < 1,$$

then Q and r_Q satisfy the equations

$$Q = T \frac{1 - r_0^2}{1 - r_0^2 T^2} \quad \text{and} \quad r_Q = r_0 \frac{1 - T^2}{1 - r_0^2 T^2}, \quad (3.20)$$

and the parameters T and r_0 are given as

$$\begin{aligned} T &= \frac{1 + Q^2 - r_Q^2 - \sqrt{(1 + Q^2 - r_Q^2)^2 - 4Q^2}}{2Q} \quad \text{and} \\ r_0 &= \frac{1 - Q^2 + r_Q^2 - \sqrt{(1 - Q^2 + r_Q^2)^2 - 4r_Q^2}}{2r_Q}. \end{aligned} \quad (3.21)$$

In particular, the angular parameter φ of \mathcal{Q} and w is identical. Moreover $r_0 > r_Q$ and $T > Q$.

Proof. First, we relate the unknown radius r_0 with the action of w . Using the fact that w^{-1} (a Möbius transform) maps circles onto circles and has an axis of symmetry in direction $e^{i\varphi}$ gives

$$w^{-1}(\pm r_0 e^{-i\varphi}) = \frac{\pm r_0 + T}{1 + Tr_0} \stackrel{!}{=} Q \pm r_Q,$$

thus by adding the equations for “+” and “-”, we get

$$2Q = \frac{r_0 + T}{1 - Tr_0} - \frac{r_0 + T}{1 + Tr_0} = 2T \frac{1 - r_0^2}{1 - T^2 r_0^2}$$

3. Sensitivity analysis of the complete electrode model

which is the first equality in (3.20), while subtraction yields

$$2r_{\mathcal{Q}} = \frac{r_0 + T}{1 + Tr_0} + \frac{r_0 - T}{1 - Tr_0} = 2r_0 \frac{1 - T^2}{1 - r_0^2 T^2},$$

which is the second equality. Resolving the quadratic terms (3.20) for T and r_0 and picking the solutions in $[0, 1]$ gives the claimed expressions (3.21), see [SYB84, section 5]. \square

Lemma 3.8 states that any non-centered disk can be mapped onto a centered disk by a Möbius transform, i.e. a conformal map operating on the unit disk. We will use this for solving a CEM forward problem for non-centered inhomogeneities. The following theorem shows that a non-concentric CEM forward problem can be reduced to a modification of a *centered* forward problem:

Theorem 3.9 (Conformal mapping of the CEM). *Let $\Omega = B_1(\mathcal{O})$ with electrodes $E_1, \dots, E_L \subset \partial\Omega$ and contact impedances $z_1, \dots, z_L > 0$. For $\sigma_1 > 0$, $\eta \in \mathbb{R}$ such that $\sigma_1 + \eta > c$, $\mathcal{Q} = (Q, \varphi) \in [0, 1) \times [0, 2\pi)$ and $0 < r_{\mathcal{Q}} < 1 - Q$, consider the conductivity*

$$\sigma = \sigma_1 + \eta \chi_{B_{\mathcal{Q}}(r_{\mathcal{Q}})} \in L_+^\infty(\Omega). \quad (3.22)$$

For $I \in \mathbb{R}_>^L$, let (u, U) be the solution of (2.17) in the above setting with Dirichlet and Neumann traces $f = u|_{\partial\Omega}$ and $j_\nu = \sigma_1 \frac{\partial u}{\partial r}|_{\partial\Omega}$, respectively. Let w be the conformal map with parameters φ and T as in Lemma 3.8 and denote by

$$\tilde{\theta} := g(\theta) := \arg(w(e^{i\theta})), \quad \text{that is} \quad \theta = g^{-1}(\tilde{\theta}) = \arg(w^{-1}(e^{i\tilde{\theta}})),$$

the boundary parametrization under conformal mapping. Finally, define by

$$u^w := u \circ w^{-1} \quad \text{and} \quad \sigma^w := \sigma \circ w^{-1}$$

the w -transformed potential and conductivity, respectively, by

$$f^w := f \circ g^{-1} \quad \text{and} \quad j_\nu^w(\tilde{\theta}) := \frac{1 - T^2}{1 + T^2 + 2T \cos(\tilde{\theta})} j_\nu(g^{-1}(\tilde{\theta})) \quad (3.23)$$

the w -transformed Dirichlet and Neumann data, respectively, and by

$$E_l^w := g(E_l) \quad \text{and} \quad z_l^w(\tilde{\theta}) := \frac{1 + T^2 + 2T \cos(\tilde{\theta})}{1 - T^2} z_l, \quad l = 1, \dots, L, \quad (3.24)$$

the w -transformed electrodes and contact impedances, respectively.

3. Sensitivity analysis of the complete electrode model

Then, I and U satisfy the w -transformed CEM equations

$$-\nabla \cdot (\sigma^w \nabla u^w) = 0 \quad \text{on } \Omega, \quad (3.25)$$

$$f^w(\tilde{\theta}) + z_l^w(\tilde{\theta}) j_\nu^w(\tilde{\theta}) = U_l \quad \text{on } E_l^w, \quad l = 1, \dots, L, \quad (3.26)$$

$$\int_{E_l^w} j_\nu^w \, dS = I_l, \quad l = 1, \dots, L, \quad (3.27)$$

$$j_\nu^w = 0 \quad \text{on } \partial\Omega \setminus \{E_1^w \cup \dots \cup E_L^w\}, \quad (3.28)$$

This means that the ND map R_σ of the initial problem agrees with the ND map R_σ^w of the w -transformed problem.

Note that the contact impedances z_l^w in Theorem 3.9 are varying in angular direction along each electrode, so equations (3.25)–(3.28) are an extension of the classical CEM model (2.12)–(2.15).

Proof of Theorem 3.9. Set

$$w_r := |w|, \quad w_{\tilde{r}}^{-1} := |w^{-1}|, \quad w_\theta := \arg(w), \quad w_{\tilde{\theta}}^{-1} := \arg(w^{-1}).$$

Being conformal maps, w and w^{-1} satisfy the Cauchy-Riemann equations. In particular, we have at the boundary that

$$g'(\theta) = \frac{\partial w_\theta}{\partial \theta}(r, \theta) \Big|_{r=1} = \frac{\partial w_r}{\partial r}(r, \theta) \Big|_{r=1} \quad \text{and} \quad (g^{-1})'(\tilde{\theta}) = \frac{\partial w_{\tilde{\theta}}^{-1}}{\partial \tilde{\theta}}(\tilde{r}, \tilde{\theta}) \Big|_{\tilde{r}=1} = \frac{\partial w_{\tilde{r}}^{-1}}{\partial \tilde{r}}(\tilde{r}, \tilde{\theta}) \Big|_{\tilde{r}=1}.$$

By the cosine rule, we find that

$$\begin{aligned} (w_r(r, \theta))^2 &= \frac{|re^{i(\theta-\varphi)} - T|^2}{|1 - rTe^{i(\theta-\varphi)}|^2} = \frac{r^2 + T^2 + 2rT \cos(\theta - \varphi)}{1 + r^2T^2 + 2rT \cos(\theta - \varphi)} \quad \text{and} \\ (w_{\tilde{r}}^{-1}(\tilde{r}, \tilde{\theta}))^2 &= \frac{|\tilde{r}e^{i\tilde{\theta}} - T|^2}{|1 + \tilde{r}Te^{i\tilde{\theta}}|^2} = \frac{\tilde{r}^2 + T^2 - 2\tilde{r}T \cos(\tilde{\theta})}{1 + \tilde{r}^2T^2 - 2\tilde{r}T \cos(\tilde{\theta})}, \end{aligned}$$

resulting (after some more algebra) in

$$\begin{aligned} g'(\theta) &= \frac{\partial w_r}{\partial r}(r, \theta) \Big|_{r=1} = \frac{1 - T^2}{1 + T^2 - 2T \cos(\theta - \varphi)} \quad \text{and} \\ (g^{-1})'(\tilde{\theta}) &= \frac{\partial w_{\tilde{r}}^{-1}}{\partial \tilde{r}}(\tilde{r}, \tilde{\theta}) \Big|_{\tilde{r}=1} = \frac{1 - T^2}{1 + T^2 + 2T \cos(\tilde{\theta})}. \end{aligned} \quad (3.29)$$

Moreover, it follows from (3.19) that the modulus is constant along the boundary in angular direction. Again using the Cauchy-Riemann equations, this gives

$$0 = \frac{\partial w_r}{\partial \theta}(r, \theta) \Big|_{r=1} = - \frac{\partial w_\theta}{\partial r}(r, \theta) \Big|_{r=1} \quad \text{and} \quad 0 = \frac{\partial w_{\tilde{r}}^{-1}}{\partial \tilde{\theta}}(\tilde{r}, \tilde{\theta}) \Big|_{\tilde{r}=1} = - \frac{\partial w_{\tilde{\theta}}^{-1}}{\partial \tilde{r}}(\tilde{r}, \tilde{\theta}) \Big|_{\tilde{r}=1}.$$

3. Sensitivity analysis of the complete electrode model

When transforming a potential u defined on the unit disk conformally to u^w by

$$u^w(w(z)) = u(z), \quad \text{i.e.} \quad u^w(z) = u(w^{-1}(z)),$$

then (3.25) is a classical result for elliptic PDEs under conformal mapping, see e.g. [Neh52, SL91]. Moreover, $u^w(1, \tilde{\theta}) = u(w^{-1}(1, \tilde{\theta})) = f(g^{-1}(\tilde{\theta})) = f^w(\tilde{\theta})$. For $\sigma \equiv \sigma_1$ near the boundary and using the two-dimensional chain-rule in polar coordinates, the transformed Neumann data reads

$$\begin{aligned} \sigma_1 \frac{\partial u^w}{\partial \tilde{r}}(\tilde{r}, \tilde{\theta}) \Big|_{\tilde{r}=1} &= \sigma_1 \frac{\partial}{\partial \tilde{r}}(u \circ w^{-1})(\tilde{r}, \tilde{\theta}) \Big|_{\tilde{r}=1} \\ &= \sigma_1 \frac{\partial u}{\partial r}(w^{-1}(\tilde{r}, \tilde{\theta})) \frac{\partial w_{\tilde{r}}^{-1}}{\partial \tilde{r}}(\tilde{r}, \tilde{\theta}) \Big|_{\tilde{r}=1} + \underbrace{\sigma_1 \frac{\partial u}{\partial \theta}(w^{-1}(\tilde{r}, \tilde{\theta})) \frac{w_{\tilde{\theta}}^{-1}}{\partial \tilde{r}}(\tilde{r}, \tilde{\theta}) \Big|_{\tilde{r}=1}}_{=0} \\ &= \frac{1 - T^2}{1 + T^2 + 2T \cos(\tilde{\theta})} j_\nu(g^{-1}(\tilde{\theta})) = j_\nu^w(\tilde{\theta}). \end{aligned} \quad (3.30)$$

This immediately implies (3.28). Moreover for $\theta \in E_l$, that is $\tilde{\theta} = g(\theta) \in E_l^w$, we have that

$$\begin{aligned} U_l &= f(\theta) + z_l j_\nu(\theta) = f(g^{-1}(\tilde{\theta})) + z_l j_\nu(g^{-1}(\tilde{\theta})) \\ &= f^w(\tilde{\theta}) + z_l \frac{1 + R^2 + 2R \cos(\tilde{\theta})}{1 - R^2} j_\nu^w(\tilde{\theta}) = f^w(\tilde{\theta}) + z_l^w(\tilde{\theta}) j_\nu^w(\tilde{\theta}) = U_l^w \end{aligned}$$

for $l = 1, \dots, L$, which is (3.26).

Finally, we obtain (3.27) by a change of variables in (2.14) together with (3.30) and (3.29) as

$$\begin{aligned} I_l &= \int_{E_l} j_\nu(\theta) \, d\theta = \int_{g(E_l)} j_\nu(g^{-1}(\tilde{\theta})) (g^{-1})'(\tilde{\theta}) \, d\tilde{\theta} \\ &\stackrel{(3.30)}{=} \int_{E_l^w} \frac{1 + T^2 + 2T \cos(\tilde{\theta})}{1 - T^2} j_\nu^w(\tilde{\theta}) (g^{-1})'(\tilde{\theta}) \, d\tilde{\theta} \stackrel{(3.29)}{=} \int_{E_l^w} j_\nu^w(\tilde{\theta}) \, d\tilde{\theta}. \end{aligned} \quad \square$$

As in the preceding section 3.2.1, the conformal image of the non-concentric conductivity is concentric, thus the transformed Dirichlet and Neumann data can again be expressed by Fourier series as

$$f^w(\tilde{\theta}) = u^w(1, \tilde{\theta}) = \tilde{u}_0 + \sum_{k=1}^{\infty} \tilde{a}_k \cos(k\tilde{\theta}) + \tilde{b}_k \sin(k\tilde{\theta}) \quad \text{and} \quad (3.31)$$

$$j_\nu^w(\tilde{\theta}) = \sigma_1 \frac{\partial u^w}{\partial \tilde{r}}(1, \tilde{\theta}) = \sigma_1 \sum_{k=1}^{\infty} d_k \left(\tilde{a}_k \cos(k\tilde{\theta}) + \tilde{b}_k \sin(k\tilde{\theta}) \right), \quad (3.32)$$

for some Fourier coefficients $\tilde{u}_0, \tilde{a}_k, \tilde{b}_k, k \in \mathbb{N}$ (the tilde indicates that the coefficients originate from the set of equations (3.25)–(3.28)).

The key result of this section is that these coefficients can again be obtained from the corresponding electrode potential $U \in \mathbb{R}_{\diamond}^L$ by an infinite linear system of equations, similar to (3.14) for the concentric case. Due to the somewhat lengthy expressions for the coefficients of this new linear system, its

3. Sensitivity analysis of the complete electrode model

definitions and the proof of the following theorem are given in Appendix B.

Theorem 3.10 (Fourier coefficients for the extended CEM). *The coefficients \tilde{u}_0 and $\tilde{a}_k, \tilde{b}_k, k \in \mathbb{N}$, of (3.31) and (3.32) satisfy the linear system (B.3).*

Proof. See Appendix B. □

Again, by solving a truncated version of equation (B.3), the Fourier coefficients \tilde{u}_0 and $\tilde{a}_k, \tilde{b}_k, k = 1, \dots, N$, of the potential f^w and the current j_ν^w can be obtained from the electrode potentials U_1, \dots, U_L . For the computation of the corresponding current vector, it is reasonable to integrate over the right-hand side of (B.1) by the same argument as previously for (3.11). This yields

$$I_l = \frac{1 - T^2}{(1 + T^2)z_l} \left(2\omega_l(U_l - \tilde{u}_0) - \sum_{k=1}^{\infty} \tilde{a}_k \tilde{s}_l(k) - \tilde{b}_k \tilde{c}_l(k) \right) + \frac{T\sigma_1}{1 + T^2} \sum_{k=1}^{\infty} d_k \left[\tilde{a}_k (\tilde{s}_l(k-1) + \tilde{s}_l(k+1)) - \tilde{b}_k (\tilde{c}_l(k-1) + \tilde{c}_l(k+1)) \right], \quad (3.33)$$

where $\tilde{s}_l(k)$ and $\tilde{c}_l(k)$ are defined analogously to (3.9), replacing θ_l by $\tilde{\theta}_l$ and ω_l by $\tilde{\omega}_l, l = 1, \dots, L$. Again, Remark 3.4 applies regarding the truncation. In this case, the truncation index depends on the conformally mapped electrodes and thus on \mathcal{Q} and $r_{\mathcal{Q}}$. For all following computations, we set

$$N^w := \min \{ 1000 + 32 N_{\min}^w, N_{\max} \}, \quad \text{where} \quad N_{\min}^w := \lceil 2\pi / \min \{ |E_1^w|, \dots, |E_L^w| \} \rceil, \quad (3.34)$$

and N_{\max} should be chosen with respect to the system memory limit since $N_{\min}^w \rightarrow \infty$ for $\mathcal{Q} \rightarrow \partial\Omega$. In all our computations implemented in MATLAB, we set $N_{\max} = 32000$ on a workstation with 120 GB of memory. This truncation limit is attained only very close to the boundary, e.g. for small electrodes and $Q > 0.95$. Computations were performed for $L = 5$ and $L = 8$ in sections 3.5.1 and 3.5.2 and for $L = 16$ in section 3.5.3 and in the numerical examples of section 6.4.1.

Then for σ as in (3.22), we can compute the current-to-voltage map R_σ by Algorithm 2.

We conclude this section with the following

Remark 3.11. The scaling of the complex plane $z \mapsto \alpha z, \alpha > 0$, is a conformal map. The normal current density resulting from a transformed potential is $j_\nu \mapsto \alpha^{-1} j_\nu$. The corresponding boundary settings for preserving the ND map are $E_l \mapsto \alpha E_l$ and $z_l \mapsto \alpha z_l$. Thus, we can consider disks of arbitrary size.

Algorithm 2: Analytic CEM forward solution by conformal mapping

input : Conductivity values σ_1, σ_0 , perturbation geometry $\mathcal{Q} = (\varphi, Q), r_{\mathcal{Q}}$, electrode parameters $E_l, z_l, l = 1, \dots, L$.

output: Current-to-voltage map R_{σ} .

- 1 Choose a basis $\mathcal{U} = (U^{(1)} | \dots | U^{(L-1)})$ of $\mathbb{R}_{\mathcal{Q}}^L$;
 - 2 Define a truncation index N (e.g. by (3.34));
 - 3 Compute parameters T and r_0 by (3.21);
 - 4 Apply conformal map w to obtain E_l^w and z_l^w ;
 - 5 **for** $m = 1$ **to** $L - 1$ **do**
 - 6 Compute $\tilde{u}_0^{(m)}, \tilde{a}_k^{(m)}, \tilde{b}_k^{(m)}, k = 1, \dots, N$, by solving the truncated system (B.3) with coefficients given by (B.4);
 - 7 Compute $I_l^{(m)}$ for $l = 1, \dots, L$ by equation (3.33).
 - 8 **end**
 - 9 Compute $R_{\sigma} = \mathcal{U} \cdot (I^{(1)} | \dots | I^{(L-1)})^+$;
-

3.3. Sensitivity distribution on the disk

With the analytic tool of the previous section, the sensitivity for detecting circular conductivity perturbations can be tracked throughout the domain $\Omega = B_1(\mathcal{C})$. To that end, we fix a background conductivity $\sigma_1 > 1$, a perturbation value $\eta \neq 0$ such that $\sigma_1 + \eta > c$, and a sensitivity level $\lambda > 0$. Then for $\mathcal{Q} = (Q, \varphi) \in \Omega$, we determine the radius $r_{\mathcal{Q}}$ such that $\lambda_{(\sigma_1 + \eta \chi_{B_{\mathcal{Q}}(r_{\mathcal{Q}})}), \sigma_1} = \lambda$.

The radius $r_{\mathcal{Q}}$ is determined iteratively by computing multiple forward solutions. Due to the monotonicity of the sensitivity, this can be done by a simple line search strategy. In our experiments, we observe a locally almost linear relation between the perturbation size and the sensitivity. Thus for some initial guess $r_{\mathcal{Q}}^{(0)} > 0$, we use the iterative strategy of Algorithm 3 to obtain an approximation to $r_{\mathcal{Q}}$.

In our tests, Algorithm 3 converges quickly, usually in 2–5 iterations for a relative tolerance of $\Delta\lambda = 0.01$ if $r_{\mathcal{Q}}^{(0)}$ is within an order of magnitude from $r_{\mathcal{Q}}$.

With this algorithm, we “sample” the perturbation sizes for a fixed sensitivity $\lambda > 0$ at a set of points inside the domain. That way, we obtain a sensitivity map for a certain background, contrast, and electrode setting.

Figures 3.3(a)–(c) display sensitivity maps for different electrode geometries. The sensitivity distribution is visualized by plotting the perturbation area

$$A_{\mathcal{Q}}^{(k)} := \pi r_{\mathcal{Q}^{(k)}}^2 \quad \text{versus location} \quad \mathcal{Q}^{(k)}, \quad k = 1, \dots, K,$$

(black dots and colored interpolation) for $K = 1185$ equi-distributed sample points. For a better idea of the sensitivity distribution, these figures also show contour lines for the values $A_{\mathcal{Q}}^{(k)}$.

3. Sensitivity analysis of the complete electrode model

Algorithm 3: Iterative computation of $r_{\mathcal{Q}}$

input : $\sigma_1, \eta, \mathcal{Q}$, initial guess $r_{\mathcal{Q}}^{(0)}$, target sensitivity λ , relative tolerance $\Delta\lambda$, electrode parameters.

output: Approximation for $r_{\mathcal{Q}}$.

- 1 Set $k = 0, A^{(-1)} = 0, \lambda^{(-1)} = 0$;
- 2 Set $\sigma^{(0)} = \sigma_1 + \eta\chi_{B_{r_{\mathcal{Q}}^{(0)}}(\mathcal{Q})}$;
- 3 Compute $\lambda^{(0)} = \lambda_{\sigma^{(0)}, \sigma_1}$ using Algorithm 2;
- 4 **while** $|\lambda^{(k)} - \lambda| / \lambda > \Delta\lambda$ **do**
- 5 Set $A^{(k)} = \pi(r^{(k)})^2, a^{(k)} = \frac{A^{(k)} - A^{(k-1)}}{\lambda^{(k)} - \lambda^{(k-1)}}, b^{(k)} = \lambda^{(k)} - a^{(k)}A^{(k)}$;
- 6 Set $r_{\mathcal{Q}}^{(k+1)} = \sqrt{\frac{\lambda - b^{(k)}}{\pi a^{(k)}}}$; // **Affine fit** $\lambda = a^{(k)}\pi(r_{\mathcal{Q}}^{(k+1)})^2 + b^{(k)}$
- 7 Set $k \leftarrow k + 1$;
- 8 Set $\sigma^{(k)} = \sigma_1 + \eta\chi_{B_{r_{\mathcal{Q}}^{(k)}}(\mathcal{Q})}$;
- 9 Compute $\lambda^{(k)} = \lambda_{\sigma^{(k)}, \sigma_1}$ using Algorithm 2;
- 10 **end**
- 11 Set $r_{\mathcal{Q}} = r_{\mathcal{Q}}^{(k)}$;

The computation parameters are

$$\sigma_1 = 1, \quad \eta = 1, \quad \lambda = 0.01, \quad \Delta\lambda = 0.01, \quad z_1, \dots, z_L = 0.01, \quad M = L,$$

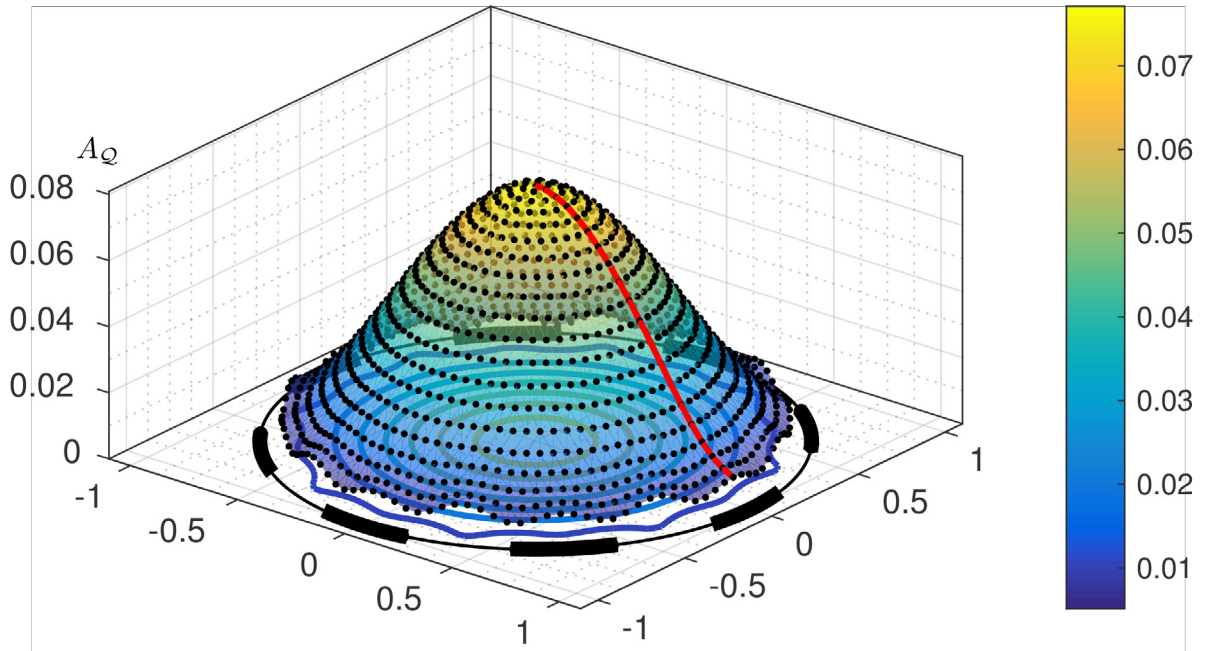
and adjacent currents \mathcal{I}_{adj} are used. The number of Fourier coefficients is chosen by (3.34). In contrast to the continuum model, the sensitivity distribution is non-concentric and highly dependent on the electrode configuration.

Figure 3.3(d) shows $A_{\mathcal{Q}}$ versus \mathcal{Q} plots in radial direction from the center of the disk to an electrode center at the boundary for $L = 8$ electrodes (cf. red line in Figure 3.3(a)) and $L = 16$ electrodes, with electrode width $|E_l| = \frac{\pi}{16}$ in the latter case. For this concentric electrode arrangement, we observe a roughly sigmoidal (“S-shaped”) behaviour in radial direction. We also observe that increasing the number of electrodes does *not* increase the sensitivity near the center of the disk, but greatly increases sensitivity near the boundary.

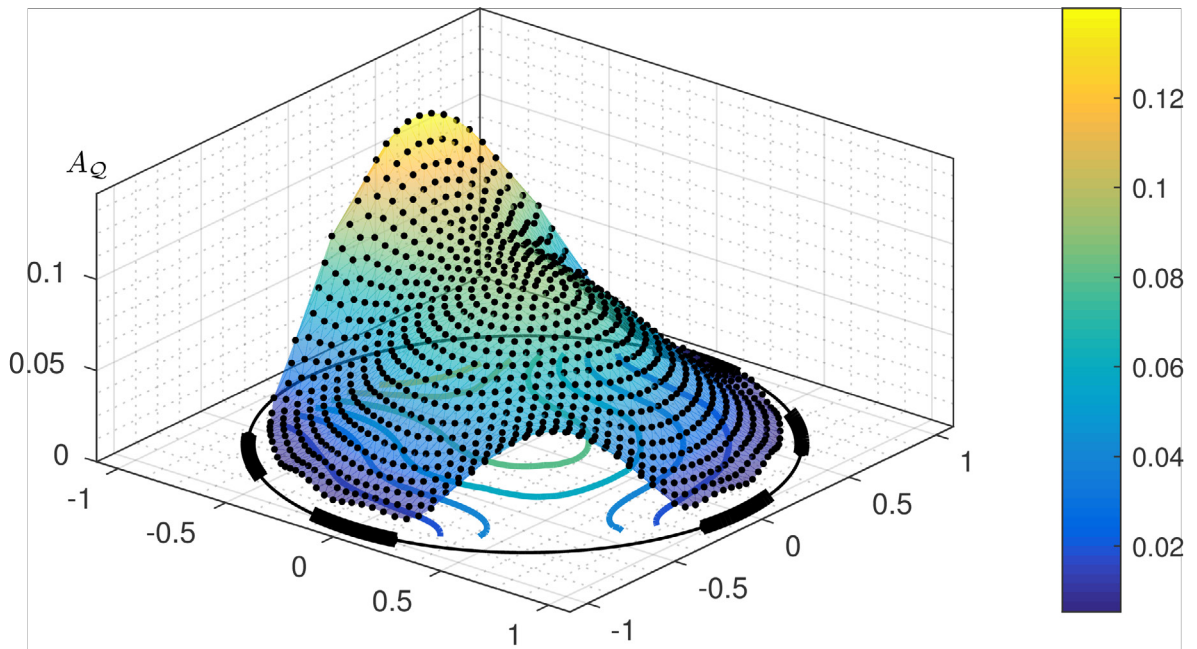
In the following section, we will investigate how the measurement sensitivity of the CEM compares to the sensitivity of Calderón’s model.

3. Sensitivity analysis of the complete electrode model

Figure 3.3.: Sensitivity maps for various electrode configurations on the unit disk: Perturbation areas versus perturbation centers ($Q \mapsto A_Q = \pi r_Q^2$, black dots), interpolation (colored surface) and “equal sensitivity” contour lines (bottom).



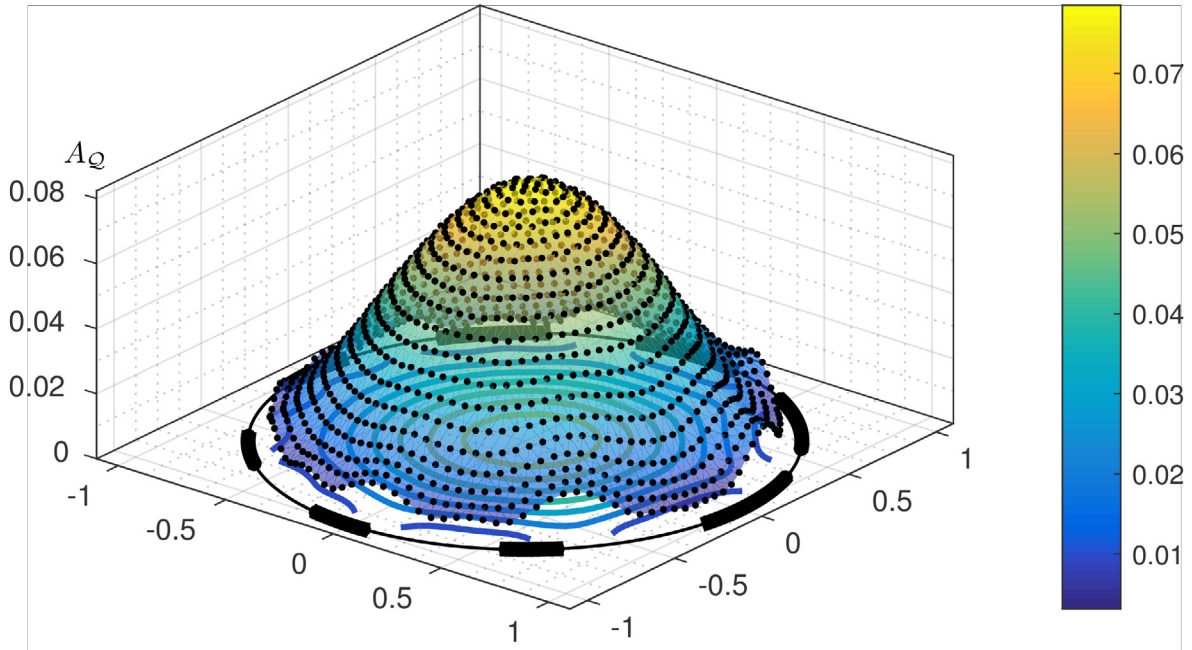
(a) Concentric electrode configuration with $L = 8$ electrodes, $|E_1|, \dots, |E_8| = \frac{\pi}{8}$. Although the sensitivity map appears almost radially symmetric, it has notable changes in angular direction near the electrodes, which is highlighted by the contour plot. The red line shows the sensitivity change in radial direction from the domain center towards the center of the first electrode; cf. Figure 3.3(d).



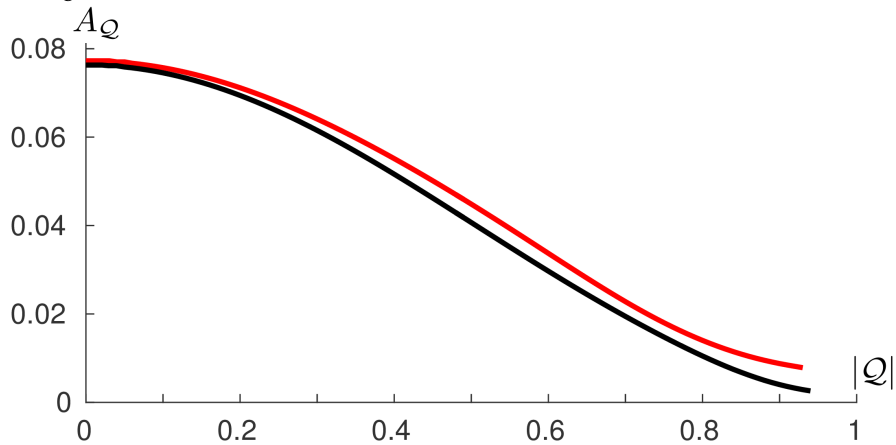
(b) Same configuration as in Figure 3.3(a), but with three electrodes removed ($L = 5$). The sensitivity decreases significantly in the areas where the electrodes are removed, resulting in bigger values for A_Q .

3. Sensitivity analysis of the complete electrode model

[Figure 3.3 continued]



(c) Setting as in Figure 3.3(a), but with varying electrode sizes, leading to different sensitivities near small and big electrodes.



(d) Red line: A_Q versus $|Q|$ along a radial line for the concentric electrode arrangement; cf. Figure 3.3(a). The plot stops at $|Q| = 0.93$ because closer to the boundary, the radius r_Q to preserve sensitivity $\lambda = 0.01$ would exceed the domain boundary.

Black line: A_Q versus Q for a concentric 16 electrode arrangement, $|E_l| = \frac{\pi}{16}$. The sensitivity increases significantly near the boundary, but not at the center of the domain.

3.4. Comparison of Calderón’s model and the complete electrode model

We now compare the behaviour of the CEM with Calderón’s model. To that end, we compare the sensitivity results of the previous section with an estimate for Calderón’s model in 3.4.1 and with results of MacMillan et al. [MMM04] in 3.4.2.

3.4.1. A sensitivity estimate for Calderón’s model

In the introduction of section 3.1, it was pointed out that it is difficult to compare the “spectral” sensitivity $\lambda_{\sigma, \tilde{\sigma}}^*$ (3.1) of Calderón’s model with the “Frobenius type” measurement sensitivities $|\lambda|_{\sigma, \tilde{\sigma}}$ (3.2) and $\lambda_{\sigma, \tilde{\sigma}}$ (3.3) of the CEM depending on the choice of the current frame. Nonetheless, we can compare the sensitivities of both models to find similarities and differences of the sensitivity behaviour.

To that end, we need to obtain sensitivity information for the continuum model for circular perturbations. For σ as in (3.4), the eigenvalues and eigenfunctions of \mathcal{R}_σ are given by (3.6) and (3.7) as

$$\tau_{\sigma, k} := (\sigma_1 d_k)^{-1} \quad \text{and} \quad \cos(k \cdot) / \sqrt{\pi}, \quad \sin(k \cdot) / \sqrt{\pi}, \quad k \in \mathbb{N},$$

with d_k given by (3.5). In the homogeneous case $\sigma_0 = \sigma_1$, we have that $d_k = k$ and thus, $\|R_{\sigma_1}\|_2 = \sigma_1^{-1}$ (in particular $\|\mathcal{R}_1\|_2 = 1$, so $\lambda_{\sigma_1, 1}^*$ is already a normalized/relative quantity).

For centered conducting perturbations in (3.4), i.e. $\sigma_0 = \sigma_1 + \eta$, $\eta > 0$, we have that $-1 < c_1 < c_2 < \dots < 0$ for d_k in (3.5). This means that

$$\|(\mathcal{R}_\sigma - \mathcal{R}_{\sigma_1})f_k\|_{L^2(\partial\Omega)} = |\tau_{\sigma, k} - \tau_{\sigma_1, k}| \|f_k\| = \left| \frac{1 + c_k}{\sigma_1 k (1 - c_k)} - \frac{1}{\sigma_1 k} \right| = \frac{-2c_k}{\sigma_1 k (1 - c_k)}$$

is decreasing in k for eigenfunctions f_k . The sensitivity for detecting centered perturbations in Calderón’s model (cf. equation (3.1)) is thus given by

$$\lambda_{\sigma, \sigma_1}^* = \frac{-2c_1}{\sigma_1 (1 - c_1)}, \quad c_1 = \frac{\sigma_1 / \sigma_0 - 1}{\sigma_1 / \sigma_0 + 1} r_0^2.$$

Solving this for r_0 yields

$$r_0 = \sqrt{\frac{\lambda_{\sigma, \sigma_1}^* \sigma_1 (\sigma_1 / \sigma_0 + 1)}{(2 - \lambda_{\sigma, \sigma_1}^* \sigma_1) (1 - \sigma_1 / \sigma_0)}} \quad \text{for} \quad \frac{\sigma_1}{\sigma_0} < 1, \quad 0 \leq \lambda_{\sigma, \sigma_1}^* \leq \frac{2}{\sigma_1} \quad \text{and} \quad \lambda_{\sigma, \sigma_1}^* \leq \frac{1}{\sigma_1} - \frac{1}{\sigma_0}.$$

The restrictions on $\lambda_{\sigma, \sigma_1}^*$ guarantee that $0 \leq r_0 \leq 1$. For the special case $\sigma_1 = 1$, $\eta = \sigma_0 - \sigma_1 = 1$

3. Sensitivity analysis of the complete electrode model

considered in the previous section, we obtain

$$r_0 = \sqrt{\frac{3\lambda_{\sigma_1,1}^*}{2 - \lambda_{\sigma_1,1}^*}} \quad \text{for } 0 \leq \lambda_{\sigma_1,1}^* < \frac{1}{2}.$$

As in the CEM, the relation between the perturbation area πr_0^2 and the corresponding sensitivity $\lambda_{\sigma_1,1}^*$ is almost linear locally. This is shown in Figure 3.4, where πr_0^2 is plotted versus $\lambda_{\sigma_1,1}^*$ for $\lambda_{\sigma_1,1}^* \in [0, 1/2)$.

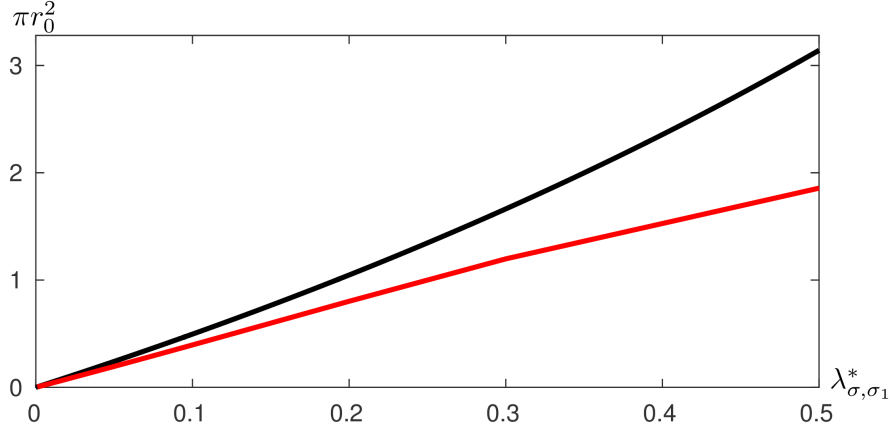


Figure 3.4.: Perturbation area versus sensitivity for $\sigma_1 = 1$ and $\eta = 1$ on the unit disk. **Black line:** Continuum model sensitivities $\lambda_{\sigma,\sigma_1}^* \mapsto \pi r_0^2$ for $\lambda_{\sigma,\sigma_1}^* \in [0, 1/2)$. **Red line:** CEM sensitivities $\lambda_{\sigma,\sigma_1} \mapsto A_{\mathcal{Q}}$ in the symmetric 8 electrode setting of Figure 3.3(a). In both cases, the relation is almost linear locally.

Unfortunately for non-concentric perturbations, we are not aware of a closed-form formula to compute the sensitivity versus a homogeneous background. However, we can use conformal maps to derive a lower bound. To that end, let again $\mathcal{Q} = (Q, \varphi) \in B_1(\mathcal{O})$ and consider the conformal map w^{-1} that maps $B_{r_0}(\mathcal{O})$ onto $B_{r_{\mathcal{Q}}}(Q)$ for some $r_{\mathcal{Q}} > 0$. The parameters are given by (3.20) as

$$T = T(Q, r_0) = \frac{r_0^2 - 1 + \sqrt{(1 - r_0^2)^2 + 4Q^2 r_0^2}}{2Q r_0^2} \quad \text{and} \quad r_{\mathcal{Q}} = r_0 \frac{1 - T(Q, r_0)^2}{1 - r_0^2 T(Q, r_0)^2}. \quad (3.35)$$

Using (3.29) for w^{-1} , any boundary potential f_k and the corresponding normal current $j_{\nu,k}$ are transformed to

$$f_k^{w^{-1}}(\theta) = f_k(g(\theta)) \quad \text{and} \quad j_{\nu,k}^{w^{-1}}(\theta) = \frac{1 - T(Q, r_0)^2}{1 + T(Q, r_0)^2 - 2T(Q, r_0) \cos(\theta - \vartheta)} j_{\nu,k}(g(\theta)),$$

which is (3.30) for w^{-1} instead of w .

Denote by $\sigma_w = \sigma \circ w$ the w^{-1} -transformed conductivity, i.e. $\sigma_w(w^{-1}(x)) = \sigma(x)$. Although we do not know the singular system of \mathcal{R}_{σ_w} explicitly, we can get a lower bound for $\lambda_{\sigma_w, \sigma_1}^*$ by considering the boundary potential $f = \cos(\cdot)/\sqrt{\pi}$ with eigenvalue $\tau_{\sigma} = (\sigma_1 d_1)^{-1}$. Using the conformal mapping

3. Sensitivity analysis of the complete electrode model

properties $\mathcal{R}_{\sigma_w} j_\nu^{w^{-1}} = \tau_\sigma f^{w^{-1}}$ and $R_{\sigma_1} j_\nu^{w^{-1}} = \tau_{\sigma_1} f^{w^{-1}}$ and substituting $f^{w^{-1}}$ and $j_\nu^{w^{-1}}$ into the definition of $\lambda_{\sigma_w, \sigma_1}^*$, we obtain

$$\lambda_{\sigma_w, \sigma_1}^* \geq \frac{\|(R_{\sigma_w} - R_{\sigma_1}) j_\nu^{w^{-1}}\|_2}{\|j_\nu^{w^{-1}}\|_2} = |\tau_\sigma - \tau_{\sigma_1}| \frac{\|f^{w^{-1}}\|_2}{\|j_\nu^{w^{-1}}\|_2} = \alpha_w \lambda_{\sigma, \sigma_1}^*, \quad \text{where} \quad \alpha_w = \frac{\|f^{w^{-1}}\|_2}{\|j_\nu^{w^{-1}}\|_2}.$$

To find the radius r_0 resulting in $\lambda_{\sigma_w, \sigma_1}^* \geq \lambda = \alpha_w \lambda_{\sigma, \sigma_1}^*$ for some fixed $\lambda > 0$, we need to solve the implicit equation

$$r_0 = \sqrt{\frac{\alpha_w^{-1} \lambda \sigma_1 (\sigma_1 / \sigma_0 + 1)}{(2 - \alpha_w^{-1} \lambda \sigma_1) (1 - \sigma_1 / \sigma_0)}}.$$

It is implicit because the parameter T of the conformal map w^{-1} and thus α_w depend on r_0 . However for $\alpha_w^{-1} \lambda \ll 1$, r_0^2 depends almost linearly on λ and the solution can be found quickly by the fixed-point iteration

$$r_{0,k+1} = \sqrt{\frac{\alpha_{w_k}^{-1} \lambda \sigma_1 (\sigma_1 / \sigma_0 + 1)}{(2 - \alpha_{w_k}^{-1} \lambda \sigma_1) (1 - \sigma_1 / \sigma_0)}}, \quad r_{0,0} = \sqrt{\frac{\lambda \sigma_1 (\sigma_1 / \sigma_0 + 1)}{(2 - \lambda \sigma_1) (1 - \sigma_1 / \sigma_0)}},$$

where w_k^{-1} is the conformal map with parameter $T = T(Q, r_{0,k})$.

Once r_0 is found (to arbitrary precision), we can explicitly compute the size $A_Q = \pi r_Q^2$ of a conductivity perturbation centered about Q and resulting in sensitivity $\lambda_{\sigma_w, \sigma_1}^* \geq \lambda$. In particular, $A_Q \rightarrow 0$ as $Q \rightarrow 1$ which is illustrated for $\sigma_1 = 1$ and various contrasts $\eta \in \{1, 10, 100\}$, i.e. $\sigma_0 = \sigma_1 + \eta \in \{2, 11, 101\}$, in Figure 3.5. The perturbation size is clearly nonlinear in the contrast and again sigmoidal in the location; cf. Figure 3.3(d).

3.4.2. Comparison with results of MacMillan et al.

In [MMM04], the detectability of perturbations in conductivity from a finite set of Neumann data for the continuum boundary model is investigated. The central result in this work, [MMM04, Corollary 2.5 and section 2.3.2.], is an estimate of the form

$$\|\mathcal{R}_\sigma j_\nu - f\|_{H^{1/2}(\partial\Omega)} + \epsilon \geq \sup_{j_1, j_2 \neq 0} \frac{C |\int_\Omega (\sigma - \tilde{\sigma}) \nabla u_1 \cdot \nabla u_2 \, dx|}{\|j_1\|_{H^{-1/2}(\partial\Omega)} \|j_2\|_{H^{-1/2}(\partial\Omega)}}, \quad j_\nu \in \mathcal{I}^*, \quad C = \max_{z \in \Omega} \frac{\sigma(z)}{\tilde{\sigma}(z)}, \quad (3.36)$$

where $\mathcal{I}^* \subset H_\diamond^{-1/2}(\partial\Omega)$ is a given finite set of Neumann data, $f = \mathcal{R}_{\tilde{\sigma}} j_\nu + \epsilon_n$ is noisy Dirichlet data, u_k is a potential for σ satisfying $\mathcal{R}_\sigma j_k = u_k|_{\partial\Omega}$ for Neumann data $j_k \in H_\diamond^{-1/2}(\partial\Omega)$, $k \in \{1, 2\}$, and $\epsilon = \epsilon(\epsilon_n, j_\nu)$ is an error term depending on the data error ϵ_n and the non-optimality of j_ν for distinguishing σ from $\tilde{\sigma}$. Given a fixed $\epsilon > 0$, meshes called *graded grids* are generated in [MMM04,

3. Sensitivity analysis of the complete electrode model

section 2.3.2.] by finding the sizes $A_\eta = |\text{supp}(\eta)|$ of local perturbations $\eta = \sigma - \tilde{\sigma}$ such that

$$\sup_{j_1, j_2 \neq 0} C \left| \int_{\text{supp}(\eta)} \eta \nabla u_1 \cdot \nabla u_2 \, dx \right| \|j_1\|_{H^{-1/2}(\partial\Omega)}^{-1} \|j_2\|_{H^{-1/2}(\partial\Omega)}^{-1} = \epsilon. \quad (3.37)$$

To compare the radial resolution of the graded grids with our results, we plot A_η versus the center of $\text{supp}(\eta)$ in Figure 3.5 (marked with asterisks). Lacking an explicit formula, the information was obtained from the left grid of [MMM04, Fig. 3.1], where $\epsilon = 0.1$ and $\max|\eta| = 1$ are considered. The perturbation sizes for a fixed ϵ show a similar radial behaviour as our continuum sensitivities of the previous sections.

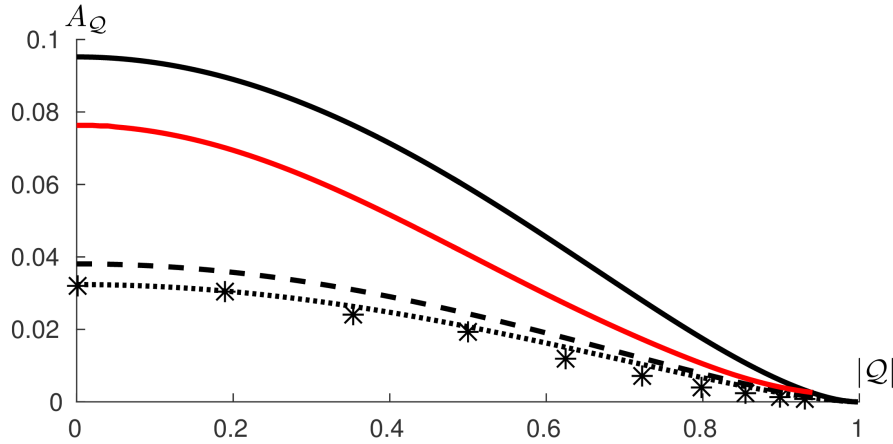


Figure 3.5.: **CEM sensitivity (red line):** Relative sensitivity for the 16 electrode configuration; as in Fig. 3.3(d).

Spectral sensitivity of Calderón’s model (black lines): Perturbation size versus radial position is plotted ($|Q| \mapsto A_Q$) for the lower bound $0.02 = \lambda \leq \lambda_{\sigma_w, \sigma_1}^*$, background $\sigma_1 = 1$ and the contrasts $\eta = 1$ (solid line), $\eta = 10$ (dashed) and $\eta = 100$ (dotted) as described in section 3.4.1.

Sensitivity by MacMillan et al. (asterisks): Sensitivity plot $\text{center}(\eta) \mapsto A_\eta$ from analysis by MacMillan et al. [MMM04], as described in section 3.4.2. The sensitivity behaviour towards the boundary, although in a different norm, is similar to our results of section 3.4.1.

3.5. Sensitivity-based discretizations

For solving the ICP numerically, the discretized conductivity space \mathcal{D}_P was introduced in section 2.3. This discretization is a trade-off between achievable resolution of the reconstructed image, the underdetermination of the inverse problem, and the computational cost. The previous section shows that the sizes of detectable conductivity perturbations vary greatly throughout the domain. For EIT with noisy data, we can not expect to recover conductivity details which have a sensitivity below the noise level. Thus, it is reasonable to discretize the conductivity space adaptively based on the

3. Sensitivity analysis of the complete electrode model

sensitivity information: In regions of low sensitivity, we can discretize coarsely to limit the number of unknowns, while refining the discretization in regions of high sensitivity allows us to resolve details that would be lost otherwise. A positive side-effect is that from the local “blockiness” of the discretization, we already get a visual idea of the local resolution that can be expected. This helps for distinguishing artifacts from information contained in the image.

One way to generate piecewise constant discretizations that reflect the local sensitivity is to use a meshing algorithm which is capable of generating tailored local mesh sizes. Then, the interpolation of the local sensitivity samples as in Figures 3.3(a)–(c) can be used as a local mesh size function⁵.

A more straight-forward discretization approach is given in this section. In 3.5.1, we will “fill” the domain with non-overlapping circles obtained from the analytic solution for a fixed sensitivity $\lambda > 0$. Applying a Voronoi tessellation to the circle centers, we obtain a discretization with cells having roughly homogeneous sensitivity for conductivity changes at constants.

In almost concentric settings, we observed a behaviour of the perturbation sizes which is roughly sigmoidal with respect to the electrode distance. Using this observation, we define a heuristic approximation of sensitivity based discretizations in 3.5.2 which can be computed rapidly. The concept is extended to non-circular domains in 3.5.3, and for triangulations in 3.5.4.

3.5.1. Optimal resolution meshes on the disk

The design idea of sensitivity based (piecewise constant) discretizations is that changes in each conductivity basis coefficient result in roughly the same amount of change in the measurements. For circular domains and circular perturbations, we can use Algorithm 3 to determine perturbation sizes that satisfy this criterion. A set of non-overlapping circular perturbations, each leading to $\lambda_{\sigma, \sigma_1} = 0.02$, is shown in Figure 3.6(a).

Recall that we want to obtain a *partition* \mathcal{P} of the entire domain, which is not possible with non-overlapping circles. To obtain a partition, we thus need to assign the space outside the circles to some cells. A natural way to obtain a partition of Ω with one cell for each circle is to apply a *Voronoi tessellation* to the circle centers, and truncate it at the domain boundary. This does *not* guarantee that the entire circle is contained in the cell belonging to the circle center, but gives good results nonetheless in all of our tests.

However, the Voronoi cells can be considerably bigger than their corresponding circles, in particular if the circles were not packed densely in Ω . The set of circles in Figure 3.6(a) was obtained from the sampled sensitivities in Figure 3.3(a) by successively adding or rejecting perturbation supports corresponding to the points $\mathcal{Q}^{(k)}$, $k = 1, \dots, K$, as described in Algorithm 4. The problem here is that the set of $K = 1185$ test points is rather coarse for the purpose of filling the domain densely.

⁵With appropriate extrapolation outside the convex hull.

3. Sensitivity analysis of the complete electrode model

Algorithm 4: Sensitivity based domain discretization using a Voronoi tessellation.

input : Domain and electrode geometry, conductivity values $\sigma_1, \sigma_0 > 0$, sensitivity $\lambda > 0$, ordered set of points $\mathcal{T} = (\mathcal{Q}^{(1)}, \dots, \mathcal{Q}^{(K)}) \subset \Omega$.

output: Domain discretization \mathcal{P} .

```

1 Set  $\mathcal{B} = \emptyset, \mathcal{C} = \emptyset$ ;
2 repeat
3   Pick the first element  $\mathcal{Q}$  from  $\mathcal{T}$  and set  $\mathcal{T} := \mathcal{T} \setminus \mathcal{Q}$ ;
4   Determine  $r_{\mathcal{Q}}$  by Algorithm 3;
5   if  $B_{r_{\mathcal{Q}}}(\mathcal{Q}) \subset B_1(\mathcal{O})$  and  $B_{r_{\mathcal{Q}}}(\mathcal{Q}) \cap \mathcal{C} = \emptyset$  then
6     | Set  $\mathcal{B} := \mathcal{B} \cup \mathcal{Q}, \mathcal{C} := \mathcal{C} \cup B_{r_{\mathcal{Q}}}(\mathcal{Q}), \mathcal{T} := \mathcal{T} \setminus B_{r_{\mathcal{Q}}}(\mathcal{Q})$ ;
7   end
8 until  $\mathcal{T} = \emptyset$ ;
9 Set  $\mathcal{P}$  as Voronoi tessellation of  $\mathcal{B}$ , truncated to  $B_1(\mathcal{O})$ ;

```

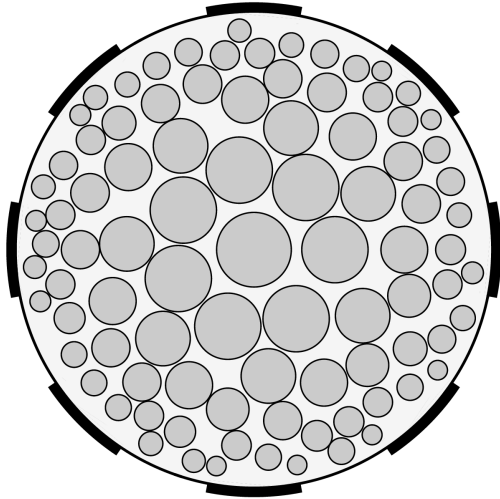
Thus, one could either choose a much finer test set beforehand, or interpolate the perturbation areas linearly between the sample points on a much finer set of points. To avoid negative values when extrapolating linearly outside the convex hull of the sample points, we define

$$A_{\min} := \frac{1}{2} \min_{k=1, \dots, K} A_{\mathcal{Q}^{(k)}}$$

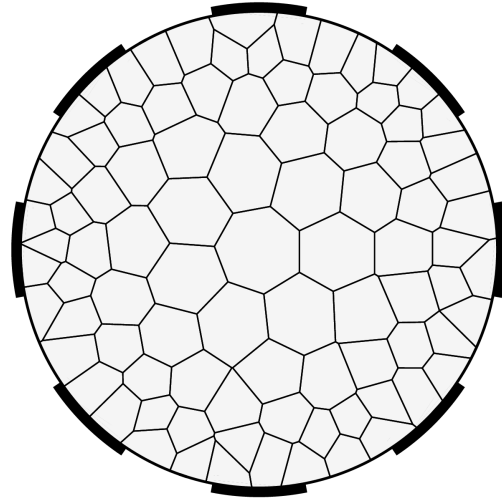
as a lower bound for the extrapolated perturbation areas. This is done, using 80081 interpolation points, in Figure 3.6(c). Figures 3.6(b) and (d) show the truncated Voronoi tessellations corresponding to (a) and (c). Figures 3.6(e) and (f) show Voronoi tessellations corresponding to the geometries of Figures 3.3(b) and 3.3(c).

3. Sensitivity analysis of the complete electrode model

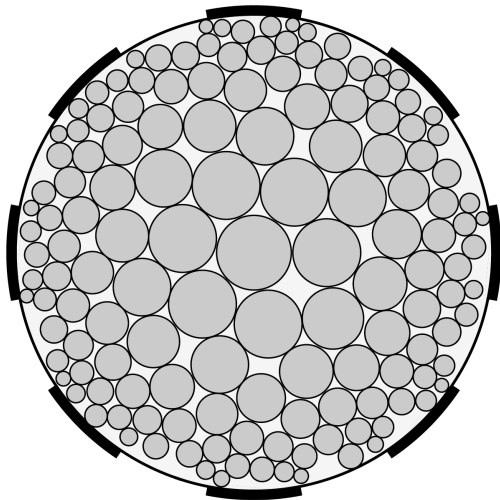
Figure 3.6.: Non-overlapping perturbations and Voronoi tessellations generated by Algorithm 4.



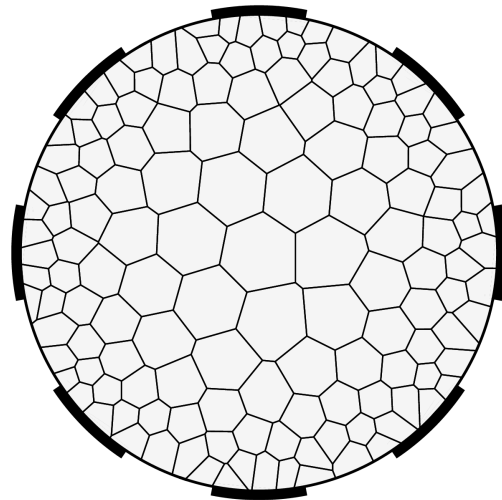
(a) Set of non-overlapping perturbations, each having a sensitivity of $\lambda = 0.02$ in the setting of Figure 3.6(a). $K = 1185$ sample points were used.



(b) Voronoi tessellation corresponding to the perturbation centers of Figure 3.6(a) (90 cells).



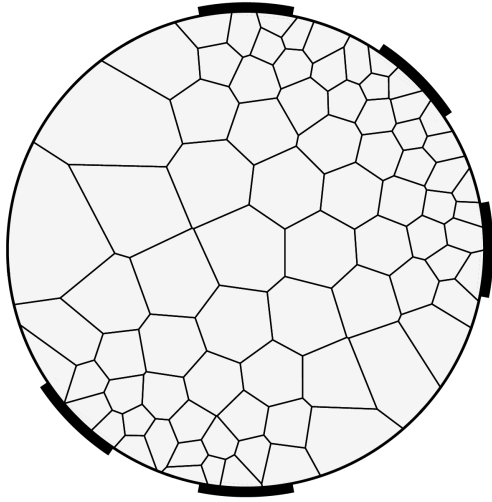
(c) The perturbation areas of Figure 3.6(a) were interpolated/extrapolated on a set of 80081 points before applying Algorithm 4.



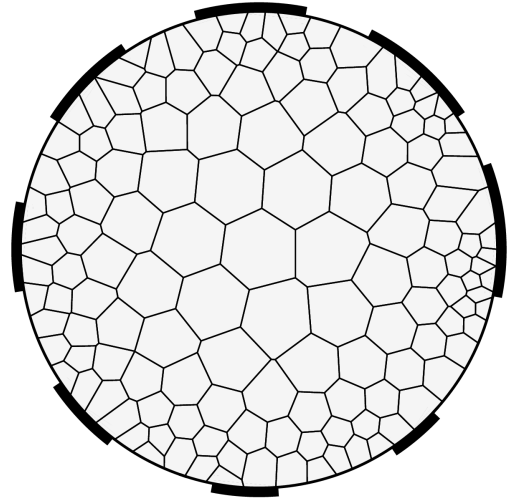
(d) Voronoi tessellation corresponding to the perturbation centers of Figure 3.6(c) (142 cells).

3. Sensitivity analysis of the complete electrode model

[Figure 3.6 continued.]



(e) Voronoi tessellation corresponding to the 5 electrode setting of Figure 3.3(b) (80 cells).



(f) Voronoi tessellation corresponding to the varying size 8 electrode setting of Figure 3.3(c) (143 cells).

3.5.2. A heuristic approximation of sensitivity based discretizations

In the computation of the analytic CEM solutions by Algorithm 2, a linear system with a dense $(2N + 1) \times (2N + 1)$ coefficient matrix needs to be initialized and solved (by QR factorization), where N is the truncation index of the Fourier sum. Although this matrix is reasonably conditioned even for large N , the memory and computation time increase quadratically. Figure 3.7 shows the truncation index N and the computation time (in seconds) in our non-optimized MATLAB implementation versus the location \mathcal{Q} in the settings of Figure 3.3(c), i.e. for 8 symmetric electrodes and $\lambda = 0.02$. In particular, the computation of the analytic solution is costly near the boundary, and Algorithm 4 for computing the sensitivity based discretization is mainly of theoretical interest, but not feasible in practice.

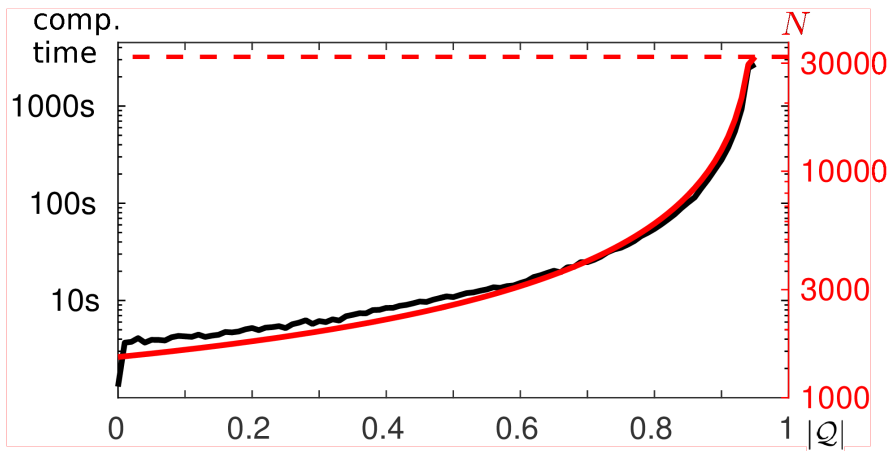


Figure 3.7.: Computational effort for initializing the matrix coefficients and solving the linear system (3.14): Truncation index N (red) and computation time (black, in seconds) versus the radial parameter \mathcal{Q} of the perturbation center \mathcal{Q} . The dashed line marks our limit $N_{\max} = 32000$. Setting as in Figure 3.3(a).

To reduce the computation time drastically, we want to exploit the sigmoidal behaviour (cf. Figure 3.3(d)) of the sensitivity by using a heuristic sigmoidal approximation of the sensitivity map. In Figures 3.3(a)–(c), we observe that the perturbation size decreases as the perturbation center approximates electrode corners. This is because the current density $\|\sigma \nabla u\|$ is very high in these locations, thus changing σ there leads to bigger changes in the boundary potentials.

Assume now that we know, for some $\lambda > 0$ and some electrode setting, the perturbation size $A_{\mathcal{Q}}$ at the disk center. Denote by E_l^- and E_l^+ the left and right electrode corners of the l th electrode. Moreover define, for each $\mathcal{Q} \in \Omega$, the distance to the closest left and right electrode corners by

$$d_{\mathcal{Q}}^{\pm} := \min_{l=1, \dots, L} |\mathcal{Q} - E_l^{\pm}|,$$

3. Sensitivity analysis of the complete electrode model

and denote their maximum values by $d_{\max}^{\pm} := \max_{\mathcal{Q} \in \Omega} \{d_{\mathcal{Q}}^{\pm}\}$. Finally define, for all $\mathcal{Q} \in \Omega$,

$$r_{\mathcal{Q}}^H := r_{\text{lim}} \left(1 - \sqrt{\frac{d_{\mathcal{Q}}^+ \cdot d_{\mathcal{Q}}^-}{d_{\max}^+ \cdot d_{\max}^-}} \right), \quad 0 \ll r_{\text{lim}} < 1,$$

which is a kind of “normalized radial parameter” with respect to the closest electrode corners.

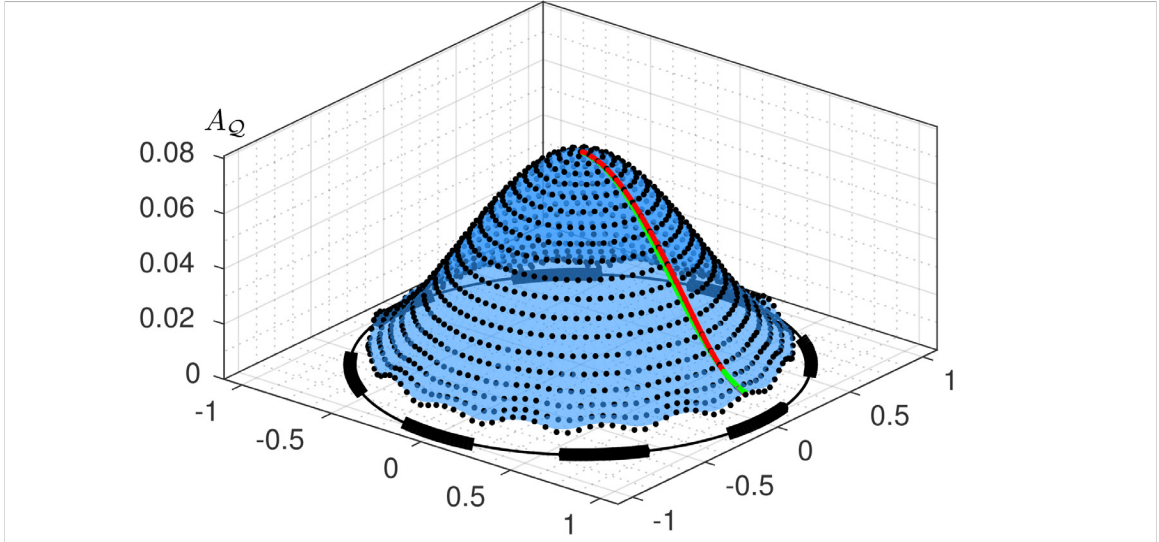
Then, our proposed heuristic approximation $A_{\mathcal{Q}}^H$ for the perturbation size $A_{\mathcal{Q}}$ is given by a scaled and shifted cosine function:

$$A_{\mathcal{Q}}^H := \frac{A_{\mathcal{O}}}{2} \left(1 + \cos \left(\pi r_{\mathcal{Q}}^H \right) \right). \quad (3.38)$$

The parameter $r_{\text{lim}} < 1$ is introduced to avoid $r_{\mathcal{Q}}^H \rightarrow 1$ and thus $A_{\mathcal{Q}}^H \rightarrow 0$. In the following, we let $r_{\text{lim}} = 2 \frac{|E_{\min}|}{|\partial\Omega|}$, where $|E_{\min}| = \min\{|E_1|, \dots, |E_L|\}$, to account for the increased resolution obtained near electrodes when using smaller electrodes.

Figure 3.8 contains plots of the sampled sensitivities $A_{\mathcal{Q}}$ (black dots) and the heuristic approximations $A_{\mathcal{Q}}^H$ (blue surface). The approximation is very good in particular in the symmetric electrode setting, and somewhat off near the boundary where the electrode setting is very asymmetric.

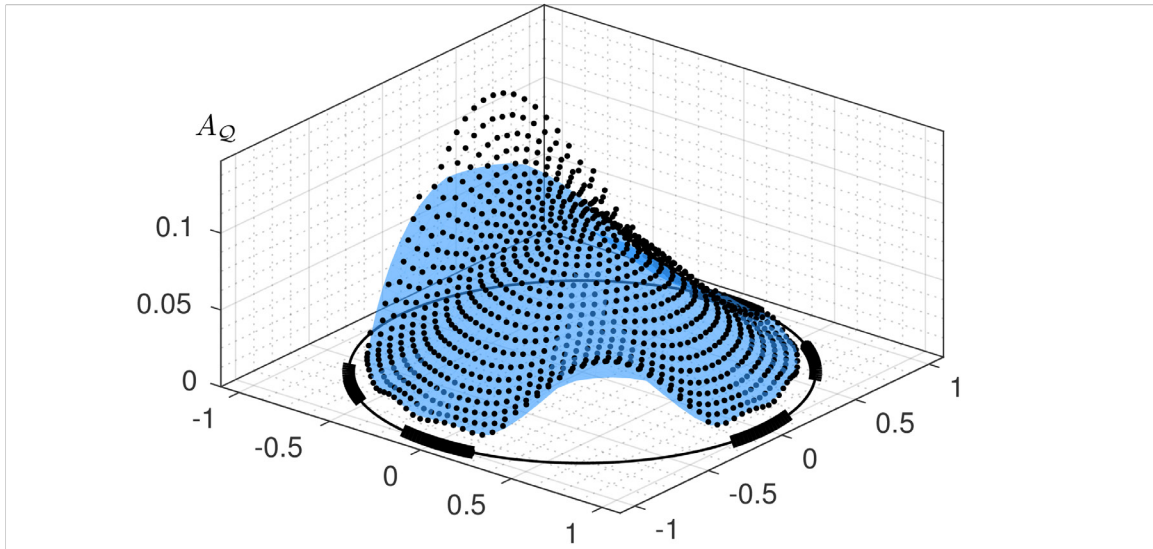
Figure 3.8.: Heuristic approximations $A_{\mathcal{Q}}^H$ (blue surface) to the sensitivities $A_{\mathcal{Q}}$ (black dots) of Figures 3.3(a)–(c).



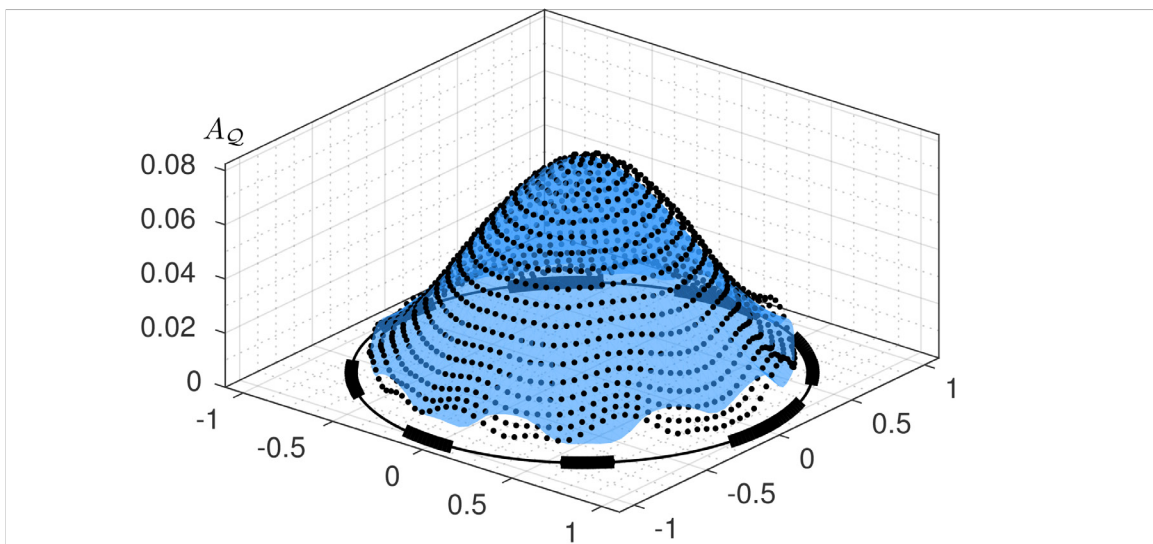
(a) Approximation for the setting of Figure 3.3(a). The red line shows the radial behaviour of the sensitivity samples while the green line shows the heuristic approximation at the same locations.

3. Sensitivity analysis of the complete electrode model

[Figure 3.8 continued]



(b) Approximation for the setting of Figure 3.3(b). The perturbation sizes are well approximated in most regions, but somewhat under-estimated near the three removed electrodes.



(c) Approximation for the setting of Figure 3.3(a). The heuristic is good in the interior of the domain, but is slightly off near the electrodes.

3. Sensitivity analysis of the complete electrode model

Remark 3.12. Definition (3.38) is just a (crude) heuristic, so it is probably a bad approximation in some specific electrode settings. In particular, it does not use information about the measurement current frame or contact impedances explicitly. Moreover, it approaches zero as \mathcal{Q} approaches an electrode corner, which is not necessarily the case for $A_{\mathcal{Q}}$. However, it works well for our almost symmetrical electrode configurations, low contact impedances and adjacent currents.

When using the heuristic, the computational cost is reduced to solving one single linear system with $2N + 1 \approx 3000$ unknowns and takes only about one second in our MATLAB implementation, instead of a few days for evaluating $A_{\mathcal{Q}}$ for hundreds of sample points near the boundary.

Moreover, the sensitivity information in the definition of $A_{\mathcal{Q}}^H$ is solely contained in the perturbation size $A_{\mathcal{O}}$ at the disk center, which we observed to be roughly linear over a wide range of sensitivity values in section 3.4.1 and in Figure 3.4 therein. Thus, we define a *sensitivity dependent* heuristic for a sensitivity based perturbation size estimate by

$$A_{\mathcal{Q}}^H(\lambda) := \frac{\lambda}{\lambda_0} \frac{A_{\mathcal{O}}}{2} \left(1 + \cos \left(\pi r_{\mathcal{Q}}^H \right) \right), \quad (3.39)$$

where λ_0 is the sensitivity for computing $A_{\mathcal{O}}$. With (3.39), we can generate approximations of adaptive sensitivity based discretizations, called *adaptive meshes* in the following, for arbitrary sensitivities.

3.5.3. Adaptive meshes for simply connected domains

The analytic forward solutions and the sensitivity analysis of the previous sections are restricted to circular domains. They rely on the closed-form conformal maps on the unit disk. The Riemann mapping theorem guarantees conformal maps from any simply connected domain in \mathbb{R}^2 onto the unit disk. However, the corresponding conformal map is usually not available in closed form, so the transformed Dirichlet data, Neumann data and contact impedances can not be expressed in closed form as in (3.23) and (3.24).

One possible way to overcome this is to compute the transformation numerically, e.g. by the Schwarz-Christoffel mapping [Neh52], and to approximate the resulting (non-constant) contact impedances by the constants

$$\bar{z}_l^w := |E_l^w| |E_l|^{-1} z_l, \quad (3.40)$$

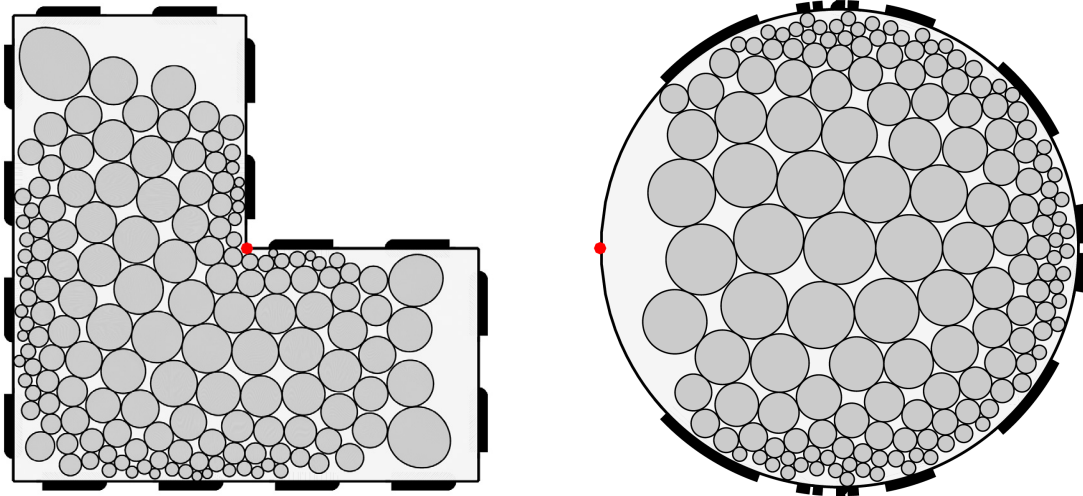
where E_l^w are the conformally mapped electrodes. This approximation is reasonable for sufficiently small electrodes and low contact impedances. For the resulting conformally mapped setting on the unit disk, we can then compute a sensitivity based discretization, and map it back onto the initial domain using the inverse conformal map. Figure 3.9 shows an L-shaped domain with 16 electrodes

3. Sensitivity analysis of the complete electrode model

and its conformal image, on which the sensitivity based discretization was computed. The conformal mapping was performed in MATLAB using the Schwarz-Christoffel toolbox (version 2.3) provided by Tobin A. Driscoll on <http://www.math.udel.edu/~driscoll/SC>. Again, we also compute the heuristic adaptive meshes instead of evaluating the sensitivity explicitly. Note that the conformal mapping is *unique only up to Möbius transforms*, i.e. the transformations given in (3.18). In our example we have chosen, among all Möbius transforms, the one (up to rotation) that maximizes the minimum electrode length.

Figure 3.9 emphasizes a limitation of the conformal mapping approach: Non-convex domains, in particular with re-entrant corners, can lead to very small electrodes. Thus for the Fourier-based approach, a very high number of Fourier coefficients is required to resolve the boundary potentials and currents in the representations (3.31) and (3.32). In particular, the truncation limit $N_{\max} = 32000$ was attained already for points with radial parameter $Q > 0.85$. This means that a reliable computation of the analytic forward solution is impractical near the boundary. However, the heuristic approximation gives good results; see Figures 3.9(c), (d), (f).

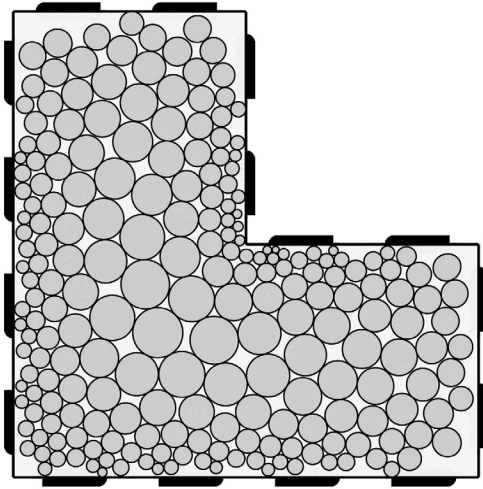
Figure 3.9.: L-shaped geometry (a) and its conformal image on the unit disk (b). The re-entrant corner of the L-shape corresponds to the leftmost point of the circle (red dots). On the circular domain, the sensitivity based discretization is performed and the resulting disks are mapped back to the original domain.



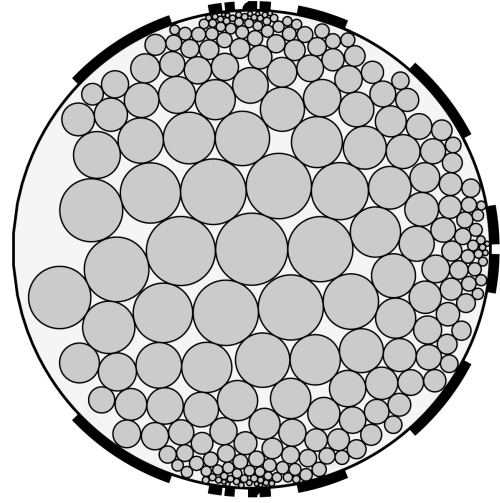
(a) L-shaped domain containing the conformal images of the circular perturbations A_Q of (b) for $\lambda = 0.02$.

(b) Conformal image of (a) and circular perturbations from Algorithm 4 for $L = 16$, $z_l = 0.01$, $l = 1, \dots, L$, and $\lambda = 0.02$.

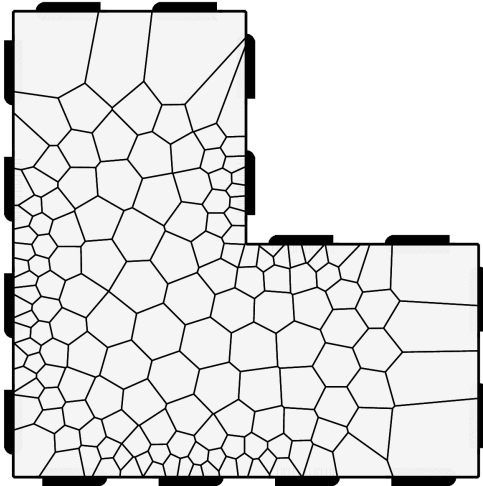
[Figure 3.9 continued]



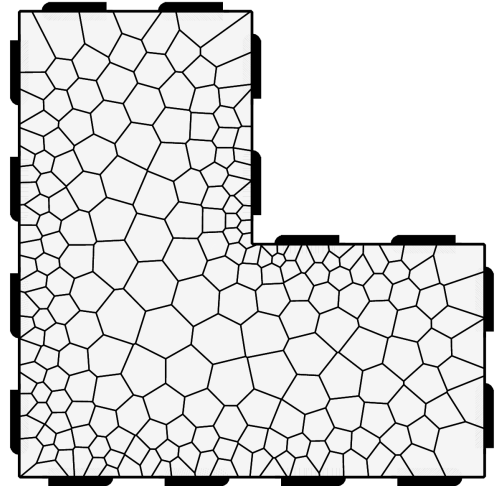
(c) As in (a), but using the heuristics A_Q^H .



(d) As in (b), but using the heuristics A_Q^H .



(e) Voronoi tessellation of (a).



(f) Voronoi tessellation of (c).

3.5.4. Adaptive triangulations

The Voronoi based domain partition presented previously is based on the availability of explicit forward solutions for circular perturbations. In practice, we rarely want to compute thousands of these forward solutions, which motivated the heuristic approximation of these meshes in sections 3.5.2 and 3.5.3. However in both cases, we end up with a partition of the domain which is not conforming with FEM triangulations; i.e. the FEM triangulation is not a refinement of the conductivity discretization given by Voronoi tessellation. Thus, non-trivial projections need to be applied between computing the forward solution and evaluating the linearized problem. This might impact

3. Sensitivity analysis of the complete electrode model

the convergence properties of the Newton algorithm in particular near the stopping criterion.

To overcome that issue, we will generate sensitivity based conductivity *triangulations*. For convenience of implementation, we fix the number of triangles in this discretization, rather than a target sensitivity value. As a starting point, we take a generic triangulation Δ of the domain with $|\Delta|$ triangles. This triangulation is most likely very irregular with respect to the sensitivity for perturbations on each triangle. Then by (3.39), we determine the heuristic sensitivity for each triangle. Next, we refine triangles in Δ with higher-than-average sensitivity successively, thus reducing their heuristic sensitivity. We repeat this process until a target number of $P_t \in \mathbb{N}$ triangles is reached, that is, $|\Delta| \geq P_t$.

In [LR06, section 5 and Figure 2], adaptively refined triangulations are used for computing the FEM forward solutions. They are generated by solving multiple forward problems on a generic mesh and refining this mesh successively at triangles where big “jumps” of the computed interior potential occur. This can be done e.g. using the `pdejumps` and `pdeadworst` functions from the PDE-toolbox. The advantage of our heuristic method is that no forward solutions need to be computed, which decreases the initialization time of the discretization significantly (by one order of magnitude in our MATLAB implementation).

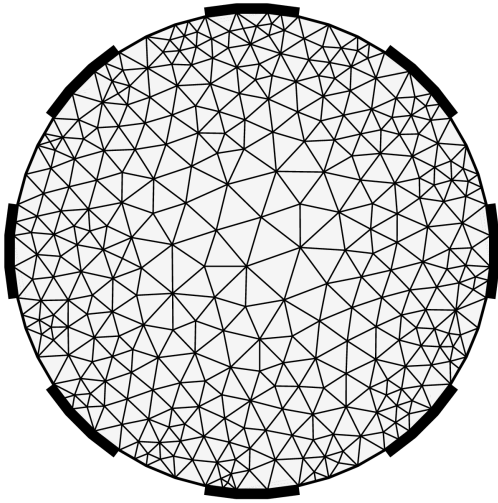
Figure 3.10(a) shows a coarse generic triangulation of a circular setting with 8 electrodes, generated by the MATLAB PDE-toolbox function `initmesh`. It has $|\Delta| = 628$ triangles. Figures 3.10(b) and (c) show adaptive refinements of this mesh for $P_t = 1500$ and $P_t = 5000$, respectively. Figure 3.10(d) shows an adaptive refinement generated using the functions `pdejumps` and `pdeadworst`.

Due to their refinement near the electrodes, these sensitivity based triangulations are also suitable for solving forward problems by the FEM if P_t is sufficiently high and the triangles are not too irregular. The latter can be achieved by an appropriate refinement strategy for the triangles, e.g. by dividing a triangle on the longest edge, or refining it “regularly” into four triangles by connecting the side midpoints.

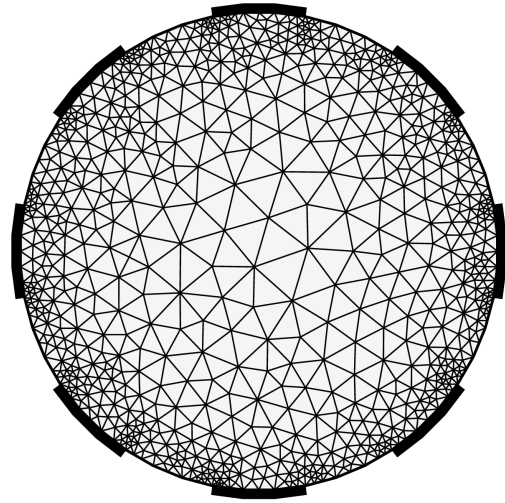
In summary, the sensitivity based triangulations are easy to use, have desired sensitivity properties for piecewise constant conductivity discretizations, and are suitable for solving the discretized forward problem by finite elements, thus we will use them in most of our numerical examples in chapter 6. Nonetheless, examples using the Voronoi-based conductivity discretizations will also be presented.

3. Sensitivity analysis of the complete electrode model

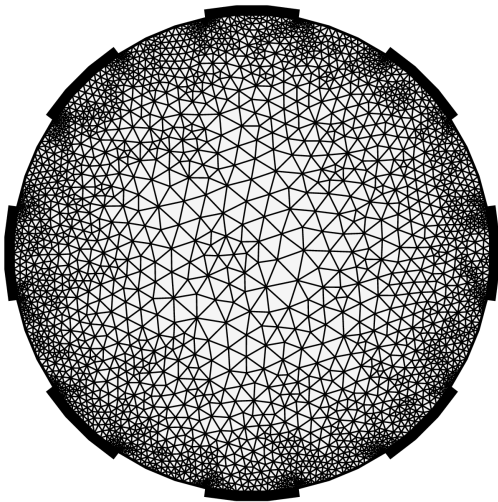
Figure 3.10.: Triangulation and adaptive refinements of a circular domain with 8 electrodes.



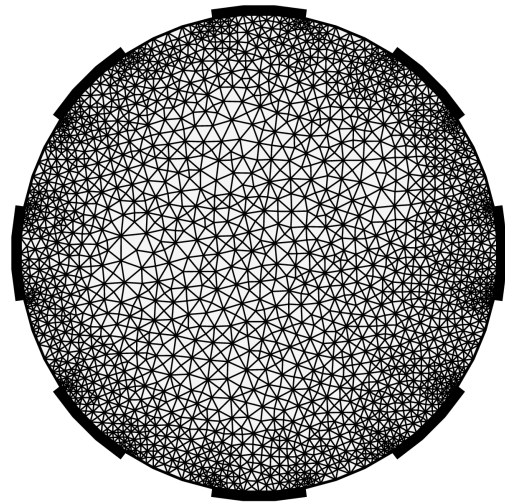
(a) Generic triangulation of a polygonal approximation of the disk with 628 triangles. Computation time in our MATLAB implementation: 0.09s.



(b) Adaptive refinement with 1507 triangles, based on the heuristic formula (3.39). Computation time: 0.26s.



(c) Adaptive refinement with 5028 triangles, based on the heuristic formula (3.39). Computation time: 0.63s.



(d) Adaptive refinement with 5019 triangles, generated using the MATLAB PDE-toolbox functions `pdejumps` and `pdeadworst`; cf. also [LR06, Fig. 2], where a similar mesh is generated. Computation time in our MATLAB implementation: 5.6s.

3.6. Sensitivity analysis: conclusions

The purpose of chapter 3 was to get insights about the conductivity information contained in CEM data. To that end, Definition 3.1 of the measurement sensitivities proved to be a useful tool: The absolute sensitivity (equation (3.2)) allowed to define a notion of distinguishability (Definition 3.2). With this definition, upper limits for the resolution of a particular geometry, electrode setting and background conductivity could be obtained by sampling the sensitivity for locally perturbed conductivities. Moreover, a relative sensitivity was introduced (eq. (3.3)) which is more robust with respect to the absolute conductivity values. It was used to generate sensitivity based conductivity discretizations (Algorithm 4). These discretizations give a locally adaptive trade-off between degrees of freedom and expected resolution for the ICP.

To evaluate the sensitivities, novel analytic forward solutions for conductivities with circular perturbations on the disk were introduced. They were derived from the known continuum model forward operator for concentric conductivities, which was extended first for the CEM by introducing a linear system of equations for the Fourier coefficients of the solution (Theorem 3.3), and then for non-concentric perturbations by applying conformal mapping (Theorem 3.10). By approximating non-constant contact impedances with constants, the conformal mapping approach was extended to generate sensitivity based discretizations for non-circular domains (section 3.5.3).

Finally, the behaviour of the sensitivity for perturbations approaching boundary electrodes was studied. Based on the observed sigmoidal behaviour, a heuristic for the perturbation support for a given sensitivity was introduced (eq. (3.38)). This heuristic was used to rapidly approximate sensitivity based discretizations, avoiding many evaluations of the forward operator. This heuristic can be used to obtain sensitivity based triangulations for the conductivity, which was demonstrated in section 3.5.4. Reconstructions using sensitivity based conductivity discretizations and their approximations will be presented in chapter 6.

4. Model-aware inversion

In the preceding chapter, the link between conductivity changes and data changes was studied to get quantitative information about the resolution limits of a given EIT setting. In this chapter, we return to more general domains Ω in two and three dimensions and pick up the central questions given in the introduction of this work:

How can the ICP be solved in a “model-aware” way, using all the information contained in the data and obtained from the model? Moreover, can “abstract” design parameters be eliminated to make it convenient to use?

Our starting point for the design of such an inversion scheme is the inexact Newton-type method CG-REGINN [Rie99, Rie05, LR06] which was presented in section 2.4.7 and in Algorithm 1. It has several valuable properties: Newton-type methods are well-understood analytically and numerically, make use of the Fréchet-differentiability of the forward operator, and are very flexible, which will be used in chapter 5. Moreover, the conjugate gradient regularization scheme is quick as it minimizes the number of required iterations for the linearized system, which greatly reduces error amplification.

This chapter is organized as follows: In section 4.1, we derive initializations for the Newton iteration. These comprise model parameters such as the contact impedances of the electrodes, an initial conductivity guess, and a stopping criterion for the Newton iteration.

In section 4.2, we investigate the problems introduced by the constrainedness and severe nonlinearity of the ICP. Using a parameter transformation, we can reformulate the ICP to be unconstrained, which is advantageous for iterative inversion.

A crucial aspect of the ICP is its underdetermination. It appears in the Newton iteration when solving the discretized linearized system, which is heavily underdetermined for typical discretizations. This introduces a design choice: We need to pick a unique solution from the underdetermined system. A natural choice is a solution with few oscillations. In section 4.3, we will prove that such solutions can be obtained by minimization in a weighted L^2 norm. For constant conductivities, these weights coincide with the weights of the well-known one-step linearization algorithm NOSER [CIN⁺90], which is a popular choice to date for solving the linearized problem.

The instability of the ICP appears both in the overall Newton iteration and in each linearized problem: Due to the measurement noise, the measured data is not necessarily in the range of the forward operator. Thus, the outer iteration might not converge to an arbitrarily small residual, and the linearized problem might yield highly oscillatory solutions even when using the weighted norm minimization. To tackle the instability, we compute a regularized solution of the linearized system using an incomplete conjugate gradient scheme (CG-REGINN, [Rie05]) in each iteration, and we stop the iteration according to Morozov’s discrepancy principle. With a slight modification of REGINN presented in section 4.4, the scheme is free of user-defined design parameters.

All steps are combined to a *model-aware Newton-type inversion scheme* (MANTIS) in section 4.5. Afterwards, we will emphasize the flexibility of this framework by presenting several problem-specific extensions to the model in chapter 5. Finally, the framework will be applied to an extensive set of numerical examples in chapter 6.

Some parts of the work presented in this chapter were previously published, with slight modifications, in the journal *Inverse Problems* [WR15].

4.1. Initialization

A proper initialization of the Newton algorithm is important for two reasons: The measured data is very sensitive to modelling errors of the setting, and Newton’s method converges only locally in general. For most part of this work, we will assume that a good estimate of the geometry of the setting is known, i.e. the shape of the domain and the size and location of the electrodes. This is justified by advances in measurement technology like electrode belts that can determine their own shape [NKI⁺15], or when the boundary geometry was obtained previously, e.g. by CT/MRT images for the human skull. While it is possible to recover this geometry simultaneously with the conductivity from the measured data [VKV⁺02, DHSS13a], in this case a great part of the information contained in the measured data is used for obtaining the boundary shape. Consequently, it is “lost” for the conductivity reconstruction: The resulting conductivity is typically very smooth, especially near the boundary, and shapes of conductivity perturbations are often not recovered correctly. Nonetheless, the MANTIS framework is capable of incorporating these simultaneous reconstructions, which will be demonstrated in chapter 5 by reconstructing electrode sizes and positions along with the conductivity.

In contrast, the contact impedance at the electrodes is a quantity that can not be obtained “from the outside”. However, a good estimate can be obtained from the data, which will be shown in section 4.1.1. On top of that, the presented estimate also yields a best-matching constant conductivity for the measured data (sometimes called “background conductivity”). This best-matching constant will be used as an initial guess for the Newton iteration.

To stop the Newton iteration, REGINN uses Morozov's discrepancy principle (2.33). In practical applications, the noise level δ is unknown. Fortunately, the measured EIT data is redundant for all commonly used measurement current frames. This will be exploited in 4.1.2 for deriving a noise level estimate from the data.

4.1.1. Conductivity and contact impedance initialization

A well-known [CIN⁺90] initial guess of the conductivity is based on the continuum model, more precisely on the fact that (2.5) is Laplace's equation for constant conductivities:

$$\text{If } \sigma = \sigma_0 \chi_\Omega, \quad \text{then potentials } u \text{ for } \sigma \text{ satisfy } \Delta u = 0,$$

i.e. a partial differential equation which is independent of σ_0 . Obtaining the constant $\sigma_0 \in \mathbb{R}_+$ from the knowledge of the continuum ND operator \mathcal{R}_σ can be formulated as a *linear problem* by considering the *resistivity* $\rho := \sigma^{-1} = \sigma_0^{-1} \chi_\Omega$. The map

$$\rho_0 \mapsto \left(\rho_0^{-1} \nabla_\nu u \mapsto u|_{\partial\Omega} \right) = \left(\nabla_\nu u \mapsto \rho_0 u|_{\partial\Omega} \right) \quad (4.1)$$

is linear in $\rho_0 := \sigma_0^{-1} > 0$.

Assume now in the continuum model that for some domain Ω , we have conductivities

$$\sigma = \sigma_0 \chi_\Omega \quad \text{and} \quad \tilde{\sigma} = 1 \chi_\Omega$$

and that we apply a set of $M \in \mathbb{N}$ boundary current densities

$$j_\nu^{(m)} \in H_\diamond^{1/2-\alpha}(\partial\Omega), \quad m = 1, \dots, M,$$

to both conductivity settings. At a set of $L \in \mathbb{N}$ points $x_1, \dots, x_L \in \partial\Omega$, we make point evaluations¹

$$V_l^{(m)} := u^{(m)}|_{\partial\Omega}(x_l) \quad \text{and} \quad \tilde{V}_l^{(m)} := \tilde{u}^{(m)}|_{\partial\Omega}(x_l), \quad l = 1, \dots, L, \quad m = 1, \dots, M,$$

where, for $m = 1, \dots, M$, $u^{(m)}$ and $\tilde{u}^{(m)}$ are the unique solutions of

$$\begin{aligned} \Delta u^{(m)} = \Delta \tilde{u}^{(m)} &= 0 && \text{on } \Omega, \\ \sigma_0 \nabla_\nu u^{(m)} = \nabla_\nu \tilde{u}^{(m)} &= j_\nu^{(m)} && \text{on } \partial\Omega, \end{aligned}$$

normalized such that $\sum_{l=1}^L V_l^{(m)} = \sum_{l=1}^L \tilde{V}_l^{(m)} = 0$. Due to the linearity in ρ_0 , we get

$$V_l^{(m)} = \rho_0 \tilde{V}_l^{(m)} \quad \text{for } l = 1, \dots, L, \quad m = 1, \dots, M. \quad (4.2)$$

¹This is possible since $u^{(m)}|_{\partial\Omega} \in H^{3/2-\alpha}(\partial\Omega)$, in particular the trace is continuous.

4. Model-aware inversion

To estimate the unknown value σ_0 , we interpret $V_l^{(m)}$ as some given potential measurements of a setting, while $\tilde{V}_l^{(m)}$ are simulated forward solutions for unit conductivity in the same geometry. In theory, σ_0 could be obtained by (4.2) from a single potential measurement. However, when the measured potentials are noisy, we can try to minimize the error of the estimate of σ_0 over all measurements.

Definition 4.1 (Continuum model conductivity estimate). By minimizing the functional

$$\sum_{m=1}^M \sum_{l=1}^L \left(V_l^{(m)} - \frac{1}{\sigma_0} \tilde{V}_l^{(m)} \right)^2,$$

we obtain the *continuum model conductivity estimate* for the best-matching constant conductivity

$$\sigma^{\text{cont}} := \frac{\sum_{m=1}^M \sum_{l=1}^L \left(\tilde{V}_l^{(m)} \right)^2}{\sum_{m=1}^M \sum_{l=1}^L V_l^{(m)} \tilde{V}_l^{(m)}}; \quad (4.3)$$

see [CIN⁺90].

A similar estimate can be obtained for the shunt model (cf. equation (2.8) and subsequent). To that end, assume that we have $L \in \mathbb{N}$ electrodes E_1, \dots, E_L and, for a set of $M \in \mathbb{N}$ current patterns $I^{(1)}, \dots, I^{(M)} \in \mathbb{R}_{\diamond}^L$, denote by

$$U_l^{(m)} \equiv u^{(m)}|_{E_l} \quad \text{and} \quad \tilde{U}_l^{(m)} \equiv \tilde{u}^{(m)}|_{E_l}$$

the corresponding electrode potentials, where $u^{(m)}, \tilde{u}^{(m)} \in H^1(\Omega)$ and $j_{\nu}^{(m)} \in H_{\diamond}^{-1/2}(\partial\Omega)$ are uniquely defined by

$$\begin{aligned} \int_{E_l} j_{\nu}^{(m)} \, dS &= I_l^{(m)}, \\ j_{\nu}^{(m)} &\equiv 0 && \text{on } \partial\Omega \setminus \{E_1, \dots, E_L\}, \\ j_{\nu}^{(m)} &= \sigma_0 \nabla_{\nu} u^{(m)} = \nabla_{\nu} \tilde{u}^{(m)} && \text{on } \partial\Omega, \\ 0 &= \Delta u^{(m)} = \Delta \tilde{u}^{(m)}, \end{aligned}$$

for $m = 1, \dots, M$; see chapter 2 and [SCI92]. Green's identity for the harmonic functions $u^{(m)}$ and $\tilde{u}^{(m)}$ yields

$$\int_{\Omega} \nabla u^{(m)} \nabla \tilde{u}^{(m)} \, dx = \int_{\partial\Omega} \tilde{u}^{(m)} \nabla_{\nu} u^{(m)} \, dS = \int_{\partial\Omega} u^{(m)} \nabla_{\nu} \tilde{u}^{(m)} \, dS.$$

4. Model-aware inversion

In particular, we obtain

$$\sum_{l=1}^L \tilde{U}_l^{(m)} \underbrace{I_l^{(m)}}_{=\int_{E_l} j_\nu^{(m)} dS} = \int_{\partial\Omega} \tilde{u}^{(m)} j_\nu^{(m)} dS = \sigma_0 \int_{\partial\Omega} u^{(m)} j_\nu^{(m)} dS = \sigma_0 \sum_{l=1}^L U_l^{(m)} I_l^{(m)}. \quad (4.4)$$

Definition 4.2 (Shunt model conductivity estimate). For noisy potential data, minimizing the error

$$\sum_{m=1}^M \left(\left(\sum_{l=1}^L U_l^{(m)} I_l^{(m)} \right) - \frac{1}{\sigma_0} \left(\sum_{l=1}^L \tilde{U}_l^{(m)} I_l^{(m)} \right) \right)^2,$$

over all measurements gives the *shunt model conductivity estimate* for the best-matching constant conductivity value

$$\sigma^{\text{shunt}} := \frac{\sum_{m=1}^M \left(\sum_{l=1}^L \tilde{U}_l^{(m)} I_l^{(m)} \right)^2}{\sum_{m=1}^M \left(\sum_{l=1}^L U_l^{(m)} I_l^{(m)} \right) \left(\sum_{l=1}^L \tilde{U}_l^{(m)} I_l^{(m)} \right)}. \quad (4.5)$$

Because of the aforementioned potential drop caused by the contact impedances at the electrodes in the CEM, the conductivity estimates (4.3) and (4.5) become increasingly inaccurate for the CEM as the contact impedances increase (the CEM approaches the shunt model as $z_l \rightarrow 0$, $l = 1, \dots, L$). We propose a modified version of (4.5) to approximate a best-constant conductivity estimate for the CEM which incorporates the contact impedances. In the CEM, we have from (2.13) and (2.14) that

$$u^{(m)}|_{E_l} + z_l j_\nu^{(m)}|_{E_l} \equiv U_l^{(m)} \quad \text{and} \quad \int_{E_l} j_\nu^{(m)} dS = I_l^{(m)}, \quad l = 1, \dots, L, \quad m = 1, \dots, M,$$

while $j_\nu^{(m)} = 0$ on the gaps. The same holds for $\tilde{u}^{(m)}$ and $\tilde{U}^{(m)}$ in the reference setting. Unfortunately, we can not apply Green's identity as in (4.4) since $u^{(m)}$ and $\tilde{u}^{(m)}$ are not constant at the electrodes, thus they can not be simply moved in and out of the integral. However, assuming that the electrodes are small and sufficiently far apart from each other, it is reasonable to assume that the interior potentials are roughly constant along each electrode, which yields the approximation

$$u^{(m)} = U^{(m)} - z_l j_\nu \approx \text{const.} = U_l^{(m)} - z_l \frac{I_l^{(m)}}{|E_l|}, \quad (4.6)$$

where the non-constant normal current j_ν was approximated by its mean value. Note that by the trace theorem, $u^{(m)}|_{E_l} \in H^{1-\alpha}(E_l)$ and thus $j_\nu|_{E_l} = z_l^{-1}(U_l^{(m)} - u^{(m)}) \in H^{1-\alpha}(E_l)$ for all $\alpha > 0$, i.e. the normal current density has increased smoothness when restricted to an electrode. Repeating

4. Model-aware inversion

this approximation for the reference data, we get

$$\tilde{u}^{(m)} = \tilde{U}^{(m)} - \tilde{z}_l j_\nu \approx \tilde{U}_l^{(m)} - \tilde{z}_l \frac{I_l^{(m)}}{|E_l|}, \quad (4.7)$$

where $\tilde{z}_1, \dots, \tilde{z}_l > 0$ denote the contact impedances of the reference setting. Substituting these CEM approximations into (4.4), we get

$$\sum_{l=1}^L \left(\tilde{U}_l^{(m)} - \tilde{z}_l |E_l|^{-1} I_l^{(m)} \right) I_l^{(m)} \approx \sigma_0 \sum_{l=1}^L \left(U_l^{(m)} - z_l |E_l|^{-1} I_l^{(m)} \right) I_l^{(m)} \quad (4.8)$$

for $m = 1, \dots, M$. Analogously to the continuum model and the shunt model, we minimize the estimation error over all measurements, which gives

Definition 4.3 (CEM conductivity estimate). A CEM approximation for the best-matching constant conductivity value is given by the *CEM conductivity estimate*

$$\sigma^{\text{CEM}} := \frac{\sum_{m=1}^M \left(\sum_{l=1}^L \left(\tilde{U}_l^{(m)} - \frac{\tilde{z}_l}{|E_l|} I_l^{(m)} \right) I_l^{(m)} \right)^2}{\sum_{m=1}^M \left(\sum_{l=1}^L \left(U_l^{(m)} - \frac{z_l}{|E_l|} I_l^{(m)} \right) I_l^{(m)} \right) \left(\sum_{l=1}^L \left(\tilde{U}_l^{(m)} - \frac{\tilde{z}_l}{|E_l|} I_l^{(m)} \right) I_l^{(m)} \right)}. \quad (4.9)$$

To emphasize the dependence of the estimate on the current frame $\mathcal{I} = (I^{(1)}, \dots, I^{(M)})$ and the corresponding measurements \mathcal{U} , we write

$$\sigma^{\text{CEM}} = \sigma^{\text{CEM}}(\mathcal{I}, \mathcal{U}).$$

Table 4.1 lists the conductivity estimates σ_0^{cont} , σ_0^{shunt} and σ^{CEM} from noise-free and noisy simulated CEM data with $L = 16$ electrodes for various contact impedances. The CEM estimates σ^{CEM} are good approximations of the true conductivity value ($\sigma_0 = 0.25$ in our example), while the continuum and shunt approximations get worse for increasing contact impedance values. The forward data was computed on a circular domain using the analytic forward solutions derived in chapter 3 for a full set of $M = 16$ adjacent currents. Pseudo-random noise was added by the noise model (2.19), where the variance v was scaled to obtain a (fairly high) noise level of $\delta = 0.1$. To avoid inverse crime, the simulated data $U^{(m)}$ was computed using the analytic solution of chapter 3, while the reference data $\tilde{U}^{(m)}$ was computed using a FEM with 6000 triangles refined near the electrodes.

The CEM conductivity estimate gives accurate results for a wide range of contact impedances. We also evaluated the estimates in other geometries, like oval domains, square shaped domains, and the L-shaped domain of Figure 3.9. The resulting estimates are very similar to those of the circular domain given in Table 4.1, therefore these numbers are omitted.

There is, however, a drawback of the presented estimates: The contact impedances z_l and \tilde{z}_l need to be known. The values \tilde{z}_l are uncritical as we can choose them freely for our reference computations.

4. Model-aware inversion

noise \ $z = z_l =$		1.00×10^{-3}	1.00×10^{-2}	1.00×10^{-1}	$1.00 \times 10^{+0}$	$1.00 \times 10^{+1}$
$\delta = 0$	σ^{cont}	2.47×10^{-1}	2.63×10^{-1}	3.64×10^{-1}	7.34×10^{-1}	9.61×10^{-1}
	σ^{shunt}	2.47×10^{-1}	2.65×10^{-1}	3.73×10^{-1}	7.38×10^{-1}	9.62×10^{-1}
	σ^{CEM}	2.45×10^{-1}	2.50×10^{-1}	2.53×10^{-1}	2.49×10^{-1}	2.50×10^{-1}
$\delta = 0.1$	σ^{cont}	2.47×10^{-1}	2.63×10^{-1}	3.65×10^{-1}	7.35×10^{-1}	9.62×10^{-1}
	σ^{shunt}	2.47×10^{-1}	2.65×10^{-1}	3.73×10^{-1}	7.38×10^{-1}	9.62×10^{-1}
	σ^{CEM}	2.46×10^{-1}	2.50×10^{-1}	2.53×10^{-1}	2.49×10^{-1}	2.50×10^{-1}

Table 4.1.: Conductivity estimates based on the continuum model (σ^{cont}), shunt model (σ^{shunt}) and CEM (σ^{CEM}). With increasing contact impedances, the continuum and shunt model estimates get highly inaccurate because they ignore the potential drop caused by the contact impedances.

Setting: True conductivity $\sigma_0 = 2.50 \times 10^{-1}$. Circular domain with 16 equi-spaced electrodes covering 50% of the boundary and normalized adjacent current patterns.

However, the true contact impedances z_l of our measurement setting are typically not available, as was pointed out at the beginning of this section. Thus, we want to estimate them simultaneously with σ_0 from the M equations (4.8). Unfortunately when using the same ansatz as for the best-matching conductivity, this problem is underdetermined as we have $L + 1$ unknowns and $M \leq L$ equations. However, they can often be assumed to be roughly constant:

$$z_l \approx z > 0 \quad \text{for } l = 1, \dots, L.$$

Using this assumption, we can rewrite equations (4.8) as

$$a_m \rho_0 + b_m z = c_m, \quad m = 1, \dots, M, \quad \text{where}$$

$$a_m = \sum_{l=1}^L \left(\tilde{U}_l^{(m)} - \tilde{z}_l |E_l|^{-1} I_l^{(m)} \right) I_l^{(m)}, \quad b_m = \sum_{l=1}^L |E_l|^{-1} \left(I_l^{(m)} \right)^2, \quad c_m = \sum_{l=1}^L U_l^{(m)} I_l^{(m)},$$

and $\rho_0 = \sigma_0^{-1}$ as before. We arrive at the overdetermined linear regression problem

$$\begin{pmatrix} a_1 & b_1 \\ \vdots & \vdots \\ a_M & b_M \end{pmatrix} \begin{pmatrix} \rho_0 \\ z \end{pmatrix} = \begin{pmatrix} c_1 \\ \vdots \\ c_M \end{pmatrix}, \quad (4.10)$$

4. Model-aware inversion

which can be solved in the least-squares sense as before. Thus, we obtain an estimate for the constant z as a “by-product” when determining the best-matching constant conductivity value for a given set of measured data. We denote the least-squares solutions of (4.10) by $\hat{\rho}_0$ and \hat{z} . In rare cases, usually when $z \ll \rho_0$, the resulting least-squares solution \hat{z} might be inaccurate and even negative due to approximation or data errors. However, the exact value of the contact impedance is not important in that case since the forward operator is very insensitive² to the contact impedances if all $z_l \ll \rho_0$.

Definition 4.4 (CEM conductivity+contact impedance estimate). For $0 < z_{\min} \ll 1$, we define the *CEM contact impedance estimate* as

$$z^{\text{CEM},z} := \max \{ \hat{z}, z_{\min} \}.$$

Moreover, we define the corresponding conductivity estimate as

$$\sigma^{\text{CEM},z} := \begin{cases} \hat{\rho}_0^{-1}, & z^{\text{CEM}} > z_{\min}, \\ \sigma^{\text{CEM}} \text{ using } z_l \equiv z_{\min} \text{ in (4.8)}, & \text{otherwise.} \end{cases}$$

Initializing the contact impedances to z_{\min} is a “safety rule” when the simultaneous estimate fails. Throughout this work, we use $z_{\min} := 10^{-4} \cdot \min \{ |E_l| : l = 1, \dots, L \}$. We will always remark when this minimum is attained in the numerical examples.

Remark 4.5 (Choice of the arbitrary contact impedance). To get a good approximation in (4.7), it is advisable to choose the arbitrary contact impedances \tilde{z}_l small. However for $\tilde{z}_l \rightarrow 0$, the FEM computation of $\tilde{U}^{(m)}$ gets unstable. We obtained good results when using $\tilde{z}_l := 10^{-3}$, $l = 1, \dots, L$, in all our numerical examples.

²The reason is that in this case, the potential drop at the electrodes is negligible compared to the potential gradient in the interior. From a physical point of view, most of the energy of an applied current is dissipated inside the object, and not on the electrode-object interfaces.

4. Model-aware inversion

Remark 4.6 (Underdetermination of the regression problem). For some special geometries and current frames, the system (4.10) is underdetermined. This is the case for example in our radially symmetric setting of Table 4.1, leading to $a_1 = \dots = a_M$, $b_1 = \dots = b_M$ and $c_1 = \dots = c_M$ when using adjacent currents. Since the current-to-voltage map R_σ is linear, a simple way to resolve underdetermination is to perform a basis transformation in \mathbb{R}_\diamond^L : If $\mathcal{I}_* = (I_*^{(1)}, \dots, I_*^{(L-1)}) \in \mathbb{R}_\diamond^{L \times L-1}$ forms an orthonormal basis of \mathbb{R}_\diamond^L , we replace $I^{(m)}$ by $I_*^{(m)}$, $U^{(m)}$ by $U_*^{(m)}$, and $\tilde{U}^{(m)}$ by $\tilde{U}_*^{(m)}$ in (4.10), where

$$U_*^{(m)} := (U^{(1)}, \dots, U^{(M)}) \mathcal{I}^+ I_*^{(m)} \quad \tilde{U}^{(m)} := (\tilde{U}^{(1)}, \dots, \tilde{U}^{(M)}) \mathcal{I}^+ I_*^{(m)},$$

and \mathcal{I}^+ denotes the pseudo-inverse of \mathcal{I} . In our numerical evaluations, we tested both the reduced discrete cosine³ basis and the discrete Haar-wavelet⁴ basis for \mathcal{I}_* . Both choices resolved underdetermination and worked equally well. In practice, one can check the condition of the coefficient matrix in (4.10), and perform a basis transform only if the condition is bad.

Simultaneous estimates for the conductivity constant σ_0 and contact impedance z are shown in Table 4.2 and Table 4.3. The settings are identical to the setting of Table 4.1. In Table 4.3, the robustness of the estimates was evaluated by adding noise to the measurements $U_l^{(m)}$ according to the noise model (2.19), and using contact impedances which vary by $\pm 10\%$, i.e.

$$z_l = \underbrace{\left(1 + \frac{1}{10} n_l\right)}_{\in [0.9, 1.1]} z,$$

where $n_l \stackrel{\text{iid}}{\sim} u[-1, 1]$, i.e. the variations are independent uniformly distributed pseudo-random numbers for $l = 1, \dots, L$. All conductivity estimates are close to the exact value $\sigma_0 = 0.25$. The contact impedance estimates are also quite accurate unless $z \ll \rho_0$.

z	1.00×10^{-3}	1.00×10^{-2}	1.00×10^{-1}	$1.00 \times 10^{+0}$	$1.00 \times 10^{+1}$
$z^{\text{CEM}, z}$	6.64×10^{-4}	1.63×10^{-2}	1.20×10^{-1}	$1.03 \times 10^{+0}$	$1.00 \times 10^{+1}$
$\sigma^{\text{CEM}, z}$	2.50×10^{-1}	2.49×10^{-1}	2.46×10^{-1}	2.43×10^{-1}	2.42×10^{-1}

Table 4.2.: Best-matching constant conductivity and contact impedance estimates for the CEM. The exact conductivity is $\sigma_0 = 2.50 \times 10^{-1}$. Setting as in Table 4.1. The Haar-Wavelet basis transformation was applied to remove redundancy in the data and to obtain an overdetermined problem, as described in Remark 4.6.

³Discrete cosine transform basis, omitting the constant vector. In our MATLAB implementation, we used the rows of the matrix provided by the command `dctmtx`.

⁴Discrete Haar-wavelet basis (orthonormal vectors), omitting the constant vector. For this basis, the number of electrodes L must be a power of 2.

4. Model-aware inversion

z	1.00×10^{-3}	1.00×10^{-2}	1.00×10^{-1}	$1.00 \times 10^{+0}$	$1.00 \times 10^{+1}$
$z^{\text{CEM},z}$	1.08×10^{-2}	2.54×10^{-2}	1.31×10^{-1}	$1.06 \times 10^{+0}$	$1.03 \times 10^{+1}$
$\sigma^{\text{CEM},z}$	2.50×10^{-1}	2.49×10^{-1}	2.46×10^{-1}	2.43×10^{-1}	2.41×10^{-1}

Table 4.3.: Setting as in Table 4.2, but with noisy data ($\delta = 0.1$) and non-constant contact impedances, i.e. $z_l = (1 + \frac{1}{10}n_l)z$, where $n_l \stackrel{\text{iid}}{\sim} u[-1, 1]$ for $l = 1, \dots, L$.

4.1.2. Noise level initialization

To use Morozov's discrepancy principle as a stopping rule for Newton's method, an estimate of the data noise level is required. For many inverse problems, this noise level is inaccessible, and heuristic stopping criteria like the L-curve method or generalized cross validation are used instead. Fortunately, CEM data is redundant, and this redundancy can be exploited to estimate the data noise level δ .

Assume that we have a current frame \mathcal{I} of full rank $L - 1$. In the noiseless case, the current-to-voltage map $F(\sigma) = \mathcal{U}\mathcal{I}^+$ is *symmetric*. However for noisy data \mathcal{U}^v as in (2.19), this is (most certainly) not the case. By

$$E^v := \mathcal{U}^v \mathcal{I}^+ - (\mathcal{U}^v \mathcal{I}^+)^{\top} \quad \text{and} \quad e_v := \|E^v\|_{\text{Fro}}^2,$$

we denote the *symmetry error matrix* and *symmetry error*, respectively. In particular, e_v can be computed from the measured data \mathcal{U}^v without knowing the values of v or δ . From this quantity, we derive an estimate for δ .

Recalling that $\mathcal{U}^v = \mathcal{U} + N^v$, we have

$$E^v = (\mathcal{U} + N^v)\mathcal{I}^+ - ((\mathcal{U} + N^v)\mathcal{I}^+)^{\top} = \underbrace{\mathcal{U}\mathcal{I}^+ - (\mathcal{U}\mathcal{I}^+)^{\top}}_{=0 \text{ (symmetry)}} + N^v \mathcal{I}^+ - (N^v \mathcal{I}^+)^{\top},$$

which gives

$$E_{kl}^v = \begin{cases} 0, & k = l, \\ \sum_{j=1}^L N_{kj}^v \mathcal{I}_{jl}^+ - N_{lj}^v \mathcal{I}_{jk}^+, & 1 \leq k \neq l \leq L. \end{cases}$$

In particular, each entry of the symmetry error matrix is a weighted sum of iid zero mean random entries. From the linearity of the expected value, we get

$$\begin{aligned} \mathbb{E} e_v &= \mathbb{E} \|E^v\|_{\text{Fro}}^2 = \sum_{k,l=1}^L \mathbb{E} (E_{k,l}^v)^2 = \sum_{j=1}^L (\mathcal{I}_{jl}^+)^2 \underbrace{\mathbb{E} (N_{kj}^v)^2}_{=v} + (\mathcal{I}_{jk}^+)^2 \underbrace{\mathbb{E} (N_{lj}^v)^2}_{=v} \\ &= v \sum_{k \neq l} \|\mathcal{I}_l^+\|_2^2 + \|\mathcal{I}_k^+\|_2^2 = 2(L-1) \|\mathcal{I}^+\|_{\text{Fro}}^2 v. \end{aligned}$$

4. Model-aware inversion

Using the Chi distribution of $\delta = \|N^v\|_{\text{Fro}}$ (cf. section 2.2.2), we obtain

$$\mathbb{E}\delta = \mathbb{E} \|N^v\|_{\text{Fro}} = \sqrt{2} \frac{\Gamma\left(\frac{ML+1}{2}\right)}{\Gamma\left(\frac{ML}{2}\right)} \sqrt{v} \approx \sqrt{MLv}. \quad (4.11)$$

Since the gamma function grows as the factorial, the commonly used approximation in (4.11) is helpful for evaluating Γ for typical L (≥ 16) and M (≥ 15). It is based on the asymptotic

$$\lim_{t \rightarrow \infty} \Gamma(t + \alpha)(\Gamma(t))^{-1} t^{-\alpha} = 1.$$

To get an estimate for the noise level, we now combine the previous results. In the computation of the expected values, the realizations e_v and E^v were (in an abusive notation) replaced by its model random variables. Replacing the expected values by the computable quantities, we get an estimate

$$v^{\text{CEM}} := \frac{e_v}{2(L-1)} \left\| \mathcal{I}^+ \right\|_{\text{Fro}}^{-2}$$

for the underlying noise variance and an estimate

$$\delta^{\text{CEM}} := \sqrt{MLv^{\text{CEM}}} \quad (4.12)$$

for the data noise level.

Some evaluations of this estimate are shown in Table 4.4. To generate the measured data, the previously introduced adjacent, cosine and Haar-wavelet current frames were used. Pseudo-random noise was generated according to (2.20) with a relative measurement precision η varying over several orders of magnitude. A new, independent realization of noise was generated for each η and each measurement basis. The conductivity and electrode setting are the same as in Table 4.1. In all evaluations, the true noise level δ is within 6% of the estimated noise level δ^{CEM} , that is, $|1 - \delta/\delta^{\text{CEM}}| < 0.06$. This accuracy is important when using the approximation δ^{CEM} instead of the unknown δ in Morozov's discrepancy principle.

η	δ_{adjacent}	$\delta_{\text{adjacent}}^{\text{CEM}}$	δ_{cosine}	$\delta_{\text{cosine}}^{\text{CEM}}$	δ_{Haar}	$\delta_{\text{Haar}}^{\text{CEM}}$	$ 1 - \delta/\delta^{\text{CEM}} $
1.0×10^{-4}	1.10×10^{-3}	1.09×10^{-3}	1.44×10^{-3}	1.51×10^{-3}	1.68×10^{-3}	1.62×10^{-3}	< 5%
1.0×10^{-3}	1.12×10^{-2}	1.17×10^{-2}	1.64×10^{-2}	1.69×10^{-2}	1.82×10^{-2}	1.72×10^{-2}	< 6%
1.0×10^{-2}	1.08×10^{-1}	1.07×10^{-1}	1.53×10^{-1}	1.60×10^{-1}	1.68×10^{-1}	1.73×10^{-1}	< 5%
1.0×10^{-1}	$1.11 \times 10^{+0}$	$1.06 \times 10^{+0}$	$1.60 \times 10^{+0}$	$1.67 \times 10^{+0}$	$1.51 \times 10^{+0}$	$1.57 \times 10^{+0}$	< 5%

Table 4.4.: Estimates of the data noise for simulated data with additive pseudo-random normal noise of variance $\hat{v}(\eta)$ using adjacent, cosine and Haar current patterns. Each pair of columns shows the exact noise $\delta = \|N^{\hat{v}(\eta)}\|_{\text{Fro}}$ and its corresponding estimated noise δ^{CEM} . An independent realization of $N^{\hat{v}(\eta)}$ was generated for each estimate, using the seeds $k \cdot 10^j$ for the Mersenne twister with $k = 1, \dots, 4$ (contact impedances) and $j = 0, \dots, 2$ (current frames). Setting as in Table 4.1.

4.1.3. Measurement protocol and incomplete data

Throughout this work, we assume that for each current vector $I = (I_1, \dots, I_L)^\top \in \mathbb{R}_\diamond^L$ (*stimulation pattern*), a vector of potentials $U = (U_1, \dots, U_L)^\top \in \mathbb{R}_\diamond^L$ is measured. In practice, the measurement protocol for acquiring data can be different. For example, some measurement equipments do not measure potentials (against a grounding point), but measure potential differences, i.e. voltages between two electrodes (for example neighboring electrodes) explicitly. That means that the current-to-potential map R_σ must be replaced by a current-to-voltage map, e.g. by

$$I \mapsto V = \begin{pmatrix} U_2 - U_1 \\ U_3 - U_2 \\ \vdots \\ U_L - U_{L-1} \\ U_1 - U_L \end{pmatrix}.$$

Since V can be obtained from U by a basis transform, all theoretical results in this work also hold when considering the current-to-voltage map instead of the current-to-potential map. *However, the noise model might differ.*

Matters get more complicated when current-carrying electrodes are excluded from voltage measurements, leading to incomplete data. A common example is the incomplete adjacent-current-to-voltage map

$$I_{\text{adj}}^{(m)} \mapsto \begin{pmatrix} U_2 - U_1 \\ \vdots \\ U_{m-1} - U_{m-2} \\ U_{m+2} - U_{m+1} \\ \vdots \\ U_1 - U_L \end{pmatrix},$$

that is, all entries from current-carrying electrodes are excluded from the voltage measurements.

This is common practice in many applications in electrical engineering, mainly because the measurements are considered unreliable due to the contact impedances. However in the CEM, the contact impedances are incorporated into the model, thus the measurements on current-carrying electrodes are valuable. In equations (4.9) and (4.10), we see that the product $U_l I_l$ appears in each term, which vanishes if $I_l = 0$. This means that only potentials from current-carrying electrodes are used in the contact impedance and conductivity estimate, and in fact a reliable estimate of the contact impedances is impossible without this data.

If potential/voltage measurements on the current-carrying electrodes are omitted, we conclude that an accurate estimate of the contact impedances is not available. In this case, the contact impedan-

4. Model-aware inversion

ces can be initialized to a small generic constant⁵. However, an initial guess for the background conductivity σ^{CEM} is still possible using these constants.

Moreover, an estimate for the noise level is also possible in this case by exploiting the *reciprocity principle* for passive quadripoles

$$U_{l+1}^{(m)} - U_l^{(m)} = U_{m+1}^{(l)} - U_m^{(l)}, \quad m \notin \{l-1, l, l+1\} \pmod{L}$$

for noiseless data. Then, a noise estimate similar to (4.12) can be obtained by considering an appropriate noise model and the symmetry error

$$\sum \left| (U_{l+1}^{(m)} - U_l^{(m)}) - (U_{m+1}^{(l)} - U_m^{(l)}) \right|^2,$$

where the sum is taken over all available reciprocity pairs.

4.2. Nonlinearity and constrainedness

The ICP is a constrained and highly nonlinear problem, both for Calderón's model and for the CEM. This can lead to several problems for Newton-type algorithms as they solve unconstrained problems by linearization. Firstly, a Newton update can give negative conductivities or – if the step size is reduced accordingly – result in very slow convergence. This is particularly bad since the nonlinearity of the forward map and thus the linearization error increase as the conductivity approaches zero. Our numerical examples in section 6.2 will illustrate this effect. A classical and popular method to obtain an unconstrained problem is to recover the logarithm of the conductivity,

$$\log \sigma, \quad \text{or} \quad -\log \sigma = \log \frac{1}{\sigma};$$

see [BS87]. This approach is also motivated by the filtered back-projection approach for EIT [Vau97]. To improve the convergence speed of a Newton-type method and to increase its convergence radius, we aim to reduce the nonlinearity of the ICP. Unfortunately, the ICP for the CEM is always nonlinear, even in the most simple case when considering a one-dimensional conductivity space, due to the impact of the contact impedances.

Thus to motivate coefficient transformations, we will again look at the most simple model first, i.e. Calderón's model for constant conductivities, as in equation (4.1).

When recovering inclusions inside a constant background, ND data is most sensitive to the background conductivity, thus improving the linearity with respect to the background is reasonable. Improving the linearity is particularly useful when recovering inclusions in an unknown constant background by linear (one-step) methods. This has been investigated in detail for lung EIT [GA14], where reconstructions of σ , $\log \sigma$ and $\rho = \frac{1}{\sigma}$ with the (one-step) NOSER algorithm [CIN⁺90] are

⁵E.g. $z_l^{\text{generic}} = |E_l|$, $l = 1, \dots, L$.

4. Model-aware inversion

compared. However, recovering the resistivity is again a constrained problem ($\rho > 0$). Conversely to the conductivity case, linearization error increases for very small resistivities in the non-constant case.

Instead of linearizing F directly, we want to apply the Newton step to an operator for the transformed conductivity. To that end, we consider injective C^1 -transformations

$$t_* : (0, \infty) \rightarrow \mathbb{R}, \quad \sigma \mapsto t_*(\sigma) =: \sigma_*,$$

and their corresponding transformed continuum and CEM forward operators defined by

$$\begin{aligned} \mathcal{F}_*(t_*(\sigma)) &= \mathcal{F}(\sigma), \quad \text{that is,} \quad \mathcal{F}_*(\sigma_*) = \mathcal{F}(t_*^{-1}(\sigma_*)), \quad \text{and} \\ F_*(t_*(\sigma)) &= F(\sigma), \quad \text{that is,} \quad F_*(\sigma_*) = F(t_*^{-1}(\sigma_*)). \end{aligned} \quad (4.13)$$

Identifying a scalar $\sigma > 0$ with its constant conductivity $\sigma \chi_\Omega$ on Ω and interpreting the forward operator as a function with scalar argument σ , we have for Calderón's model that

$$\mathcal{F}(\sigma) = \frac{1}{\sigma} \mathcal{F}(1), \quad \text{thus} \quad \mathcal{F}'(\sigma) = \frac{-1}{\sigma^2} \mathcal{F}(1) \quad (4.14)$$

for the derivative in unit direction. Under transformation, we get

$$\mathcal{F}'_*(\sigma_*) = \left[\mathcal{F}(t_*^{-1}(\sigma_*)) \right]' = \frac{-(t_*^{-1})'(\sigma_*)}{[t_*^{-1}(\sigma_*)]^2} \mathcal{F}(1) = s_*(\sigma_*) \mathcal{F}(1)$$

for $s_*(\cdot) := -(t_*^{-1})'(\cdot) [t_*^{-1}(\cdot)]^{-2}$ on the range of t_* .

Now, if $s'_* \equiv 0$, then s_* and thus \mathcal{F}'_* are constant, hence \mathcal{F}_* is linear. In that sense, $|s'_*(t_*(\sigma))|$ is an indicator for the nonlinearity of \mathcal{F}_* at a conductivity constant σ . In particular for $t_\rho(\sigma) := \frac{1}{\sigma}$, we have that

$$t_\rho^{-1}(\sigma_*) = \sigma_*^{-1}, \quad (t_\rho^{-1})'(t_\rho(\sigma)) = -\sigma^2, \quad \text{and} \quad \left| s'_\rho(t_\rho(\sigma)) \right| \equiv 0,$$

which is the linearity of Calderón's problem for constant resistivities.

Our goal is to obtain a transformation t_* that is unconstrained (like $\log(\sigma)$), but has limited nonlinearity at constants (like t_ρ). To that end, we introduce the transformation

$$t_\alpha(\sigma) := (1 - \alpha)\sigma^{-1} - \alpha\sigma \quad (4.15)$$

for some parameter $\alpha \in (0, 1)$. Being the sum of two strictly decreasing C^1 functions on $(0, \infty)$, t_α is clearly injective. Since $t_\alpha(\sigma) \rightarrow \infty$ ($\sigma \rightarrow 0$) and $t_\alpha(\sigma) \rightarrow -\infty$ ($\sigma \rightarrow \infty$), this transformation gives an unconstrained parameter. Moreover, we have that

$$t_\alpha^{-1}(t) = \frac{\sqrt{4\alpha(1-\alpha)+t^2}-t}{2\alpha}, \quad (t_\alpha^{-1})'(t_\alpha(\sigma)) = \frac{-\sigma^2}{(1-\alpha)+\alpha\sigma^2} \quad \text{and} \quad |s'_\alpha(t_\alpha(\sigma))| = \frac{2\alpha\sigma^3}{(1+\alpha(\sigma^2-1))^3}.$$

The parameter α is a trade-off between reconstructing the resistivity ($\alpha \rightarrow 0$) and the conductivity

4. Model-aware inversion

($\alpha \rightarrow 1$). It controls the maximum nonlinearity of t_α and its occurrence:

$$\max_{\sigma \in (0, \infty)} |s'_\alpha(t_\alpha(\sigma))| = s'_\alpha(0) = \frac{\alpha}{4(\alpha(1-\alpha))^{\frac{3}{2}}}, \quad \arg \max_{\sigma \in (0, \infty)} |s'_\alpha(t_\alpha(\sigma))| = \sqrt{\alpha^{-1} - 1}.$$

The maximum nonlinearity is minimized at $\hat{\alpha} = 0.25$, so in a sense, this is an optimal choice.

Definition 4.7 (σ - ρ -transform). In the remainder of this work, we call

$$t_{\hat{\alpha}}: (0, \infty) \rightarrow (-\infty, \infty), \quad t_{\hat{\alpha}}(\sigma) = \frac{3}{4\sigma} - \frac{\sigma}{4} = \frac{3 - \sigma^2}{4\sigma},$$

the σ - ρ -transform, as it is a convex combination of the negative conductivity and the resistivity. The particular choice $\hat{\alpha} = 0.25$ in (4.15) is optimal in the sense that $\max_{\sigma \in (0, \infty)} |s'_*(t_*(\sigma))|$ is minimized over all $\alpha \in (0, 1)$.

For numerical stability and for some theoretical results, the boundedness of the conductivity from above and below (2.6) is crucial. These bounds can be realized explicitly using a tangent-type transformation. One example is the following transformation, which concatenates a scaled and shifted log-transform with a tangent to restrict the conductivity to the interval $(c_{\min}, c_{\max}) \subset (0, \infty)$.

Definition 4.8 (tan-log-transform). In the remainder of this work, we call

$$t_{\text{tl}}: (c_{\min}, c_{\max}) \rightarrow (-\infty, \infty), \quad t_{\text{tl}}(\sigma) = \tan\left(\frac{\pi(\log(\sigma) - \log(c_{\min}))}{\log(c_{\max}) - \log(c_{\min})} - \frac{\pi}{2}\right)$$

the tan-log-transform. It is strictly monotonous and continuously differentiable as a concatenation of strictly monotonous and continuously differential functions.

One possibility is to initialize the constants with respect to the initial guess $\sigma^{\text{CEM}, z}$, for example as $c_{\min} = \sigma^{\text{CEM}, z} \times 10^{-2}$ and $c_{\max} = \sigma^{\text{CEM}, z} \times 10^{+2}$, respectively.

In the following, we will consider conductivity transformations for non-homogeneous conductivities and for the CEM. In particular, we are interested in transforming piecewise constant conductivities $\sigma \in \mathcal{D}_p(\Omega)$. The transformation is then interpreted as

$$t_*(\sigma) = t_*(\sigma_1)\chi_{\Omega_1} + \dots + t_*(\sigma_p)\chi_{\Omega_p} \in L^\infty(\Omega) \quad \text{for } \sigma \in \mathcal{D}_p.$$

In particular, the positivity constraint for the coefficients $t_*(\sigma_p)$ is dropped. For solving the linearized problem in the transformed setting, we need to compute the Fréchet derivative of the transformed operator F_* . Using the chain rule, we get the Jacobian – evaluated in the p th unit direction of the discretized conductivity space – by

$$\left. \frac{\partial F_*(\sigma_*)}{(\partial \sigma_*)_p} \right|_{t_*(\sigma)} = \left. \frac{\partial F(t_*^{-1}(\sigma_*))}{(\partial \sigma_*)_p} \right|_{t_*(\sigma)} = \left. \frac{\partial F(\sigma)}{(\partial \sigma)_p} \right|_{\sigma} \left. \frac{\partial t_*^{-1}(\sigma_*)}{(\partial \sigma_*)_p} \right|_{t_*(\sigma)} = [F'(\sigma)]_p \left((t_*^{-1})'(t_*(\sigma)) \right)_p. \quad (4.16)$$

4. Model-aware inversion

Table 4.5 summarizes some properties of interest, i.e. the inverse map t_*^{-1} , the nonlinearity indicator $|s'_*(t_*(\sigma))|$, the Jacobian amplification $(t_*^{-1})'(t_*(\sigma))$, and the range, of some transformations which are considered in the remainder of this work.

Transformation t_*	$t_*^{-1}(\sigma_*)$	$ s'_*(t_*(\sigma)) $	$(t_*^{-1})'(t_*(\sigma))$	$t_*(0, \infty)$
$t_{\text{Id}}(\sigma) = \sigma$	σ_*	$2\sigma^{-3}$	1	$(0, \infty)$
$t_{\log}(\sigma) = -\log(\sigma)$	$e^{-\sigma_*}$	σ^{-1}	$-\sigma$	$(\infty, -\infty)$
$t_\rho(\sigma) = \sigma^{-1}$	σ_*^{-1}	0	$-\sigma^2$	$(\infty, 0)$
$t_{\hat{\alpha}}(\sigma) = \frac{3 - \sigma^2}{4\sigma}$	$\sqrt{3 + 4\sigma_*^2} - 2\sigma_*$	$\frac{32\sigma^3}{(3 + \sigma^2)^3}$	$\frac{-4\sigma^2}{3 + \sigma^2}$	$(\infty, -\infty)$
$t_{\text{tl}}(\sigma) = \tan\left(\frac{\pi(\log(\sigma) - \log(c_{\min}))}{\log(c_{\max}) - \log(c_{\min})} - \frac{\pi}{2}\right)$	$\frac{\exp[\log(a) + (\log(b) - \log(a)) \cdot \pi^{-1}(\tan^{-1}(\sigma_*) + \frac{\pi}{2})]}{\pi^{-1}(\tan^{-1}(\sigma_*) + \frac{\pi}{2})}$	(omitted)	(omitted)	$t_{\text{tl}}(c_{\min}, c_{\max}) = (-\infty, \infty)$

Table 4.5.: Properties (inverse map, nonlinearity indicator, Jacobian amplification and range) of various conductivity transformations.

For solving the transformed ICP using the inexact Newton-type Algorithm 1, line 3 therein needs to be replaced by

$$\text{“Find } \eta_*^{(k)} \text{ satisfying } \left\| (F_*)'_{\mathcal{I}}(t_*(\sigma^{(k)})) \eta_*^{(k)} - d^{(k)} \right\| \leq \theta^{(k)} \left\| d^{(k)} \right\|; \text{”} \quad (4.17)$$

and line 4 needs to be replaced by

$$\text{“Set } \sigma^{(k+1)} = t_*^{-1}(t_*(\sigma^{(k)}) + \eta_*^{(k)}); \text{”}.$$

4.3. Underdetermination and prior assumptions

The linearized problem

$$\text{Find } \eta_* \in L^\infty(\Omega) \text{ satisfying } (F_*)'_{\mathcal{I}}(\sigma_*) \eta_* = d \quad (4.18)$$

is highly underdetermined and severely ill-posed. We solve its discretization up to a certain tolerance in each Newton step (4.17). By using these tolerances we control the amount of regularization (REGINN), but do not resolve the underdetermination of the problem. Thus, we need additional assumptions to obtain uniqueness.

We will formulate these assumptions first for the untransformed CEM forward operator $F_{\mathcal{I}}$, and consider the transformed setting in section 4.3.3.

The discretized linearized problem can be formulated as a linear system of equations for the coefficients of the conductivity update. To that end, define the *sensitivity matrix* $S = S(\sigma) \in \mathbb{R}^{K \times P}$, where

4. Model-aware inversion

$K = LM$, column-wise by

$$S_p = \text{col}(F_{\mathcal{I}}'(\sigma)\chi_{\Omega_p}), \quad p = 1, \dots, P, \quad (4.19)$$

and $\text{col}(\cdot)$ denotes the operation of stacking a matrix into a column vector column-wise. Recall that $\chi_{\Omega_1}, \dots, \chi_{\Omega_P}$ are the (orthogonal) basis functions used to generate the discretized conductivity space $\mathcal{D}_{\mathcal{P}}$ for a partition $\{\Omega_1, \dots, \Omega_P\}$ of Ω .

In the following, boldface symbols denote the coefficient vectors corresponding to conductivities and conductivity updates, e.g. $\boldsymbol{\sigma} \in \mathbb{R}_+^P$ and $\boldsymbol{\eta} \in \mathbb{R}^P$ such that

$$\boldsymbol{\sigma} \hat{=} \sigma = \boldsymbol{\sigma}_1 \chi_{\Omega_1} + \dots + \boldsymbol{\sigma}_P \chi_{\Omega_P} \in \mathcal{D}_{\mathcal{P}} \subset L_+^{\infty}(\Omega)$$

and

$$\boldsymbol{\eta} \hat{=} \eta = \boldsymbol{\eta}_1 \chi_{\Omega_1} + \dots + \boldsymbol{\eta}_P \chi_{\Omega_P} \in L^{\infty}(\Omega),$$

respectively. Finally, we define the nonlinear residual vector by $\boldsymbol{d} = \text{col}(\mathcal{U}^v - F_{\mathcal{I}}(\sigma))$. Then, the linear system for the coefficient vector reads

$$\text{Find } \boldsymbol{\eta} \in \mathbb{R}^P \text{ satisfying } S\boldsymbol{\eta} = \boldsymbol{d}. \quad (4.20)$$

4.3.1. A reconstruction prior for the Newton update

In the coefficient notation (4.20), it is clear that the problem is underdetermined since for commonly used discretizations and settings, we have that $|\mathcal{D}_{\mathcal{P}}| = P \gg K = LM$. Thus, we need to make a design choice which solution to pick for the Newton update. To that end, we introduce a prior assumption on the conductivity. We first consider the most simple case of underdetermination by assuming that two columns S_p and S_q of S are collinear, that is,

$$S_q = \beta S_p \quad \text{for some } \beta \in \mathbb{R} \setminus \{0\} \quad \text{and some } 1 \leq p, q \leq P.$$

Then, the linear combination of unit vectors $e_q - \beta e_p$ is in the Null space of S . This means that we have (at least) one degree of freedom in choosing $\boldsymbol{\eta}_q$ versus $\boldsymbol{\eta}_p$ in the solution $\boldsymbol{\eta}$ of (4.20).

Physically, the conductivity is a material property represented by a piecewise constant function. Starting from a constant initial conductivity guess, it is thus reasonable to update indistinguishable coefficients by the same amount:

$$\text{If } \boldsymbol{\sigma}_p = \boldsymbol{\sigma}_q \quad \text{and} \quad S_q = \beta S_p, \quad \text{then find a solution } \boldsymbol{\eta} \text{ to (4.20) such that } \boldsymbol{\eta}_p = \text{sign}(\beta)\boldsymbol{\eta}_q.$$

More colloquially, we do not want to introduce arbitrary oscillations in the Newton update which are not justified by the measurements.

On the other hand, if $\boldsymbol{\sigma}_q \neq \boldsymbol{\sigma}_p$, then we already have an oscillation in the conductivity, so choosing $\boldsymbol{\eta}_p = \text{sign}(\beta)\boldsymbol{\eta}_q$ is not helpful in preventing oscillations. Instead, motivated by the inverse pro-

4. Model-aware inversion

portionality (4.1) of a homogeneous conductivity on the measured potentials, we will choose the conductivity updates proportional to the local conductivity value to compensate for that effect. This is postulated in the following prior on the solutions of the linearized system:

Definition 4.9 (Reconstruction prior). Assume that $S_q = \beta S_p$ for some $p, q \in \{1, \dots, P\}$ and some $\beta \in \mathbb{R} \setminus \{0\}$, which means that (4.20) is underdetermined in the coefficients $\boldsymbol{\eta}_{\{p,q\}}$ for all right-hand sides $\mathbf{d} \in \mathbb{R}^K$. Then, we want to set $\boldsymbol{\eta}_{\{p,q\}}$ proportional to their local conductivities $\sigma_{\{p,q\}}$, that is,

$$\frac{\boldsymbol{\eta}_p}{\sigma_p} = \frac{\text{sign}(\beta)\boldsymbol{\eta}_q}{\sigma_q}. \quad (4.21)$$

A solution $\boldsymbol{\eta}$ to $S\boldsymbol{\eta} = \mathbf{d}$ satisfying this criterion for all pairwise collinear columns of S is said to satisfy the *reconstruction prior*.

The central result of this section is that a solution satisfying the reconstruction prior can be obtained by considering a weighted pseudo-inverse matrix of S . This will be formulated in Theorem 4.11 and Corollary 4.12. To formulate the results, we need to define weighted minimum norm solutions.

Definition 4.10 (Weighted minimum norm solution). Denote, for a positive definite weight matrix $0 < W \in \mathbb{R}^{P \times P}$, a weighted inner product and its induced norm by

$$\langle \cdot, \cdot \rangle_W = \langle \cdot, W \cdot \rangle_{\mathbb{R}^P} \quad \text{and} \quad \|\cdot\|_W = \|W^{1/2} \cdot\|_2,$$

respectively. Then, we define a *weighted minimum norm solution* $\boldsymbol{\eta}^{+W}$ of the linear problem $S\boldsymbol{\eta} = \mathbf{d}$ by

$$\boldsymbol{\eta}^+ = \boldsymbol{\eta}^+(\mathbf{d}) = S^{+W} \mathbf{d} = \arg \min_{\boldsymbol{\eta} \in \mathcal{N}(S)^\perp_W} \|S\boldsymbol{\eta} - \mathbf{d}\|_2, \quad (4.22)$$

where \perp_W denotes orthogonality with respect to the weighted inner product and thus, S^{+W} is a weighted pseudo-inverse of S .

For a diagonal weight matrix, a relation between the weights, the weighted minimum norm solution (4.22) and a sensitivity matrix S with collinear columns is now given by

Theorem 4.11. Consider the situation of (4.22) with $S \in \mathbb{R}^{K \times P}$ and assume that $S_q = \beta S_p$ for some $p, q \in \{1, \dots, P\}$ and some $\beta \in \mathbb{R} \setminus \{0\}$. Further, let $W = \text{diag}(w_1, \dots, w_P) > 0$. Then, we have the proportionality relation

$$\frac{w_p}{\|S_p\|_2} \boldsymbol{\eta}_p^{+W}(\mathbf{d}) = \frac{\text{sign}(\beta)w_q}{\|S_q\|_2} \boldsymbol{\eta}_q^{+W}(\mathbf{d})$$

for all $\mathbf{d} \in \mathbb{R}^K$.

4. Model-aware inversion

Proof. Let $K, P \in \mathbb{N}$, $\mathbf{w}_1, \dots, \mathbf{w}_P > 0$ and $W = \text{diag}(\mathbf{w}_1, \dots, \mathbf{w}_P)$. Further, let $X = (\mathbb{R}^P, \langle \cdot, \cdot \rangle_W)$ and $Y = (\mathbb{R}^K, \langle \cdot, \cdot \rangle)$, i.e. X is equipped with a weighted inner product and Y is equipped with the standard inner product. Consider

$$S = (S_1, \dots, S_P) \in \mathbb{R}^{K \times P}$$

as an operator from X to Y and let $N = \text{rank}(S) \leq \min\{K, P\}$.

Denote, for some $\mathbf{d} \in \mathbb{R}^K$, by $\boldsymbol{\eta}^{+w} = \boldsymbol{\eta}^{+w}(\mathbf{d}) \in \mathbb{R}^P$ the (unique) minimizer of $\|S\boldsymbol{\eta} - \mathbf{d}\|_2$ in $\mathcal{N}(S)^{\perp w}$, the W -orthogonal complement of the null space of S . Let $S = UZV^*$ be the (reduced) singular value decomposition of the operator S with singular values $\zeta_1 > \dots > \zeta_N > 0$ and singular vectors $v^{(1)}, \dots, v^{(N)} \in X$, $u^{(1)}, \dots, u^{(N)} \in Y$, that is

$$U = (u^{(1)} | \dots | u^{(N)}), \quad Z = \text{diag}(\zeta_1, \dots, \zeta_N), \quad V = (v^{(1)} | \dots | v^{(N)}),$$

U unitary in $(\text{range}(S), \langle \cdot, \cdot \rangle) \subset Y$, V unitary in $(\mathcal{N}(S)^{\perp w}, \langle \cdot, \cdot \rangle_W) \subset X$. The adjoint operators are thus given as $U^* = U^\top$ and $V^* = V^\top W$. Then, $\boldsymbol{\eta}^{+w}$ is given by the pseudo-inverse S^{+w} of S as

$$\boldsymbol{\eta}^{+w}(\mathbf{d}) = S^{+w} \mathbf{d} = (VZ^{-1}U^*)\mathbf{d}.$$

We now want to investigate under which circumstances two coefficients $\boldsymbol{\eta}_p^{+w}(\mathbf{d}), \boldsymbol{\eta}_q^{+w}(\mathbf{d})$ are proportional for all $\mathbf{d} \in Y$. Denote by $v_\top^{(1)}, \dots, v_\top^{(P)} \in \mathbb{R}^N$ the columns of V^\top . For any $p, q \in \{1, \dots, P\}$ and any $\alpha_p, \alpha_q \in \mathbb{R} \setminus \{0\}$, we have the equivalence

$$\begin{aligned} 0 &= \alpha_q \boldsymbol{\eta}_q^{+w} - \alpha_p \boldsymbol{\eta}_p^{+w} = (\alpha_q e_q - \alpha_p e_p)^\top S^{+w} \mathbf{d} \quad \forall \mathbf{d} \in Y \\ \iff 0 &= \left((S^{+w})^\top (\alpha_q e_q - \alpha_p e_p) \right)^\top \mathbf{d} \quad \forall \mathbf{d} \in Y \\ \iff 0 &= (U^*)^\top Z^{-1} V^\top (\alpha_q e_q - \alpha_p e_p) \\ \iff 0 &= \underbrace{(U^*)^\top Z^{-1}}_{\text{full rank } (=N)} (\alpha_q v_\top^{(q)} - \alpha_p v_\top^{(p)}) \\ \iff \alpha_p v_\top^{(p)} &= \alpha_q v_\top^{(q)}. \end{aligned} \tag{4.23}$$

Assume now that two columns S_p and S_q are linearly dependent, that is, $S_q = \beta S_p$ for some $\beta \in \mathbb{R} \setminus \{0\}$. We then observe that

$$\begin{aligned} 0 &= S_q - \beta S_p = S(e_q - \beta e_p) = (UZV^*)(e_q - \beta e_p) = \underbrace{UZ}_{\text{full rank } (=N)} V^\top W(e_q - \beta e_p) \\ \iff 0 &= V^\top W(e_q - \beta e_p) \\ \iff \beta w_p v_\top^{(p)} &= w_q v_\top^{(q)}. \end{aligned} \tag{4.24}$$

4. Model-aware inversion

Equivalence between (4.23) and (4.24) holds for $\frac{\alpha_p}{\alpha_q} = \frac{\beta w_p}{w_q}$. In this case, we have

$$S_q = \beta S_p \iff \alpha_q \boldsymbol{\eta}_q^{+w} = \alpha_p \boldsymbol{\eta}_p^{+w} \quad \forall \mathbf{d} \in Y. \quad (4.25)$$

Since $|\beta| = \frac{\|S_q\|_2}{\|S_p\|_2}$, we get $\frac{\alpha_p}{\alpha_q} = \frac{\text{sign}(\beta) \|S_q\|_2 w_p}{\|S_p\|_2 w_q}$. Substituting this into (4.25) completes the proof. \square

Theorem 4.11 illustrates how the scaling of the columns of S has an effect on the solution coefficients of the linear system. However, the weights can be used to compensate this effect. We immediately get a set of weights enforcing the reconstruction prior by the following

Corollary 4.12. *For*

$$W_{S,\boldsymbol{\sigma}} := \text{diag} \left(\|S_1\|_2 \boldsymbol{\sigma}_1^{-1}, \dots, \|S_P\|_2 \boldsymbol{\sigma}_P^{-1} \right), \quad (4.26)$$

the weighted minimum norm solution $\boldsymbol{\eta}^{+w_{S,\boldsymbol{\sigma}}}$ given by (4.22) satisfies the reconstruction prior.

Roughly speaking, the weights can be used to “stretch” orthogonality to compensate for the scaling differences of the columns of S . As the pseudo-inverse is unique, we resolve underdetermination and satisfy the reconstruction prior simultaneously by choosing $\boldsymbol{\eta}^{+w_{S,\boldsymbol{\sigma}}}$ as the Newton update. We also get the following estimate for “almost collinear” columns of S :

Corollary 4.13. *Assume that S_p and S_q are almost collinear, that is, $S_q = \beta S_p + \kappa \mathbf{k}$, $S_p \perp \mathbf{k} \in \mathbb{R}^P$, $\|\mathbf{k}\|_2 = 1$, $\beta \in \mathbb{R} \setminus \{0\}$, $\kappa > 0$. Then,*

$$\left| \frac{\mathbf{w}_p}{\|S_p\|_2} \boldsymbol{\eta}_p^{+w}(\mathbf{d}) - \frac{\text{sign}(\beta) \mathbf{w}_q}{\|S_q\|_2} \boldsymbol{\eta}_q^{+w}(\mathbf{d}) \right| \leq \zeta_{\min}^{-1} \left(\kappa \zeta_{\min}^{-1} \|S_q\|^{-1} + c_\kappa \right) \|\mathbf{d}\|_2.$$

where ζ_{\min} is the smallest non-zero singular value of S and $c_\kappa = \mathcal{O}(\kappa^2)$ as $\kappa \rightarrow 0$. In particular, the right-hand side vanishes as $\kappa \rightarrow 0$ if and only if $\mathbf{k} \in \text{span}\{S_l : l \in \{1, \dots, P\} \setminus q\}$.

Note that $S_p \perp \mathbf{k}$ is not a restriction since \mathbf{k} can be split into orthogonal parts, and Corollary 4.13 holds for modified constants β and κ .

Proof of Corollary 4.13. Using the singular value decomposition of S as in the proof of Theorem 4.11, we have that

$$\kappa \mathbf{k} = S_q - \beta S_p = (UZV^*) (e_q - \beta e_p) = UZ \left(w_q v_{\dagger}^{(q)} - \beta w_p v_{\dagger}^{(p)} \right).$$

Since $\beta = \text{sign}(\beta) \frac{\sqrt{\|S_q\|_2^2 - \kappa^2}}{\|S_p\|_2}$ (Pythagoras), it follows for $\alpha_p = \frac{w_p}{\|S_p\|_2}$ and $\alpha_q = \frac{\text{sign}(\beta) w_q}{\|S_q\|_2}$ that

$$\|S_q\|_2 \left\| \alpha_q v_{\dagger}^{(q)} - \frac{\sqrt{\|S_q\|_2^2 - \kappa^2}}{\|S_q\|_2} \alpha_p v_{\dagger}^{(p)} \right\|_2 = \kappa \|Z^{-1} U^{\top} \mathbf{k}\|_2 \leq \kappa \|Z^{-1}\|_2.$$

4. Model-aware inversion

Using the triangle inequality, we obtain

$$\left\| \alpha_q v_+^{(q)} - \alpha_p v_+^{(p)} \right\|_2 \leq \kappa \left\| Z^{-1} \right\|_2 \left\| S_q \right\|_2^{-1} + c_\kappa, \quad \text{where} \quad c_\kappa = \left| 1 - \frac{\sqrt{\left\| S_q \right\|_2^2 - \kappa^2}}{\left\| S_q \right\|_2} \right| |\alpha_p| \left\| v_+^{(p)} \right\|_2,$$

and conclude that $c_\kappa = \mathcal{O}(\kappa^2)$ as $\kappa \rightarrow 0$. Again using the pseudo-inverse representations of the solution coefficients $\boldsymbol{\eta}_p^{+w}$ and $\boldsymbol{\eta}_q^{+w}$, we get

$$\begin{aligned} \left| \alpha_q \boldsymbol{\eta}_q^{+w} - \alpha_p \boldsymbol{\eta}_p^{+w} \right| &= \left| \left((U^*)^\top Z^{-1} V^\top (\alpha_q e_q - \alpha_p e_p) \right)^\top \mathbf{d} \right| \\ &\leq \left\| Z^{-1} \right\|_2 \left\| \alpha_q v_+^{(q)} - \alpha_p v_+^{(p)} \right\|_2 \left\| \mathbf{d} \right\|_2 \leq \left\| Z^{-1} \right\|_2 \left(\kappa \left\| Z^{-1} \right\|_2 \left\| S_q \right\|_2^{-1} + c_\kappa \right) \left\| \mathbf{d} \right\|_2. \end{aligned}$$

Note that in this expression, the singular values of S and thus Z^{-1} depend on \mathbf{k} and κ . Recalling that $\mathbf{k} = \frac{1}{\kappa} (S_q - \beta S_p) \in \text{span}\{S_1, \dots, S_P\}$ and denoting by $S^0 := (S_1, \dots, S_p, \dots, S_{q-1}, \beta S_p, S_{q+1}, \dots, S_P)$ the sensitivity matrix for $\kappa = 0$, we have to consider two cases as $\kappa \rightarrow 0$:

(i) $\text{rank}(S^0) < \text{rank}(S)$:

This occurs if and only if $\mathbf{k} \notin \text{span}\{S_1^0, \dots, S_P^0\} = \text{span}\{S_l : l \in \{1, \dots, P\} \setminus q\}$. From the continuity of the singular values in the matrix entries, we have that the minimum singular value ζ_{\min} of S vanishes as $\kappa \rightarrow 0$, thus $\left\| Z^{-1} \right\|_2 = \zeta_{\min}^{-1} \rightarrow \infty$.

(ii) $\text{rank}(S^0) = \text{rank}(S)$:

Again by the continuity of the singular values, ζ_{\min} approaches the smallest non-zero singular value of S^0 as $\kappa \rightarrow 0$, thus $\left\| Z^{-1} \right\|_2$ is bounded and $\alpha_q \boldsymbol{\eta}_q^{+w} \rightarrow \alpha_p \boldsymbol{\eta}_p^{+w}$ as $\kappa \rightarrow 0$.

Thus for $\alpha_p = \frac{w_p}{\left\| S_p \right\|_2}$ and $\alpha_q = \frac{\text{sign}(\beta) w_q}{\left\| S_q \right\|_2}$, this completes the proof. \square

For $W = W_{S, \sigma}$, Corollary 4.13 states that if two columns of S are almost collinear relative to the rest of the columns, then their coefficients in the weighted pseudo-inverse are almost proportional to the local conductivity. In practice, neighboring cells will often have corresponding columns in the sensitivity matrix which are ‘‘almost linearly dependent’’ in the sense of Corollary 4.13, in particular for very fine discretizations. Then, using the weights $W_{S, \sigma}$ causes their conductivity coefficient updates to be ‘‘almost’’ proportional to the local conductivity values, thus reducing oscillations of the conductivity in the Newton iteration.

In addition to the weights $W_{S, \sigma}$ we will also consider the weights

$$W_{\text{Id}} = \text{Id}, \quad W_S := \text{diag}(\left\| S_1 \right\|_2, \dots, \left\| S_P \right\|_2) \quad \text{and} \quad W_\sigma := \text{diag}(\sigma_1^{-1}, \dots, \sigma_P^{-1}), \quad (4.27)$$

in our numerical examples in chapter 6. The unit weights W_{Id} lead to the standard pseudo-inverse solution in the coefficient space, while the weights W_S normalize only for the column norms and the weights W_σ only normalize for the local resistivity values, respectively. The positive effect of W_S on conductivity updates has been observed in [CIN⁺90, CF02, SZTO08, Oh09], although without

a thorough analysis of the reasons⁶. Theorem 4.11 and Corollary 4.13 fill this gap by showing that the weights W_S lead to non-oscillatory updates. At constant background, in particular for one-step linearizations like NOSER, they are identical to the weights $W_{S,\sigma}$ and give updates satisfying the reconstruction prior (4.21). Since the weights W_S appear in the Tikhonov functional of the popular NOSER algorithm [CIN⁺90], they are sometimes called NOSER prior in EIT literature. To our knowledge, the weights $W_{S,\sigma}$ have not been considered previously.

4.3.2. Continuum interpretation of the weighted inner product

In Definition 4.10, a weighted coefficient space with inner product $\langle \cdot, \cdot \rangle_W$ was introduced to obtain a desired property for the coefficients $\boldsymbol{\eta}$ of the conductivity update η . How can this solution be interpreted in the continuum formulation (4.18)? The canonical inner product on $\mathcal{D}_{\mathcal{P}}$ is

$$\langle \eta, \xi \rangle_{L^2(\Omega)} = \int_{\Omega} \eta(x)\xi(x) \, dx.$$

If we can find a *weight function* $w \in L^{\infty}_{+}(\Omega)$ such that a *weighted inner product*

$$\langle \eta, \xi \rangle_w = \int_{\Omega} \eta(x)\xi(x)w(x) \, dx$$

on $\mathcal{D}_{\mathcal{P}}$ satisfies

$$\langle \boldsymbol{\eta}, \boldsymbol{\xi} \rangle_W = \langle \eta, \xi \rangle_w, \tag{4.28}$$

then $(\mathbb{R}^P, \langle \cdot, \cdot \rangle_W)$ and $(\mathcal{D}_{\mathcal{P}}, \langle \cdot, \cdot \rangle_w)$ are isometrically isomorphic. If $W = \text{diag}(\mathbf{w}_1, \dots, \mathbf{w}_P)$, we have that

$$\langle \boldsymbol{\eta}, \boldsymbol{\xi} \rangle_W = \sum_{p=1}^P \boldsymbol{\eta}_p \boldsymbol{\xi}_p \mathbf{w}_p \stackrel{!}{=} \sum_{p=1}^P \boldsymbol{\eta}_p \boldsymbol{\xi}_p \int_{\Omega_p} w(x) \, dx = \langle \eta, \xi \rangle_w,$$

thus, (4.28) is satisfied e.g. for the piecewise constant weight function

$$w(x) := \sum_{p=1}^P |\Omega_p|^{-1} \mathbf{w}_p \chi_{\Omega_p}(x).$$

Then, $\eta^{+w} \in \mathcal{D}_{\mathcal{P}}$ corresponding to the coefficient vector $\boldsymbol{\eta}^{+w}$ is characterized by

$$\boldsymbol{\eta}^{+w} = \arg \min_{\boldsymbol{\eta} \in \mathcal{N}(F'_{\mathcal{I}}(\sigma))^{\perp w} \cap \mathcal{D}_{\mathcal{P}}} \|F'_{\mathcal{I}}(\sigma)\boldsymbol{\eta} - \mathbf{d}\|_{\text{Fro}}, \tag{4.29}$$

where $F'_{\mathcal{I}}(\sigma)$ is considered as an operator on $\mathcal{D}_{\mathcal{P}}$. The Frobenius norm in (4.29) is due to the identity $\|\mathbf{d}\|_2 = \|\text{col}(\mathbf{d})\|_2 = \|\mathbf{d}\|_{\text{Fro}}$.

⁶In [SZTO08], the improved reconstructions when using the weights W_S are explained by an observed decrease $3 \cdot 10^{17} \rightarrow 1 \cdot 10^{17}$ of the condition of $S\boldsymbol{\eta} = \mathbf{d}$. Although improving the condition helps to stabilize the solution, we feel that the main impact of these weights is how they modify orthogonality, and thus which types of solutions are promoted in case of underdetermination.

4. Model-aware inversion

For the special cases $W = W_S$ and $W = W_{S,\sigma}$, we make the following interesting observation in the continuum representation. Recall definition (4.19) of the sensitivity matrix

$$S_p = \text{col} (F'_I(\sigma)\chi_{\Omega_p}) = \text{col} \left(- \int_{\Omega_p} \left(\nabla u^{(l)}(x) \cdot \nabla u^{(m)}(x) \right)_{l,m=1,\dots,L} \mathcal{I} dx \right), \quad (4.30)$$

where $u^{(l)}$, $l = 1, \dots, L$, are the first components of the forward solutions of the variational formulation (2.17) for currents $I_\diamond^{(l)}$ as described in section 2.3.3. For piecewise constant conductivities, we have that $u^{(l)}|_{\Omega_p} \in C^\infty(\Omega_p)$ for each $l = 1, \dots, L$ and $p = 1, \dots, P$, thus the *sensitivity function*

$$\bar{v}_I(x) := \left\| \left(\nabla u^{(l)}(x) \cdot \nabla u^{(m)}(x) \right)_{l,m=1,\dots,L} \mathcal{I} \right\|_{\text{Fro}}$$

is piecewise continuous. Taking the Euclidean norm in (4.30), we get $\bar{v}_I(x)|_{\Omega_p} \approx \|S_p\|_2$ on Ω_p for sufficiently refined discretizations \mathcal{P} . Note that \bar{v} is independent of \mathcal{P} for a fixed conductivity σ . Hence, the weight functions w_S and $w_{S,\sigma}$ corresponding to the weight matrices W_S and $W_{S,\sigma}$, i.e. given by

$$w_S(x) := \sum_{p=1}^P |\Omega_p|^{-1} \|S_p\|_2 \chi_{\Omega_p}(x) \quad \text{and} \quad w_{S,\sigma}(x) := \sum_{p=1}^P |\Omega_p|^{-1} \|S_p\|_2 \sigma_p^{-1} \chi_{\Omega_p}(x),$$

satisfy $w_S \approx \bar{v}$ and $w_{S,\sigma} \approx \bar{v}\sigma^{-1}$ on Ω for \mathcal{P} sufficiently fine, i.e. they are almost independent of the discretization geometry. We conclude with the following observation:

The weights $W_{S,\sigma}$ lead to unique Newton updates $\eta^{+w_{S,\sigma}}$ which are almost independent of the local discretization geometry and whose coefficients $\eta^{+w_{S,\sigma}} = \text{col}(\eta^{+w_{S,\sigma}})$ satisfy the reconstruction prior.

4.3.3. The reconstruction prior for the transformed forward operator

When considering a transformed forward operator F_* , i.e. updating the transformed conductivity $\sigma_* = t_*(\sigma)$ in each Newton step, the inverse transformation t_*^{-1} scales the conductivity updates and thus removes the property introduced by the reconstruction prior. In particular after the k -th Newton step, we have by Taylor expansion that

$$\sigma^{(k+1)} = t_*^{-1}(\sigma_*^{(k)} + \eta_*^{(k)}) = \underbrace{t_*^{-1}(\sigma_*^{(k)})}_{=\sigma^{(k)}} + \eta_*^{(k)} (t_*^{-1})'(\sigma_*^{(k)}) + o(\eta_*^{(k)}),$$

thus

$$\eta^{(k)} := \sigma^{(k+1)} - \sigma^{(k)} = \eta_*^{(k)} \left((t_*^{-1})'(\sigma_*^{(k)}) \right) + o(\eta_*^{(k)}).$$

This means that, when using the weights $W_{S,\sigma}$, the reconstruction prior is violated (to first order) by the factor $t_*^{-1}(\sigma_*^{(k)})$ after the inverse transform. To compensate for this effect, we can replace the

4. Model-aware inversion

weights $W_{S, \sigma}$ by the weights

$$W_{S_*, \sigma} = \text{diag} \left\{ (t_*^{-1})'(t_*(\sigma_1)) \|(S_*)_1\|_2 \sigma_1^{-1}, \dots, (t_*^{-1})'(t_*(\sigma_P)) \|(S_*)_P\|_2 \sigma_P^{-1} \right\}, \quad (4.31)$$

where S_* is the sensitivity matrix for the transformed problem, i.e.

$$(S_*)_p = \text{col} \left((F_*)'_T(t_*(\sigma)) [\chi_{\Omega_p}] \right), \quad p = 1, \dots, P. \quad (4.32)$$

Then, if $S_p \parallel S_q$, we have that $(S_*)_p \parallel (S_*)_q$, and Theorem 4.11 yields that

$$\underbrace{(\boldsymbol{\eta}_*^{(k)})_p \left((t_*^{-1})'((\boldsymbol{\sigma}_*^{(k)})_p) \right)}_{=(\boldsymbol{\eta}^{(k)})_p + o((\boldsymbol{\eta}_*^{(k)})_p)} \frac{1}{\boldsymbol{\sigma}_p^{(k)}} = \frac{w_p (\boldsymbol{\eta}_*^{(k)})_p}{\|(S_*)_p\|_2} \stackrel{\text{Th.4.11}}{=} \frac{w_q (\boldsymbol{\eta}_*^{(k)})_q}{\|(S_*)_q\|_2} = \underbrace{(\boldsymbol{\eta}_*^{(k)})_q \left((t_*^{-1})'((\boldsymbol{\sigma}_*^{(k)})_q) \right)}_{=(\boldsymbol{\eta}^{(k)})_q + o((\boldsymbol{\eta}_*^{(k)})_q)} \frac{1}{\boldsymbol{\sigma}_q^{(k)}}$$

for $w_p = (W_{S_*, \sigma^{(k)}})_{pp}$. This shows that the reconstruction prior is preserved to first order when using the weights $W_{S_*, \sigma}$. An interesting observation is that $|(t_{\log}^{-1})'(t_{\log}(\boldsymbol{\sigma})) \boldsymbol{\sigma}^{-1}| \equiv 1$, meaning that the log-transform inherits the conductivity-scaling implicitly: $W_{S_{\log}, \sigma} = W_{S_{\log}}$. The weight matrix W_{S_*} is defined accordingly (cf. equation (4.27)).

The compensation of the transformation in the weights raises an interesting question: Is the conductivity transformation still useful, since its scaling effects are compensated in the weights to preserve the reconstruction prior?

By the definition of the weighted minimum norm solution (4.22) for S_* , the weights only come into play if the null space of S_* is nontrivial; otherwise, $\mathcal{N}(S_*)^\perp = \mathcal{N}(S_*)^{\perp w} = \mathbb{R}^P$ independently of the weights. However, the transformation still allows us to obtain an unconstrained problem. Moreover, when considering inexact Newton updates $\boldsymbol{\eta}_*$ satisfying

$$\|S_* \boldsymbol{\eta}_* - \mathbf{d}\|_2 \leq \theta \|\mathbf{d}\|_2 \quad \text{and} \quad \boldsymbol{\eta}_* \in \mathcal{N}(S_*)^{\perp w}, \quad (4.33)$$

the transformation influences which solution of the non-unique problem (4.33) is chosen. This inequality is the coefficient-version of the inexact Newton update criterion (2.32) for the transformed forward operator.

In other words, the reconstruction prior and thus the weights $W_{S_*, \sigma}$ are designed to avoid oscillations when resolving underdetermination of the linear problem, while the transformation is chosen to obtain an unconstrained problem and possibly reduce the nonlinearity of the forward operator, although the latter was only studied for homogeneous conductivities.

4.4. Inexact Newton updates and regularization parameters

In chapter 2, we outlined the concept of inexact Newton updates satisfying (2.32) to deal with the instability of the linearized problem (2.30). In the coefficient notation for the transformed forward

4. Model-aware inversion

operator, we compute inexact Newton updates satisfying (4.33). To that end, a *weighted regularized conjugate gradient* (cg) method will be formulated.

4.4.1. Weighted conjugate gradient iteration

Denote by

$$S_*^{(k)} \tag{4.34}$$

the transformed sensitivity matrix for conductivity $\sigma^{(k)}$. Moreover, denote by

$$\mathcal{K}_*^{k,l} := \mathcal{K}_l \left((S_*^{(k)})' S_*^{(k)}, (S_*^{(k)})' \mathbf{d}_k \right) \subset \mathcal{N}(S_*^{(k)})^\perp, \quad k \in \mathbb{N}_0, \quad l \in \mathbb{N},$$

the l -th Krylov space (cf. eq. (2.35)) of the k -th Newton iteration. Here,

$$(S_*^{(k)})' := (S_*^{(k)})^\top (W^{(k)})^{-1}.$$

denotes the adjoint matrix of $S_*^{(k)}$ with respect to the weighted inner product $\langle \cdot, \cdot \rangle_{W^{(k)}}$, i.e. satisfying

$$x^\top (S_*^{(k)})' W^{(k)} y = \langle x, (S_*^{(k)})' y \rangle_{W^{(k)}} = \langle S_*^{(k)} x, y \rangle_{\mathbb{R}^{LM}} = x^\top (S_*^{(k)})^\top y \quad \text{for all } x \in \mathbb{R}^P, y \in \mathbb{R}^{LM}.$$

The l -th conjugate gradient iterate $\boldsymbol{\eta}_*^{(k,l)}$ in the k -th Newton iteration then satisfies

$$\boldsymbol{\eta}_*^{(k,l)} = \arg \min_{\boldsymbol{\eta}_* \in \mathcal{K}_*^{k,l}} \left\| S_*^{(k)} \boldsymbol{\eta}_* - \mathbf{d}^{(k)} \right\|_{\mathbb{R}^{LM}},$$

cf. equation (2.34). In particular, $\boldsymbol{\eta}_*^{(k,l)} \in \mathcal{N}(S_*^{(k)})^\perp$ and the residual is monotonously decreasing since $\mathcal{K}_*^{k,l_1} \subset \mathcal{K}_*^{k,l_2}$ for $l_1 \leq l_2$. By $l_*^{(k)}$, we denote the unique integer satisfying

$$\left\| S_*^{(k)} \boldsymbol{\eta}_*^{(k,l_*^{(k)})} - \mathbf{d}^{(k)} \right\|_{\mathbb{R}^{LM}} \leq \theta^{(k)} \left\| \mathbf{d}^{(k)} \right\|_{\mathbb{R}^{LM}} < \left\| S_*^{(k)} \boldsymbol{\eta}_*^{(k,l)} - \mathbf{d}^{(k)} \right\|_{\mathbb{R}^{LM}} \quad \text{for } l = 1, \dots, l_*^{(k)} - 1,$$

for a parameter $\theta^{(k)} \in (0, 1]$. This parameter has a regularizing effect on the linear system since $\boldsymbol{\eta}_*^{(k,l_*^{(k)})}$ gets highly oscillatory as $\theta^{(k)} \rightarrow 0$.

4.4.2. Safeguarding for the linear problem

In some examples, e.g. in the problems with additional degrees of freedom which will be introduced in chapter 5, we observed that

$$\left\| S_*^{(k)} \boldsymbol{\eta}_*^{(k,l_*^{(k)})} \right\| \ll \theta^{(k)} \left\| \mathbf{d}^{(k)} \right\|_{\mathbb{R}^{LM}}$$

for $l_*^{(k)}$ very small (e.g. 1). This means that even a single cg step, i.e. a steepest descent decrease, may undershoot the intended relative decrease $\theta^{(k)}$ by far, possibly preventing the desired regularization

4. Model-aware inversion

effect. For that reason, we define the (preliminary) Newton update as

$$\bar{\boldsymbol{\eta}}_*^{(k, l_*^{(k)})} := \begin{cases} \boldsymbol{\eta}_*^{(k, l_*^{(k)})}, & \left\| S_*^{(k)} \boldsymbol{\eta}_*^{(k, l_*^{(k)})} \right\| \geq \theta^{(k)} \|\mathbf{d}^{(k)}\|_{\mathbb{R}^{LM}}, \\ \boldsymbol{\eta}_*^{(k, l_*^{(k)})} - \bar{\lambda}^{(k)} \left(\boldsymbol{\eta}_*^{(k, l_*^{(k)})} - \boldsymbol{\eta}_*^{(k, l_*^{(k)}-1)} \right), & \text{otherwise,} \end{cases}$$

where $\bar{\lambda}^{(k)} \in (0, 1)$ is chosen⁷ such that the equality

$$\left\| S_*^{(k)} \bar{\boldsymbol{\eta}}_*^{(k, l_*^{(k)})} \right\| = \theta^{(k)} \|\mathbf{d}^{(k)}\|_{\mathbb{R}^{LM}}$$

holds. This way, we exactly meet the desired level of regularization by the inexact Newton update.

4.4.3. Safeguarding for the nonlinear problem

When using $l_*^{(k)}$ as a stopping index, one can observe in some numerical examples that $l_*^{(k)}$ drastically increases in the last few Newton steps, i.e. shortly before the discrepancy principle is reached. This leads to unnecessarily high oscillations in these Newton updates due to under-regularization. The described behaviour has been observed already in [Rie99], and a *safeguarding* rule

$$\theta^{(k)} \geq \tau \delta \left\| \mathcal{U}^{(k-1)} - \mathcal{U}^v \right\|_{\text{Fro}}^{-1}$$

for the thresholds $\theta^{(k)}$ was introduced to counter this effect; see [Rie99, eq. (6.2)]. We adopt this strategy and additionally limit the maximum number of conjugate gradient iterations in each step explicitly, i.e. we introduce numbers $l_{\max}^{(k)} \in \mathbb{N}$ and set

$$l^{(k)} = \min \left\{ l_*^{(k)}, l_{\max}^{(k)} \right\}.$$

The Newton update in the coefficient notation is then chosen as

$$\boldsymbol{\eta}_*^{(k)} := \bar{\boldsymbol{\eta}}_*^{(k, l^{(k)})},$$

leading to the new conductivity iterate $\boldsymbol{\sigma}_*^{(k+1)} = \boldsymbol{\sigma}_*^{(k)} + \bar{\boldsymbol{\eta}}_*^{(k, l^{(k)})}$.

4.4.4. Regularized weighted conjugate gradient algorithm

The conjugate gradient method for computing an inexact Newton update with a weighted coefficient norm is summarized in Algorithm 5. For the iteration limit $l_{\max}^{(k)} = \infty$ and ignoring the linear safeguarding (lines 12–14), Algorithm 5 coincides with [Rie05, Fig. 3.1] for $X = (\mathbb{R}^P, \langle \cdot, \cdot \rangle_{W^{(k)}})$ and $Y = \mathbb{R}^{LM}$ in the notation therein, with the stopping criterion given in [Rie05, Fig. 1.1].

⁷Finding $\lambda^{(k)}$ is straight-forward since we are dealing with a linear problem.

Algorithm 5: Regularized weighted conjugate gradient method

input : Sensitivity matrix $S_*^{(k)}$, nonlinear residual $\mathbf{d}^{(k)}$, weights $W^{(k)}$;
tolerance $\theta^{(k)} \in (0, 1]$, iteration limit $l_{\max}^{(k)} \in \mathbb{N}$.
output: Inexact Newton update $\boldsymbol{\eta}_*$, number of iterations $l^{(k)}$.

- 1 Set $\boldsymbol{\eta} = 0$, $\mathbf{d} = \mathbf{d}^{(k)}$, $\beta = 0$, $l = 0$;
- 2 **repeat**
- 3 $l = l + 1$;
- 4 $\mathbf{v} = (S_*^{(k)})^\top (W^{(k)})^{-1} \mathbf{d}$;
- 5 $\mathbf{u} = \mathbf{v} + \|\mathbf{v}\|_{W^{(k)}}^2 \beta \mathbf{u}$;
- 6 $\mathbf{y} = S_*^{(k)} \mathbf{u}$;
- 7 $\alpha = \|\mathbf{v}\|_{W^{(k)}}^2 / \|\mathbf{y}\|_2^2$;
- 8 $\boldsymbol{\eta} = \boldsymbol{\eta} + \alpha \mathbf{u}$;
- 9 $\mathbf{d} = \mathbf{d} - \alpha \mathbf{y}$;
- 10 $\beta = \|\mathbf{v}\|_{W^{(k)}}^{-2}$;
- 11 **until** $\|\mathbf{d}\|_2 \leq \theta^{(k)} \|\mathbf{d}^{(k)}\|_2$ or $l \geq l_{\max}^{(k)}$;
- 12 **if** $\theta^{(k)} < 1$ and $\|\mathbf{d}\|_2 < \theta^{(k)} \|\mathbf{d}^{(k)}\|_2$ **then**
- 13 $\boldsymbol{\eta} = \boldsymbol{\eta} - \left(\frac{\theta^{(k)} \|\mathbf{d}^{(k)}\|_2 - \|\mathbf{d}\|_2}{\|\mathbf{d} + \alpha \mathbf{y}\|_2 - \|\mathbf{d}\|_2} \right) \alpha \mathbf{u}$; // Scale last cg step to meet $\theta^{(k)}$
- 14 **end**
- 15 Set $\boldsymbol{\eta}_*^{(k)} = \boldsymbol{\eta}$, $l^{(k)} = l$;

4.4.5. Stopping rule and REGINN parameters

Finally, the Newton iteration is stopped by Morozov's discrepancy principle (2.33). By $k_* \in \mathbb{N}$, we denote the unique index satisfying

$$\left\| \mathcal{U}_*^{(k_*)} - \mathcal{U}^v \right\|_{\text{Fro}} \leq \tau \delta < \left\| \mathcal{U}_*^{(k)} - \mathcal{U}^v \right\|_{\text{Fro}} \quad \text{for all } k \in \{0, \dots, k_* - 1\},$$

where

$$\mathcal{U}_*^{(k)} = (F_*)_{\mathcal{I}} \left(\sigma_*^{(k)} \right).$$

Our inexact Newton iteration is completely defined as soon as we specify the REGINN parameters τ , δ , and $\theta^{(k)}$ for $k = 0, \dots, k_*$. Since the exact noise level of the data is unknown, we use our estimate (4.12). Motivated by the accuracy of this noise level estimate ($\pm 6\%$ in our examples presented in Table 4.4), we set

$$\tau := 1.1 \quad \text{and} \quad \delta := \delta^{\text{CEM}} \tag{4.35}$$

throughout this work.

4. Model-aware inversion

Remark 4.14. If significant model errors are expected, e.g. due to an unknown domain geometry, increasing τ might help to ensure convergence. However, this was not necessary for our data, and the above constant was sufficient for the convergence of all of our numerical examples, including the examples using the measured data from the tank experiments.

To choose the parameters $\theta^{(k)}$ of the conjugate gradient iteration, we pick up the parameter strategy of [Rie99] with a slight modification to eliminate the parameters which need setting-specific hand-tuning. The first Newton iteration suffers most from the nonlinearity of the problem due to the possibly large residual. Thus, we set

$$l_{\max}^{(0)} := 1 \quad \text{and} \quad \theta^{(0)} := 1$$

to make only one iteration and maximize regularization in the first Newton step. After this step, we want to allow for a moderate increase of iterations to increase the speed of convergence, but limit it to keep the regularization effect of the parameter choice. For the second iteration, we thus set

$$l_{\max}^{(1)} := 2l_{\max}^{(0)} = 2 \quad \text{and} \quad \theta^{(1)} := \frac{\|\mathbf{d}^{(1)}\|_2}{\|\mathbf{d}^{(0)}\|_2} \in (0, 1),$$

where $\mathbf{d}^{(0)}$ and $\mathbf{d}^{(1)}$ are the nonlinear residuals before the first and before the second Newton iteration, respectively. After that, we have enough information to use the REGINN parameter strategy for $\theta^{(k)}$ proposed by [Rie99]. Using this strategy, the relative decrease parameter is given by

$$\theta^{(k)} = \theta_{\max} \cdot \max \left\{ \theta_*^{(k)}, \tau \delta \left\| \mathcal{U}_*^{(k)} - \mathcal{U}^v \right\|_{\text{Fro}}^{-1} \right\}, \quad (4.36)$$

where

$$\theta_*^{(k)} = \begin{cases} 1, & k = 0, \\ \|\mathbf{d}^{(1)}\|_2 / \|\mathbf{d}^{(0)}\|_2, & k = 1, \\ 1 - \frac{l^{(k-2)}}{l^{(k-1)}} (1 - \theta^{(k-1)}), & k \geq 2 \wedge l^{(k-1)} > l^{(k-2)}, \\ \gamma \theta^{(k-1)}, & \text{otherwise,} \end{cases}$$

$l^{(k)}$ is the number of conjugate gradient iterations of the k -th Newton iteration, and γ and θ_{\max} should be chosen close to 1, although their exact value is not critical. We set

$$\gamma := 0.99 \quad \text{and} \quad \theta_{\max} = \sqrt{\gamma} \quad (4.37)$$

throughout this work. Finally, we set $l_{\max}^{(k)} = l^{(k-1)} + l^{(k-2)}$ for $k \geq 2$ to allow for a ‘‘controlled’’ increase of conjugate gradient iterations in each successive Newton step. In summary, the iteration

limits are

$$l_{\max}^{(k)} = \begin{cases} 1, & k = 0, \\ 2, & k = 1, \\ l^{(k-1)} + l^{(k-2)}, & k \geq 2. \end{cases} \quad (4.38)$$

The regularization effect of (4.36) was studied in detail in [Rie99, Rie05]. In our modified version (4.35)–(4.38), the parameter strategy is initialized dynamically a-posteriori for each reconstruction and does not require “hand tuning” in different settings to obtain good results.

4.5. A model-aware Newton-type inversion scheme

In section 2.4.7, we formulated a generic version of the inexact Newton-type method CG-REGINN as a basis for solving the ICP (Algorithm 1).

With the construction of suitable discretizations (section 3.5), the initialization of the relevant parameters (section 4.1), the design of tailored parameter transformations (section 4.2) and weighted spaces (section 4.3), and finally with the definition of a robust choice of regularization parameters (section 4.4), we have gathered all ingredients for our model-aware Newton-type inversion scheme (MANTIS) based on CG-REGINN. The entire scheme is shown in Algorithm 6. The evaluation of the forward operator and the sensitivity matrix can be done using the FEM as described in section 2.3.3 and equation (4.19).

Algorithm 6: MANTIS: Model-aware Newton-type inversion scheme for the ICP of the CEM

input : Measurement pattern \mathcal{I} , noisy data \mathcal{U}^v , boundary and electrode geometry information.

output: Conductivity estimate σ .

- 1 Set stopping parameters $\delta = \delta^{\text{CEM}}$ and $\tau = 1.1$, see eq. (4.12), (4.35) and Remark (4.14);
 - 2 Initialize FEM triangulation Δ , e.g. by adaptive triangulation as in section 3.5.4;
 - 3 Initialize discretized conductivity space $\mathcal{D}_{\mathcal{P}}$, e.g. using⁸ $\mathcal{P} = \Delta$ or using one of the schemes proposed in section 3.5;
 - 4 Initialize contact impedances $z^{\text{CEM},z}$ and conductivity $\sigma^{(0)} = \sigma^{\text{CEM},z}$ as in Definition 4.4;
 - 5 Apply conductivity transformation $\sigma_*^{(0)} = t_*(\sigma^{(0)})$;
 - 6 Set $k = 0$, $d^{(0)} = \mathcal{U}^v - (F_*)_{\mathcal{I}}(\sigma_*^{(0)})$;
 - 7 **while** $\|d_{Fro}^{(k)}\| > \tau\delta$ **do**
 - 8 Compute $\theta^{(k)}$ by (4.36) and $l_{\max}^{(k)}$ by (4.38);
 - 9 Compute $S_*^{(k)}$ (cf. (4.34)) by the FEM approximation (section 2.3.3) of (4.32);
 - 10 Compute weights $W^{(k)} = W_{S_*^{(k)}, \sigma_*^{(k)}}$;
 - 11 Compute⁹ $\boldsymbol{\eta}_*^{(k)}$ and $l^{(k)}$ by Algorithm 5;
 - 12 Set $\sigma_*^{(k+1)} = \sigma_*^{(k)} + \boldsymbol{\eta}_*^{(k)}$;
 - 13 Set $d^{(k+1)} = \mathcal{U}^v - (F_*)_{\mathcal{I}}(\sigma_*^{(k+1)})$;
 - 14 Set $k = k + 1$;
 - 15 **end**
 - 16 Set $\sigma = t_*^{-1}(\sigma_*^{(k)})$;
-

⁸If Δ is not a refinement of \mathcal{P} , non-trivial projection operators need to be added to the algorithm before each evaluation of the forward operator and the sensitivity matrix; see Remark 2.13. These projections are omitted here for better readability.

⁹Recall that boldface variables represent coefficient column vectors.

5. Problem-specific extensions to the inversion scheme

The generality and versatility of Newton-type methods are major reasons for their popularity and success. Since the basic framework qualifies for a broad class of optimization problems, it can be adapted or extended to solve highly problem-specific tasks.

In this chapter, we present three extensions of MANTIS: First, we extend the Newton scheme to handle uncertainties in the boundary model in section 5.1. To that end, we make use of the Fréchet differentiability of the forward operator with respect to the electrode geometry and the contact impedances. Therein, tailored parameter transformations ensure the consistency of the boundary model. Next, we demonstrate in section 5.2 that the use of sparsity-promoting Banach space methods for REGINN, as studied in [MRLa14, MR14, Mar15], fits seamlessly into the MANTIS framework. Finally, we present a heuristic scheme for encouraging piecewise constant conductivity solutions by successive nonlinear filtering of the Newton iterates in section 5.3.

5.1. Recovering model parameters

In the previous chapters, we required the boundary model – or a good approximation of it – to be known. It is needed for example to evaluate the forward operator and to compute its Fréchet derivative in each Newton step. In some applications, e.g. in brain EIT or in process tomography, this assumption is justified since the geometry is known a-priori, or it can be obtained by other imaging modalities such as CT or MRI. However for dynamic imaging of soft tissue such as lung monitoring, the boundary model, i.e. the shape of the object, the locations of the electrodes, and even the contact impedances, may change over time. Thus, it is difficult to determine and track the boundary geometry accurately.

As with the measurement noise and the contact impedances in section 4.1, one can try to obtain boundary information directly from the measured data. When using Newton-type methods, a key ingredient for this concept is the Fréchet differentiability of the forward operator with respect to the boundary shape, the electrode size and location and the contact impedances; see e.g. [DHSS13a], [DHH⁺12], and [VKV⁺02], respectively.

However, this approach has a fundamental issue: The (already underdetermined) problem of recovering a conductivity is extended to the even more ambiguous problem of recovering both the conductivity, the boundary shape, the electrode sizes and locations, and the contact impedances simultaneously from the limited set of measurements. The most obvious ambiguity is due to the conformal equivalence of EIT settings, which was used in chapter 3 first to generate different electrode geometries resulting in the same CEM forward operator, and later to approximate sensitivity based discretizations for non-circular domains. One such example is shown in Figure 5.1. For small contact impedances, these settings are by construction indistinguishable by their measurement data, which is emphasized by the following remark.

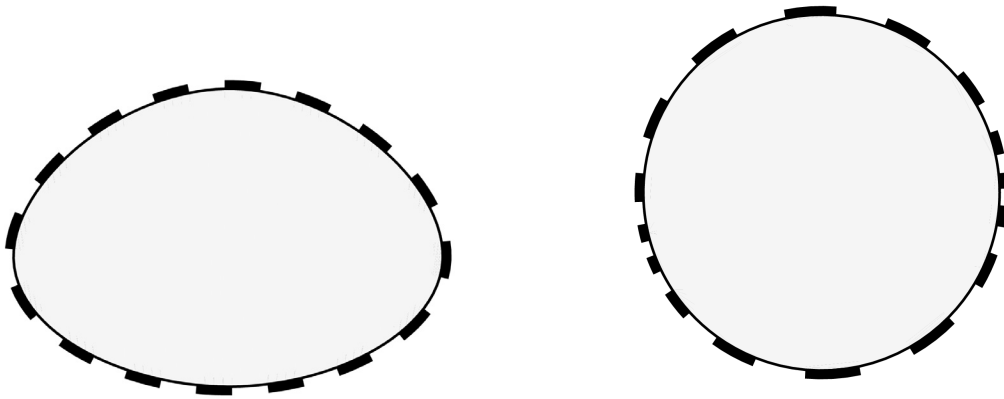


Figure 5.1.: Simply connected domain with 16 electrodes (left) and a conformally equivalent setting on the unit disk (right). Any Moebius transformation of the right setting is also conformally equivalent to the left setting. The conformal image was computed approximately using the Schwarz-Christoffel MATLAB toolbox (version 2.3) provided by Tobin A. Driscoll (cf. chapter 3).

Remark 5.1 (Ambiguity due to conformal equivalence).

- (a) Strictly speaking, the transformed CEM setting (3.25)–(3.28) is not a valid complete electrode model in the classical sense, since the contact impedances are not constant along each electrode. However, if the contact impedances are very small compared to the interior impedance ($z_1, \dots, z_L \ll \sigma^{-1}$ or simply $z \approx 0$), the exact distributions of the contact impedances along the electrodes have practically no influence on the measured data: they are indistinguishable from constant contact impedances even at very low measurement noise. Moreover, it is not even clear whether the contact impedances in real applications are homogeneous or varying along the electrodes.

5. Problem-specific extensions to the inversion scheme

- (b) In 3D settings, the underdetermination is even more severe, since we have additional degrees of freedom for changing the domain shape and electrode positions, sizes and shapes. Thus, as in the 2D case, we can not expect unique geometry information from the measured data.

As a consequence, if the geometry is unknown and the contact impedances are small, the best we can hope for is to obtain *one conformal equivalent* of the true boundary geometry from the measured data.

Another ambiguity is obtained for the electrode sizes and the contact impedances. For small electrodes and sufficiently big gaps, a constant ratio of electrode size versus contact impedance ($|E_l|z_l^{-1} = \text{const.}$) leads to practically indistinguishable electrode data in the presence of measurement noise.

Since Newton-type methods are local by nature, we assume to have at least a rough initial guess of the domain shape and the distribution of electrodes along the boundary to start with – an initial guess for the contact impedances then follows from Definition 4.4. In this scenario, Newton-type optimization of the boundary geometry will typically converge to a local solution, i.e. a conformally equivalent setting “close” to the initial guess.

We now gather the necessary differentiability results for the forward operator and then assemble a combined Fréchet derivative to optimize for the conductivity, the electrode size and position, and the contact impedances simultaneously.

Remark 5.2 (Fixing the boundary geometry). Due to the conformal equivalence of different geometries, any measurement data can be explained on any geometry for small contact impedances. Thus, we fix the initial guess of the boundary shape. This way, we avoid computing the Fréchet derivative with respect to a certain boundary parametrization, and – more importantly – we avoid nontrivial mappings of the conductivity from the old geometry to the new one.

5.1.1. Fréchet derivative with respect to the electrode geometry

For the ease of notation, the following considerations are restricted to the 2D case. More general expressions can be found in the corresponding references.

By optimizing for the electrode geometry, we consider an extension of the ICP. Consequently, we consider an *extended forward operator* \bar{F} depending also on the electrode locations, sizes, and contact impedances:

$$\begin{aligned} \bar{F}: \mathcal{D}(F_{\mathcal{I}}) \times \mathcal{D}_{\theta} \times \mathcal{D}_{|E|} \times \mathcal{D}_z &\rightarrow \mathcal{L}(\mathbb{R}_{\infty}^L), \\ \bar{F}(\sigma, (\theta_1, \dots, \theta_L), (|E_1|, \dots, |E_L|), (z_1, \dots, z_L)) &\mapsto (\mathcal{I} \mapsto \mathcal{U}), \end{aligned}$$

5. Problem-specific extensions to the inversion scheme

where $(\theta_1, \dots, \theta_L) \in \mathcal{D}_\theta \subset [0, |\partial\Omega|)^L$ parametrizes the center points of the electrodes, $(|E_1|, \dots, |E_L|) \in \mathcal{D}_{|E|} \subset [0, |\partial\Omega|)^L$ parametrizes the electrode sizes, and $(z_1, \dots, z_L) \in \mathcal{D}_z \subset \mathbb{R}_{>0}^L$ are the electrode contact impedances. The corresponding *extended measurement operator* is denoted by

$$\bar{F}_{\mathcal{I}}: \mathcal{D}(\bar{F}) \rightarrow (\mathbb{R}_{>0}^L)^M.$$

In [DHH⁺12, Theorem 4.1 and Corollary 4.2], the Fréchet derivative of the forward operator with respect to an electrode perturbation is given about the origin, that is, at their current shape. In the 2D case, perturbing the electrode boundary simply means to move the end-points of an electrode. Moreover, the integral over the electrode boundary appearing in [DHH⁺12, Corollary 4.2] is simply a point-evaluation of the interior potential u at the electrode edges in this case. Since $u|_{\partial\Omega} \in H^{1-\alpha}(\partial\Omega)$ for any $\alpha > 0$, this point evaluation is well-defined.

The explicit formulas for the 2D case are given in the following. To that end, let

$$E_l = \{\gamma(\theta): -\omega_l \leq \theta - \theta_l \leq \omega_l\} \quad \text{for some } \theta_l \in [0, |\partial\Omega|) \quad \text{and } \omega_l > 0, \quad l = 1, \dots, L,$$

analogous to the circular geometry, where $\gamma: [0, |\partial\Omega|] \rightarrow \mathbb{R}^d$ (modulo $|\partial\Omega|$, where required) is a continuous, piecewise smooth parametrization of $\partial\Omega$ with $\gamma(0) = \gamma(|\partial\Omega|)$ and $\|\gamma'(\theta)\|_2 = 1$ almost everywhere.

By equally perturbing both electrode edges in the same direction, a *Fréchet derivative with respect to the electrode movement* is given about its current position. For the l -th electrode, it is given component-wise (omitting the arguments) by

$$\begin{aligned} \left(\frac{\partial}{\partial \theta_l} \bar{F} \right)_{k,m} &:= \left(\bar{F}'_{\theta_l} \right)_{k,m} = -z_l^{-1} \left[\left(U_l^{(k)} - u^{(k)}(\gamma(\theta_l + \omega_l)) \right) \left(U_l^{(m)} - u^{(m)}(\gamma(\theta_l + \omega_l)) \right) \right. \\ &\quad \left. - \left(U_l^{(k)} - u^{(k)}(\gamma(\theta_l - \omega_l)) \right) \left(U_l^{(m)} - u^{(m)}(\gamma(\theta_l - \omega_l)) \right) \right], \end{aligned}$$

where $(u^{(k)}, U^{(k)})$ are the solutions of (2.17) for the k -th current $I_\diamond^{(k)}$ of the \diamond -frame and for conductivity σ . When perturbing both electrode edges by the same amount in opposite direction, a *Fréchet derivative with respect to the electrode size* is given about its current size. For the l -th electrode size, it reads

$$\begin{aligned} \left(\frac{\partial}{\partial |E_l|} \bar{F} \right)_{k,m} &:= \left(\bar{F}'_{|E_l|} \right)_{k,m} = -z_l^{-1} \left[\left(U_l^{(k)} - u^{(k)}(\gamma(\theta_l + \omega_l)) \right) \left(U_l^{(m)} - u^{(m)}(\gamma(\theta_l + \omega_l)) \right) \right. \\ &\quad \left. + \left(U_l^{(k)} - u^{(k)}(\gamma(\theta_l - \omega_l)) \right) \left(U_l^{(m)} - u^{(m)}(\gamma(\theta_l - \omega_l)) \right) \right]. \end{aligned}$$

In particular, \bar{F}'_{θ_l} and $\bar{F}'_{|E_l|}$ only differ by one sign in the sum. The Fréchet derivatives for the measurement operator can again be obtained by a multiplication with the particular currents, i.e.

$$\left(\bar{F}'_{\mathcal{I}, \theta_l} \right)_{k,m} = \left(\bar{F}'_{\theta_l} I^{(m)} \right)_k \quad \text{and} \quad \left(\bar{F}'_{\mathcal{I}, |E_l|} \right)_{k,m} = \left(\bar{F}'_{|E_l|} I^{(m)} \right)_k$$

for $k, l = 1, \dots, L$ and $m = 1, \dots, M$, respectively, where $\mathcal{I} = \{I^{(1)}, \dots, I^{(M)}\}$.

5. Problem-specific extensions to the inversion scheme

In chapter 4, the positivity constraint of the conductivity was treated by a suitable conductivity transformations. The linearization of the forward operator with respect to the electrode geometry brings a similar issue: One needs to make sure that the electrodes preserve positive size, do not change order, and do not overlap. To that end, we again consider *transformations from bounded to unbounded parameter spaces* which enforce these conditions. We want to perform electrode changes independently of the neighboring electrodes, thus we introduce barriers at the gap centers. The gap centers are parametrized by

$$\hat{\theta}_l = \frac{1}{2} [(\theta_{l+1} - \omega_{l+1}) - (\theta_l + \omega_l)].$$

This situation is depicted in Figure 5.2, where the electrode center and their parameters θ_l are depicted in red, while the gap centers and their parameters $\hat{\theta}_l$ are depicted in blue.

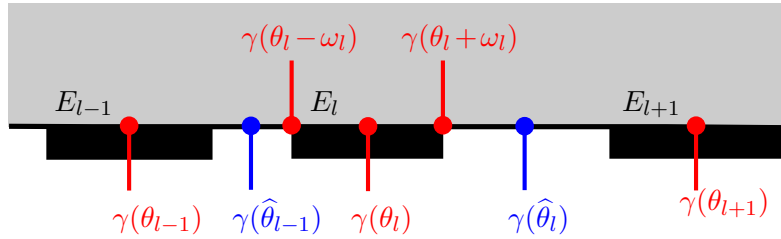


Figure 5.2.: Parametrization of the electrodes on the boundary. The gap centers $\hat{\theta}_1, \dots, \hat{\theta}_L$ will be the limits for the electrode movement and deformation in each Newton iteration.

Now we allow each electrode E_l , $l=1, \dots, L$, to move and change size within the boundary section

$$\{\gamma(\theta) : \hat{\theta}_{l-1} < \theta < \hat{\theta}_l\},$$

i.e. we want that the updated parameters $\theta_l^{(k+1)}$ and $\omega_l^{(k+1)}$ satisfy

$$\hat{\theta}_{l-1}^{(k)} < \theta_l^{(k+1)} - \omega_l^{(k+1)} < \theta_l^{(k+1)} + \omega_l^{(k+1)} < \hat{\theta}_l^{(k)} \quad (\text{modulo } |\partial\Omega|), \quad l = 1, \dots, L,$$

after the k -th Newton step. However, this is a coupled restriction for each electrode size and position. Thus, we further “split” this available space into one part for the electrode movement and another part for the electrode size change, as shown in Figure 5.3. Therein, the yellow sections of the boundary depict the parts of the boundary “reserved” for the electrode resizing, and the green sections depict the parts for the electrode movement.

For the electrode sizes and the parameters of the locations, we thus obtain restrictions from below and from above. One possibility to handle this restriction is to use a tangent-type transformation for the parameters, mapping the interval boundaries to $\pm\infty$. First, we introduce a lower bound $\zeta_l^{(k)}$

5. Problem-specific extensions to the inversion scheme

satisfying

$$0 < \zeta_l^{(k)} < \omega_l^{(k+1)}$$

for the updated half-width $w_l^{(k+1)}$ of the l -th electrode after the k -th iteration to ensure numerical stability for the FEM forward solutions¹. In our implementations, we use $\zeta_l^{(k)} := \frac{2}{3}\omega_l^{(k)}$. Moreover, let

$$\begin{aligned} \delta_l &= \frac{1}{2} \min \{ \widehat{\theta}_l - (\theta_l + \omega_l), (\theta_l - \omega_l) - \widehat{\theta}_{l-1} \} > 0, \\ \bar{\delta}_l &= \widehat{\theta}_l - \theta_l - \omega_l - \delta_l > 0, \quad \text{and} \\ \underline{\delta}_l &= \theta_l - \widehat{\theta}_{l-1} - \omega_l - \delta_l > 0 \quad (\text{all possibly modulo } |\partial\Omega|), \end{aligned}$$

for each $l = 1, \dots, L$. Using these quantities, we restrict the electrode movement in the k -th Newton step to

$$-\underline{\delta}_l^{(k)} + \theta_l^{(k)} < \theta_l^{(k+1)} < \bar{\delta}_l^{(k)} + \theta_l^{(k)} \quad (5.1)$$

and the electrode resizing to

$$\zeta_l^{(k)} < \omega_l^{(k+1)} < \omega_l^{(k)} + \delta_l^{(k)}. \quad (5.2)$$

In Figure 5.3, introduced quantities simply parametrize the boundaries of the yellow and green sections for the electrode resizing and movement, respectively.

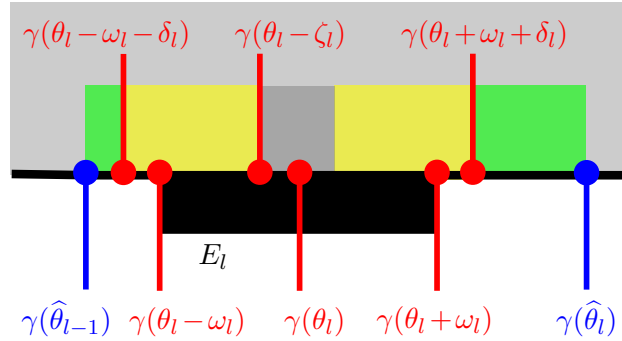


Figure 5.3.: Green: Reserved for electrode movement. Yellow: Reserved for electrode resizing. Dark gray: Preserved minimum electrode width in the k -th iteration.

¹The forward model might get unstable when electrodes or gaps shrink to a point.

5. Problem-specific extensions to the inversion scheme

One possibility for defining “tangent-type” transformation is to choose

$$t_{\theta_l, \tan}^{(k)}(\theta) = \tan \left(\frac{\pi}{\bar{\delta}_l^{(k)} + \underline{\delta}_l^{(k)}} \left(\theta + \underline{\delta}_l^{(k)} - \theta_l^{(k)} - \frac{\pi}{2} \right) \right)$$

for the position update and

$$t_{|E_l|, \tan}^{(k)}(\theta) = \tan \left(\frac{\pi}{\omega_l^{(k)} + \delta_l^{(k)} - \zeta_l^{(k)}} \left(\omega - \zeta_l^{(k)} \right) - \frac{\pi}{2} \right)$$

for size update of the l -th electrode in the k -th iteration, respectively. These transformations map the admissible interval for the position and size updates to the real line. As for the conductivity updates, the corresponding Fréchet derivatives in the transformed setting can be computed by (4.16).

We denote the corresponding (transformed) sensitivity matrices for the electrode position and size updates by $\bar{S}_\theta \in \mathbb{R}^{LM \times L}$ and $\bar{S}_{|E|} \in \mathbb{R}^{LM \times L}$, respectively, where

$$(\bar{S}_\theta)_l = \text{col} \left(\bar{F}'_{\mathcal{I}, \theta_l, \tan} \right) \quad \text{and} \quad (\bar{S}_{|E|})_l = \left(\bar{F}'_{\mathcal{I}, |E_l|, \tan} \right) \quad \text{for } l = 1, \dots, L,$$

respectively.

For convenience of notation, we moreover denote by $\bar{F}'_\sigma := F'_*$ the Fréchet derivative with respect to the (transformed) conductivity and by $\bar{S}_\sigma := S_*$ the corresponding sensitivity matrix.

5.1.2. Fréchet derivative with respect to the contact impedances

The differentiability of the forward operator with respect to the contact impedances is studied e.g. in [VKV⁺02]. In the notation of the previous section, the Fréchet derivative of the forward operator with respect to the contact impedance z_l of the l -th electrode is given by

$$\left(\frac{\partial}{\partial z_l} \bar{F} \right)_{k,m} := (\bar{F}'_{z_l})_{k,m} = -\frac{1}{z_l^2} \int_{E_l} \left(U_l^{(k)} - u^{(k)} \right) \left(U_l^{(m)} - u^{(m)} \right) \text{d}S,$$

where $(u^{(k)}, U^{(k)})$ is the solution of (2.17) for the current vector $I_\diamond^{(k)}$. The integral can be approximated with a quadrature rule on the point values of the FEM approximations of $u^{(k)}$ and $u^{(m)}$, $k, m = 1, \dots, L$. The positivity constraint can again be enforced with the log-transformation and the chain rule (4.16).

The corresponding (transformed) sensitivity matrix is denoted by \bar{S}_z .

5.1.3. Assembly of the sensitivity matrix and the weight matrix

To optimize for the conductivity, the electrode geometry, and the contact impedances simultaneously, the corresponding sensitivity matrices need to be concatenated in each Newton step. A crucial question is how to *weight* the optimization of the different unknowns against each other. For the

5. Problem-specific extensions to the inversion scheme

conductivity, we could come up with a natural weighting scheme (4.26) based on the reconstruction prior (4.21).

Due to the underdetermination, the weighting of conductivity updates versus changes of the boundary model forces us to make a design choice:

- If we have an accurate approximation of the true boundary geometry, then we should favor conductivity updates over geometry changes.
- If the boundary model is inaccurate, then we should allow for bigger changes in the boundary model.

This can be realized by specifying *penalty parameters*

$$w_\theta^{(k)} > 0, \quad w_{|E|}^{(k)} > 0, \quad \text{and} \quad w_z^{(k)} > 0,$$

in each iteration and defining weight matrices

$$\overline{W}_\theta^{(k)} = Lw_\theta^{(k)} \text{Id}_L, \quad \overline{W}_{|E|}^{(k)} = Lw_{|E|}^{(k)} \text{Id}_L, \quad \text{and} \quad \overline{W}_z^{(k)} = Lw_z^{(k)} \text{Id}_L.$$

Therein, the factor L can be considered as a normalization for the number of unknowns.

The same normalization should be applied to the diagonal weight matrix for the conductivity coefficients. For an arbitrary diagonal conductivity weight matrix $W = \text{diag}(w_1, \dots, w_P)$ (e.g. one of the weight matrices proposed in (4.27)), we define a normalized version

$$\overline{W}_\sigma = \left(\sum_{p=1}^P w_p \right) W.$$

For the combined vector of the conductivity update, electrode position updates, electrode size updates and contact impedance updates

$$\overline{\mathbf{s}}^{(k)} = (s_{\sigma_1}^{(k)}, \dots, s_{\sigma_P}^{(k)}; s_{\theta_1}^{(k)}, \dots, s_{\theta_L}^{(k)}; s_{|E_1|}^{(k)}, \dots, s_{|E_L|}^{(k)}; s_{z_1}^{(k)}, \dots, s_{z_L}^{(k)})^\top,$$

in the k -th Newton step, the combined sensitivity matrix reads

$$\overline{S}^{(k)} = \begin{pmatrix} \overline{S}_\sigma^{(k)} & \overline{S}_\theta^{(k)} & \overline{S}_{|E|}^{(k)} & \overline{S}_z^{(k)} \end{pmatrix}$$

and the combined weight matrix reads

$$\overline{W}^{(k)} = \begin{pmatrix} \overline{W}_\sigma^{(k)} & 0 & 0 & 0 \\ 0 & \overline{W}_\theta^{(k)} & 0 & 0 \\ 0 & 0 & \overline{W}_{|E|}^{(k)} & 0 \\ 0 & 0 & 0 & \overline{W}_z^{(k)} \end{pmatrix}.$$

Now, REGINN can be applied to $\overline{S}^{(k)}$ and $\overline{W}^{(k)}$ instead of $S_*^{(k)}$ and $W^{(k)}$ in each iteration to obtain the update coefficients $\overline{\mathbf{s}}^{(k)}$ for the conductivity, the electrode positions, the electrode sizes, and the

contact impedances simultaneously.

Lacking an explicit convergence result for this extended scheme, we can use the weights $w_\theta^{(k)}$, $w_{|E|}^{(k)}$, and $w_z^{(k)}$ to successively “stabilize” the boundary model. Our aim is to reduce the amount of change applied to the boundary model and freeze it completely after a certain amount of iterations. This means that the simultaneous reconstruction of conductivity and boundary model can be seen as a “pre-processing” step for the ICP.

To that end, we formally let

$$\begin{aligned} w_\theta^{(k)} &= \begin{cases} k^{\alpha_\theta} w_\theta^{(0)}, & 1 \leq k \leq K_\theta, \\ 0, & \text{otherwise,} \end{cases} \\ w_{|E|}^{(k)} &= \begin{cases} k^{\alpha_{|E|}} w_{|E|}^{(0)}, & 1 \leq k \leq K_{|E|}, \\ 0, & \text{otherwise,} \end{cases} \\ w_z^{(k)} &= \begin{cases} k^{\alpha_z} w_z^{(0)}, & 1 \leq k \leq K_z, \\ 0, & \text{otherwise,} \end{cases} \end{aligned}$$

for some penalty parameters $\alpha_\theta, \alpha_{|E|}, \alpha_z > 0$ and some stopping parameters $K_\theta, K_{|E|}, K_z \in \mathbb{N}$. The interpretation of $w_{(\cdot)}^{(k)} = 0$ is that the corresponding coefficient update vector $\bar{s}_{(\cdot)}^{(k)}$ and its sensitivity matrix $\bar{S}_{(\cdot)}^{(k)}$ are removed from the linearized system, respectively. The initial penalty parameters $w_\theta^{(0)}$, $w_{|E|}^{(0)}$, and $w_z^{(0)}$ should be chosen according to the accuracy of the initial guess of the boundary model.

Remark 5.3 (Design parameter choices for optimizing the boundary model). In our numerical experiments, we obtained good results using

$$w_\theta^{(0)} = w_{|E|}^{(0)} = 1, \quad w_z^{(0)} = 100, \quad \alpha_\theta = \alpha_{|E|} = \alpha_z = \frac{3}{2}, \quad \text{and} \quad K_\theta = K_{|E|} = K_z = 50.$$

This means that the penalty is increased for the first 50 steps. Afterwards, the optimization of the boundary model is stopped and the following Newton updates are only applied to the conductivity.

5.2. Sparsity and Banach space methods

Although the set of admissible conductivities $L_+^\infty(\Omega)$ is not a Hilbert space, we have so far considered the finite-dimensional discretized conductivity space $\mathcal{D}_{\mathcal{P}}$ and the space of the measurements $(\mathbb{R}_\diamond^L)^M$ equipped with Hilbert space structures. In particular, we made use of inner products and weighted L^2 -norms in the results of chapter 4.

5. Problem-specific extensions to the inversion scheme

Indeed, the reconstruction prior (4.21) was designed to avoid oscillations in the Newton updates, leading to smooth solutions which are characteristic for L^2 -type penalties: The Moore-Penrose pseudo-inverse minimizes the L^2 -norm over all solutions of the linear system, typically leading to smooth solutions with a fairly large support and thereby avoiding oscillatory solutions. However, solutions with small support and high peaks are also penalized. As a consequence, small-support inhomogeneities in the conductivity are usually not recovered accurately and rather “blurred out” in the reconstructions.

In some EIT applications, in particular in process tomography, the aim is to detect small-support inclusion, such as cracks or air bubbles, inside an otherwise homogeneous medium. In this case, it is natural to model the searched-for inclusions as elements of the Banach space $L^p(\Omega)$, $p \approx 1$.

The inexact Newton-type method REGINN for Banach spaces was considered, and a convergence and regularization analysis was established, in [Jin12, MRLa14, MR14] and in the PhD thesis [Mar15], to which the interested reader is referred to for details.

Some of the concepts of REGINN (and thus, of MANTIS) are easily translated to the L^p -space setting. For example, Morozov’s discrepancy principle (2.33) and the linear decrease criterion (2.32) can be formulated equivalently using the corresponding Banach space norms. However, some powerful tools like the conjugate gradient method rely on the structure of Hilbert spaces and are not available in Banach spaces. Consequently, they need to be substituted: For example, Newton updates satisfying the decrease criterion (2.32) in an L^p norm can be achieved by (usually much slower) gradient-based methods like the Landweber method, or by Tikhonov-type methods. The convergence analysis of these methods (see [Mar15] and the references therein) is more delicate and involves nontrivial maps (*duality maps*) between the Banach spaces and their duals.

The numerical examples presented in section 6.6 encourage that some techniques presented in this work, like the tailored discretizations of the conductivity space (chapter 3), the model-aware initialization of the background conductivity and the contact impedances (section 4.1), and the use of tailored weights (section 4.3) for the conductivity space², work well in the Banach spaces setting of REGINN. We present some reconstructions assuming $\sigma \in L^p(\Omega)$, $p = 1.1$, and once again refer to [Mar15] for further explanations and more numerical examples. For the linear problem, the iterated Tikhonov method is used with $\alpha = 0.1 \|\mathcal{I}\|_2$. Each Tikhonov minimizer is computed by a Landweber iteration with step size $0.001 \|\mathcal{I}\|_2^{-1}$.

²This might seem surprising at first glance since using these weights does not imply the reconstruction prior. In fact, the reconstruction prior is not desired in L^p , $p \approx 1$, settings where sparse updates are preferred. Nonetheless, we observe that using the weights (4.26) in Banach spaces reduces oscillations and artifacts in the reconstructions.

5.3. Iterated nonlinear filtering

The reconstruction prior (4.21) was formulated to avoid oscillatory conductivity updates. However, once oscillations are present in the conductivity iterate, they are typically not smoothed out afterwards (and even might be necessary for the convergence of the algorithm). Moreover, the reconstruction prior does not hold in Banach spaces, and it is not clear if the associated weights are optimal for reducing oscillations in this case.

To further reduce the amount of oscillations in the solution, while preserving the convergence of Newton's method, we can add an additional filtering step to each Newton iteration. To that end, line 12 of Algorithm 6 is replaced by

$$\sigma_*^{(k+1)} = \Phi^{(k)}(\sigma_*^{(k)} + \eta_*^{(k)}),$$

where $\Phi^{(k)}$ is series of (nonlinear) filters to suppress oscillations. To preserve convergence³, the changes made by the Newton update should “outweigh” the changes made by the filters. Hence, we require that

$$\left\| \Phi^{(k)}(\sigma_*^{(k)} + \eta_*^{(k)}) - (\sigma_*^{(k)} + \eta_*^{(k)}) \right\|_{(\mathbb{R}^P, \Omega)} \leq \alpha_\Phi^{(k)} \left\| \eta_*^{(k)} \right\|_{(\mathbb{R}^P, \Omega)}, \quad (5.3)$$

where $\{\alpha_\Phi^{(k)}\}_{k \in \mathbb{N}}$ is a decreasing zero sequence with $\alpha_\Phi^{(1)} \leq 1$, and

$$\|\sigma\|_{(\mathbb{R}^P, \Omega)}^2 = \sum_{p=1}^P \sigma_p^2 |\Omega_p| \quad \text{for } \sigma \in \mathbb{R}^P.$$

The coefficients $\alpha_\Phi^{(k)}$ can be chosen to control the desired amount of smoothing. In our numerical examples, we use $\alpha_\Phi^{(k)} = k^{-1/2}$.

In the following, we give two examples for such filters, namely *scaled median filters* and *anisotropic diffusion filters*.

Example 5.4 (Scaled median filtering). Median filtering is a simple technique commonly used in image processing for reducing highly oscillatory noise while preserving edges. In our setting, the idea is to replace each conductivity coefficient by the median of its neighbouring coefficients, i.e.

$$(\Phi(\sigma))_p = \text{median} \{ \sigma_q : \Omega_q \text{ is a neighbour of } \Omega_p \}.$$

The definition of a neighbour is not strict and depends on the geometry of the partition \mathcal{P} of Ω . For example, one could define a cell Ω_q as a neighbour of Ω_p if both cells share a common edge (or node). Each cell is typically defined to be its own neighbour. Alternatively, one could use a fixed number of “next neighbours” with minimum distance to

³We emphasize that this method is a heuristic, and no rigorous convergence theory is established in this work.

5. Problem-specific extensions to the inversion scheme

each cell. In MATLAB, this can be realized by the function `knnsearch` contained in the statistics and machine learning toolbox.

Then in each Newton step, $\Phi^{(k)}$ can be defined by

$$\Phi^{(k)}(\boldsymbol{\sigma}) = \lambda^{(k)}\Phi(\boldsymbol{\sigma}) + (1 - \lambda^{(k)})\boldsymbol{\sigma},$$

where $\lambda^{(k)} \in (0, 1]$ is chosen a-posteriori, i.e. the impact of the filtering is “scaled down” by a convex combination of the filtered and unfiltered conductivity such that (5.3) is satisfied.

A more sophisticated technique is given in the following example.

Example 5.5 (Anisotropic diffusion filter). Anisotropic diffusion is an increasingly popular technique for edge-preserving or edge-enhancing image denoising [Wei98]. To that end, we consider the solution $u \in C([0, T]; L^2(\Omega))$ of the partial differential equation

$$\partial_t u = \nabla \cdot D \nabla u, \quad u(0, \cdot) = \sigma, \quad D \nabla u|_{\partial\Omega} \cdot \nu = 0,$$

where $\sigma \in \mathcal{D}_{\mathcal{P}}$ is the continuum representation of a conductivity coefficient vector $\boldsymbol{\sigma}$, and D is a (inhomogeneous, anisotropic) diffusion tensor; see e.g. [Wei98, chapters 1.3.3, 2, 5.1] for details. In particular, D can be designed to suppress diffusion across edges of big conductivity changes, while allowing for diffusion along these edges and in regions where conductivity changes are small.

Given u , we let $\Phi^{(k)}(\boldsymbol{\sigma}) = \mathbf{u}(t^{(k)})$, where $\mathbf{u}(t)$ is the coefficient vector of a projection of $u(t)$ onto $\mathcal{D}_{\mathcal{P}}$. Since $u(t) \rightarrow \sigma$ as $t \rightarrow 0$, we can find a $t^{(k)} > 0$ a-posteriori such that (5.3) holds. In our “proof of concept” implementation, a finite difference scheme and the explicit Euler method with variable step size is used to evaluate u . The parameter $t^{(k)}$ is defined a-posteriori such that the Euler method stops one step before (5.3) is violated or when a maximum number of Euler steps is reached.

6. Numerical results

This chapter contains numerical experiments which complement the theoretical results presented in chapters 3–5. All computations are performed in the MANTIS framework (Algorithm 6). The 2D version of MANTIS was implemented as a “stand-alone” program in MATLAB (version R2013a and newer). A 3D version was integrated in the developer version of the open source MATLAB toolbox EIDORS [PL02] under GNU General Public Licence. It is available, along with several test scripts demonstrating how to use the MANTIS code in EIDORS, at SourceForge under <http://eidors3d.sourceforge.net>.

The code is written with a focus on ease-of-use rather than performance. Still, the 2D implementation can be used on any typical notebook or desktop computer, whereas at least 8 GB of RAM are recommended for 3D reconstructions in EIDORS. All results presented in this chapter were performed on, and the listed computation times refer to, an Intel i7-2720QM CPU (4 cores at 2.20 GHz) and 16 GB of RAM.

In section 6.1, we introduce several simulated and real-world measurement settings. To demonstrate the versatility of the MANTIS framework, the simulated settings cover various scenarios. These include convex and non-convex domains, varying numbers of electrodes, and different high and low contrast conductivities with small and large inclusions inside constant or non-constant background conductivities. The real-world measurements were kindly provided by Aku Seppänen (University of Eastern Finland) and Stratos Staboulis (Aalto University) [DHSS13b] and by the Rensselaer group [IMNS04].

All reconstructions use the parameter-free initialization for the contact impedances $z^{\text{CEM},z}$, the initial conductivity estimate $\sigma^{\text{CEM},z}$ (Definition 4.4), and the noise estimate δ^{CEM} (eqn. 4.12) derived in section 4.1. The 2D reconstructions use adaptive triangulations, as presented in section 3.5.4, both for the FEM computation and for the discretization of the conductivity space \mathcal{D}_P , unless stated otherwise. The number of triangles P is chosen dynamically depending on the number of electrodes L such that

$$P \approx 400L.$$

For the simulated experiments, the relative error e_{rel} between the reconstructed conductivity σ and

6. Numerical results

the exact conductivity σ_{exact} is computed numerically as

$$e_{\text{rel}} = \frac{1}{|\Delta_{\text{err}}|} \int_{\Delta_{\text{err}}} \frac{|P_{\Delta_{\text{err}}}\sigma_{\text{rec}}(x) - P_{\Delta_{\text{err}}}\sigma(x)|}{|P_{\Delta_{\text{err}}}\sigma(x)|} dx, \quad (6.1)$$

where $P_{\Delta_{\text{err}}}$ is a piecewise constant interpolation on a very fine triangulation Δ_{err} of Ω with roughly 30000–50000 triangles, and $|\Delta_{\text{err}}|$ is its total area.

In section 6.2, the impact of the weighted conductivity spaces and the conductivity transformations on the speed and quality of the reconstructions is investigated. Section 6.3 shows reconstructions of 3D models using the EIDORS implementation of MANTIS. In section 6.4, the performance of different discretizations of the conductivity space is compared. Next, we present reconstructions incorporating the recovery of model parameters, the use of sparsity promoting Banach space models, and the effect of iterated nonlinear filtering in sections 6.5, 6.6 and 6.7, respectively. Finally, we present the performance of MANTIS for measured data from saline tank experiments in section 6.8.

6.1. Numerical settings

We now introduce the settings used for the numerical experiments. All settings are denoted by a capital letter followed by a number indicating the number of electrodes; e.g. “X.16” denotes setting X with a 16 electrode configuration. If not stated otherwise, the electrodes in the 2D settings are of equal size and equally distributed along the boundary, and cover 50% of the boundary surface, i.e.

$$|E_l| = \frac{1}{2L} |\partial\Omega|, \quad l = 1, \dots, L,$$

and the contact impedances are set to

$$z_l = 0.05, \quad l = 1, \dots, L,$$

to be of roughly the same order as the values observed in the tank experiments. Measurement data is simulated for a full set of $L = M$ adjacent currents, $\mathcal{I} = \mathcal{I}_{\text{adj}} \in (\mathbb{R}_{\neq}^L)^L$, unless stated otherwise.

For simulated data, we will consider setups with 16, 32 or 64 electrodes and noise levels of $\delta^{\text{rel}} = 0.3\%$, $\delta^{\text{rel}} = 0.2\%$ and $\delta^{\text{rel}} = 0.1\%$, respectively¹.

Recall that noisy data is simulated by the noise model (2.20) described in section 2.2.2. For each setting, one independent sample of normal-distributed pseudo-random noise is generated using the MATLAB function `rand` (Mersenne twister) with different seeds. As seeds we use three-digit numbers, where the first digit is the number of the setting and the other digits are the number of electrodes, e.g. $\text{seed}_{\text{A.16}} = 116$ for setting A.16.

¹To simulate “moderate”, “good” and “very good” measurement equipment, respectively.

6. Numerical results

To avoid inverse crime, the noise-free measurement data is simulated on a much finer FEM mesh with ≈ 50000 triangles, which is *not* a refinement of the meshes used for the inversion in MANTIS. In settings A and B presented in the following, the analytic Fourier based method of section 3.2 is used to generate the data.

Throughout all examples, we observed that for the 16 electrode case (256 potential measurements, ≈ 6000 triangles), the FEM computation time T_{FEM} (in seconds) dominates over the assembly time T_{jac} of the Jacobian and the computation time T_{linear} of the linearized problem. For the 32 and 64 electrode cases, the assembly time of the Jacobian is generally more costly in our MATLAB implementation.

6.1.1. Setting A: Circular perturbation inside the unit disk

In setting A, we consider a homogeneous background conductivity on the unit disk

$$\Omega_A = B_1(0) \subset \mathbb{R}^2$$

with a circular perturbation, i.e.

$$\sigma_A = 0.25 \left(1 + 10 \chi_{B_{r_A}(x_A)} \right), \quad \text{where } x_A = 0.4 \begin{pmatrix} 1/\sqrt{2} \\ 1/\sqrt{2} \end{pmatrix} \quad \text{and } r_A = 0.25.$$

Setting A.16 is displayed in Figure 6.1. The advantage of this setting is that the data can be generated using the analytic Fourier approach, thus completely avoiding inverse crime. Table 6.1 shows the absolute noise levels δ and the resulting MANTIS initializations δ^{CEM} (equation (4.12)), $\sigma^{\text{CEM},z}$ and $z^{\text{CEM},z}$ (Definition 4.4), as well as the number of Fourier coefficients N^w (equation (3.34)) for computing the analytic forward solution.

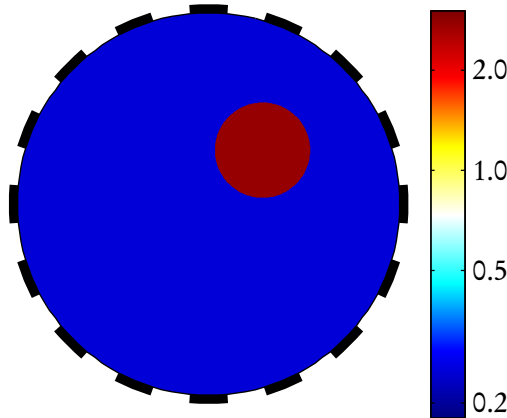


Figure 6.1.: Setting A.16: Circular conducting inclusion inside the unit disk.

6. Numerical results

Setting	δ^{rel}	δ	δ^{CEM}	$z^{\text{CEM},z}$	$\sigma^{\text{CEM},z}$	N^ω
A.16	0.3%	3.77×10^{-2}	4.03×10^{-2}	1.26×10^{-1}	2.77×10^{-1}	3585
A.32	0.2%	3.88×10^{-2}	3.57×10^{-2}	9.18×10^{-2}	2.73×10^{-1}	6172
A.64	0.1%	3.14×10^{-2}	3.35×10^{-2}	7.35×10^{-2}	2.70×10^{-1}	11345

Table 6.1.: Relative noise δ^{rel} , resulting noise level δ and the resulting MANTIS initializations δ^{CEM} , $z^{\text{CEM},z}$ and $\sigma^{\text{CEM},z}$ for setting A. N^ω denotes the number of Fourier coefficients (cf. eqn. 3.34) for computing the analytic forward solutions.

Since the inclusion has a higher conductivity than the background, we observe that the background conductivity is slightly over-estimated, and the contact impedances are also over-estimated. The noise level estimate is very accurate in all cases. Recall that independent realizations of pseudo-random noise are used for each setting.

6.1.2. Setting B: Thorax cross-section

Setting B resembles the cross-section of a human thorax with a highly conductive inclusion (“heart”, $\sigma = 0.75$), two resistive inclusions (“lungs”, $\sigma = 0.24$), and one highly resistive inclusion (“spine”, $\sigma = 0.05$) in an otherwise homogeneous background (“soft tissue”, $\sigma = 0.42$). The conductivity values are chosen to agree with those of the experimental setup [IMNS04] (this setup will be presented later). The domain Ω_B is scaled to fit into the square $[-1, 1]^2$. Setting B.16 is depicted in Figure 6.2(a).

Since the exact geometry is often unknown in practical applications, we will also perform reconstructions on a “generic” ellipsoidal approximation shown in Figure 6.2(b), denoted by \underline{B} . The domain $\Omega_{\underline{B}}$ is scaled such that $|\partial\Omega_B| = |\partial\Omega_{\underline{B}}|$. The corresponding MANTIS initializations are shown in Table 6.2.

Setting	δ^{rel}	δ	δ^{CEM}	$z^{\text{CEM},z}$	$\sigma^{\text{CEM},z}$
B.16	0.3%	2.55×10^{-2}	2.59×10^{-2}	4.08×10^{-3}	3.42×10^{-1}
B.32	0.2%	2.62×10^{-2}	2.90×10^{-2}	2.45×10^{-2}	3.48×10^{-1}
B.64	0.1%	2.08×10^{-2}	2.10×10^{-2}	3.71×10^{-2}	3.55×10^{-1}
\underline{B} .16	0.3%	2.55×10^{-2}	2.59×10^{-2}	2.31×10^{-5}	3.28×10^{-1}
\underline{B} .32	0.2%	2.62×10^{-2}	2.90×10^{-2}	8.91×10^{-3}	3.34×10^{-1}
\underline{B} .64	0.1%	2.08×10^{-2}	2.10×10^{-2}	2.95×10^{-2}	3.42×10^{-1}

Table 6.2.: MANTIS initializations for the thorax model (setting B, cf. Figure 6.2) and its approximation on an ellipse (setting \underline{B}). The estimates of the contact impedances (5.00×10^{-2}) and the background conductivity (4.20×10^{-1}) are more accurate for the exact model and when increasing the number of electrodes.

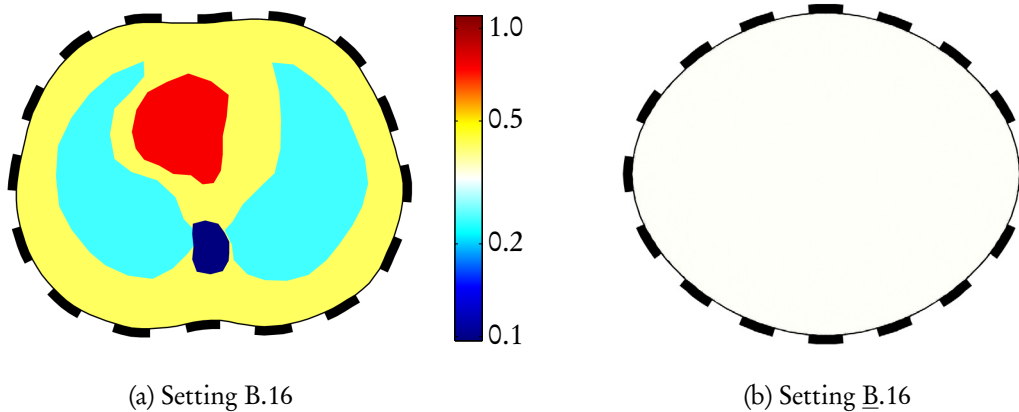


Figure 6.2.: Settings B.16 and B.16: 2D model of a human thorax (soft tissue, lungs, heart, spine) and an ellipsoidal approximation to the geometry for inversion.

6.1.3. Setting C: Mixed backgrounds and contrasts

Setting C is an “artificial benchmark” for evaluating the ability of MANTIS to recover conductivities with high- and low-contrast inclusions inside a non-homogeneous background. The domain is again the unit disk $\Omega_C = B_1(0)$. It contains high-contrast inclusions of varying shape and distance to the boundary. The background is split into two parts with different conductivity values. Setting C.16 is shown in Figure 6.3.

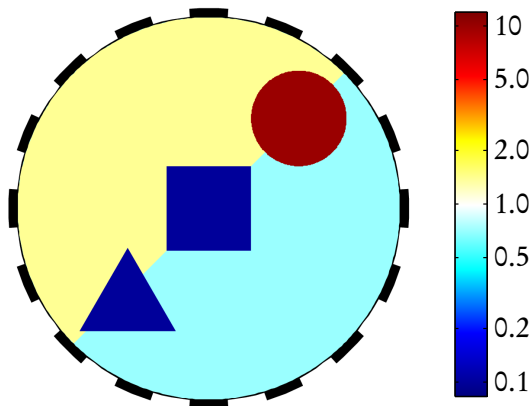


Figure 6.3.: Setting C.16: “Synthetic benchmark” conductivity with two background parts ($\sigma = \sqrt{2}$ top-left, $\sigma = 1/\sqrt{2}$ bottom-right), two highly resistive inclusions ($\sigma = 0.1$, bottom-left and center) and one highly conducting inclusion ($\sigma = 10$, top-right).

The discontinuous background poses a particular difficulty for inversion. In fact, many theoretical

6. Numerical results

results require the conductivity to be constant² or smooth³ in a neighborhood of the boundary $\partial\Omega$. The MANTIS initializations for this setting are listed in Table 6.3.

Setting	δ^{rel}	δ	δ^{CEM}	$z^{\text{CEM},z}$	$\sigma^{\text{CEM},z}$
C.16	0.3%	1.26×10^{-2}	1.20×10^{-2}	4.82×10^{-2}	8.83×10^{-1}
C.32	0.2%	1.45×10^{-2}	1.50×10^{-2}	5.07×10^{-2}	8.96×10^{-1}
C.64	0.1%	1.42×10^{-2}	1.42×10^{-2}	5.08×10^{-2}	9.08×10^{-1}

Table 6.3.: MANTIS initializations for setting C. The initial conductivity value $\sigma^{\text{CEM},z}$ lies in the interval $[1/\sqrt{2}, \sqrt{2}]$ of the two background values in all cases (cf. Figure 6.3).

6.1.4. Setting D: Non-convex domain with a non-convex inclusion

Setting D is an L-shaped domain with $|\partial\Omega_D| = 8$. The conductivity consists of a circular conducting inclusion ($\sigma = 4$) and a resistive annular inclusion ($\sigma = 1/4$) inside a unit background ($\sigma = 1$). Setting D.16 is depicted in Figure 6.4. The MANTIS initializations are listed in Table 6.4.

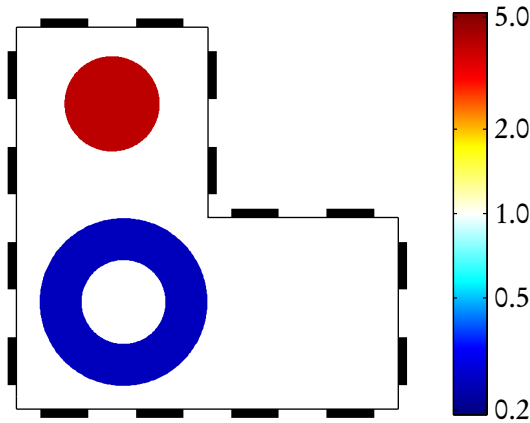


Figure 6.4.: Setting D.16: Non-convex domain with non-convex (annular) resistive inclusion ($\sigma = 1/4$) and circular conducting inclusion ($\sigma = 4$) inside a homogeneous background ($\sigma = 1$).

Setting	δ^{rel}	δ	δ^{CEM}	$z^{\text{CEM},z}$	$\sigma^{\text{CEM},z}$
D.16	0.3%	1.22×10^{-2}	1.39×10^{-2}	3.94×10^{-2}	8.39×10^{-1}
D.32	0.2%	1.41×10^{-2}	1.40×10^{-2}	4.45×10^{-2}	8.57×10^{-1}
D.64	0.1%	1.26×10^{-2}	1.23×10^{-2}	4.70×10^{-2}	8.78×10^{-1}

Table 6.4.: MANTIS initializations for setting D.

²CGO solutions, see e.g. [MS12, Chapter 14.3]

³Factorization method for the CEM, see e.g. [LHH08, section 2]

6.1.5. Setting E: 3D thorax model

To perform 3D reconstructions from simulated 3D data, the MANTIS framework was implemented in the open source MATLAB toolbox EIDORS. EIDORS is available under GPL version 2 or 3 at <http://eidors3d.sourceforge.net/>. In release 3.8, the MANTIS implementation can be found in the subfolder `dev/r_winkler/`. EIDORS uses the Netgen mesh generator which is available under LGPL at <http://sourceforge.net/projects/netgen-mesher>.

Setting E is a 3D model of the thorax of a pig. It was generated by extruding the geometry of a cross-section of the pigs chest. The shape was obtained “by hand” from the 2D computed tomography (CT) image shown in Figure 6.5 (top left). Inside this domain ($\sigma = 0.42$), a “lung” phantom ($\sigma = 0.24$) was generated by extruding the lung shape from the CT image, and a “heart” phantom ($\sigma = 0.75$) was modelled as an ellipsoid. On the boundary, 3 layers of 20 square-shaped electrodes each are modelled. Figure 6.5 shows a FEM discretization of this setting (bottom left) and a cross-sections of the model at each electrode plane (right).

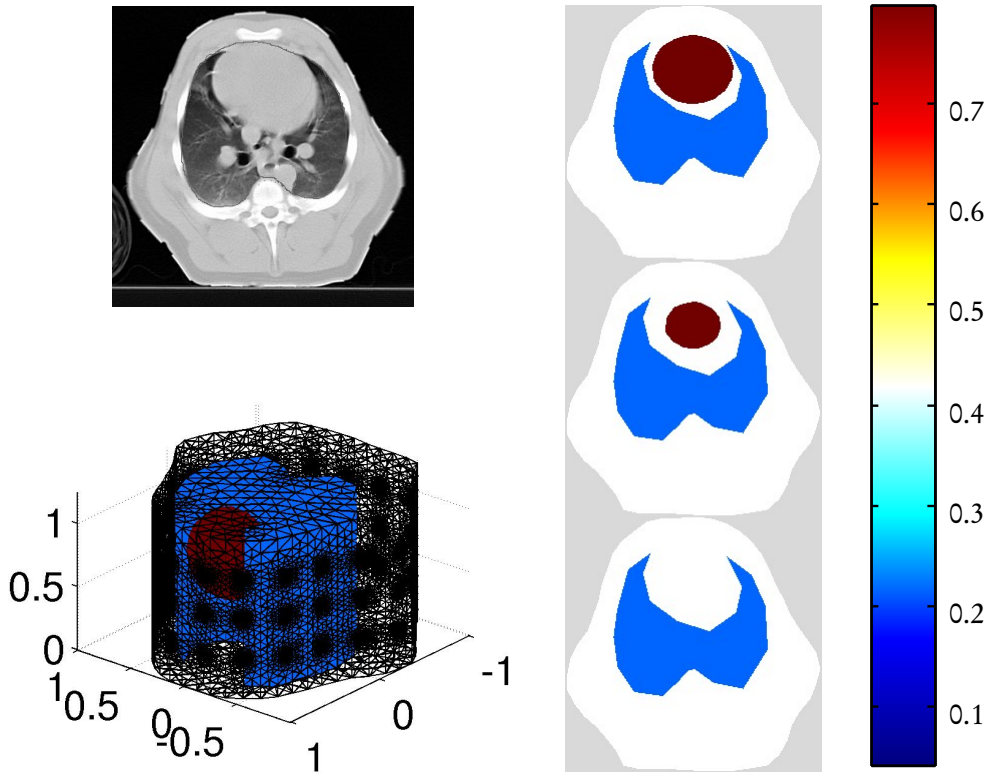


Figure 6.5.: Setting E. Top left: CT image of a pig thorax. Bottom left: Extruded 3D model from the shapes obtained from the CT image. Right: Horizontal slices through the 3D model at the center of each electrode ring.

The CT image of the pig was contributed to EIDORS by Marc Bodenstern (Universität Mainz). The MATLAB code for generating extruded FEM models was contributed by Bartłomiej Grychtol et al.; see [GLB⁺12]. The relative noise level was set to $\delta_E^{\text{rel}} = 0.1\%$. The contact impedances for the

6. Numerical results

simulation were set to $z_l = |E_l| = 0.0025$, $l = 1, \dots, L$, in this setting. The corresponding MANTIS initializations for different FEM discretizations are given in Table 6.5.

Setting	δ^{rel}	δ	δ^{CEM}	$ \Delta $	$z^{\text{CEM},z}$	$\sigma^{\text{CEM},z}$
E	0.1%	1.02×10^{-2}	9.31×10^{-2}	116311	3.51×10^{-3}	4.12×10^{-1}
				73557	3.33×10^{-3}	3.86×10^{-1}
				48560	1.60×10^{-3}	3.35×10^{-1}

Table 6.5.: MANTIS initializations for setting E, using 3 rings of 20 electrodes each. The background conductivity is $\sigma = 0.42$, the contact impedances are $z_l = 2.5 \times 10^{-3}$, $l = 1, \dots, L$. The noise level estimate δ^{CEM} is independent of the FEM refinement.

6.1.6. Setting F: Saline tank experiments, part 1

The following two settings F and G use measured data from saline tank experiments. Here, it is particularly convenient that the MANTIS framework has no problem-specific regularization parameters: It can be applied “out of the box” to all measurement settings, independently of their physical dimensions, their conductivities, their measurement equipments, or the applied current patterns.

Setting F is a tank experiment using data contributed to EIDORS by Jon Newell and David Isaacson. The measurement system is called *Rensselaer Adaptive Current Tomography (ACT 3)*. It applies trigonometric current patterns and measures potentials at 32 electrodes simultaneously at a single frequency (28.8 kHz). Details about the system can be found in [ESNI95].

The saline tank has a diameter of 30 cm. Each electrode is rectangular of height 1.6 cm and width 2.5 cm. The saline conductivity is $\sigma = 0.42$ S/m (Siemens per meter). Two agar phantoms representing lungs ($\sigma = 0.24$ S/m) and one agar phantom representing the heart ($\sigma = 0.75$ S/m) are placed inside the saline. The setting is shown in Figure 6.6. Details about the setting can be found in [IMNS04].

The MANTIS initializations are listed in Table 6.6. The contact impedances of this setting are very small, so the minimum value $z = z_{\min} = 2.5 \times 10^{-4}$ is attained. The estimated absolute noise level $\delta^{\text{CEM}} = 6.16 \times 10^{+0}$ corresponds to an estimated relative noise level of roughly⁴ 0.48%.

⁴Note that this noise level is not directly comparable to noise levels for adjacent currents, as measurements from trigonometric currents contain “more data” in some sense than measurements from adjacent currents. See [CSI⁺90] for details.

6. Numerical results

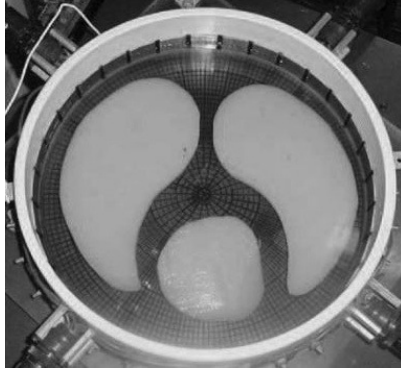


Figure 6.6.: Setting F: Saline tank with agar phantoms resembling a lung and a heart. 32 electrodes are attached to the tank surface.

Setting	$(\delta^{\text{rel}})^{\text{CEM}}$	δ^{CEM}	$z^{\text{CEM},z}$	$\sigma^{\text{CEM},z}$
F	0.48%	$6.16 \times 10^{+0}$	2.50×10^{-4} ^[1]	2.98×10^{-1}

^[1]Initialized to z_{min} .

Table 6.6.: MANTIS initializations for the saline tank experiment by Isaacson et al. [IMNS04]. The estimated relative noise level $(\delta^{\text{rel}})^{\text{CEM}}$ was computed from δ^{CEM} and the voltage amplitudes.

6.1.7. Setting G: Saline tank experiments, part 2

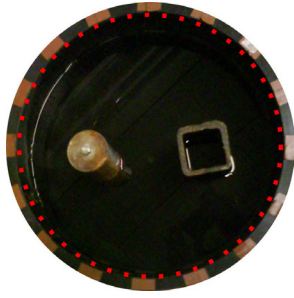
Setting G consists of various saline tank (86–106 cm circumference) experiments from data kindly provided by Aku Seppänen (University of Eastern Finland) and Stratos Staboulis (Aalto University). 16 electrodes of height 5–7 cm and width 2–2.5 cm are used in each experiment, to which 15 pair-wise currents are applied with one fixed “driving” electrode, i.e. the current frame is

$$\mathcal{I} = \left(\left(\begin{array}{c} 1 \\ -1 \\ 0 \\ \vdots \\ 0 \end{array} \right), \left(\begin{array}{c} 1 \\ 0 \\ -1 \\ \vdots \\ 0 \end{array} \right), \dots, \left(\begin{array}{c} 1 \\ 0 \\ 0 \\ \vdots \\ -1 \end{array} \right) \right).$$

Inside the saline, highly conductive (metal) and highly resistive (plastic) objects are placed. More details about the settings can be found in [DHSS13b]. The considered measurement setups are shown in Figure 6.7. They are denoted by setting G.I–G.V, respectively.

The corresponding initializations are listed in Table 6.7. We observe that the relative measurement error of the equipment in these experiments is roughly 0.25–0.50%, and that the contact impedances are very small in settings G.II–V, but quite large in setting G.I. We also note that the two resistive inclusions in setting G.III lead to a lower initial conductivity guess, compared to the other settings.

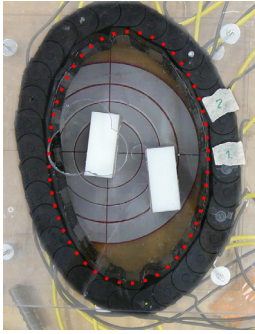
6. Numerical results



(a) Setting G.I (two conductive inclusions), circular boundary approximation.



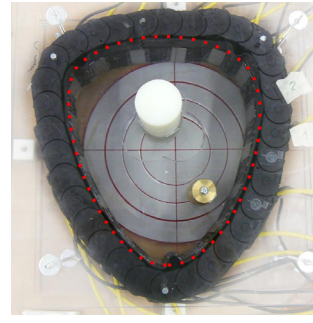
(b) Setting G.II (resistive and conductive inclusion), elliptical boundary approximation.



(c) Setting G.III (two resistive inclusions), elliptical boundary approximation.



(d) Setting G.IV (conductive and resistive inclusion), elliptical boundary approximation.



(e) Setting G.V (resistive and conductive inclusion), 3-point Bézier curve "smoothed triangle" approximation.

Figure 6.7.: Settings G.I–V: Tank experiments with 16 electrodes. The red dotted lines mark the boundary of the approximate geometry which is used for inversion. In the inversion model, the electrodes are placed equispaced along the boundary.

Setting	$(\delta^{\text{rel}})^{\text{CEM}}$	δ^{CEM}	$z^{\text{CEM},z}$	$\sigma^{\text{CEM},z}$
G.I	0.25%	1.43×10^{-2}	8.58×10^{-1}	2.64×10^{-1}
G.II	0.27%	1.98×10^{-2}	2.00×10^{-4} [1]	2.30×10^{-1}
G.III	0.47%	2.22×10^{-2}	2.00×10^{-4} [1]	2.09×10^{-1}
G.IV	0.46%	1.89×10^{-2}	3.99×10^{-2}	2.75×10^{-1}
G.V	0.39%	1.55×10^{-2}	2.00×10^{-4} [1]	2.55×10^{-1}

[1] Initialized to z_{\min} .

Table 6.7.: MANTIS initializations for the saline tank experiment by Isaacson et al. [IMNS04]. The approximate relative noise levels $(\delta^{\text{rel}})^{\text{CEM}}$ were computed from δ^{CEM} and the voltage amplitudes.

6.2. Impact of the conductivity transformation and the weights

As discussed in section 4.3, the linear system in each Newton iteration is usually highly underdetermined. The norm of the discretized conductivity space thus influences the pseudo-inverse solution, which is approximated by the regularization scheme.

In this section, MANTIS reconstructions for settings A–D are presented using identity weights W_{Id} , sensitivity-normalized weights W_{S^*} , conductivity-normalized weights W_{σ} and sensitivity and conductivity normalized weights $W_{S^*,\sigma}$, cf. equations (4.27) and (4.31).

To distinguish the individual and combined impacts of using weighted spaces and applying conductivity transformations, all combinations of weights and the conductivity transformations t_{Id} , t_{\log} , $t_{\hat{\alpha}}$ and t_{\dagger} (cf. Table 4.5) are applied to settings A and B.

Since we observe that the results for the tan-log-transform are almost identical to those of the log-transform, they are omitted in the tables and figures for the sake of clarity.

6.2.1. Results for setting A

Figure 6.8 shows reconstructions from setting A.32, i.e. data generated by the Fourier approach for $L=32$ electrodes and artificial noise $\delta^{\text{rel}}=0.2\%$. It is clearly visible that using W_{S^*} and $W_{S^*,\sigma}$ reduces oscillations in the solution; cf. Definition 4.9. We also note that the solution with the smallest error (6.8(f)) does not necessarily lead to the best visual result.

Figure 6.9 shows reconstructions using $t_{\hat{\alpha}}$ and $W_{S^*,\sigma}$ for various electrode numbers and noise levels. Increasing the number of electrodes only improves the reconstruction result in this setting if the noise level also decreases.

Tables 6.8–6.10 give further information about the performance of MANTIS for settings A.16, A.32, and A.64, respectively. We observe that the number of Newton iterations k_* usually decreases when using conductivity transformations, and that the accumulated number of cg iterations $\sum_{k=1}^{k_*} l^{(k)}$ decreases when using weighted conductivity norms.

Note that, as mentioned in section 4.3.3, the conductivity scaling in W_{σ} and $W_{S^*,\sigma}$ is cancelled out when using the log-transform, thus the corresponding reconstructions are identical (up to some variation in the computation time) to those of W_{Id} and W_{S^*} , respectively.

6. Numerical results

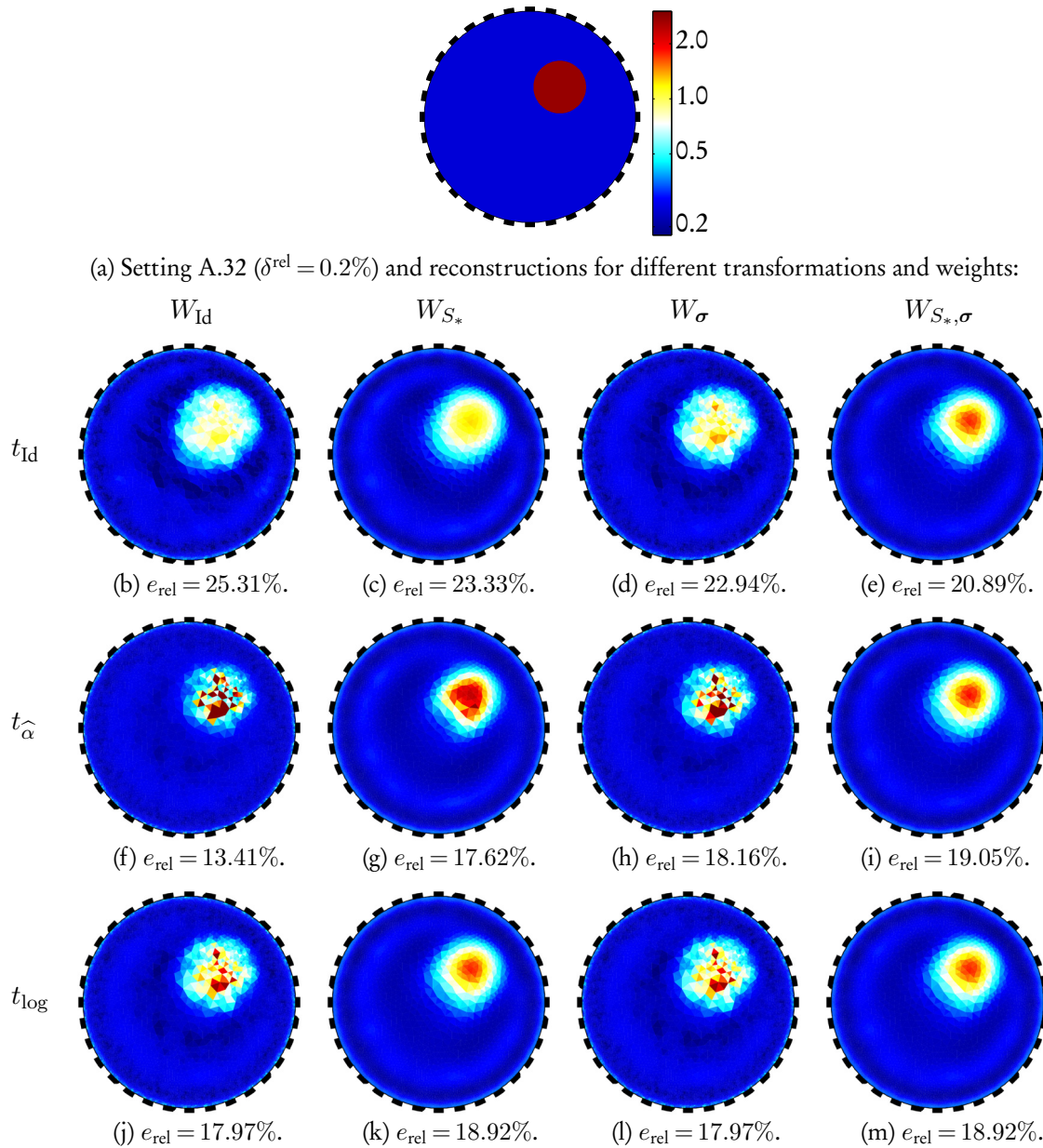


Figure 6.8.: Reconstructions from setting A.32. Using weights containing S_* reduces oscillations drastically.

6. Numerical results

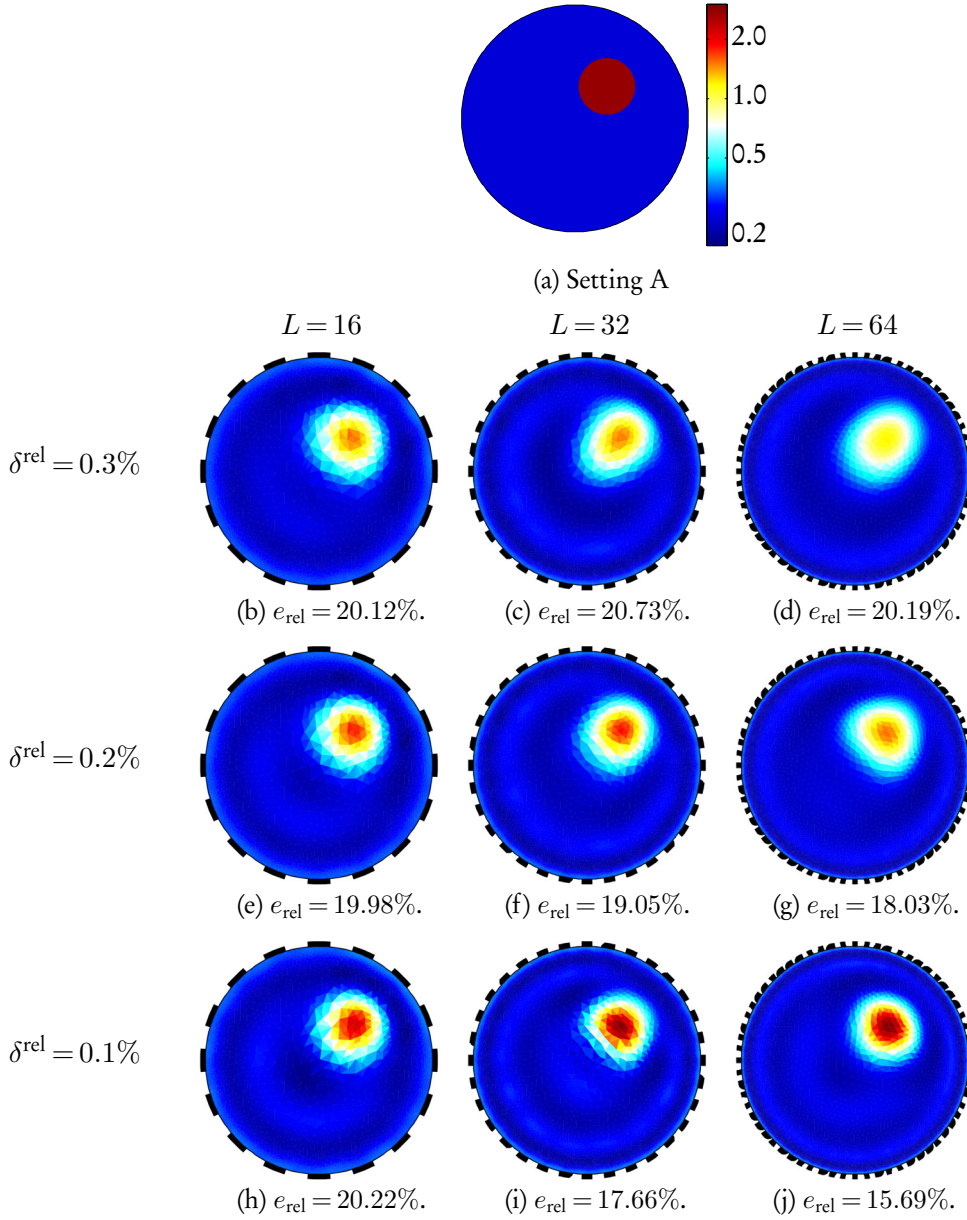


Figure 6.9.: Impact of increasing the number of electrodes and reducing the noise level. Increasing the number of electrodes only improves the reconstruction if the noise level decreases. Conductivity transformation: $t_{\hat{\alpha}}$. Weights: $W_{S_*,\sigma}$.

6. Numerical results

t_*	W	$e_{\text{rel}} (\%)$	k_*	$\sum_{k=1}^{k_*} l^{(k)}$	$\min(\sigma)$	$\max(\sigma)$	$T_{\text{FEM}} (\text{s})$	$T_{\text{jac}} (\text{s})$	$T_{\text{linear}} (\text{s})$
t_{Id}	W_{Id}	25.31	14	56	9.07×10^{-2}	9.39×10^{-1}	0.70	0.71	0.13
t_{Id}	W_{S_*}	23.33	11	43	1.54×10^{-1}	$1.00 \times 10^{+0}$	0.65	0.58	0.10
t_{Id}	W_{σ}	22.94	11	49	1.46×10^{-1}	$1.23 \times 10^{+0}$	0.53	0.50	0.11
t_{Id}	$W_{S_*, \sigma}$	20.89	10	37	1.80×10^{-1}	$1.43 \times 10^{+1}$	0.53	0.47	0.09
\hat{t}_{α}	W_{Id}	16.89	11	32	1.97×10^{-1}	9.39×10^{-1}	0.54	0.48	0.09
\hat{t}_{α}	W_{S_*}	17.84	9	31	2.00×10^{-1}	$3.01 \times 10^{+0}$	0.44	0.38	0.08
\hat{t}_{α}	W_{σ}	18.15	11	36	1.91×10^{-1}	$6.33 \times 10^{+0}$	0.54	0.48	0.09
\hat{t}_{α}	$W_{S_*, \sigma}$	20.12	10	36	1.87×10^{-1}	$1.56 \times 10^{+0}$	0.49	0.43	0.09
t_{log}	W_{Id}	20.33	12	44	1.78×10^{-1}	$2.52 \times 10^{+0}$	0.63	0.58	0.10
t_{log}	W_{S_*}	20.51	10	36	1.84×10^{-1}	$1.51 \times 10^{+0}$	0.55	0.49	0.08
t_{log}	W_{σ}	20.33	12	44	1.78×10^{-1}	$2.52 \times 10^{+0}$	0.56	0.53	0.10
t_{log}	$W_{S_*, \sigma}$	20.51	10	36	1.84×10^{-1}	$1.51 \times 10^{+0}$	0.49	0.45	0.09

Table 6.8.: **Setting A.16:** Reconstruction properties of MANTIS with $\delta^{\text{rel}} = 0.3\%$ for various conductivity transformations t_* and conductivity weights W . The columns display the relative error e_{rel} (in percent, cf. eqn. (6.1)), the number of Newton iterations k_* , the number of accumulated inner (cg) iterations, and the minimum and maximum of the recovered conductivity. The correct minimum and maximum of the conductivity in this setting is $\min(\sigma) = 2.5 \times 10^{-1}$ and $\max(\sigma) = 2.25 \times 10^{+0}$, respectively. The last three columns show the accumulated computation time (MATLAB implementation, in seconds) T_{FEM} for solving the forward problems, T_{jac} for assembling the Jacobian, and T_{linear} for solving the linear problem (cg iterations), respectively.

t_*	W	$e_{\text{rel}} (\%)$	k_*	$\sum_{k=1}^{k_*} l^{(k)}$	$\min(\sigma)$	$\max(\sigma)$	$T_{\text{FEM}} (\text{s})$	$T_{\text{jac}} (\text{s})$	$T_{\text{linear}} (\text{s})$
t_{Id}	W_{Id}	24.22	17	140	1.00×10^{-2}	$1.11 \times 10^{+0}$	2.22	5.60	2.08
t_{Id}	W_{S_*}	22.01	14	92	1.76×10^{-1}	$1.26 \times 10^{+0}$	1.83	5.52	1.36
t_{Id}	W_{σ}	21.43	15	108	1.17×10^{-1}	$1.48 \times 10^{+0}$	1.93	4.90	1.59
t_{Id}	$W_{S_*, \sigma}$	18.95	14	78	1.88×10^{-1}	$1.77 \times 10^{+0}$	1.83	4.59	1.14
\hat{t}_{α}	W_{Id}	13.41	15	79	1.94×10^{-1}	$9.21 \times 10^{+0}$	1.95	4.88	1.13
\hat{t}_{α}	W_{S_*}	17.62	14	64	2.00×10^{-1}	$2.74 \times 10^{+0}$	1.79	3.47	1.01
\hat{t}_{α}	W_{σ}	15.25	13	68	1.82×10^{-1}	$7.50 \times 10^{+0}$	1.70	4.21	1.00
\hat{t}_{α}	$W_{S_*, \sigma}$	19.05	13	73	1.92×10^{-1}	$1.86 \times 10^{+0}$	1.69	4.21	1.11
t_{log}	W_{Id}	17.97	13	84	1.62×10^{-1}	$3.69 \times 10^{+0}$	1.75	4.21	1.15
t_{log}	W_{S_*}	18.92	13	73	1.90×10^{-1}	$1.80 \times 10^{+0}$	1.69	4.18	1.08
t_{log}	W_{σ}	17.97	13	84	1.62×10^{-1}	$3.69 \times 10^{+0}$	1.72	4.25	1.23
t_{log}	$W_{S_*, \sigma}$	18.92	13	73	1.90×10^{-1}	$1.80 \times 10^{+0}$	1.72	4.24	1.09

Table 6.9.: **Setting A.32:** Reconstruction properties of MANTIS for $\delta^{\text{rel}} = 0.2\%$ (columns as in Table 6.8).

6. Numerical results

t_*	W	$e_{\text{rel}} (\%)$	k_*	$\sum_{k=1}^{k_*} l^{(k)}$	$\min(\sigma)$	$\max(\sigma)$	$T_{\text{FEM}} (\text{s})$	$T_{\text{jac}} (\text{s})$	$T_{\text{linear}} (\text{s})$
t_{Id}	W_{Id}	21.65	18	153	9.35×10^{-2}	$1.02 \times 10^{+0}$	7.31	44.31	17.09
t_{Id}	W_{S_*}	20.25	16	100	1.82×10^{-1}	$1.47 \times 10^{+0}$	6.72	40.17	11.13
t_{Id}	W_{σ}	18.18	16	123	1.51×10^{-1}	$1.37 \times 10^{+0}$	6.78	40.21	13.67
t_{Id}	$W_{S_*, \sigma}$	15.82	16	86	1.94×10^{-1}	$2.84 \times 10^{+0}$	6.72	39.20	9.72
t_{α}^{\wedge}	W_{Id}	11.71	15	93	2.07×10^{-1}	$8.75 \times 10^{+0}$	6.33	37.64	10.40
t_{α}^{\wedge}	W_{S_*}	13.73	15	81	2.03×10^{-1}	$5.32 \times 10^{+0}$	6.24	36.81	9.12
t_{α}^{\wedge}	W_{σ}	12.76	14	84	1.99×10^{-1}	$6.52 \times 10^{+0}$	5.83	34.45	9.45
t_{α}^{\wedge}	$W_{S_*, \sigma}$	15.69	17	86	1.94×10^{-1}	$2.96 \times 10^{+0}$	7.02	41.96	9.75
t_{log}	W_{Id}	15.07	15	93	1.83×10^{-1}	$2.92 \times 10^{+0}$	6.31	37.28	10.37
t_{log}	W_{S_*}	15.77	15	81	1.95×10^{-1}	$2.93 \times 10^{+0}$	6.45	37.86	9.43
t_{log}	W_{σ}	15.07	15	93	1.83×10^{-1}	$2.92 \times 10^{+0}$	6.35	37.74	10.76
t_{log}	$W_{S_*, \sigma}$	15.77	15	81	1.95×10^{-1}	$2.93 \times 10^{+0}$	6.20	37.35	9.25

Table 6.10.: **Setting A.64:** Reconstruction properties of MANTIS for $\delta^{\text{rel}} = 0.1\%$ (columns as in Table 6.8).

6.2.2. Results for setting B

As the shape and the inclusions of setting B are more complex (e.g. non-convex boundary shape and lung models), we expect MANTIS to take more Newton and cg iterations before convergence. Indeed, we find that without conductivity transformation and weights, the number of Newton iterations increases significantly compared to setting A. However, when using the transformations and the weighted norms, the number of iterations remains roughly the same, leading to a decrease of roughly 50% for the Newton iterations and a decrease of roughly 30% for the cg iterations.

In Figure 6.10, the MANTIS results of B.64 for the different transformations and weights are displayed. As for setting A, we observe that oscillations are reduced for the weights W_{S_*} and $W_{S_*,\sigma}$, leading to a better localization of the features, in particular of the heart and spine model shapes.

Figure 6.11 gives a comparison of different noise levels and electrode numbers. Here, we clearly see the improved resolution when decreasing the noise and increasing the number of electrodes. Tables 6.11–6.13 give further information about the performance of MANTIS for settings B.16, B.32, and B.64, respectively.

t_*	W	$e_{\text{rel}} (\%)$	k_*	$\sum_{k=1}^{k_*} l^{(k)}$	$\min(\sigma)$	$\max(\sigma)$	$T_{\text{FEM}} (\text{s})$	$T_{\text{jac}} (\text{s})$	$T_{\text{linear}} (\text{s})$
t_{Id}	W_{Id}	22.67	15	60	1.00×10^{-2}	8.84×10^{-1}	0.70	0.57	0.14
t_{Id}	W_{S_*}	21.09	12	41	1.63×10^{-1}	7.58×10^{-1}	0.56	0.45	0.10
t_{Id}	W_{σ}	21.89	18	53	7.08×10^{-2}	$1.11 \times 10^{+0}$	0.83	0.68	0.13
t_{Id}	$W_{S_*,\sigma}$	20.69	14	42	1.83×10^{-1}	0.90×10^{-1}	0.65	0.52	0.11
t_{α}^{\wedge}	W_{Id}	22.02	18	58	1.74×10^{-1}	$7.02 \times 10^{+0}$	0.85	0.68	0.14
t_{α}^{\wedge}	W_{S_*}	21.06	11	38	2.00×10^{-1}	$1.28 \times 10^{+0}$	0.53	0.42	0.09
t_{α}^{\wedge}	W_{σ}	21.56	18	61	1.56×10^{-1}	$4.52 \times 10^{+0}$	0.82	0.68	0.14
t_{α}^{\wedge}	$W_{S_*,\sigma}$	20.67	11	38	1.86×10^{-1}	9.31×10^{-1}	0.53	0.43	0.09
t_{log}	W_{Id}	21.40	22	59	1.26×10^{-1}	$2.03 \times 10^{+0}$	0.99	0.83	0.15
t_{log}	W_{S_*}	20.67	12	40	1.84×10^{-1}	9.17×10^{-1}	0.57	0.46	0.10
t_{log}	W_{σ}	21.40	22	59	1.26×10^{-1}	$2.03 \times 10^{+0}$	1.01	0.84	0.15
t_{log}	$W_{S_*,\sigma}$	20.67	12	40	1.84×10^{-1}	9.17×10^{-1}	0.58	0.45	0.10

Table 6.11.: **Setting B.16:** Reconstruction properties of MANTIS for $\delta^{\text{rel}} = 0.3\%$ (columns as in Table 6.8).

6. Numerical results

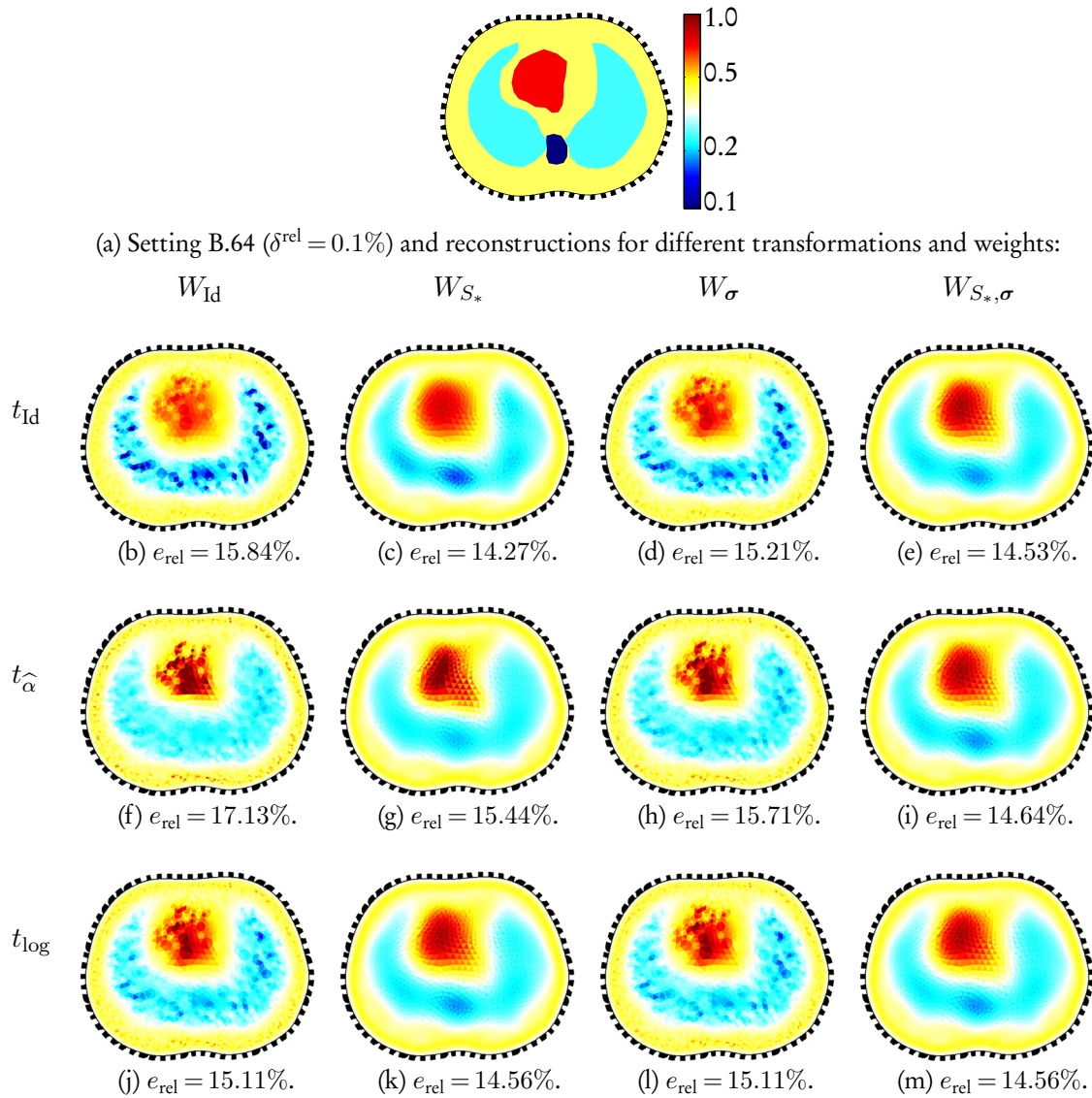


Figure 6.10.: Reconstructions from setting B.64. Using weights W_{S^*} or $W_{S^*,\sigma}$ reduces oscillations drastically.

6. Numerical results

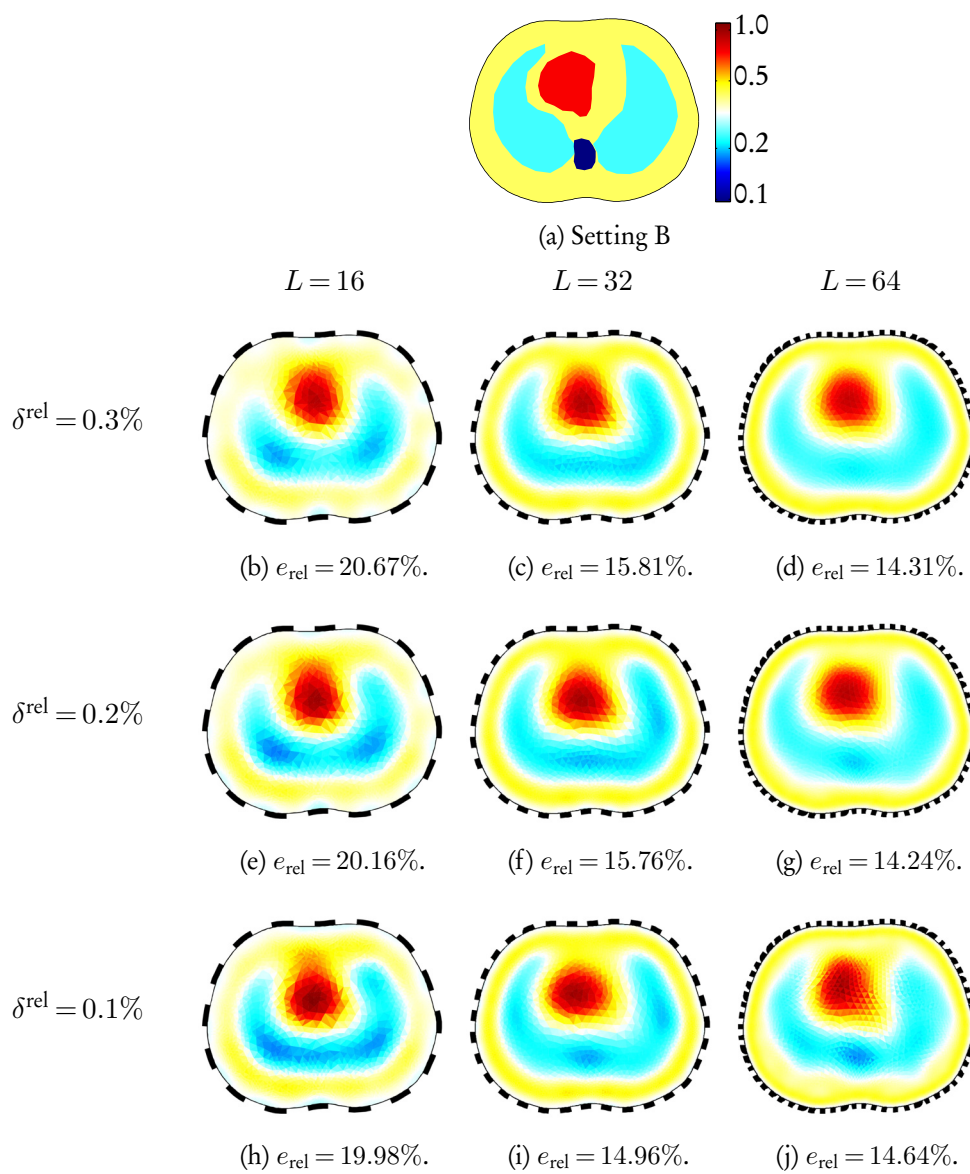


Figure 6.11.: Impact of the number of electrodes and the noise level.
 Conductivity transformation: $t_{\hat{\alpha}}$. Weights: $W_{S_*,\sigma}$.

6. Numerical results

t_*	W	e_{rel} (%)	k_*	$\sum_{k=1}^{k_*} l^{(k)}$	$\min(\sigma)$	$\max(\sigma)$	T_{FEM} (s)	T_{jac} (s)	T_{linear} (s)
t_{Id}	W_{Id}	17.44	20	63	1.90×10^{-2}	7.66×10^{-1}	2.51	6.76	1.00
t_{Id}	W_{S_*}	16.08	14	39	1.69×10^{-1}	0.78×10^{-1}	1.84	4.67	0.65
t_{Id}	W_{σ}	16.65	20	57	8.79×10^{-2}	9.04×10^{-1}	2.62	6.92	0.95
t_{Id}	$W_{S_*,\sigma}$	15.71	13	38	1.87×10^{-1}	9.44×10^{-1}	1.70	4.46	0.64
t_{α}^{\wedge}	W_{Id}	17.53	16	49	1.93×10^{-1}	$5.02 \times 10^{+0}$	2.09	5.49	0.82
t_{α}^{\wedge}	W_{S_*}	16.49	12	35	2.01×10^{-1}	$1.40 \times 10^{+0}$	1.59	4.09	0.60
t_{α}^{\wedge}	W_{σ}	16.43	16	50	1.75×10^{-1}	$2.55 \times 10^{+0}$	2.09	5.48	0.83
t_{α}^{\wedge}	$W_{S_*,\sigma}$	15.76	12	35	1.91×10^{-1}	9.77×10^{-1}	1.59	4.13	0.59
t_{log}	W_{Id}	16.17	21	56	1.47×10^{-1}	$1.32 \times 10^{+0}$	2.70	7.16	0.94
t_{log}	W_{S_*}	15.99	12	31	1.85×10^{-1}	9.84×10^{-1}	1.58	4.09	0.54
t_{log}	W_{σ}	16.17	21	56	1.47×10^{-1}	$1.32 \times 10^{+0}$	2.79	7.24	0.93
t_{log}	$W_{S_*,\sigma}$	15.99	12	31	1.85×10^{-1}	9.84×10^{-1}	1.61	4.15	0.52

Table 6.12.: **Setting B.32:** Reconstruction properties of MANTIS for $\delta^{\text{rel}} = 0.2\%$ (columns as in Table 6.8).

t_*	W	e_{rel} (%)	k_*	$\sum_{k=1}^{k_*} l^{(k)}$	$\min(\sigma)$	$\max(\sigma)$	T_{FEM} (s)	T_{jac} (s)	T_{linear} (s)
t_{Id}	W_{Id}	15.84	24	101	1.83×10^{-2}	7.93×10^{-1}	10.18	61.72	11.84
t_{Id}	W_{S_*}	14.27	28	81	1.52×10^{-1}	8.53×10^{-1}	11.66	71.66	9.89
t_{Id}	W_{σ}	15.21	32	102	9.07×10^{-2}	9.08×10^{-1}	13.77	83.76	12.52
t_{Id}	$W_{S_*,\sigma}$	14.53	23	79	1.79×10^{-1}	$1.01 \times 10^{+0}$	10.08	60.08	9.55
t_{α}^{\wedge}	W_{Id}	17.13	32	96	1.92×10^{-1}	$4.37 \times 10^{+0}$	13.57	82.46	11.76
t_{α}^{\wedge}	W_{S_*}	15.44	16	67	1.95×10^{-1}	$1.55 \times 10^{+0}$	7.04	41.84	7.78
t_{α}^{\wedge}	W_{σ}	15.71	33	90	1.75×10^{-1}	$2.20 \times 10^{+0}$	14.12	85.93	11.09
t_{α}^{\wedge}	$W_{S_*,\sigma}$	14.64	15	66	1.78×10^{-1}	$1.03 \times 10^{+0}$	6.64	38.90	7.77
t_{log}	W_{Id}	15.11	28	81	1.46×10^{-1}	$1.23 \times 10^{+0}$	12.05	72.60	10.12
t_{log}	W_{S_*}	14.56	15	67	1.78×10^{-1}	$1.01 \times 10^{+0}$	6.52	38.95	7.81
t_{log}	W_{σ}	15.11	28	81	1.46×10^{-1}	$1.23 \times 10^{+0}$	11.93	72.70	10.02
t_{log}	$W_{S_*,\sigma}$	14.56	15	67	1.78×10^{-1}	$1.01 \times 10^{+0}$	6.51	38.84	7.78

Table 6.13.: **Setting B.64:** Reconstruction properties of MANTIS for $\delta^{\text{rel}} = 0.1\%$ (columns as in Table 6.8).

6.2.3. Results for setting C

For the reconstructions of the artificial “mixed background, mixed contrast conductivity” setting C, we omit, for the sake of simplicity, the reconstructions for t_{\log} . Its behaviour is very similar to $t_{\hat{\alpha}}$, with t_{\log} having a tendency of converging slightly faster and $t_{\hat{\alpha}}$ having a tendency of a slightly lower error; see also [WR15] where this behaviour was reported for a very similar setting.

For this high contrast, mixed background conductivity, we expect the transformed and weighted inversion to be significantly faster than the untransformed case, since the nonlinearity of the problem is more severe. Indeed, we observe that when using identity weights W_{Id} and transformation t_{Id} , the Newton scheme struggles to resolve the high contrast, thus it approaches a highly oscillatory local minimum and barely converges at all⁵. However, using either *any* of the weight matrices W_{S^*} , W_{σ} , $W_{S^*,\sigma}$, or any of the proposed conductivity transformations, reduces the number of iterations drastically. The best performance is obtained when using $t_{\hat{\alpha}}$ together with $W_{S^*,\sigma}$; see Figures 6.12 and 6.13 for plots of the solutions of C.16 and C.64, and Tables 6.14 and 6.16 for the corresponding iteration counts, respectively. Although the plots are omitted, the reconstruction details for C.32 are given in Table 6.15.

t_*	W	e_{rel} (%)	k_*	$\sum_{k=1}^{k_*} l^{(k)}$	$\min(\sigma)$	$\max(\sigma)$	T_{FEM} (s)	T_{jac} (s)	T_{linear} (s)
t_{Id}	W_{Id}	50.72	400	1 173	1.00×10^{-2}	$5.34 \times 10^{+0}$	18.54	15.71	3.05
t_{Id}	W_{S^*}	41.49	13	60	1.66×10^{-2}	$5.71 \times 10^{+0}$	0.63	0.50	0.15
t_{Id}	W_{σ}	48.58	19	108	1.00×10^{-2}	$8.54 \times 10^{+0}$	0.97	0.76	0.25
t_{Id}	$W_{S^*,\sigma}$	45.32	12	44	2.80×10^{-1}	$1.06 \times 10^{+1}$	0.59	0.47	0.11
$t_{\hat{\alpha}}$	W_{Id}	53.76	12	64	2.97×10^{-1}	$1.05 \times 10^{+1}$	0.60	0.46	0.15
$t_{\hat{\alpha}}$	W_{S^*}	46.43	10	39	3.27×10^{-1}	$9.06 \times 10^{+0}$	0.49	0.38	0.10
$t_{\hat{\alpha}}$	W_{σ}	52.11	12	62	2.58×10^{-1}	$1.50 \times 10^{+1}$	0.60	0.47	0.15
$t_{\hat{\alpha}}$	$W_{S^*,\sigma}$	45.15	10	39	2.87×10^{-1}	$1.09 \times 10^{+1}$	0.50	0.38	0.10

Table 6.14.: **Setting C.16:** Reconstruction properties of MANTIS for $\delta^{\text{rel}} = 0.3\%$ (columns as in Table 6.8).

⁵Still, the error e_{rel} of the Newton iterates decreases continuously during inversion.

6. Numerical results

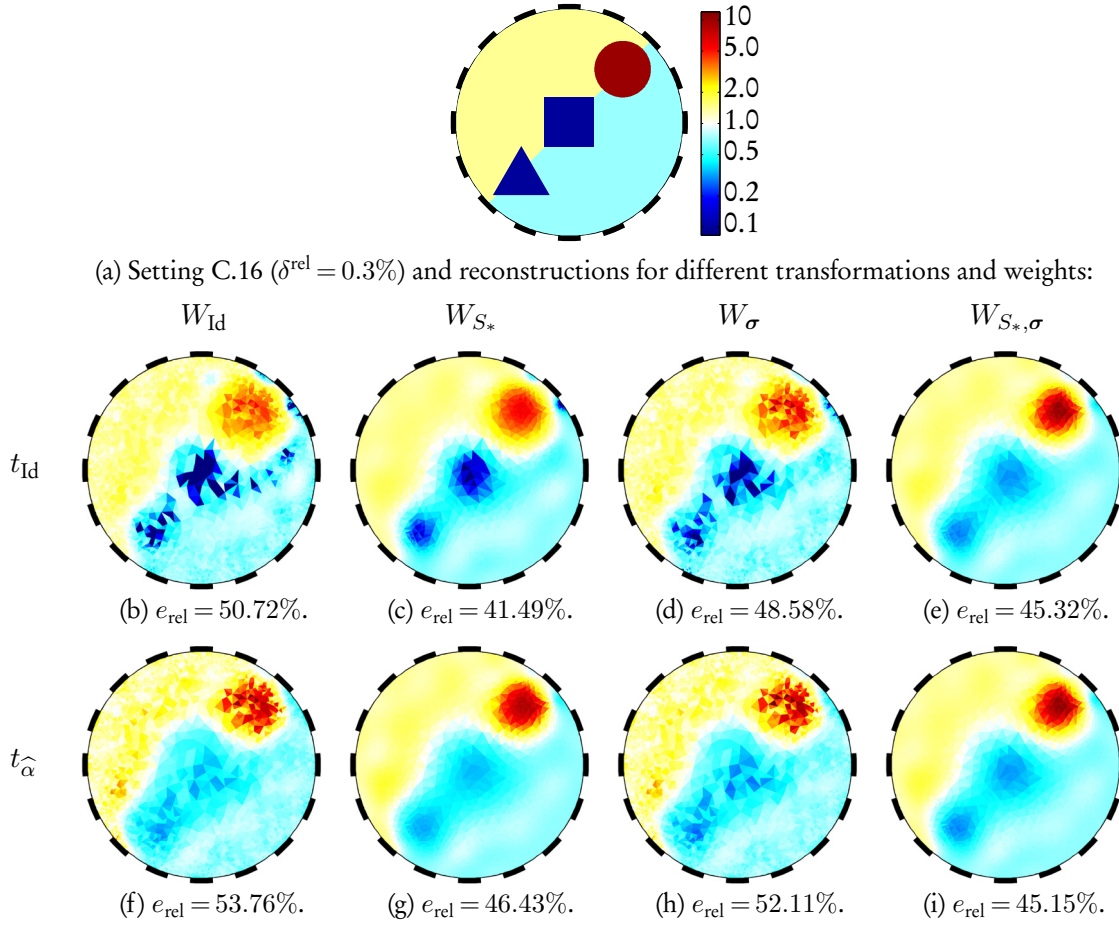


Figure 6.12.: Reconstructions from setting C.16.

t_*	W	$e_{\text{rel}} (\%)$	k_*	$\sum_{k=1}^{k_*} l^{(k)}$	$\min(\sigma)$	$\max(\sigma)$	$T_{\text{FEM}} (\text{s})$	$T_{\text{jac}} (\text{s})$	$T_{\text{linear}} (\text{s})$
t_{Id}	W_{Id}	50.40	4 563	13 726	1.00×10^{-2}	7.06×10^0	606.67	1606.34	231.25
t_{Id}	W_{S^*}	36.01	13	69	1.00×10^{-2}	8.12×10^0	1.76	4.49	1.09
t_{Id}	W_{σ}	45.78	29	237	1.00×10^{-2}	1.14×10^1	3.75	10.05	3.64
t_{Id}	$W_{S^*,\sigma}$	39.86	10	45	1.64×10^{-1}	1.79×10^1	1.37	3.46	0.72
\hat{t}_{α}	W_{Id}	48.30	16	121	2.23×10^{-1}	1.23×10^1	2.09	5.55	1.87
\hat{t}_{α}	W_{S^*}	41.24	10	47	2.47×10^{-1}	1.29×10^1	1.36	3.38	0.72
\hat{t}_{α}	W_{σ}	47.01	16	112	1.78×10^{-1}	1.90×10^1	2.11	5.51	1.71
\hat{t}_{α}	$W_{S^*,\sigma}$	39.49	10	41	1.84×10^{-1}	1.87×10^1	1.37	3.46	0.66

Table 6.15.: **Setting C.32:** Reconstruction properties of MANTIS for $\delta^{\text{rel}} = 0.2\%$ (columns as in Table 6.8).

6. Numerical results

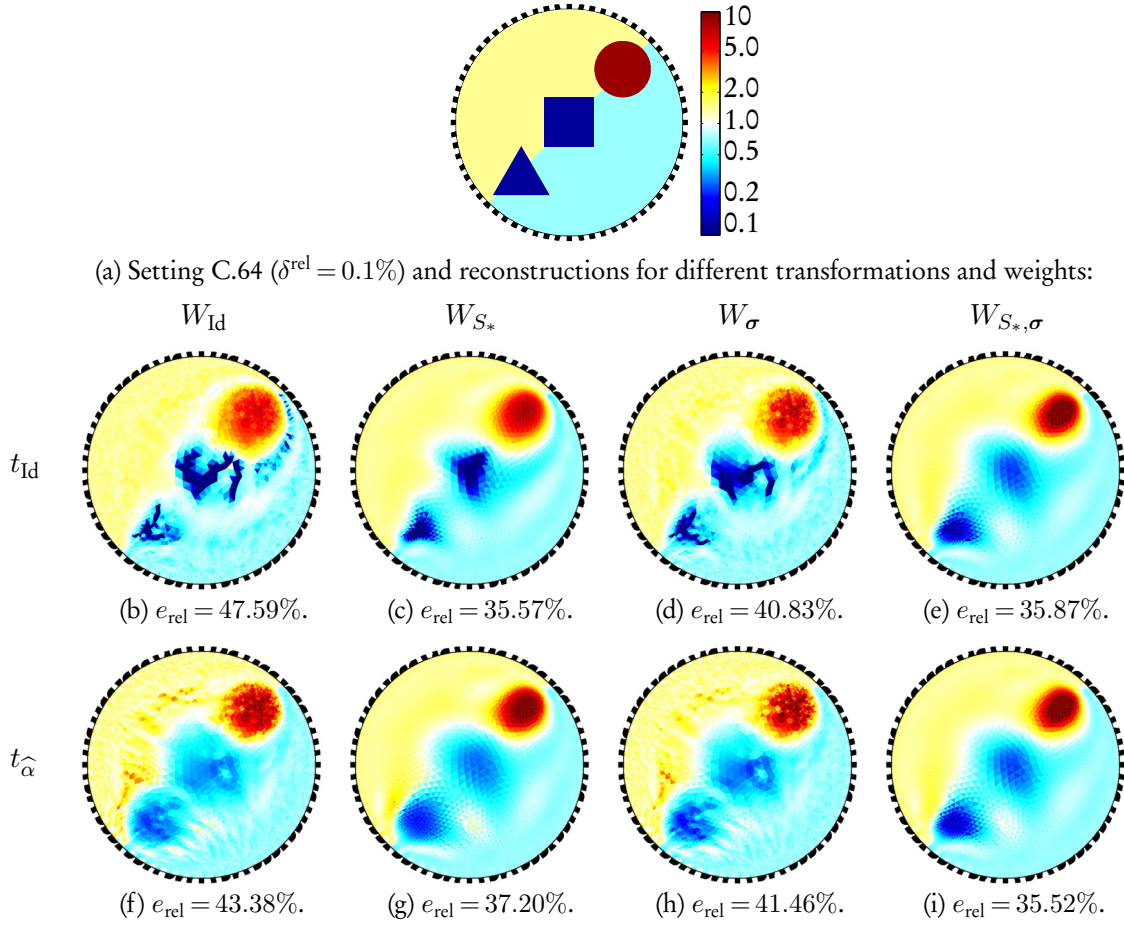


Figure 6.13.: Reconstructions from setting C.64.

t_*	W	$e_{\text{rel}} (\%)$	k_*	$\sum_{k=1}^{k_*} l^{(k)}$	$\min(\sigma)$	$\max(\sigma)$	$T_{\text{FEM}} (\text{s})$	$T_{\text{jac}} (\text{s})$	$T_{\text{linear}} (\text{s})$
t_{Id}	W_{Id}	47.59	4	832	1.00×10^{-2}	7.85×10^0	2183.22	13086.83	2115.02
t_{Id}	W_{S^*}	35.57	14	77	1.00×10^{-2}	9.25×10^0	6.17	36.04	9.23
t_{Id}	W_{σ}	40.83	32	310	1.00×10^{-2}	1.26×10^1	13.80	83.86	35.89
t_{Id}	$W_{S^*,\sigma}$	35.87	11	55	8.14×10^{-2}	2.44×10^1	4.71	27.84	6.65
\hat{t}_{α}	W_{Id}	43.38	19	200	2.16×10^{-1}	1.35×10^1	8.19	48.63	22.65
\hat{t}_{α}	W_{S^*}	37.20	11	59	1.84×10^{-1}	1.50×10^1	4.93	28.72	7.08
\hat{t}_{α}	W_{σ}	41.46	20	172	1.76×10^{-1}	2.21×10^1	8.72	52.47	20.26
\hat{t}_{α}	$W_{S^*,\sigma}$	35.52	11	52	1.06×10^{-1}	2.58×10^1	4.95	28.78	6.39

Table 6.16.: **Setting C.64:** Reconstruction properties of MANTIS for $\delta^{\text{rel}} = 0.1\%$ (columns as in Table 6.8).

6. Numerical results

The impact of the noise level and the number of electrodes is displayed in Figure 6.14. The backgrounds are resolved correctly in all settings. The inclusions are detected as well, but the contrast is better as the noise level decreases, and the features are better resolved – in particular near the boundary – as the number of electrodes increases.

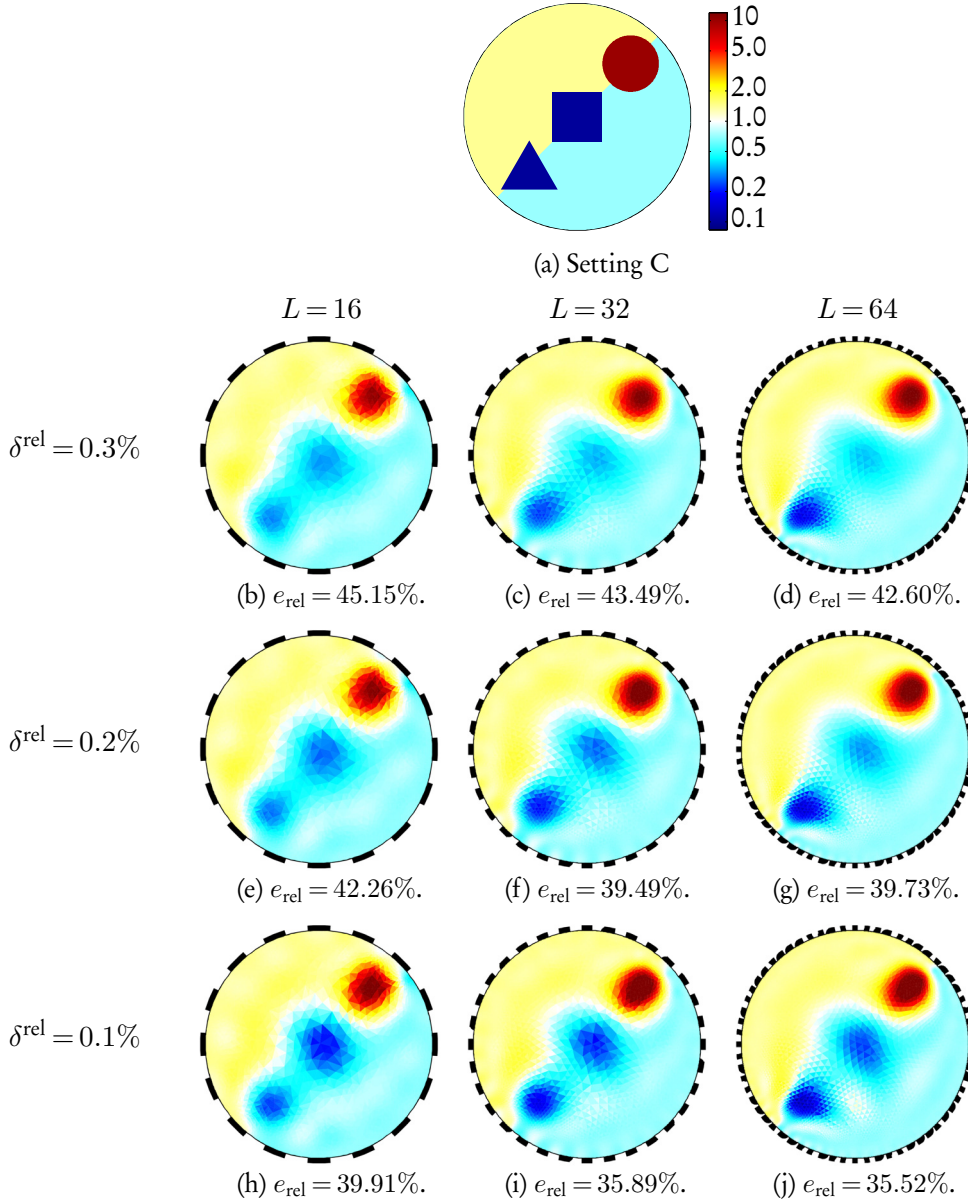


Figure 6.14.: Impact of the number of electrodes and the noise level. The contrast is improved as the noise level is reduced, while the features are better resolved as the electrode number increases. Conductivity transformation: $t_{\hat{\alpha}}$. Weights: $W_{S_*,\sigma}$.

6.2.4. Results for setting D

The impact of the weights in MANTIS in this non-convex setting is similar to the one of the previous setting: Using the identity transformation t_{Id} and identity weights W_{Id} requires significantly more Newton and cg iterations and leads to oscillatory solutions, in particular in the resistive part of the conductivity; see Figure 6.15 for the results for D.16, D.32 and D.64. Due to the similarity, we omit a detailed individual comparison of the transformations and weights for setting D as they give no additional insight into the behaviour of MANTIS.

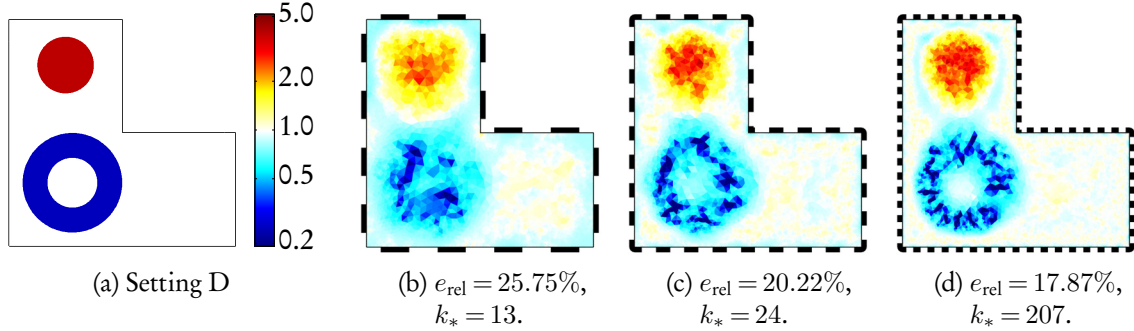


Figure 6.15.: With identity transformation (t_{Id}) and weights (W_{Id}), the solution is oscillatory and convergence is slow. Conductivity reconstructions are shown for D.16 ($\delta^{\text{rel}} = 0.3\%$) in (b), for D.32 ($\delta^{\text{rel}} = 0.2\%$) in (c) and for D.64 ($\delta^{\text{rel}} = 0.1\%$) in (d).

To assess the capability of MANTIS for recovering non-convex features inside non-convex domains, reconstructions for different noise levels and electrode numbers and using $t_{\hat{\alpha}}$ and $W_{S^*,\sigma}$ are given in Figure 6.16, supplemented by additional information in Table 6.17.

L	δ^{rel}	e_{rel} (%)	k_*	$\sum_{k=1}^{k_*} l^{(k)}$	$\min(\sigma)$	$\max(\sigma)$	T_{FEM} (s)	T_{jac} (s)	T_{linear} (s)
16	0.3	24.99	7	17	3.54×10^{-1}	$3.36 \times 10^{+0}$	0.33	0.28	0.05
16	0.2	23.87	9	31	3.98×10^{-1}	$3.74 \times 10^{+0}$	0.41	0.35	0.08
16	0.1	22.67	14	78	3.92×10^{-1}	$4.26 \times 10^{+0}$	0.64	0.57	0.19
32	0.3	20.56	8	30	4.28×10^{-1}	$4.15 \times 10^{+0}$	1.17	2.88	0.49
32	0.2	19.13	11	47	3.72×10^{-1}	$4.62 \times 10^{+0}$	1.47	3.96	0.76
32	0.1	16.46	16	98	3.16×10^{-1}	$5.22 \times 10^{+0}$	2.07	5.80	1.57
64	0.3	17.95	7	25	3.71×10^{-1}	$4.65 \times 10^{+0}$	3.25	19.00	3.20
64	0.2	16.84	9	39	3.45×10^{-1}	$4.77 \times 10^{+0}$	4.36	24.61	5.08
64	0.1	15.34	13	57	3.12×10^{-1}	$5.19 \times 10^{+0}$	5.92	35.19	7.13

Table 6.17.: **Setting D**: Reconstruction properties of MANTIS for D.16, D.32 and D.64 with various noise levels. Conductivity transformation: $t_{\hat{\alpha}}$. Weights: $W_{S^*,\sigma}$.

6. Numerical results

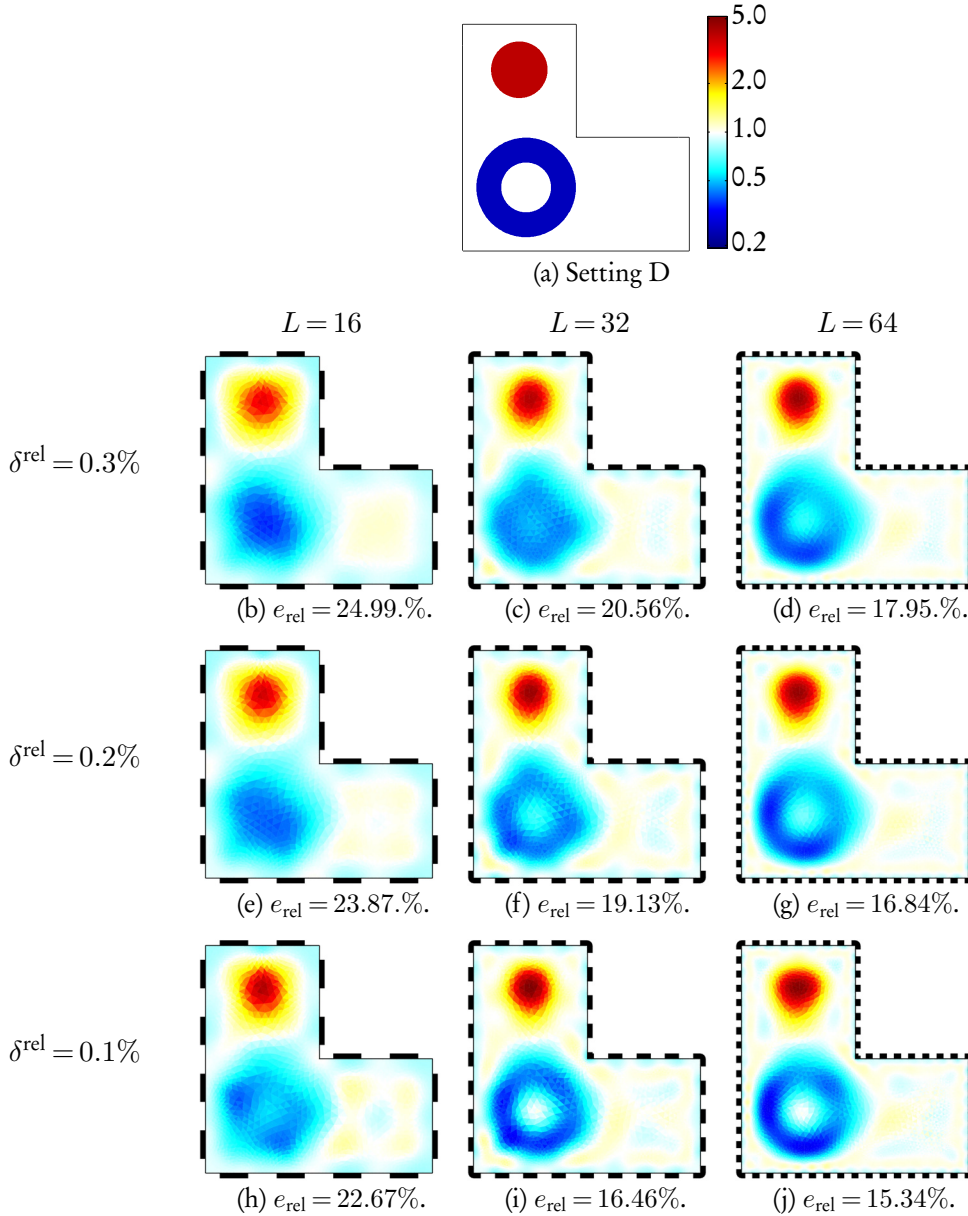


Figure 6.16.: Impact of the number of electrodes and the noise level. For higher noise level and fewer electrodes, the Newton iteration stops before the non-convex features are resolved. Conductivity transformation: $t_{\hat{\alpha}}$. Weights: $W_{S^*, \sigma}$.

6.3. 3D reconstructions

Using the Netgen mesh generator from EIDORS allows to specify different “target” mesh densities for the electrode discretization and for the interior. As the mesh is used both as a conductivity discretization and to compute the forward solution in the Newton steps, it is highly recommended to refine the mesh at the electrodes, where the potential gradients are biggest. The following recon-

6. Numerical results

structions use discretizations which are $25\times$ finer at the electrodes than in the interior. The forward mesh was generated to conform with the discontinuities of the simulated conductivity with 219851 tetrahedrons. The inverse mesh was generated independently and generically without the knowledge of the true conductivity, with far fewer tetrahedrons.

Figures 6.17(b)–(d) show MANTIS reconstructions for various mesh refinements. The quality of the forward solutions affects the quality of the initial guesses $z^{\text{CEM},z}$ and $\sigma^{\text{CEM},z}$. This influences the performance of the reconstructions significantly. The corresponding initializations and more details about the reconstructions are given in Table 6.18. Note that the increased computation time for the finer FEM discretization is partly compensated by the reduced number of Newton and cg iterations.

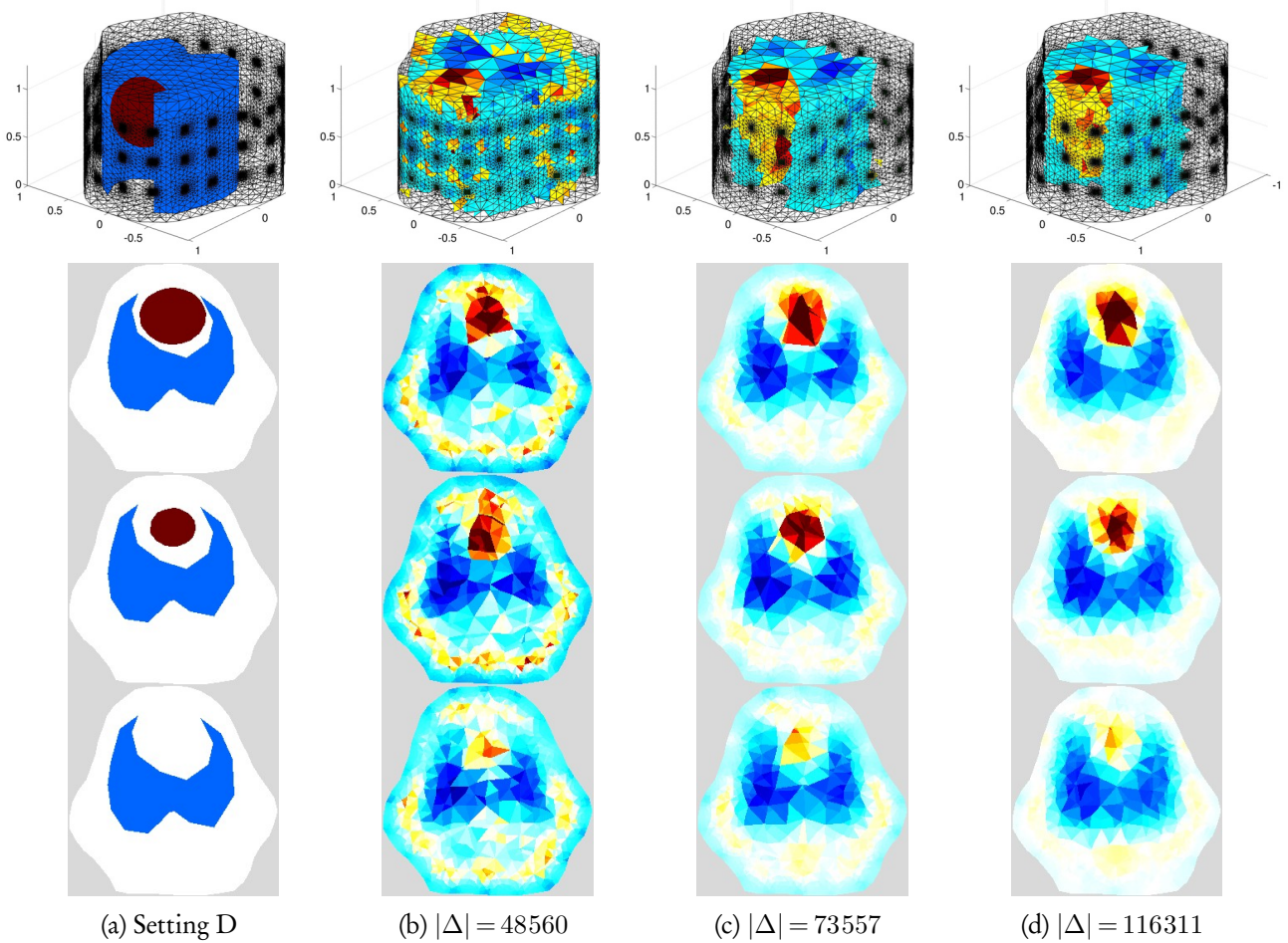


Figure 6.17.: MANTIS performance using EIDORS 3D model and different FEM refinements for the forward solver. Top: 3D model. Bottom: Horizontal slices at each electrode layer.

6. Numerical results

$ \mathcal{P} $	$z^{\text{CEM},z}$	$\sigma^{\text{CEM},z}$	k_*	$\sum_{k=1}^{k_*} l^{(k)}$	$T_{\text{FEM}} + T_{\text{jac}}$ (s)	T_{linear} (s)
116311	3.51×10^{-3}	4.12×10^{-1}	7	33	241.71	16.98
73557	3.33×10^{-3}	3.86×10^{-1}	8	40	162.30	13.90
48560	1.60×10^{-3}	3.35×10^{-1}	10	75	145.25	15.60

Table 6.18.: **Setting E:** Initializations and reconstruction properties of MANTIS for different FEM refinements.

The assembly of the Fréchet derivative $F'_{\mathcal{I}}$ of size 3600×116311 in EIDORS leads to a total memory consumption of 7.3 GB in MATLAB in our numerical example. For even larger systems, it might be advantageous to solve the weak formulation given Theorem (2.9) for each cg iteration, instead of assembling and storing the sensitivity matrix $F'_{\mathcal{I}}$ explicitly, as noted in Remark 2.14.

6.4. Reconstruction on sensitivity-based meshes

In section 3.5, sensitivity based discretizations were designed to conform with the resolution of a given EIT setting. Our goal was to find a discretization which corresponds to a given noise level (3.5.1–3.5.3), or to generate a discretization with a fixed number of cells and roughly uniform sensitivity (3.5.4). Here, we present some reconstructions on various discretizations to study their impact on the reconstruction performance.

6.4.1. Comparison of sensitivity based and uniform discretizations

Figure 6.18 shows reconstructions of the data from setting A.16 ($\delta^{\text{rel}} = 0.3\%$) for conductivity discretizations $\mathcal{D}_{\mathcal{P}}$ with varying partitions \mathcal{P} . For Figures 6.18(b) and (f), \mathcal{P} was generated by a Voronoi tessellation with the interpolation approach described in section 3.5.1. For 16 electrodes, a relative noise level of $\delta^{\text{rel}} = 0.3\%$ corresponds to a relative sensitivity of $\lambda = (\sum_{l=1}^{16} 0.003^2)^{1/2} = 0.012$, cf. equation 3.3. For computational reasons, the radii of the perturbations were computed for $\lambda_{\sigma, \sigma_1} = 0.02$, and multiplied by $\sqrt{0.012/0.02}$ to approximate inclusions of relative sensitivity 0.012. The resulting mesh consists of $|\mathcal{P}| = 434$ Voronoi cells. In Figures 6.18(c) and (g), an adaptive triangulation with $P_{\text{t}} = 434$ is used, as described in section 3.5.4. This gives $|\mathcal{P}| = 444$ triangles. In Figures 6.18(d) and (h), the domain was discretized uniformly into $|\mathcal{P}| = 437$ squares. For all reconstructions, the forward computations were performed using a much finer FEM discretization with $|\Delta| = 6510$ triangles.

Further properties of the reconstructions are listed in Table 6.19. We note that using sensitivity based discretizations of the conductivity space significantly reduces the number of Newton iterations over a uniform “pixel” discretization with the same number of degrees of freedom. Compared to the results of Table 6.8, where $|\mathcal{P}| = |\Delta| = 6510$ and no interpolation is needed, we note that the time for assembling the Jacobian and performing the cg iterations is reduced due to the lower dimension of $\mathcal{D}_{\mathcal{P}}$. However, the additional cost for the interpolations outweighs this in our implementation. Still, using a lower dimension for $\mathcal{D}_{\mathcal{P}}$ for reconstruction might be of interest when memory usage is an issue.

A similar behaviour can be observed for setting C. Reconstructions are shown in Figure 6.19 and the corresponding details are listed in Table 6.20.

6. Numerical results

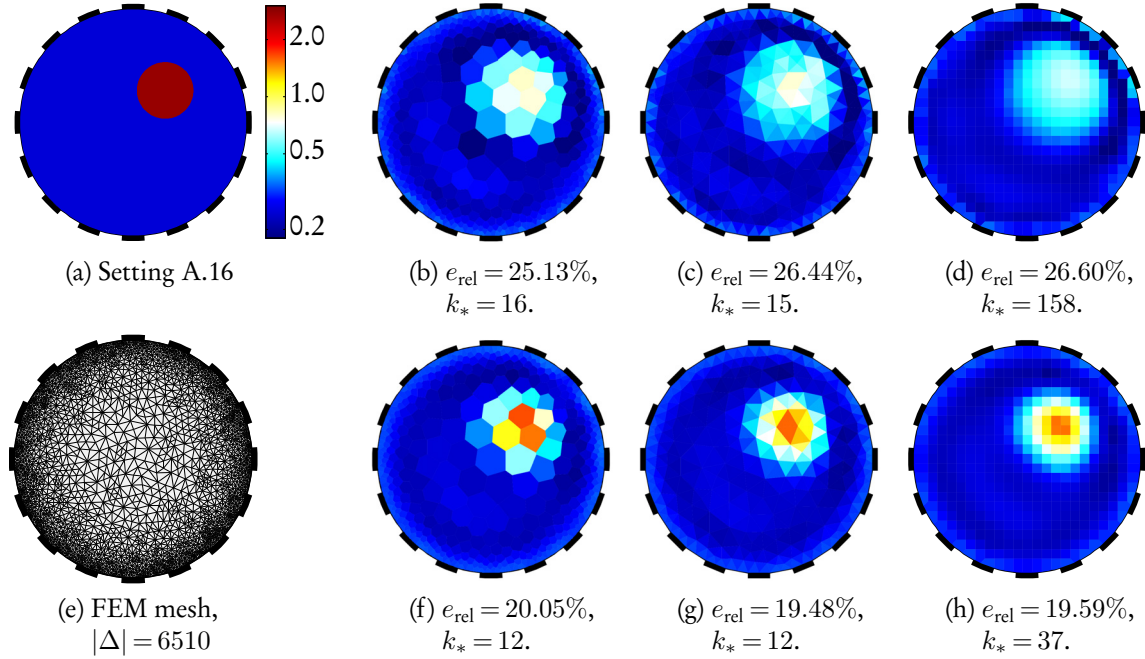


Figure 6.18.: Reconstructions for setting A.16 on different conductivity discretizations.

(b)–(d): Identity transformation t_{Id} and weights W_{Id} .

(f)–(h): σ - ρ -transform $t_{\hat{\alpha}}$ and weights $W_{S_*,\sigma}$.

Using sensitivity based discretizations in (b) and (f) or adaptive triangulations in (c) and (g) significantly reduces the number of Newton iterations over uniform conductivity discretizations in (d) and (h). For evaluating the forward operator, the FEM triangulation in (e) was used.

cond. discretization	parameters	$ \mathcal{P} $	e_{rel}	k_*	$\sum_{k=1}^{k_*} l^{(k)}$	T_{FEM}	T_{jac} (s)	T_{linear} (s)	T_{int}
sens. based (Voronoi)	$t_{\text{Id}}, W_{\text{Id}}$	434	25.13%	16	67	0.80	0.16	0.02	3.23
sens. based (Voronoi)	$t_{\hat{\alpha}}, W_{S_*,\sigma}$	434	20.05%	12	42	0.60	0.11	0.02	2.49
adaptive triangulation	$t_{\text{Id}}, W_{\text{Id}}$	444	26.44%	15	64	0.80	0.25	0.04	10.09
adaptive triangulation	$t_{\hat{\alpha}}, W_{S_*,\sigma}$	444	19.48%	12	43	0.62	0.13	0.02	2.52
uniform discretization	$t_{\text{Id}}, W_{\text{Id}}$	437	26.60%	158	456	7.72	1.62	0.20	32.80
uniform discretization	$t_{\hat{\alpha}}, W_{S_*,\sigma}$	437	19.59%	37	84	1.88	0.40	0.04	7.82

Table 6.19.: **Setting A.16:** Reconstruction properties of MANTIS for different conductivity discretizations. T_{int} denotes the total computation time (in seconds) for interpolating between the FEM discretization Δ and the conductivity mesh \mathcal{P} .

6. Numerical results

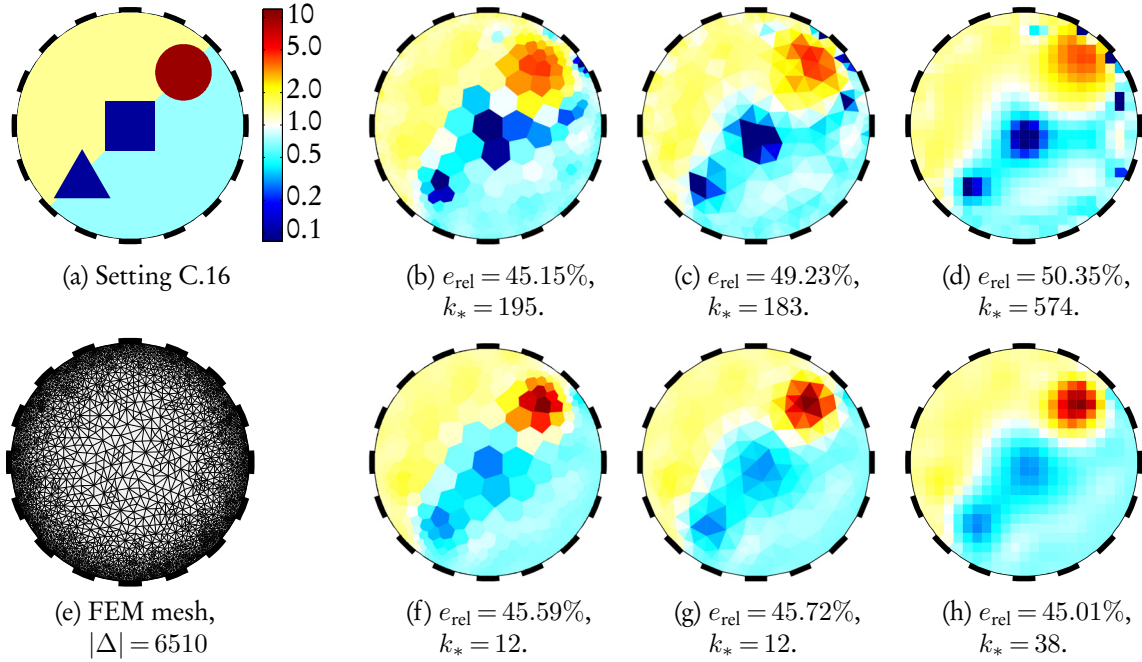


Figure 6.19.: Reconstructions for setting C.16 on different conductivity discretizations. Discretizations as described in Figure 6.18.

cond. discretization	parameters	$ \mathcal{P} $	e_{rel}	k_*	$\sum_{k=1}^{k_*} l^{(k)}$	T_{FEM}	T_{jac} (s)	T_{linear} (s)	T_{int}
sens. based (Voronoi)	$t_{\text{Id}}, W_{\text{Id}}$	434	45.15%	195	597	9.04	1.89	0.23	40.54
sens. based (Voronoi)	$t_{\hat{\alpha}}, W_{S^*, \sigma}$	434	45.49%	12	12	0.61	0.13	0.02	2.48
adaptive triangulation	$t_{\text{Id}}, W_{\text{Id}}$	444	49.23%	183	802	8.70	1.86	0.25	39.19
adaptive triangulation	$t_{\hat{\alpha}}, W_{S^*, \sigma}$	444	45.72%	12	47	0.67	0.12	0.02	2.60
uniform discretization	$t_{\text{Id}}, W_{\text{Id}}$	437	50.35%	574	1978	27.78	6.11	0.69	124.90
uniform discretization	$t_{\hat{\alpha}}, W_{S^*, \sigma}$	437	45.01%	38	91	1.87	0.38	0.04	8.11

Table 6.20.: **Setting C.16:** Reconstruction properties of MANTIS for different conductivity discretizations.

6.4.2. Impact of the discretization refinement

In section 4.3.2, we showed that the weights W_{S_*} and $W_{S_*,\sigma}$ lead to reconstructions which are asymptotically discretization independent. Here, we verify this effect numerically for settings A.32 and C.32 with $\delta^{\text{rel}} = 0.2\%$, using conductivity discretizations on meshes \mathcal{P} with $|\mathcal{P}| = 1000$ to 12000 triangles.

The evolution of the reconstruction error and the number of Newton iterations versus $|\mathcal{P}|$ is shown in Figure 6.20. The reconstruction results for 2000, 5000 and 12000 triangles are shown in Figure 6.21. We observe that the reconstructions indeed approach a “steady state” as the number of triangles increases, i.e. the reconstruction is almost independent of the discretization.

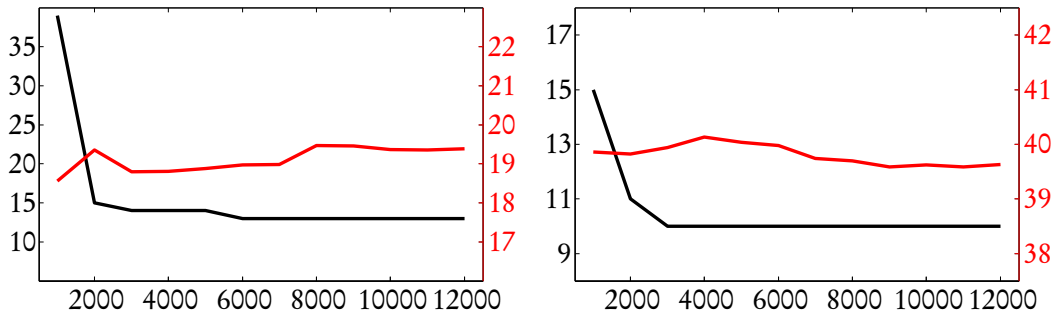


Figure 6.20.: Newton iterations (black) and reconstruction error (red, in %) for settings A.32 (left) and C.32 (right) versus number of triangles $|\mathcal{P}|$ of the conductivity discretizations based on adaptive triangulations; cf. section 3.5.4.

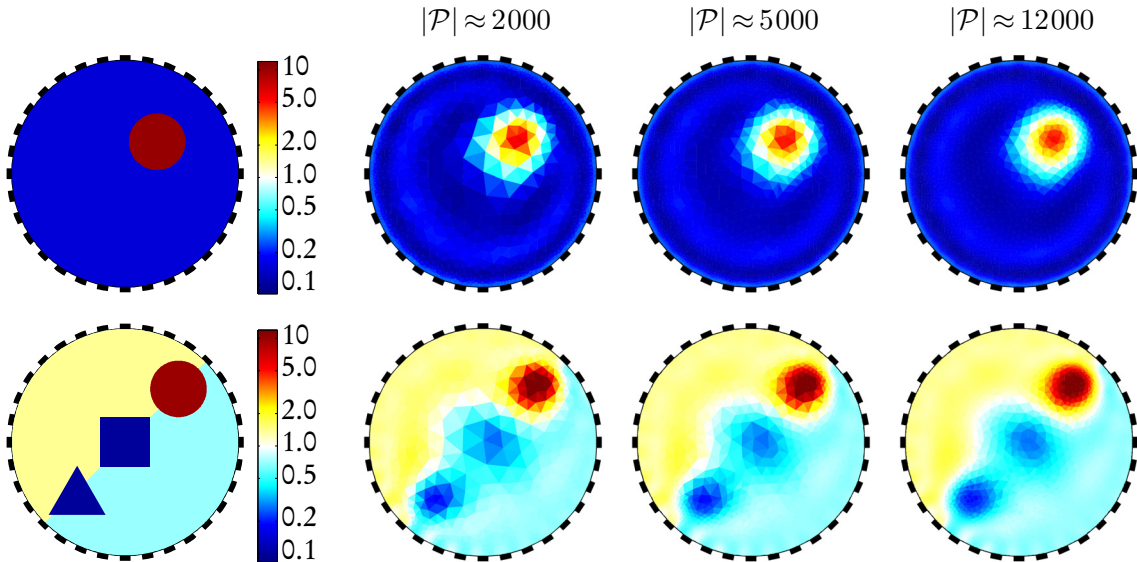


Figure 6.21.: Reconstructions of A.32 (top) and C.32 (bottom) on adaptive triangulations with different refinements.

6.5. Model parameter reconstructions

In this section we consider the extended forward operator \bar{F} introduced in section 5.1 and perform simultaneous reconstructions of the conductivity, the electrode locations and sizes, and the contact impedances.

6.5.1. Incorrect model: “badly attached” electrodes

First, we consider setting B.32 with $\delta^{\text{rel}} = 0.1\%$ and with two electrodes in the non-convex part of the boundary having a high contact impedance:

$$z_l = \begin{cases} 1, & l \in \{10, 25\}, \\ 0.05, & l \in \{1, \dots, 32\} \setminus \{10, 25\}. \end{cases}$$

In practice, this can happen e.g. when the electrodes are badly attached. This is depicted in Figure 6.22(a), with electrodes 10 and 25 colored in red. Results without and with simultaneous reconstruction of conductivity and contact impedances are shown in Figure 6.22(b) and (c), respectively. The contact impedances are recovered accurately; see Figure 6.23.

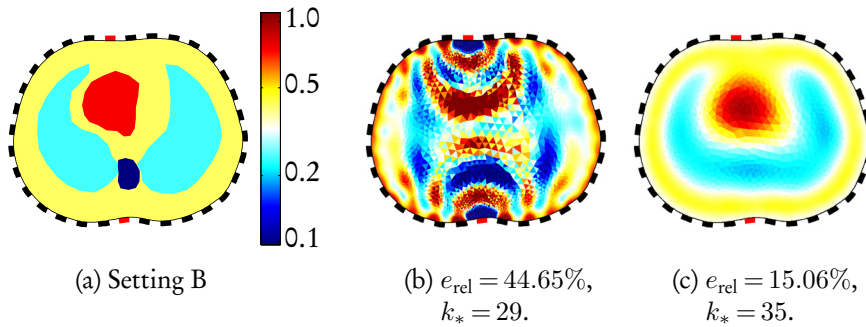


Figure 6.22.: Simulation of two “badly attached” electrodes with high contact impedances: $z_{10} = z_{25} = 1$ (red). Using the fixed initial guess $z^{\text{CEM},z} = 0.082$ for all electrodes in (b) leads to a highly resistive conductivity reconstruction near these electrodes, which in turn causes the reconstruction to fail. When recovering conductivity and individual contact impedances simultaneously, the bad contacts are accurately recovered and the conductivity reconstruction succeeds; see Figure 6.23 for the recovered contact impedances.

6. Numerical results

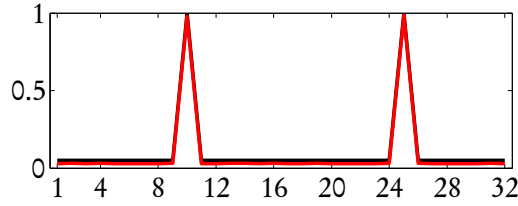


Figure 6.23.: Exact (black) and recovered (red) contact impedances at the 32 electrodes of setting B.32 with $\delta^{\text{rel}} = 0.1\%$; cf. Figure 6.22.

6.5.2. Incorrect model: highly fluctuating contact impedances

Next, we assume the contact impedances to be highly fluctuating. Thus, we let

$$z_l = 0.001 + 0.2 \cdot d_l \in [0.001, 0.201],$$

where $d_l \sim u(0,1) \in [0,1]$ are pseudo-random independently and uniformly distributed numbers generated by the MATLAB function `rand` with default seed. Again, the reconstruction fails with fixed initial guess (Figure 6.24(b)) and succeeds when recovering the contact impedances simultaneously (Figure 6.24(c)). The true and recovered contact impedances are shown in Figure 6.25.

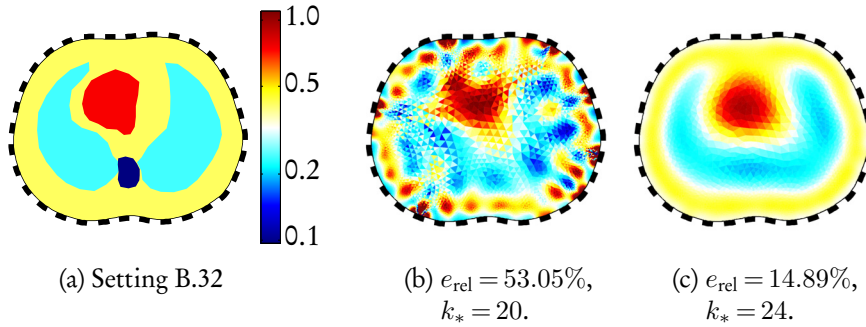


Figure 6.24.: Simulation of highly fluctuating contact impedances. When recovering conductivity and individual contact impedances simultaneously, the conductivity reconstruction succeeds; see also Figure 6.25 for the corresponding contact impedances.

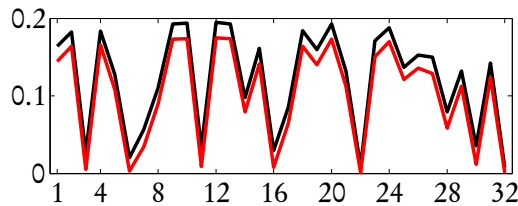


Figure 6.25.: Exact (black) and recovered (red) contact impedances at the 32 electrodes of setting B.32 with $\delta^{\text{rel}} = 0.1\%$; cf. Figure 6.24.

6.5.3. Incorrect model: wrong boundary geometry

Now, we assume that the boundary geometry is not known exactly, which is usually the case for thorax imaging. As described in section 6.1.2, recovering both the boundary shape and the electrode configuration simultaneously is an underdetermined problem. Here, we try to obtain a conformal equivalent of the true conductivity by simultaneously recovering the conductivity and the electrode positions and sizes, with the parameters given in Remark 5.3. For simplicity, a new FEM discretization is generated in each Newton step, and the conductivity discretization is held constant. As in the preceding section, the total computation is dominated by the interpolation time.

Reconstructions of the measurements of B.32 with $\delta^{\text{rel}} = 0.1\%$ on the elliptical domain of Figure 6.2(b) without and with optimizing for the electrode locations and sizes are shown in Figure 6.26(b) and (c), respectively. The reconstruction succeeds when modifying the boundary geometry, and fails otherwise. Note however that in both cases, the discrepancy principle was reached.

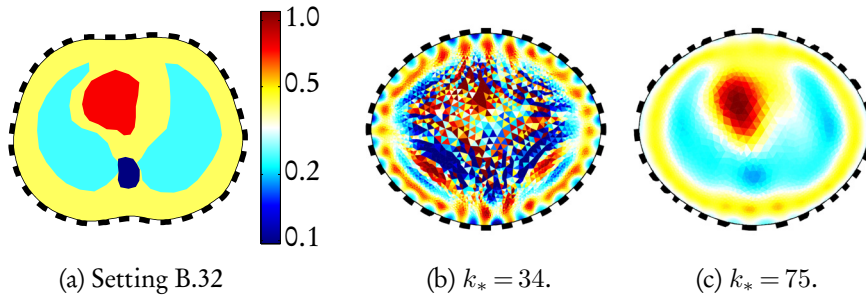


Figure 6.26.: Reconstruction on the wrong geometry: The data of setting B.32 with $\delta^{\text{rel}} = 0.1\%$ was used for inversion on an elliptical domain. If the boundary geometry is fixed, the reconstruction fails (b). When reconstructing the electrode sizes and locations simultaneously with the conductivity, the reconstruction succeeds (c).

6.5.4. Incorrect model: wrong contact impedances and boundary geometry

Finally, we optimize for all parameters of the extended forward operator \bar{F} , i.e. the conductivity, the electrode sizes and locations, and the contact impedances, simultaneously. The simulated data was generated using the same contact impedances as in section 6.5.2 and the reconstruction was performed on the same ellipse as in section 6.5.3, thus the effects of highly fluctuating contact impedances and a wrong boundary geometry appear simultaneously.

As previously mentioned, small electrodes with low contact impedances give similar data as big electrodes with high contact impedances, thus we can not expect to recover both values accurately. However, the recovered conductivity on the ellipse is a good approximation of the true conductivity on the correct geometry; see Figure 6.27.

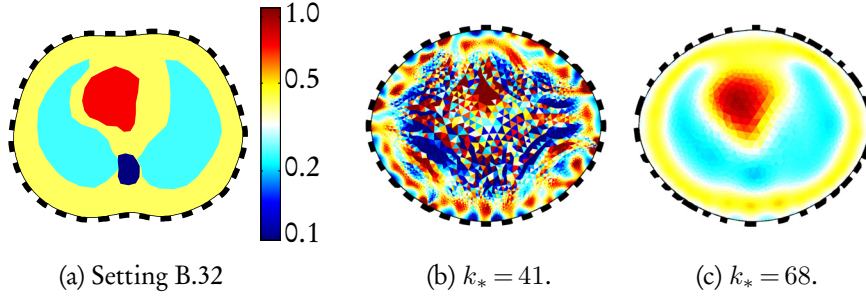


Figure 6.27.: Reconstructions for both varying contact impedances and incorrect boundary geometry. Reconstruction on a fixed wrong model fails (b), simultaneous reconstruction succeeds (c).

6.6. Banach space reconstructions

So far, we used the cg method in an $L^2(\Omega)$ (Hilbert space) setting for the conductivity to stably approximate the weighted pseudo-inverse in the linearized problem. Now, we demonstrate the versatility of MANTIS to do reconstructions in a Banach space framework, as explained in section 5.2.

In Figure 6.28, reconstructions for settings A.32, B.32, C.32, D.32 with $\delta^{\text{rel}} = 0.2\%$ are compared for the $L^2(\Omega)$ Hilbert space framework versus the $L^p(\Omega)$ Banach space framework, where $p = 1.1$. For the Banach space reconstructions, the transformations $t_{\hat{\alpha}}$ and t_{\log} and the weights W_{S_*} are used⁶; see Table 6.21.

An interesting observation is that for the Banach space reconstructions, the difference between using $t_{\hat{\alpha}}$ and t_{\log} can be significant, and the log-transform seems to give somewhat sparser supports for the reconstructed inclusions.

⁶We observed that using the weights $W_{S_*,\sigma}$ in the Banach space setting may result in convergence problems if the regularization parameters of the iterated Tikhonov method for REGINN in Banach spaces are fixed. For the weights W_{S_*} , the parameter choice seems to be more robust, so these weights are used instead.

6. Numerical results

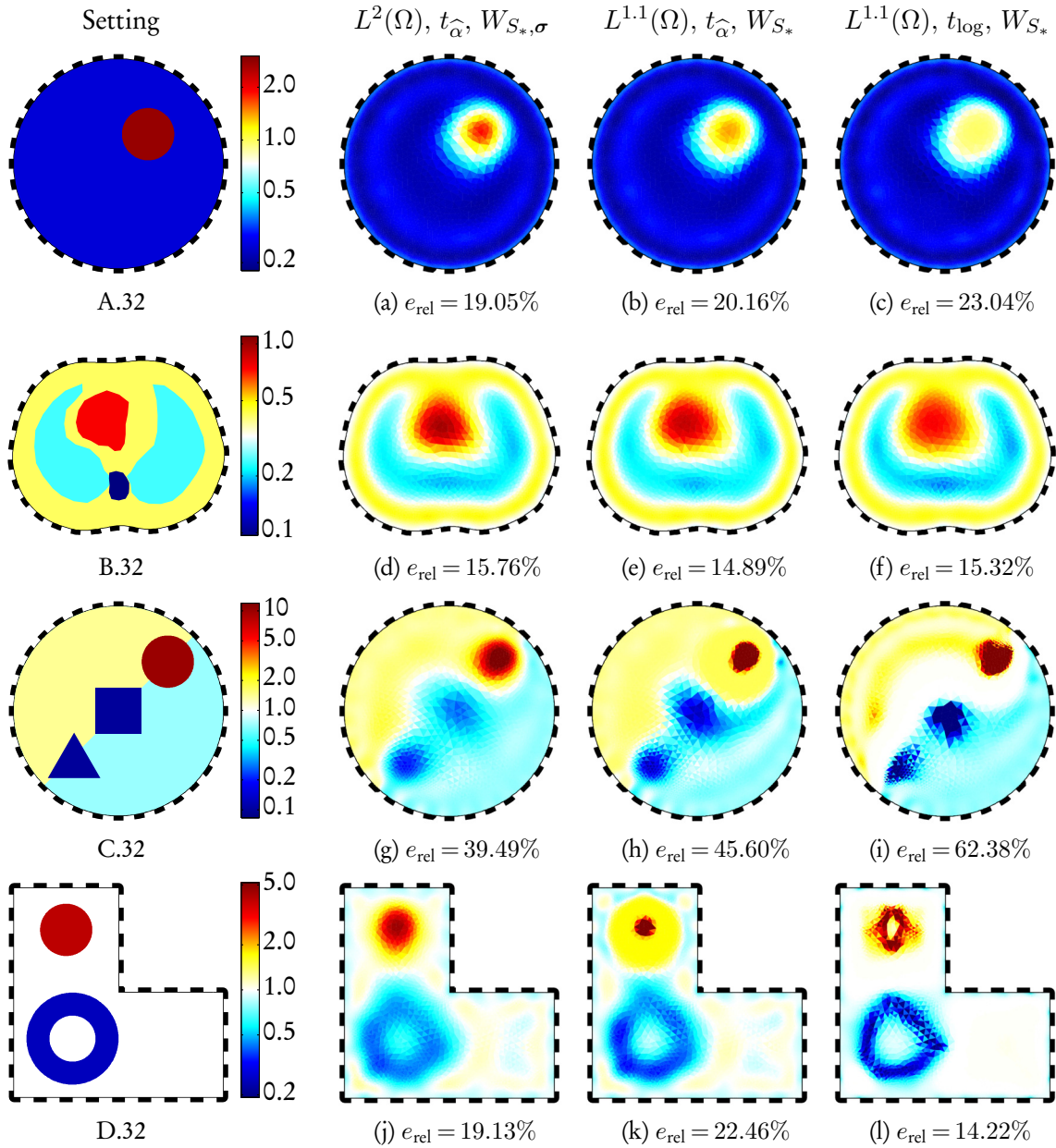


Figure 6.28.: Various settings (left column) with 32 electrodes and $\delta^{\text{rel}} = 0.2\%$ and corresponding reconstructions using the cg method on $L^2(\Omega)$ (2nd column) and the iterated Tikonov method on $L^{1.1}(\Omega)$ for $t_{\hat{\alpha}}$ (3rd column) and for t_{\log} (right column). Using t_{\log} on $L^{1.1}(\Omega)$ seems to result in the sparsest recovered inclusions. The computation times are given in Table 6.21.

6. Numerical results

setting	space	t_*	e_{rel} (%)	$\min(\sigma)$	$\max(\sigma)$	T_{FEM} (s)	T_{jac} (s)	T_{linear} (s)
A.32	L^2	\hat{t}_α	19.05%	1.92×10^{-1}	$1.86 \times 10^{+0}$	1.69	4.21	1.11
A.32	$L^{1.1}$	\hat{t}_α	20.16%	1.89×10^{-1}	$1.40 \times 10^{+0}$	0.75	1.51	386.28
A.32	$L^{1.1}$	t_{\log}	23.04%	1.75×10^{-1}	9.77×10^{-1}	0.89	1.83	492.16
B.32	L^2	\hat{t}_α	15.76%	1.91×10^{-1}	9.77×10^{-1}	1.59	4.13	0.60
B.32	$L^{1.1}$	\hat{t}_α	14.89%	1.91×10^{-1}	9.00×10^{-1}	0.65	1.12	130.45
B.32	$L^{1.1}$	t_{\log}	15.32%	1.74×10^{-1}	7.52×10^{-1}	0.39	0.73	41.40
C.32	L^2	\hat{t}_α	39.49%	1.84×10^{-1}	$1.87 \times 10^{+1}$	1.37	3.46	0.66
C.32	$L^{1.1}$	\hat{t}_α	45.60%	1.03×10^{-1}	$1.00 \times 10^{+2}$	1.73	3.93	1155.97
C.32	$L^{1.1}$	t_{\log}	62.38%	1.00×10^{-2}	$1.00 \times 10^{+2}$	1.47	3.53	600.95
D.32	L^2	\hat{t}_α	19.13%	3.72×10^{-1}	$4.62 \times 10^{+0}$	1.47	3.96	0.76
D.32	$L^{1.1}$	\hat{t}_α	22.46%	3.21×10^{-1}	$3.28 \times 10^{+1}$	1.33	3.22	1559.04
D.32	$L^{1.1}$	t_{\log}	14.22%	1.10×10^{-1}	$2.50 \times 10^{+1}$	1.78	4.66	1001.34

Table 6.21.: Properties of the Banach space reconstructions. The computation time for the linear problem (iterated Tikhonov method) is greatly increased over the corresponding cg method in the Hilbert space setting.

6.7. Reconstructions using nonlinear filtering

In the previous numerical examples, it was demonstrated that using the weights $W_{S_*,\sigma}$ and a suitable conductivity transformation (e.g. t_{\log} or $t_{\hat{\alpha}}$) leads to fast convergence and non-oscillatory solutions of MANTIS in Hilbert spaces. To further enhance piecewise constant solutions, in particular for the Banach space setting where the reconstruction prior does not hold, we pointed out in section 5.3 that iterated nonlinear filtering can be incorporated into MANTIS.

Here, we demonstrate the impact of using median filtering and anisotropic diffusion filtering for reconstructions of settings C.32 and D.32 ($\delta^{\text{rel}} = 0.2\%$) for Hilbert space and Banach space settings (cf. Figure 6.28 in the preceding section). The Hilbert space reconstructions, using $t_{\hat{\alpha}}$ and $W_{S_*,\sigma}$, are shown in Figure 6.29. Using the filters slightly improves the visual appearance of the solutions, but has no significant impact on the reconstruction error. The Banach space reconstructions, using t_{\log} and W_{S_*} due to our observations in the preceding section, are shown in Figure 6.30. Here, the reduction of oscillations is somewhat more pronounced. Further details about the Hilbert space and Banach space reconstructions are given in Tables 6.22 and 6.23, respectively.

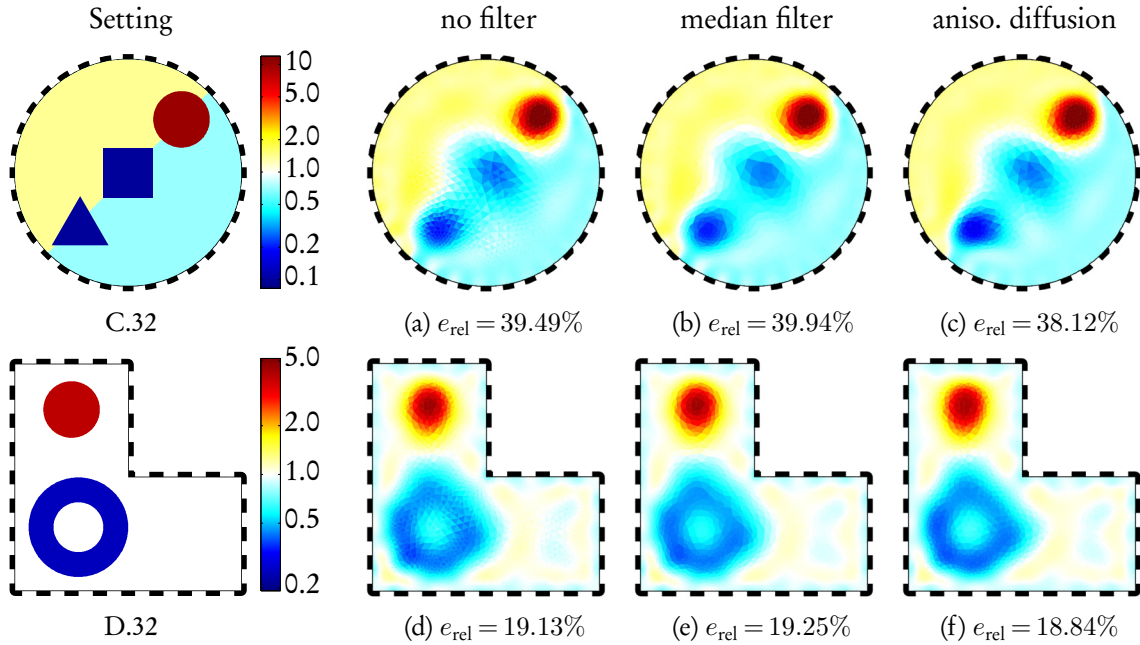


Figure 6.29.: Hilbert space ($L^2(\Omega)$) reconstructions with iterated median filtering (3rd column) and anisotropic diffusion filtering (right column), as described in section 5.3. Conductivity transformation: $t_{\hat{\alpha}}$. Weights: $W_{S_*,\sigma}$.

From these reconstructions, we conclude that the anisotropic diffusion filter gives slightly improved results over the “simple” median filter, but at greatly increased computational cost, in particular since our MATLAB implementation of the anisotropic diffusion just serves as a proof of concept and is highly non-optimized.

6. Numerical results

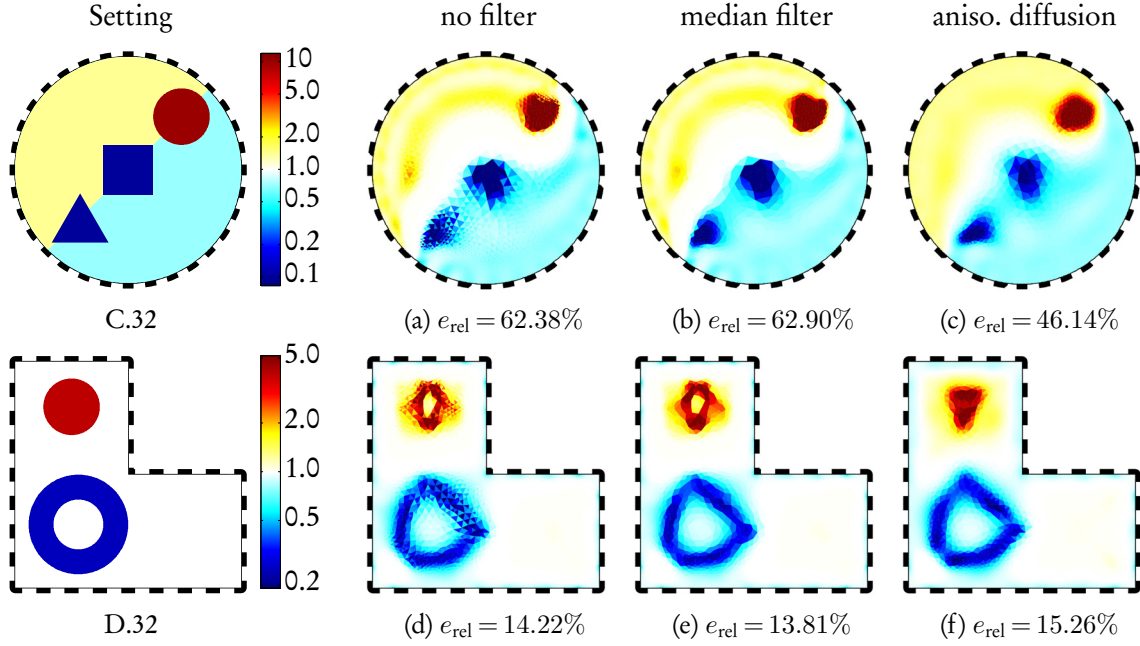


Figure 6.30.: Banach space ($L^1(\Omega)$) reconstructions with iterated median filtering (3rd column) and anisotropic diffusion filtering (right column). Conductivity transformation: t_{\log} . Weights: W_{S_*} .

setting	filter	e_{rel} (%)	k_*	$\min(\sigma)$	$\max(\sigma)$	T_{FEM} (s)	T_{jac} (s)	T_{linear} (s)	T_{filter} (s)
C.32	–	39.49%	10	1.84×10^{-1}	$1.87 \times 10^{+1}$	1.37	3.46	0.66	–
C.32	median	39.94%	10	2.04×10^{-1}	$1.76 \times 10^{+1}$	1.34	3.51	0.66	3.69
C.32	diffusion	38.12%	42	1.74×10^{-1}	$1.87 \times 10^{+1}$	5.33	14.75	1.71	240.47
D.32	–	19.13%	11	3.72×10^{-1}	$4.62 \times 10^{+0}$	1.47	3.96	0.76	–
D.32	median	19.25%	11	3.97×10^{-1}	$4.51 \times 10^{+0}$	1.47	4.00	0.81	4.04
D.32	diffusion	18.84%	56	3.96×10^{-1}	$4.33 \times 10^{+0}$	6.71	20.10	2.39	274.15

Table 6.22.: Properties of the Hilbert space reconstructions using median or anisotropic diffusion filtering. Conductivity transformation: $t_{\hat{\alpha}}$. Weights: $W_{S_*, \sigma}$.

setting	filter	e_{rel} (%)	k_*	$\min(\sigma)$	$\max(\sigma)$	T_{FEM} (s)	T_{jac} (s)	T_{linear} (s)	T_{filter} (s)
C.32	–	62.38%	10	1.00×10^{-2}	$1.00 \times 10^{+2}$	1.46	3.53	600.95	–
C.32	median	62.90%	11	1.00×10^{-2}	$1.00 \times 10^{+2}$	1.51	3.85	423.78	4.14
C.32	diffusion	46.14%	15	2.90×10^{-2}	$1.00 \times 10^{+2}$	2.02	5.27	242.88	161.16
D.32	–	14.22%	12	1.10×10^{-1}	$2.50 \times 10^{+1}$	1.78	4.66	1001.34	–
D.32	median	13.80%	10	2.17×10^{-1}	$1.33 \times 10^{+1}$	1.53	3.86	1246.57	4.08
D.32	diffusion	15.26%	27	1.68×10^{-1}	$9.34 \times 10^{+0}$	3.69	10.19	1338.63	166.22

Table 6.23.: Properties of the Banach space reconstructions using median or anisotropic diffusion filtering. Conductivity transformation: t_{\log} . Weights: W_{S_*} .

6.8. Tank data reconstructions

Finally, we apply MANTIS to the measured tank data of settings F and G. Due to the experiences gathered in the preceding numerical simulations, we will apply MANTIS with the transformation $t_{\hat{\alpha}}$ and the weights $W_{S_*,\sigma}$ both with and without optimizing the electrode parameters in the Hilbert space setting, and with the transformation t_{\log} and the weights W_{S_*} in the Banach space setting. Due to our observations in the preceding numerical example, we use iterated anisotropic diffusion filtering steps to discourage oscillatory solutions for the Banach space reconstructions.

In Figure 6.31, reconstructions for settings F and G.I–G.V in the Hilbert space setting ($t_{\hat{\alpha}}, W_{S_*,\sigma}$) are shown when recovering no electrode parameters (2nd column), recovering only the contact impedances (3rd column), and recovering both the contact impedances and the electrode sizes and locations (4th column) simultaneously along with the conductivity.

Unfortunately, the scaling of the weights for the extended forward operator \bar{F} is not suitable for Banach space reconstructions, since the duality mapping is not linear. To obtain useful results, we used the column-norm weights W_{S_*} for the whole extended sensitivity matrix \bar{S} , and the damping factors from Remark 5.3, but with $w_{\theta}^{(0)} = w_{|E|}^{(0)} = w_z^{(0)} = 1$. These reconstructions are shown in the rightmost column of Figure 6.31. Reconstruction details, including the time T_{mesh} for generating the forward meshes in each iteration (in seconds), are given in Table 6.24.

We observe that the artifacts due to boundary mis-modelling are successfully reduced using the simultaneous reconstruction, and that both the Hilbert space and the Banach space reconstructions recover the inclusions accurately (except for Figure 6.31(t), where the conductive inclusion is not resolved with satisfactory contrast from the background).

6. Numerical results

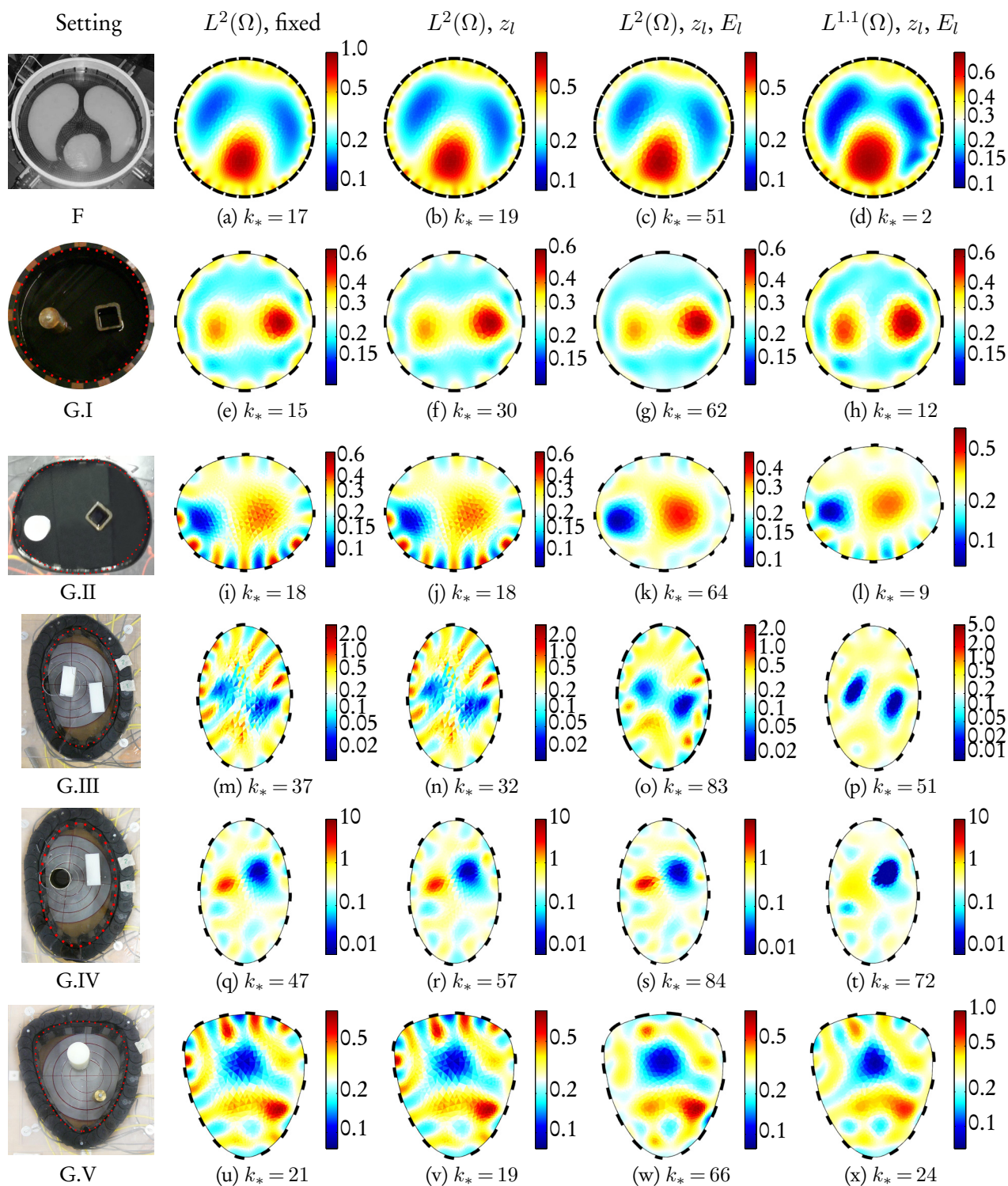


Figure 6.31.: MANTIS results for the tank experiments F (1st row) and G.I – G.V (2nd through 6th row). Lacking reference values, the color bars are scaled to the reconstructed conductivity limits.

6. Numerical results

setting	space	unknowns	k_*	T_{FEM} (s)	T_{jac} (s)	T_{linear} (s)	T_{mesh} (s)
F	$L^2(\Omega)$	σ	17	2.35	5.88	0.58	3.46
	$L^2(\Omega)$	σ, z_l	19	2.58	7.30	0.66	3.27
	$L^2(\Omega)$	σ, z_l, E_l	51	6.58	22.35	2.13	144.58
	$L^{1.1}(\Omega)$	σ, z_l, E_l	2	0.39	0.89	56.84	10.30
G.I	$L^2(\Omega)$	σ	15	0.71	0.59	0.15	1.38
	$L^2(\Omega)$	σ, z_l	30	1.56	1.69	0.24	1.39
	$L^2(\Omega)$	σ, z_l, E_l	62	2.96	3.52	1.10	76.70
	$L^{1.1}(\Omega)$	σ, z_l, E_l	12	0.68	0.88	83.00	24.41
G.II	$L^2(\Omega)$	σ	18	0.83	0.72	0.14	1.34
	$L^2(\Omega)$	σ, z_l	18	0.87	0.93	0.13	1.38
	$L^2(\Omega)$	σ, z_l, E_l	64	2.90	3.45	0.31	84.16
	$L^{1.1}(\Omega)$	σ, z_l, E_l	9	0.47	0.59	57.42	19.93
G.III	$L^2(\Omega)$	σ	37	1.80	1.44	0.32	1.60
	$L^2(\Omega)$	σ, z_l	32	1.51	1.58	0.29	1.65
	$L^2(\Omega)$	σ, z_l, E_l	83	4.02	4.46	0.58	76.07
	$L^{1.1}(\Omega)$	σ, z_l, E_l	51	2.86	3.57	738.37	117.50
G.IV	$L^2(\Omega)$	σ	47	2.18	1.89	0.48	2.29
	$L^2(\Omega)$	σ, z_l	57	2.78	3.10	0.57	2.37
	$L^2(\Omega)$	σ, z_l, E_l	84	3.93	4.38	0.77	79.73
	$L^{1.1}(\Omega)$	σ, z_l, E_l	72	3.97	4.57	1481.60	108.59
G.V	$L^2(\Omega)$	σ	21	1.02	0.81	0.22	1.61
	$L^2(\Omega)$	σ, z_l	19	0.89	0.94	0.20	1.50
	$L^2(\Omega)$	σ, z_l, E_l	66	3.07	3.67	0.42	75.80
	$L^{1.1}(\Omega)$	σ, z_l, E_l	24	1.15	1.44	382.67	27.03

Table 6.24.: Newton iterations and computation times for the tank experiment reconstructions. In our MATLAB implementation, the times for re-meshing and for the linear system in the Banach space setting dominate over the other parts.

6.9. Behaviour of the inexact Newton parameters during inversion

The design idea of the parameter strategy for REGINN in MANTIS was to apply regularization by approximating solutions to the linear system in low-dimensional Krylov subspaces, and then gradually increase the Krylov space dimension to reach the discrepancy principle and obtain convergence. If the tangential cone condition holds and the parameter τ is big enough, we know that both the error and the residual decrease monotonously [Rie05]. In our examples, the tangential cone condition is not satisfied, and $\tau = 1.1$ is chosen rather small. Nonetheless, the parameter strategy yields good results in all reconstructions. In Figure 6.32, we display the behaviour of the parameters $\theta^{(k)}$ and the number⁷ of inner iterations for various reconstructions.

The update rule for the tolerances successfully leads to a gradual increase of cg iterations. Note how

⁷Since we are using the cg method, this is also the dimension of the Krylov subspace in which the solution of the the linear problem is approximated.

6. Numerical results

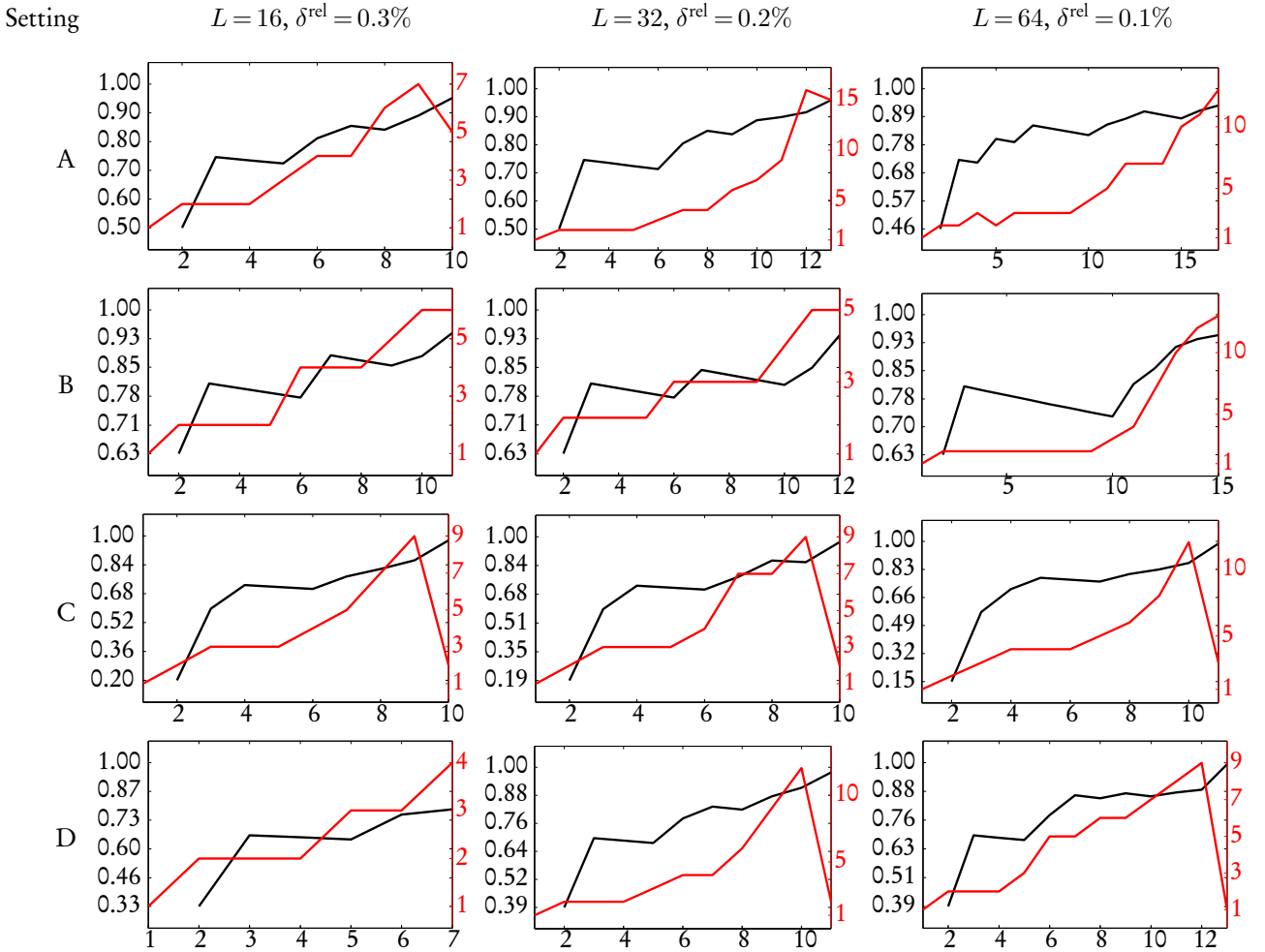


Figure 6.32.: Evolution of the REGINN tolerances $\theta^{(k)}$ (black) and the number of cg iterations $l_*^{(k)}$ (red) for during the Newton iterations, i.e. for $k = 1, \dots, k_*$. The update rule for the tolerances successfully leads to a gradual increase of cg iterations.

the safeguarding rule can lead to a jump down in the number of cg iterations in the last Newton step, thereby preventing an unnecessary decrease of the amount of regularization.

At this point, we want to comment on the computation of the Fréchet derivative; cf. section 2.3.3. The Fréchet derivative can either be evaluated in each step of the conjugate gradient iteration using formulation (2.18), which is basically the same computational effort as solving one forward problem. Alternatively, the entire Jacobian can be assembled explicitly using equation (2.22) once for an entire Newton step, independently of the number of cg iterations. Depending on the number of cg iterations, either the former or the latter might be advantageous. In particular, one could solve each weak formulation for the first Newton steps when the number of cg iterations is small, and switch to the latter once the number of cg iterations increase. Since we did not focus on optimizing the computation times – in particular, the assembly of the Fréchet derivative is not multi-threaded in

6. Numerical results

our implementation – we did not evaluate such a scheme numerically.

Finally, we display the evolution of the nonlinear residual and the reconstruction error in Figure 6.33.

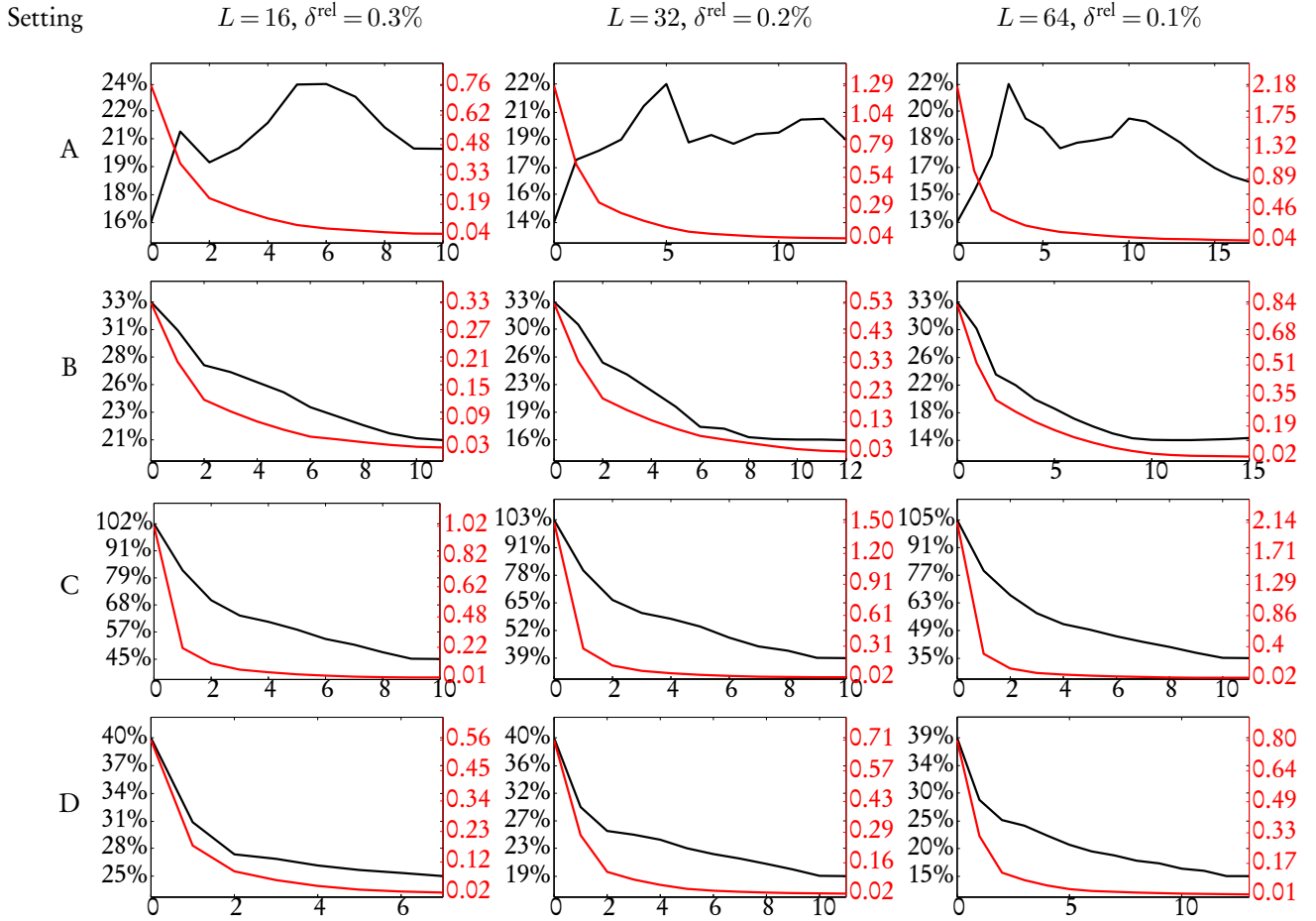


Figure 6.33.: Evolution of the nonlinear residual (red) and the reconstruction error (black) over the Newton iterations. The nonlinear residual mostly decreases monotonically, except for setting A.

The nonlinear residual decreases monotonically in all examples. The reconstruction error decreases monotonically in most examples, except for setting A. Although the reconstruction error increases in some Newton iterations for setting A, we observed in our experiments that the inclusions get more pronounced in each Newton step, so the visual quality of the reconstructions still improves monotonically.

7. Conclusions

Electrical impedance tomography (EIT) opens up numerous new possibilities in tomographic imaging. It is cost effective, portable, suitable for long-term monitoring, and allows for distinguishing objects by their conductivity which are possibly indistinguishable by other imaging methods. However, despite more than 30 years of research in this field, its full potential is not yet available in clinical and industrial applications. A main reason for this is the inherent instability of the underlying mathematical problem. Possible applications and the diagnostic value of EIT depend on the quality of EIT images, that is, on their resolution and their reliability. Moreover, computational efficiency and ease of use are desired for clinical routine.

7.1. Contributions to the field of research

This work contributes to the development of EIT in two regards:

- By *providing new theoretical insights* into the underlying mathematical model and
- by *optimizing and extending* an efficient general purpose inexact Newton scheme to harmonize with the inverse conductivity problem of EIT.

All theoretical findings were *complemented by extensive numerical studies*.

New insights into the model: The complete electrode model (CEM) was established mathematically – and its physical accuracy was verified – already in the early 1990s. An accurate evaluation of the forward operator, i.e. the computation of the current-to-voltage map for a given conductivity, is of both theoretical and practical interest. However, analytic solutions are rare due to the indirect (Robin-type) nature of the boundary conditions. Hence, the forward problem is commonly solved numerically by the finite element method (FEM). An analytic forward solution of the 2D model for circular domains and concentric piecewise constant conductivities was given in [SCI92] using a Fourier expansion of the interior potential, and with a different approach in [Dem11] for homogeneous conductivities. In chapter 3 of the present work, both results could be generalized to non-concentric conductivities.

7. Conclusions

The highly accurate forward solutions obtained by this analytic approach were used in section 3.3 to study the impact of local conductivity changes to the measurements. The resulting *local sensitivity* information is valuable for quantifying the instability of the inverse problem locally. It was used to obtain a *theoretically justified discretization* of the conductivity space. In section 6.4, this discretization yielded improved numerical results over uniform discretizations.

Moreover, the analytic solutions served as input data for our numerical simulations (setting A; see section 6.1.1). When simulating data and solving the inverse problem by the same numerical method, it may occur that imperfections of this method cancel out; this effect is known as *inverse crime*. Using the analytic approach to generate input data and the FEM for inversion, we avoid inverse crime and thereby increase the reliability of the corresponding numerical experiments.

A model-tailored inversion algorithm for EIT: Iterative Newton-type schemes are a popular choice for solving nonlinear optimization problems. Among these methods, the inexact Newton method CG-REGINN is particularly fast and incorporates a regularization strategy, making it suitable for ill-posed problems [Rie05]. However, Newton-type methods are designed to solve unconstrained nonlinear problems locally by linearization. This raises issues for the inverse problem in EIT, which has a positivity constraint on the conductivity and is highly nonlinear.

To resolve these issues, each step of the Newton scheme was investigated in this work and, if necessary, modified to harmonize with the inverse conductivity problem for the CEM:

- Newton-type methods converge to a local solution, thus a well-founded initialization of the Newton scheme is crucial for obtaining good results. Our conductivity initialization (Definition 4.4) was designed to account for the contact impedances of the model. In the presence of contact impedances, it yields more accurate initial guesses than the commonly used initialization (4.3) which is based on the continuum model.
- Along with the conductivity initialization, we obtained an initial guess for the contact impedances of the electrodes. These quantities are usually unknown, yet required to solve the forward problem in each Newton step.
- A good approximation of the data noise level is crucial for stopping the Newton iterations. It was obtained in section 4.1.2 from redundancy of the data due to a symmetry property of the model. Using this estimate with Morozov's discrepancy principle yielded good results in all numerical examples of this work. It was especially useful for the data obtained from saline tank experiments, where the amount and the distribution of the measurement noise is unknown.
- The severe nonlinearity of the forward operator and the constrainedness of the conductivity may cause Newton-type inversions to converge very slowly, to converge to a highly oscillatory local minimum, or to fail by violating the positivity constraint. However, the positivity constraint can be removed and the nonlinearity can possibly be reduced by applying Newton's

7. Conclusions

method to a transformed forward operator. This is often done by considering the logarithm of the conductivity, which is free of sign restrictions. However, other transformations can be used instead. A general framework for transformed forward operators was introduced and a novel transformation with an optimality property for constant conductivities was proposed in section 4.2. Applying this transformation resolved convergence issues and significantly improved the speed of the inversion in the presented numerical evaluations in section 6.2.

- An important design option of REGINN is the norm used for the discretized conductivity space. In section 4.3, it was shown how the choice of the norm affects the resulting Newton update in each iteration. A central result of this work, Theorem 4.22, states that using a weighted norm with the weights of equation (4.26) leads to Newton updates which satisfy the reconstruction prior (4.21). This prior was designed to avoid spurious oscillations in the updates. Another notable property of this weighted norm is that for sufficiently fine conductivity discretizations, the Newton update is almost independent of the discretization. This was shown using a continuum interpretation of the weighted norm in section 4.3.2.
- To be useful in clinical routine, the inversion scheme must be robust and convenient to use. For that reason, the regularization parameter strategy of REGINN was slightly modified by eliminating user-defined parameters.

The resulting inversion scheme for the CEM which contains all these improvements, called model-aware Newton-type inversion scheme (MANTIS), was tested extensively in chapter 6. The simulated settings A–D therein were designed to cover a wide variety of possible scenarios, comprising various boundary shapes, homogeneous and heterogeneous conductivity background, high and low contrast conductivity perturbations of different shape and distance to the boundary, and various electrode counts and data noise levels. The 3D setting E was realized by implementing MANTIS in the open source MATLAB toolbox EIDORS. Finally, settings F and G are based on real measurements from tank experiments with different measurement equipments and different (trigonometric and pairwise) current patterns. In all scenarios, the tailored algorithm modifications resulted in significant improvements over the generic inversion scheme. Moreover, MANTIS was successfully applied to all settings “out of the box”, that is, there was no need to adjust regularization parameters manually for any of the numerical examples.

Problem specific extensions: Finally, the versatility of MANTIS was demonstrated in chapter 5 by adding several *problem specific extensions* to the inversion scheme:

- Unknown model parameters, like electrode positions and sizes and varying contact impedances, can be recovered simultaneously with the conductivity. This makes MANTIS suitable for many EIT applications for which the boundary geometry is not known accurately. The transformation framework introduced for the conductivity was also useful for the reconstruction of the boundary parameters. This was verified numerically in section 6.5.

7. Conclusions

- A Banach space version of REGINN was used instead of CG-REGINN in the MANTIS framework to promote conductivities with sparse inhomogeneities. This is useful e.g. in material testing, where objects are tested for cracks, air bubbles, or other small-support inclusions inside an otherwise homogeneous material. In section 6.6, it was verified that the $L^{1,1}(\Omega)$ setting along with the log-conductivity transformation significantly promotes the sparsity of reconstructed inclusions, compared to the Hilbert space setting.
- Iterated nonlinear filtering was introduced in section 5.3 and used in section 6.7 to further promote non-oscillatory solutions. It was helpful in particular when using the Banach space version of REGINN.

In summary, the proposed inversion scheme MANTIS is both self-contained and versatile. It can be used to solve the inverse problem of EIT in a holistic manner, it is capable of incorporating various additional constraints like smoothness or sparsity assumptions, and it can handle model uncertainties. Based on the inexact Newton method CG-REGINN, it is computationally efficient, in terms of computation time as well as memory usage, when solving the linear problem. Lastly, it is free of design parameters and thus convenient to use for a variety of potential applications in medical and industrial imaging.

7.2. Limitations and future research

Theoretical limitations and open problems: The analytic solution for non-centered perturbations on circular domains was obtained using the rich conformal structure of the 2D case. Although of theoretical interest, there are to date no analytic forward solutions (known to the author) to compute the sensitivity of 3D geometries. Note that a similar discrepancy exists for the inverse problem in Calderón’s model, where uniqueness in the 2D case was established for general $L^{\infty}_{\mp}(\Omega)$ conductivities using complex geometrical optics solutions, but uniqueness in higher dimensions was only shown for (piecewise) smoother spaces [Uhl09].

The conformal structure in 2D also has implications on the recoverability of the boundary geometry from measurement data. While the conductivity can be recovered arbitrarily well in the noiseless case, provided that sufficiently many electrodes are used [LR08], the conformal equivalence of electrode configurations suggests that recovering the boundary geometry in the CEM is an inherently underdetermined problem; cf. Remark 5.1. This means that a rough guess of the boundary shape, the electrode and gap sizes, and some prior knowledge about the conductivity is required to obtain good results. For example, in the literature the conductivity is assumed to be constant or very smooth near the boundary in all cases (known to the author) in which the boundary shape is recovered; see e.g. [KLO05, NKK11, DHSS13a]. Instead of recovering the boundary shape, we restricted ourselves to recovering the electrode geometry along the boundary in sections 6.5.3 and 6.5.4. An

interesting question for future research is if and how the true geometry can be recovered from conformally equivalent reconstructions under additional assumptions, e.g. when the true electrode and gap sizes are known.

Computational efficiency: While the analytic forward solutions derived in chapter 3 were used as a valuable tool for analyzing the model sensitivity, we did not focus on maximizing computational efficiency for initializing and solving of the truncated linear system (B.3). Thus, the computation times shown in Figure 3.7 can be considered at least partly due to our non-optimized “proof of concept” MATLAB implementation.

Another “proof of concept” implementation was used in our numerical examples when recovering the electrode sizes and positions. Therein, a new finite element mesh was generated in each iteration and the conductivity was interpolated accordingly. This may be avoided by successively refining the triangulation to conform with the updated electrode edges.

To further enhance the computational efficiency of MANTIS in terms of memory usage, a Kaczmarz variant of REGINN may be used, as described in [MRLa14] for the Banach space setting. Some early preliminary results however suggest that the Kaczmarz approach does not improve the quality of the reconstruction in MANTIS. Moreover, it might introduce additional artifacts in the reconstructions. As memory consumption was not an issue in our numerical examples, a Kaczmarz version of MANTIS was not pursued any further within this work.

Application to clinical EIT data: In chapter 6, an extensive numerical evaluation based on simulated data and measured tank data was presented. Although clearly of practical interest, numerical examples using clinical EIT data are beyond the scope of this work. The same holds true for time-resolved data. Here, iterative methods like MANTIS have the potential of reducing the computation time of successive images by using preceding results to initialize the Newton iteration.

7.3. Final considerations

The paradigm of this work was to address the inverse problem of EIT in a holistic manner. In particular, “generic” assumptions of the inversion scheme were systematically replaced by justified information that was gathered from the model or extracted from the measurement data.

Although each part of the inversion was designed to harmonize with the whole scheme, the individual modifications can also be considered as a “set of tools” to improve other existing inversion techniques. For example, the presented initializations and the suggested discretization strategy might be useful for other iterative inversion schemes.

Moreover, the choice of the conductivity transformation arose from the question “*Is there a way to make the problem more suitable for linearization?*”. The untransformed forward operator of the CEM

7. *Conclusions*

turned out to be particularly unsuitable for linearization. Thus, a transformation of the forward operator might be considered for any gradient-based inversion scheme applied to EIT.

Lastly, the proposed weighted norm for the conductivity space with the weights (4.31) contains information about the Jacobian of the measurement operator. This means that the norm depends not purely on the conductivity, but also on the measurement operator, that is, on the information about the conductivity contained in the measurements.

In summary, the performance and reliability of the considered inversion scheme for EIT was improved by eliminating sources of instabilities, by abandoning generic assumptions, and by gathering and using prior knowledge about the specific setting and model.

Appendix

A. A wealth of inversion approaches

Since the formulation of Calderón’s problem, a wealth of approaches to analyze and solve the ICP has been proposed, reflecting entirely different points of view of electrical engineers, physicians, and mathematicians, on the “same” physical problem.

An early concept is a filtered back-projection variant for the ICP, which is motivated by the propagation of currents in homogeneous media and by concepts used in X-ray computed tomography (where the name stems from) [BB84, SV90]. However, the propagation of currents inside the object is modelled quite crude, with currents flowing rather localized than following the path of least resistance. Moreover, the electrode behaviour is neglected. Although being fast and yielding acceptable results in some clinical applications [Dö99], this method is considered deprecated [Hol04] since the development of more advanced methods.

An approach motivated by electrical engineering is a simplified model of the propagation of currents inside the object, given by a resistor network [BDGV08]. The charm of this approach is that results from graph theory guarantee a unique solution of the resistor network problem [CM00] for certain electrode configurations, which then can be projected back on the domain to obtain a conductivity distribution. Moreover, a shunting effect of the electrodes can be considered in the model. This method is justified mathematically for near-constant conductivities, but the inversion algorithm, a sort of “layer stripping” method inside the resistor network to compute the resistances, is exponentially unstable, similar to the continuum layer stripping algorithm [SCII91]. Thus, the concept succeeds only for few electrodes and very low noise.

A whole field of entirely different, “purely mathematical” approaches originates from Calderón’s continuum formulation of the ICP and uses a class of exponentially growing and decreasing functions, the *complex geometrical optics* (CGO) solutions to the Laplace problem. The use of CGO solutions and the transformation of Calderón’s problem to a Schrödinger equation led to a series of uniqueness proofs for Calderón’s problem in two and three dimensions for conductivities with decreasing regularity assumptions [SU87, Nac96, AP06]. Some of the proofs are constructive, yielding direct reconstruction algorithms like [KV87] or the D-bar method [SMI00]. All methods are based on the continuum boundary model, require very accurate data and assume constant conductivity near the object surface. A comprehensive overview of the history, the construction and some modifications and extensions to these solutions is given in [MS12].

A. A wealth of inversion approaches

All previously described methods lack an accurate modelling of the electrode behaviour. One reason is that the boundary description of the CEM is bulky: Direct “pointwise” access to Dirichlet (potential) data is lost due to the contact impedances, and a direct application of Neumann (current density) data is impossible due to the shunting effect of the electrodes. This makes it hard to analyze the CEM in closed-form terms. However, two fundamental results link Calderón’s model to the CEM. Firstly, the celebrated factorization method for inverse scattering problems [CK96, Kir98] can be applied to the Calderón’s problem [Bru01], more precisely, to the difference of the forward operators for homogeneous and perturbed conductivities. Applying the factorization method to this difference data shows that the support of the inclusions from a connected background can be uniquely identified by a direct, parallel reconstruction algorithm, which is a fundamental result in its own right [BH00]. Additionally, this difference of forward operators can be approached by its CEM equivalents as the number of electrodes increases [LHH08]. The key observation here is that some effects introduced by electrodes cancel out in the difference data, making it easier to address the CEM analytically. A remarkable consequence is that the linearized problem of the ICP for the CEM has a unique solution, i.e. the Fréchet derivative of the forward operator is injective for a large class of discretized conductivity spaces, assuming that the number of electrodes is big enough, yet finite [LR08].

Finally, there is a wide variety of iterative regularized Newton-type methods, arguably the most renowned technique for solving nonlinear ill-posed inverse problems [KNS08]. They stem from the fact that the forward operators of the ICP are differentiable [KKS00]. Thus, they can be successively linearized to find a conductivity fitting the observed data, e.g. by minimizing a regularized output-least-squares functional. Newton-type methods are appealing for solving the ICP of the CEM for several reasons. Most importantly, the forward operator of the CEM and its Fréchet derivative can be evaluated stably and at moderate computational cost using the finite element method (FEM) [PL02]. This means that all electrode effects modelled by the CEM are considered. Moreover, Newton-type methods are well understood analytically and numerically, and many modifications and extensions are known to improve the speed and radius of convergence, to address instabilities arising from ill-posedness, data noise, and mis-modelling, or to reduce computation time. Variants include the Gauß-Newton method, the Levenberg-Marquardt method, Quasi-Newton methods and inexact Newton methods with various penalty/smoothing terms; see e.g. [YWT87, WHWT93, RGA96, CCT05, LR06] and the review article [Hol04]. We explicitly include the nonlinear Tikhonov regularization and its probabilistic sibling in the Bayesian framework here, as the minimizer of the Tikhonov functional and the MAP solution of the Bayesian model are usually determined by Newton-type algorithms; see e.g. [VVK⁺98, KKS00]. Prominent reductions of Newton’s method are one-step linearizations, like the Tikhonov-regularized NOSER algorithm [CIN⁺90] and a total-variation-regularized algorithm [DS94]. To further reduce the computational effort in these one-step approaches, the Fréchet derivative at a constant conductivity and for a fixed geometry is usually pre-computed and factorized.

A. A wealth of inversion approaches

In summary, different approaches have emerged and prevailed for very different reasons, including simplicity, ease of use, rigorous application of concepts from uniqueness results, and explicit design of regularization strategies in standard nonlinear inversion frameworks.

B. Fourier coefficients of the extended complete electrode model

Proof of Theorem 3.10. In contrast to Theorem 3.3, we now have to deal with non-constant contact impedances z_l^w which complicate the integral expressions.

In the preceding proof, the reciprocal of the contact impedance appears in (3.12) due to equation (3.10). However, the reciprocal of the transformed conductivity z_l^w (cf. (3.24)) is unsuitable for closed-form integration when multiplied by cosine or sine terms as it contains a $\cos(\tilde{\theta})$ term in the denominator. To solve (3.26) for j_ν^w and yet avoid $\frac{1}{\cos(\tilde{\theta})}$ terms on either side of the equation, we use the representation

$$\frac{1+T^2}{1-T^2} j_\nu^w(\tilde{\theta}) = \begin{cases} \frac{1}{z_l} (U_l - f^w(\tilde{\theta})) - \frac{2T \cos(\tilde{\theta})}{1-T^2} j_\nu^w(\tilde{\theta}) & \text{on } E_l^w, \\ 0 & \text{otherwise.} \end{cases} \quad (\text{B.1})$$

As in the centered case, we substitute the Fourier representations (3.31) and (3.32) of f^w and j_ν^w into (B.1) and multiply both sides with the test functions $\cos(n\tilde{\theta})$, $n \in \mathbb{N}_0$, and $\sin(n\tilde{\theta})$, $n \in \mathbb{N}$, respectively. Then, we again integrate in $\tilde{\theta}$ over $[0, 2\pi)$. For better readability, we use $t(n\tilde{\theta})$ as a placeholder for any of these (cosine and sine) test functions. On the left-hand side, we get

$$\int_0^{2\pi} t(n\tilde{\theta}) \frac{1+T^2}{1-T^2} j_\nu^w(\tilde{\theta}) d\tilde{\theta} = \begin{cases} 0 & \text{for } n = 0, \\ \pi\sigma_1 \frac{1+T^2}{1-T^2} d_n \tilde{a}_n & \text{for the cosine terms,} \\ \pi\sigma_1 \frac{1+T^2}{1-T^2} d_n \tilde{b}_n & \text{for the sine terms.} \end{cases} \quad (\text{B.2})$$

On the right-hand side, we get

$$\begin{aligned} & \sum_{l=1}^L \frac{U_l}{z_l} \int_{\tilde{\theta}_l - \tilde{\omega}_l}^{\tilde{\theta}_l + \tilde{\omega}_l} t(n\tilde{\theta}) d\tilde{\theta} - \tilde{u}_0 \sum_{l=1}^L \frac{1}{z_l} \int_{\tilde{\theta}_l - \tilde{\omega}_l}^{\tilde{\theta}_l + \tilde{\omega}_l} t(n\tilde{\theta}) d\tilde{\theta} \\ & - \sum_{k=1}^{\infty} \tilde{a}_k \sum_{l=1}^L \left[\frac{1}{z_l} \int_{\tilde{\theta}_l - \tilde{\omega}_l}^{\tilde{\theta}_l + \tilde{\omega}_l} t(n\tilde{\theta}) \cos(k\tilde{\theta}) d\tilde{\theta} + \frac{2T\sigma_1 d_k}{1-T^2} \int_{\tilde{\theta}_l - \tilde{\omega}_l}^{\tilde{\theta}_l + \tilde{\omega}_l} t(n\tilde{\theta}) \cos(\tilde{\theta}) \cos(k\tilde{\theta}) d\tilde{\theta} \right] \\ & - \sum_{k=1}^{\infty} \tilde{b}_k \sum_{l=1}^L \left[\frac{1}{z_l} \int_{\tilde{\theta}_l - \tilde{\omega}_l}^{\tilde{\theta}_l + \tilde{\omega}_l} t(n\tilde{\theta}) \sin(k\tilde{\theta}) d\tilde{\theta} + \frac{2T\sigma_1 d_k}{1-T^2} \int_{\tilde{\theta}_l - \tilde{\omega}_l}^{\tilde{\theta}_l + \tilde{\omega}_l} t(n\tilde{\theta}) \cos(\tilde{\theta}) \sin(k\tilde{\theta}) d\tilde{\theta} \right], \end{aligned}$$

B. Fourier coefficients of the extended complete electrode model

where $\tilde{\theta}_l$ and $\tilde{\omega}_l$ denote the centers and half-widths of the electrodes E_l^w respectively for $l = 1, \dots, L$. We again rearrange each equation to be used as one row of a linear system of equations for \tilde{u}_0 and $\tilde{a}_k, \tilde{b}_k, k \in \mathbb{N}$, and return to the notation of (3.14). In the conformally mapped case, we get (with the same abusive ordering) the system

$$\begin{pmatrix} \tilde{A} & \tilde{B}^1 \\ \tilde{B}^2 & \tilde{C} \end{pmatrix} (\tilde{u}_0, \tilde{a}_1, \tilde{a}_2, \dots, \tilde{b}_1, \tilde{b}_2, \dots)^\top = \begin{pmatrix} \tilde{r}^U \\ \tilde{s}^U \end{pmatrix}. \quad (\text{B.3})$$

The coefficients are given by

$$\begin{aligned} \tilde{A}_{nk} &= \sum_{l=1}^L \frac{1}{z_l} \int_{\tilde{\theta}_l - \tilde{\omega}_l}^{\tilde{\theta}_l + \tilde{\omega}_l} \cos(n\tilde{\theta}) \cos(k\tilde{\theta}) \, d\tilde{\theta} + \delta_{nk} \pi \sigma_1 \frac{1 + T^2}{1 - T^2} d_k \\ &\quad + \frac{2T\sigma_1 d_k}{1 - T^2} \sum_{l=1}^L \int_{\tilde{\theta}_l - \tilde{\omega}_l}^{\tilde{\theta}_l + \tilde{\omega}_l} \cos(n\tilde{\theta}) \cos(\tilde{\theta}) \cos(k\tilde{\theta}) \, d\tilde{\theta} \\ &= \sum_{l=1}^L \frac{1}{2z_l} [\tilde{s}_l(k - n) + \tilde{s}_l(k + n)] + \delta_{nk} \pi \sigma_1 \frac{1 + T^2}{1 - T^2} d_k \\ &\quad + \frac{T\sigma_1 d_k}{2(1 - T^2)} \sum_{l=1}^L [\tilde{s}_l(\alpha_{n,k}) + \tilde{s}_l(\beta_{n,k}) + \tilde{s}_l(\gamma_{n,k}) + \tilde{s}_l(\kappa_{n,k})], \quad n \in \mathbb{N}_0, k \in \mathbb{N}_0, \end{aligned} \quad (\text{B.4})$$

$$\begin{aligned} \tilde{B}_{nk}^1 &= \sum_{l=1}^L \frac{1}{z_l} \int_{\tilde{\theta}_l - \tilde{\omega}_l}^{\tilde{\theta}_l + \tilde{\omega}_l} \cos(n\tilde{\theta}) \sin(k\tilde{\theta}) \, d\tilde{\theta} \\ &\quad + \frac{2T\sigma_1 d_k}{1 - T^2} \sum_{l=1}^L \int_{\tilde{\theta}_l - \tilde{\omega}_l}^{\tilde{\theta}_l + \tilde{\omega}_l} \cos(n\tilde{\theta}) \cos(\tilde{\theta}) \sin(k\tilde{\theta}) \, d\tilde{\theta} \\ &= \sum_{l=1}^L \frac{1}{2z_l} [\tilde{c}_l(k - n) + \tilde{c}_l(k + n)] \\ &\quad + \frac{T\sigma_1 d_k}{2(1 - T^2)} \sum_{l=1}^L [\tilde{c}_l(\alpha_{n,k}) + \tilde{c}_l(\beta_{n,k}) - \tilde{c}_l(\gamma_{n,k}) - \tilde{c}_l(\kappa_{n,k})], \quad n \in \mathbb{N}_0, k \in \mathbb{N}, \end{aligned}$$

$$\begin{aligned} \tilde{B}_{nk}^2 &= \sum_{l=1}^L \frac{1}{z_l} \int_{\tilde{\theta}_l - \tilde{\omega}_l}^{\tilde{\theta}_l + \tilde{\omega}_l} \sin(n\tilde{\theta}) \cos(k\tilde{\theta}) \, d\tilde{\theta} \\ &\quad + \frac{2T\sigma_1 d_k}{1 - T^2} \sum_{l=1}^L \int_{\tilde{\theta}_l - \tilde{\omega}_l}^{\tilde{\theta}_l + \tilde{\omega}_l} \sin(n\tilde{\theta}) \cos(\tilde{\theta}) \cos(k\tilde{\theta}) \, d\tilde{\theta} \\ &= \sum_{l=1}^L \frac{1}{2z_l} [\tilde{c}_l(n - k) + \tilde{c}_l(n + k)] \\ &\quad + \frac{T\sigma_1 d_k}{2(1 - T^2)} \sum_{l=1}^L [\tilde{c}_l(\alpha_{k,n}) + \tilde{c}_l(\beta_{k,n}) - \tilde{c}_l(\gamma_{k,n}) - \tilde{c}_l(\kappa_{k,n})], \quad n \in \mathbb{N}, k \in \mathbb{N}_0, \end{aligned}$$

B. Fourier coefficients of the extended complete electrode model

$$\begin{aligned}
\tilde{C}_{nk} &= \sum_{l=1}^L \frac{1}{z_l} \int_{\tilde{\theta}_l - \tilde{\omega}_l}^{\tilde{\theta}_l + \tilde{\omega}_l} \sin(n\tilde{\theta}) \sin(k\tilde{\theta}) \, d\tilde{\theta} + \delta_{nk} \pi \sigma_1 \frac{1+T^2}{1-T^2} d_k \\
&\quad + \frac{2T\sigma_1 d_k}{1-T^2} \sum_{l=1}^L \int_{\tilde{\theta}_l - \tilde{\omega}_l}^{\tilde{\theta}_l + \tilde{\omega}_l} \sin(n\tilde{\theta}) \cos(\tilde{\theta}) \sin(k\tilde{\theta}) \, d\tilde{\theta} \\
&= \sum_{l=1}^L \frac{1}{2z_l} [\tilde{s}_l(k-n) - \tilde{s}_l(k+n)] + \delta_{nk} \pi \sigma_1 \frac{1+T^2}{1-T^2} d_k \\
&\quad + \frac{T\sigma_1 d_k}{2(1-T^2)} \sum_{l=1}^L [-\tilde{s}_l(\alpha_{n,k}) + \tilde{s}_l(\beta_{n,k}) + \tilde{s}_l(\gamma_{n,k}) - \tilde{s}_l(\kappa_{n,k})], \quad n \in \mathbb{N}, k \in \mathbb{N},
\end{aligned}$$

$$\begin{aligned}
\tilde{r}_n^U &= \sum_{l=1}^L \frac{U_l}{z_l} \int_{\tilde{\theta}_l - \tilde{\omega}_l}^{\tilde{\theta}_l + \tilde{\omega}_l} \cos(n\tilde{\theta}) \, d\tilde{\theta} = \sum_{l=1}^L \frac{U_l}{z_l} \tilde{s}_l(n), \quad n \in \mathbb{N}_0, \\
\tilde{s}_n^U &= \sum_{l=1}^L \frac{U_l}{z_l} \int_{\tilde{\theta}_l - \tilde{\omega}_l}^{\tilde{\theta}_l + \tilde{\omega}_l} \sin(n\tilde{\theta}) \, d\tilde{\theta} = - \sum_{l=1}^L \frac{U_l}{z_l} \tilde{c}_l(n). \quad n \in \mathbb{N}.
\end{aligned}$$

with Kronecker delta δ_{nk} , d_k as in (3.5),

$$\alpha_{n,k} := -k - n + 1, \quad \beta_{n,k} := -k + n + 1, \quad \gamma_{n,k} := k - n + 1, \quad \kappa_{n,k} := k + n + 1,$$

and $\tilde{s}_l(k), \tilde{c}_l(k)$ defined analogously to $s_l(k), c_l(k)$ in (3.9), replacing θ_l and ω_l therein by $\tilde{\theta}_l$ and $\tilde{\omega}_l$, respectively, for $l = 1, \dots, L$.

Note in particular that in contrast to the previous proof, $\tilde{B}_{nk}^1 \neq \tilde{B}_{kn}^2$ in general for $T > 0$ due to the influence of the coefficients d_k . \square

Bibliography

- [Ale88] G Alessandrini. Stable determination of conductivity by boundary measurements. *Applicable Analysis*, 27(1-3):153–172, 1988.
- [Ale90] G Alessandrini. Singular solutions of elliptic equations and the determination of conductivity by boundary measurements. *Journal of differential equations*, 84(2):252–272, 1990.
- [AP06] K Astala and L Päivärinta. Calderón’s inverse conductivity problem in the plane. *Annals of Mathematics*, pages 265–299, 2006.
- [BB84] DC Barber and BH Brown. Applied potential tomography. *Journal of Physics E: Scientific Instruments*, 17(9):723, 1984.
- [BDGV08] L Borcea, V Druskin, and F Guevara Vasquez. Electrical impedance tomography with resistor networks. *Inverse Problems*, 24(3):035013, 2008.
- [BH00] M Brühl and M Hanke. Numerical implementation of two noniterative methods for locating inclusions by impedance tomography. *Inverse Problems*, 16(4):1029, 2000.
- [Bru99] M Brühl. *Gebietserkennung in der elektrischen Impedanztomographie*. PhD thesis, Fakultät für Mathematik der Universität Karlsruhe (TH), 1999.
- [Bru01] M Brühl. Explicit characterization of inclusions in electrical impedance tomography. *SIAM Journal on Mathematical Analysis*, 32(6):1327–1341, 2001.
- [BS87] DC Barber and AD Seagar. Fast reconstruction of resistance images. *Clinical Physics and Physiological Measurement*, 8(4A):47, 1987.
- [Cal80] AP Calderón. On an inverse boundary value problem. In *Seminar on Numerical Analysis and its Applications to Continuum Physics*, pages 65–73. Soc. Brasileira de Matemática, 1980.
- [CCT05] ET Chung, TF Chan, and XC Tai. Electrical impedance tomography using level set representation and total variational regularization. *Journal of Computational Physics*, 205(1):357–372, 2005.

Bibliography

- [CF02] MT Clay and TC Ferree. Weighted regularization in electrical impedance tomography with applications to acute cerebral stroke. *Medical Imaging, IEEE Transactions on*, 21(6):629–637, 2002.
- [CI92] M Cheney and D Isaacson. Distinguishability in impedance imaging. *Biomedical Engineering, IEEE Transactions on*, 39(8):852–860, 1992.
- [CIN⁺90] M Cheney, D Isaacson, JC Newell, S Simske, and JC Goble. NOSER: An algorithm for solving the inverse conductivity problem. *International Journal of Imaging Systems and Technology*, 2(2):66–75, 1990.
- [CING89] KS Cheng, D Isaacson, JC Newell, and DG Gisser. Electrode models for electric current computed tomography. *Biomedical Engineering, IEEE Transactions on*, 36(9):918–924, 1989.
- [CK96] D Colton and A Kirsch. A simple method for solving inverse scattering problems in the resonance region. *Inverse problems*, 12(4):383–393, 1996.
- [CM00] EB Curtis and JA Morrow. *Inverse problems for electrical networks*, volume 13. World Scientific, 2000.
- [CSI⁺90] K Cheng, SJ Simske, D Isaacson, JC Newell, and DG Gisser. Errors due to measuring voltage on current-carrying electrodes in electric current computed tomography. *Biomedical Engineering, IEEE Transactions on*, 37(1):60–65, 1990.
- [Dem11] E Demidenko. An analytic solution to the homogeneous EIT problem on the 2d disk and its application to estimation of electrode contact impedances. *Physiological Measurement*, 32(9):1453–1471, 2011.
- [DHH⁺12] J Dardé, H Hakula, N Hyvönen, S Staboulis, and E Somersalo. Fine-tuning electrode information in electrical impedance tomography. *Inverse Problems and Imaging*, 6(3):399–421, 2012.
- [DHSP05] E Demidenko, A Hartov, N Soni, and KD Paulsen. On optimal current patterns for electrical impedance tomography. *Biomedical Engineering, IEEE Transactions on*, 52(2):238–248, 2 2005.
- [DHSS13a] J Dardé, N Hyvönen, A Seppänen, and S Staboulis. Simultaneous reconstruction of outer boundary shape and admittivity distribution in electrical impedance tomography. *SIAM Journal on Imaging Sciences*, 6(1):176–198, 2013.
- [DHSS13b] J Dardé, N Hyvönen, A Seppänen, and S Staboulis. Simultaneous recovery of admittivity and body shape in electrical impedance tomography: an experimental evaluation. *Inverse Problems*, 29(8):085004, 2013.

Bibliography

- [Dob92] DC Dobson. Estimates on resolution and stabilization for the linearized inverse conductivity problem. *Inverse problems*, 8(1):71–81, 1992.
- [DS94] DC Dobson and F Santosa. An image-enhancement technique for electrical impedance tomography. *Inverse Problems*, 10(2):317, 1994.
- [Dö99] O Dössel. *Bildgebende Verfahren in der Medizin: Von der Technik zur medizinischen Anwendung*. Springer, 1999.
- [ESNI95] PM Edic, GJ Saulnier, JC Newell, and D Isaacson. A real-time electrical impedance tomograph. *Biomedical Engineering, IEEE Transactions on*, 42(9):849–859, 1995.
- [FEHP11] C Forbes, M Evans, N Hastings, and B Peacock. *Statistical Distributions*. Wiley, 4 edition, 2011.
- [FM26] H Fricke and S Morse. The electric capacity of tumors of the breast. *The Journal of Cancer Research*, 10(3):340–376, 1926.
- [Fre00] Inéz Frerichs. Electrical impedance tomography (EIT) in applications related to lung and ventilation: a review of experimental and clinical activities. *Physiological Measurement*, 21(2):R1–R21, 2000.
- [GA14] B Grychtol and A Adler. Choice of reconstructed tissue properties affects interpretation of lung EIT images. *Physiological measurement*, 35(6):1035, 2014.
- [GIN90] DG Gisser, D Isaacson, and JC Newell. Electric current computed tomography and eigenvalues. *SIAM Journal on Applied Mathematics*, 50(6):1623–1634, 1990.
- [GLB⁺12] B Grychtol, WRB Lionheart, M Bodenstern, GK Wolf, and A Adler. Impact of model shape mismatch on reconstruction quality in electrical impedance tomography. *Medical Imaging, IEEE Transactions on*, 31(9):1754–1760, 9 2012.
- [Han92] PC Hansen. Analysis of discrete ill-posed problems by means of the L-curve. *SIAM review*, 34(4):561–580, 1992.
- [Han97] M Hanke. Regularizing properties of a truncated Newton-cg algorithm for nonlinear inverse problems. *Numerical Functional Analysis and Optimization*, 18(9–10):971–993, 1997.
- [HLU15] B Harrach, E Lee, and M Ullrich. Combining frequency-difference and ultrasound modulated electrical impedance tomography. *Inverse Problems*, 31(9):095003, 2015.
- [Hol93] D Holder. *Clinical and physiological applications of electrical impedance tomography*. CRC Press, 1993.
- [Hol04] DS Holder. *Electrical Impedance Tomography: Methods, History and Applications*. Series in Medical Physics and Biomedical Engineering. Taylor & Francis, 2004.

Bibliography

- [HU13] B Harrach and M Ullrich. Monotony based inclusion detection in EIT for realistic electrode models. *Journal of Physics: Conference Series*, 434(1):012076, 2013.
- [HW78] RP Henderson and JG Webster. An impedance camera for spatially specific measurements of the thorax. *Biomedical Engineering, IEEE Transactions on*, BME-25(3):250–254, 5 1978.
- [Hyv04] N Hyvönen. Complete electrode model of electrical impedance tomography: Approximation properties and characterization of inclusions. *SIAM Journal on Applied Mathematics*, 64(3):902–931, 2004.
- [IMNS04] D Isaacson, JL Mueller, JC Newell, and S Siltanen. Reconstructions of chest phantoms by the D-bar method for electrical impedance tomography. *Medical Imaging, IEEE Transactions on*, 23(7):821–828, 2004.
- [Isa86] D Isaacson. Distinguishability of conductivities by electric current computed tomography. *Medical Imaging, IEEE Transactions on*, 5(2):91–95, 1986.
- [Jin12] Q Jin. Inexact newton–landweber iteration for solving nonlinear inverse problems in banach spaces. *Inverse Problems*, 28(6):065002, 2012.
- [JM12] B Jin and P Maaß. An analysis of electrical impedance tomography with applications to Tikhonov regularization. *ESAIM: Control, Optimisation and Calculus of Variations*, 18(04):1027–1048, 2012.
- [Kir98] A Kirsch. Characterization of the shape of a scattering obstacle using the spectral data of the far field operator. *Inverse problems*, 14(6):1489, 1998.
- [KKSV00] JP Kaipio, V Kolehmainen, E Somersalo, and M Vauhkonen. Statistical inversion and monte carlo sampling methods in electrical impedance tomography. *Inverse Problems*, 16(5):1487, 2000.
- [KLO05] V Kolehmainen, M Lassas, and P Ola. The inverse conductivity problem with an imperfectly known boundary. *SIAM Journal on Applied Mathematics*, 66(2):365–383, 2005.
- [KNS08] B Kaltenbacher, A Neubauer, and O Scherzer. *Iterative Regularization Methods for Non-linear Ill-Posed Problems*. Radon Series on Computational and Applied Mathematics. De Gruyter, 2008.
- [KV87] RV Kohn and M Vogelius. Relaxation of a variational method for impedance computed tomography. *Communications on Pure and Applied Mathematics*, 40(6):745–777, 1987.
- [Lan36] RE Langer. On the determination of earth conductivity from observed surface potentials. *Bull. Amer. Math. Soc.*, 42(10):747–754, 10 1936.

Bibliography

- [LHH08] A Lechleiter, N Hyvönen, and H Hakula. The factorization method applied to the complete electrode model of impedance tomography. *SIAM Journal on Applied Mathematics*, 68(4):1097–1121, 2008.
- [LKM01] WRB Lionheart, J Kaipio, and CN McLeod. Generalized optimal current patterns and electrical safety in EIT. *Physiological Measurement*, 22(1):85–90, 2001.
- [LR06] A Lechleiter and A Rieder. Newton regularizations for impedance tomography: a numerical study. *Inverse Problems*, 22(6):1967–1987, 2006.
- [LR08] A Lechleiter and A Rieder. Newton regularizations for impedance tomography: convergence by local injectivity. *Inverse Problems*, 24(6):065009, 2008.
- [LR10] A Lechleiter and A Rieder. Towards a general convergence theory for inexact Newton regularizations. *Numerische Mathematik*, 114(3):521–548, 2010.
- [Mar15] F Margotti. *On Inexact Newton Methods for Inverse Problems in Banach Spaces*. PhD thesis, Karlsruher Institut für Technologie, 2015.
- [McL00] WCH McLean. *Strongly Elliptic Systems and Boundary Integral Equations*. Cambridge University Press, 2000.
- [MMM04] HR MacMillan, TA Manteuffel, and SF McCormick. First-order system least squares and electrical impedance tomography. *SIAM journal on numerical analysis*, 42(2):461–483, 2004.
- [MR14] F Margotti and A Rieder. An inexact Newton regularization in Banach spaces based on the nonstationary iterated tikhonov method. *Journal of Inverse and Ill-posed Problems*, 23:373–392, 2014.
- [MRLa14] F Margotti, A Rieder, and A Leitão. A Kaczmarz version of the REGINN-Landweber iteration for ill-posed problems in Banach spaces. *SIAM Journal on Numerical Analysis*, 52(3):1439–1465, 2014.
- [MS12] JL Mueller and S Siltanen. *Linear and Nonlinear Inverse Problems with Practical Applications*, volume 10 of *Computational Science and Engineering*. SIAM, 2012.
- [Nac96] AI Nachman. Global uniqueness for a two-dimensional inverse boundary value problem. *Annals of Mathematics*, pages 71–96, 1996.
- [Neh52] Z Nehari. *Conformal mapping*. 1952, volume 13. McGraw-Hill Book Company, Inc., New York MR, 1952.

Bibliography

- [NKI⁺15] S Nebuya, T Koike, Y Iwashita, H Kumagai, K Soma, M Arai, H Imai, and BH Brown. A wearable electrical impedance tomography system - its features and clinical application. In J Solà, F Braun, and A Adler, editors, *Proceedings of the 16th International Conference on Biomedical Applications of Electrical Impedance Tomography*, page 83. CSEM SA, 2015.
- [NKK11] A Nissinen, V Kolehmainen, and J Kaipio. Compensation of modelling errors due to unknown domain boundary in electrical impedance tomography. *Medical Imaging, IEEE Transactions on*, 30(2):231–242, 2011.
- [Oh09] Sungho Oh. *Compensation of shape change artifacts and spatially-variant image reconstruction problems in electrical impedance tomography*. PhD thesis, University of Florida, 2009.
- [Pal02] VP Palamodov. Gabor analysis of the continuum model for impedance tomography. *Arkiv för Matematik*, 40(1):169–187, 2002.
- [PL02] N Polydorides and W Lionheart. A MATLAB-based toolkit for three-dimensional electrical impedance tomography: A contribution to the EIDORS project. *Measurement Science and Technology*, 13(12), 2002.
- [RGA96] W Ruan, R Guardo, and A Adler. Experimental evaluation of two iterative reconstruction methods for induced current electrical impedance tomography. *Medical Imaging, IEEE Transactions on*, 15(2):180–187, 4 1996.
- [Rie99] A Rieder. On the regularization of nonlinear ill-posed problems via inexact Newton iterations. *Inverse Problems*, 15(1):309–327, 1999.
- [Rie03] A Rieder. *Keine Probleme mit Inversen Problemen: Eine Einführung in ihre stabile Lösung*. Vieweg+ Teubner Verlag, 2003.
- [Rie05] A Rieder. Inexact Newton regularization using conjugate gradients as inner iteration. *SIAM Journal on Numerical Analysis*, 43(2):604–622, 2005.
- [SBB87] AD Seagar, DC Barber, and BH Brown. Theoretical limits to sensitivity and resolution in impedance imaging. *Clinical Physics and Physiological Measurement*, 8(4A):13–31, 1987.
- [SCI92] E Somersalo, M Cheney, and D Isaacson. Existence and uniqueness for electrode models for electric current computed tomography. *SIAM Journal on Applied Mathematics*, 52(4):1023–1040, 1992.
- [SCII91] E Somersalo, M Cheney, D Isaacson, and E Isaacson. Layer stripping: a direct numerical method for impedance imaging. *Inverse Problems*, 7(6):899, 1991.

Bibliography

- [SKW05] JK Seo, O Kwon, and EJ Woo. Magnetic resonance electrical impedance tomography (MREIT): conductivity and current density imaging. *Journal of Physics: Conference Series*, 12(1):140, 2005.
- [SL91] R Schinzinger and PAA Laura. *Conformal mapping: methods and applications*. Elsevier, Amsterdam, 1991.
- [Sli33] LB Slichter. The interpretation of the resistivity prospecting method for horizontal structures. *Journal of Applied Physics*, 4(9):307–322, 1933.
- [SMI00] S Siltanen, J Mueller, and D Isaacson. An implementation of the reconstruction algorithm of A Nachman for the 2d inverse conductivity problem. *Inverse Problems*, 16(3):681, 2000.
- [SSBS88] AJ Surowiec, SS Stuchly, JR Barr, and A Swarup. Dielectric properties of breast carcinoma and the surrounding tissues. *Biomedical Engineering, IEEE Transactions on*, 35(4):257–263, 4 1988.
- [SU87] J Sylvester and G Uhlmann. A global uniqueness theorem for an inverse boundary value problem. *Annals of Mathematics*, 125(1):153–169, 1987.
- [SV90] F Santos and M Vogelius. A backprojection algorithm for electrical impedance imaging. *SIAM J. Appl. Math.*, 50(1):216–243, 1 1990.
- [SYB84] AD Seagar, TS Yeo, and RHT Bates. Full-wave computed tomography. Part 2: Resolution limits. *IEE Proceedings A (Physical Science, Measurement and Instrumentation, Management and Education, Reviews)*, 131(8):616–622, 1984.
- [Syl90] J Sylvester. An anisotropic inverse boundary value problem. *Communications on Pure and Applied Mathematics*, 43(2):201–232, 1990.
- [SZTO08] RJ Sadleir, SU Zhang, AS Tucker, and Sungho Oh. Imaging and quantification of anomaly volume using an eight-electrode 'hemiarrray' EIT reconstruction method. *Physiological measurement*, 29(8):913–927, 2008.
- [Uhl09] G Uhlmann. Electrical impedance tomography and Calderón's problem. *Inverse Problems*, 25(12):123011, 2009.
- [Vau97] M Vauhkonen. *Electrical impedance tomography and prior information*. PhD thesis, University of Kuopio, 1997.
- [VKV⁺02] T Vilhunen, JP Kaipio, PJ Vauhkonen, T Savolainen, and M Vauhkonen. Simultaneous reconstruction of electrode contact impedances and internal electrical properties: I. theory. *Measurement Science and Technology*, 13(12):1848–1854, 2002.

Bibliography

- [VVK⁺98] M Vauhkonen, D Vadasz, PA Karjalainen, E Somersalo, and JP Kaipio. Tikhonov regularization and prior information in electrical impedance tomography. *Medical Imaging, IEEE Transactions on*, 17(2):285–293, 1998.
- [Wah77] G Wahba. Practical approximate solutions to linear operator equations when the data are noisy. *SIAM Journal on Numerical Analysis*, 14(4):651–667, 1977.
- [WB95] RA Williams and MS Beck. *Process Tomography*. Butterworth-Heinemann, Oxford, 1995.
- [Wei98] J Weickert. *Anisotropic diffusion in image processing*. ECMI series. Teubner, Stuttgart, 1998.
- [WHWT93] EJ Woo, P Hua, JG Webster, and WJ Tompkins. A robust image reconstruction algorithm and its parallel implementation in electrical impedance tomography. *Medical Imaging, IEEE Transactions on*, 12(2):137–146, Jun 1993.
- [WR14] R Winkler and A Rieder. Resolution-controlled conductivity discretization in electrical impedance tomography. *SIAM Journal on Imaging Sciences*, 7(4):2048–2077, 2014.
- [WR15] R Winkler and A Rieder. Model-aware Newton-type inversion scheme for electrical impedance tomography. *Inverse Problems*, 31(4):045009, 2015.
- [YWT87] TJ Yorkey, JG Webster, and WJ Tompkins. Comparing reconstruction algorithms for electrical impedance tomography. *Biomedical Engineering, IEEE Transactions on*, BME-34(11):843–852, 11 1987.